



UNIVERSITY OF DOUALA
FACULTY OF SCIENCES
POSTGRADUATE SCHOOL FOR
PURE AND APPLIED SCIENCES

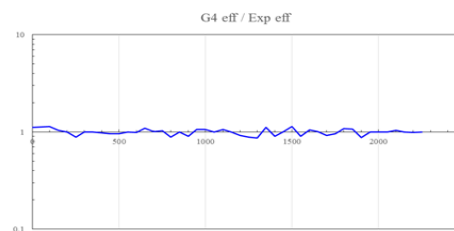
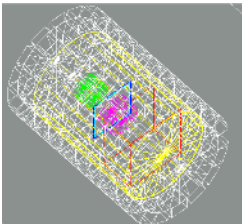
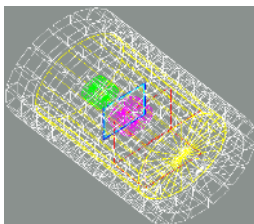
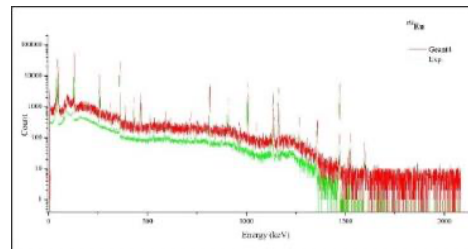
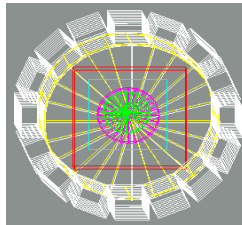
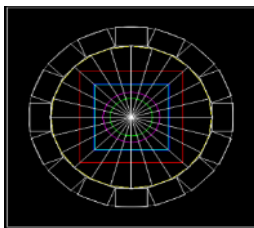


UNIVERSITE DE LIEGE
FACULTE DES SCIENCES
SPECTROSCOPIE ATOMIQUE ET
NUCLEAIRE, ARCHEOMETRIE

Study of the natural radioactivity background of the Douala University Campuses and surrounding by Nuclear Techniques: Validation by GEANT4 Monte Carlo simulations

Cebastien Joel

GUEMBOU SHOUOP



January 2022



UNIVERSITY OF DOUALA
FACULTY OF SCIENCES
POSTGRADUATE SCHOOL FOR
PURE AND APPLIED SCIENCES

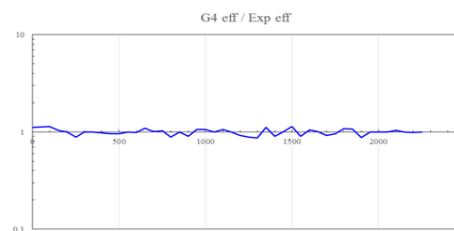
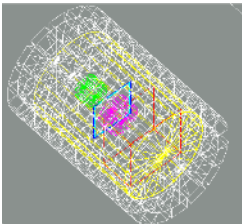
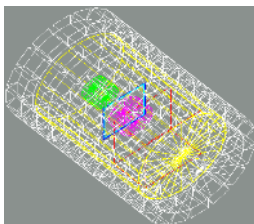
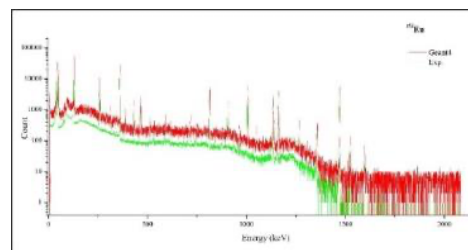
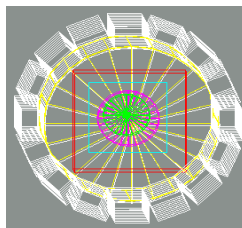
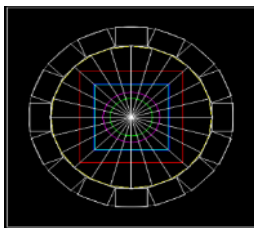


UNIVERSITE DE LIEGE
FACULTE DES SCIENCES
SPECTROSCOPIE ATOMIQUE ET
NUCLEAIRE, ARCHEOMETRIE

Study of the natural radioactivity background of the Douala University Campuses and surrounding by Nuclear Techniques: Validation by GEANT4 Monte Carlo simulations

Cebastien Joel

GUEMBOU SHOUOP



January 2022

This work was partially supported by DREAMS Project grant from European Commission coordinated by the University of Porto (10 months of support).
Support also came from the IPNAS under the supervision of

David STRIVAY (Professor)

Acknowledgements

I remember writing the acknowledgements for my Master's thesis, and how difficult it was to include everyone who helped me both professionally and personally that year. Given the vastly increased scope of my thesis project, I will here attempt to express my thanks and gratitude with some degree of concision and restraint, as to account for everyone would require a small book in itself. For those whose names are not included in this section, I always remember that thanking hundred people does not end the list of those who helped me by much or a little during this achievement. So, I will try to be brief.

This work would not have been possible without the financial support of the University of Liege (through the Atomic and Nuclear Spectroscopy, Archeometry Laboratory known as "Spectroscopy Atomique et Nucleaire, Archeometrie" or SANA) and the DREAM ACP 2015 project (European Commission coordinated by the University of Porto) with the grant number DR14DM5893. I am especially indebted to **David STRIVAY**, Ousmanou MOTAPON, and **Maurice NDONTCHUENG MOYO** who have been working hard to support my thesis goals, to provide me with academic advices and protective time to pursue those goals and to advise me for years in different matters. Your eternal optimism and faith in people will stay with me for a while. As my teachers, guides, mentors, and friends, you have all taught me more than I could ever credit any of you. It was a big deal to combine your tasks and my personal life goals. But you have all shown me through your actions what a good scientist and person should be as well as provided me with a work environment in which I have been able to flourish both professionally and personally. **David** - Thank you for teaching me how to manage financial support and produce valuable result, how to sleep on a bar stool, and valorize and appreciate the work we have to do. Thank you for teaching me to come out of my silence and present what is in my mind at conferences and summer schools. **Maurice** - thank you for reminding me that a PhD thesis is not just a period project, but a life one.

My sincere gratitude goes to **NGUENANG**, the head of the Department of Physics and to **MUKENGUE**, the head of the Faculty of Science for administrative support of my PhD thesis. **Augustin SIMO**, thank you for the support from the National Radiation Protection Agency of Cameroon in the sense that the professional skills I got when working with you helped me to come close to real after PhD life. I am also grateful for the γ -ray spectrometry laboratory equipment.

I'm grateful to the Atomic and Nuclear Spectroscopy, Archeometry (SANA) staff of the University of Liege and the academic staff of the Laboratory of Fundamental Physics of the University of Douala. I refer to **Anne-Laure VILLEMENOT**, **Martine LOVATO**, **Rita SANTOS**, **Monique MARCOURT**, and **Fatima MARINHO** for administrative assistance of the part of the project that has been developed at the University of Liege. When referring to the University of Douala, I would

Acknowledgements

like to thank **Alexandre NGWA EBONGUE, Rene YAMAPI, Andre LENOUE, David MONKAM, NOUPA, Cyril KENFACK, DAFOUNANSOU,** and **Alex NDENGUE** for all their support during my academic growing.

I am grateful to everyone whom I have had the pleasure to work with during this thesis report and other related projects, especially my lab coworker members including **Gregoire CHENE, Elodie HERENS, Catherine DEFEYT, Manon D'HAENENS, Mathieu CLAR,** and **Saïd RAKKAA** and all of the interns I worked with including **Eric NGUELEM, Samafou PENABE, Theophile TCHAKOUA,** Eric EFON and mentored including **Steve KAYO, Mineur NDIEULA, Cynthia NOUBEWO, Marie NGOYEM, Patricia DEGBE,** and **Diane BOKWA.** I also thank all my graduate student cohort at the University of Douala, **Ruth NANA, Laetitia MBETKWE, Gervais CHENDJOU,** and **Nadine TSAGUE.**

Then, there are many of my colleagues, personal friends, or classmates, who are too numerous to mention individually. But some of them as **Michael KOAGNE, Martial TAGA, Duclair NGOMPE, Yves KWINDOU, Guizimo TONGYANG, Samuel BADJE,** and **Serge TAKOUKAM** were special as they helped me to view life the right way and to live with godly principles.

Each member of my Dissertation Committee has provided me extensive personal and professional guidance and taught me a great deal about scientific research and life. I really appreciate your advices and encouragements. To be bold, strong, and courageous, I did need your expression of love and your smile. I would especially thank **Nathalie FAGEL** and other thesis committee members.

No one has been more important in my life while pursuing this PhD project than my family. I would like to thank my ultimate role models, my mother **Francoise KOAGNE** and my three siblings, whose love, guidance, and strength are with me in whatever I chose to do. I would also like to thank my cousin, uncles and aunts, who have always been there to cheer me up and help me see the life as a beautiful gift where everything we accomplish could be celebrated with a cup of whisky. Thanks to my uncle **David NOUFE,** his wife **Alice NOUFE** (my second mother), their daughters **Hershelle** (named **Melody** “my baby”) and **Jael NOUFE** for always being there, playing with and supporting me. Thank you to my friends out of the scope of the science. Thanks to **Giresse NOUFE, Anne MEKUO, Uriel NGNIAGUEPAHA, Sylvain & Adeline TAGNE, Jacob & Justine TCHOUMTCHOUA,** and **Lena.**

Last but not the least, I would like to thank my lovely wife **Rebecca KESEPPE MADOUTSA epse GUEMBOU** who was always a source of strength and support during the finalization of this thesis.

Abstract

The present thesis focused on an ionizing radiation monitoring project of the soils of the University of Douala campuses (campus 1 and 2) and surrounding, in the Littoral region of Cameroon. The purpose was to provide a baseline to document the conditions present at the time of sampling. The methodology used γ -ray spectrometry-based High Purity Germanium detector (HPGe), both Energy Dispersive X-Ray Fluorescence (EDXRF) and Wavelength Dispersive X-Ray Fluorescence (WDXRF) spectrometry for sample's elemental characterization, and the Monte Carlo simulation-based Geant4 toolkit for detector efficiency calibration. The Geant4 toolkit also provides the opportunity to optimize the detection systems using computer simulations and greatly reduces the need for expensive (radiation exposure to calibration sources) testing in the laboratory.

The assessment of $^{238,235}\text{U}$, ^{232}Th , ^{137}Cs , and ^{40}K concentration was done by measuring soil and sand samples by γ spectrometry-based High Purity Germanium detectors (HPGe). Both laboratories of the National Radiation Protection Agency (NRPA) of Cameroon and the Atomic and Nuclear Spectroscopy, Archeometry Laboratory of the University of Liege were used for experiments. Geochemical characterization of soil samples, origin determination, and provenience were accessed by X-ray spectroscopy. By comparing the results of two detectors and the technics used according to the detector type, improvements on the γ spectrometry methodology were made. The relative uncertainty activity concentration was calculated for ^{226}Ra , ^{232}Th , and ^{40}K . The average report between the GC0818-7600SL model and the BEGe-6530 model was the main outcome that suggested real attention that should be paid when selecting the radionuclide to be investigated on a specific type of detector. The BEGe detector was found to be more suitable for low γ energy emitters measurement, compared to the GC0818-7600SL model, found more efficient for high energy γ emitters.

The potential radiological hazards parameters were assessed by calculating successively the following parameters from using those sands in the construction of dwellings and large buildings: Radium Equivalent activity (R_{eq}), Outdoor absorbed γ dose rate (D_{out}), Annual Effective Dose rate (AED), Internal hazard (H_{in}) and external hazard (H_{ex}) indexes, and α and γ indexes for sand samples used as building materials. Results obtained show that Annual Effective Dose absorbed by in-habitants due to the use of the investigated sand as construction materials was found to be below 1.0 mSv y^{-1} . Therefore, sand used as building materials from the investigated quarries appears to be radio-logically safe for building construction and for the environment (beaches, built houses, ...) where people could safely spend time. Soil characterization using EDXRF in the present study provided an overview of the geological origin or provenience of the investigated area. As a result, the analyzed soil samples could be classified chemically as Fe-soil and are illustrative dregs from the Continental margin because of the high concentration of Fe in all the investigated samples. These data record the elemental composition and the natural radionuclide's radioactivity levels of the studied area and could be set as reference database information in the region, in Cameroon as well as for the Gulf of Guinea's data.

Monte Carlo validation based on the GEANT4 toolkit has been used to validate the efficiency calibration of the system, and it has been noticed that the combination of γ -ray spectrometry, the development of related Monte Carlo methods, and the GEANT4 (GEometry ANd Tracking) toolkit developed for γ spectrometry simulation are compelling and useful for detector characterization nowadays. It can then be concluded that the Monte Carlo simulation gives more prominent adaptability, greater flexibility, gained time, precision, and accuracy when determining the detector response and efficiency in the routine of environmental radioactivity monitoring.

Keywords : *Natural radionuclides; Monte Carlo Simulation; GEANT4; γ -ray Spectrometry; XRF; HPGe*

Résumé

La présente thèse porte sur un projet de surveillance de l'exposition aux rayonnements ionisants naturels des sols des campus de l'Université de Douala (campus 1 et 2) et alentours, dans la région du Littoral Cameroun. Le but est de fournir une base de référence pour documenter les conditions présentes au moment de l'échantillonnage afin de mesurer la contamination artificielle à la suite des accidents nucléaires. La méthodologie est basée sur l'utilisation d'un détecteur de Germanium haute pureté pour la spectrométrie γ , la spectrométrie de fluorescence X à dispersion d'énergie (EDXRF) et de fluorescence X à dispersion en longueur d'onde (WDXRF) pour la caractérisation élémentaire de l'échantillon et la simulation Monte Carlo. La boîte à outils Geant4 a été utilisée pour l'étalonnage de l'efficacité des détecteurs.

L'évaluation des concentrations de ^{238}U , ^{235}U , ^{232}Th , ^{137}Cs et ^{40}K a été effectuée en mesurant des échantillons de sol et de sable par la spectrométrie γ . Les deux laboratoires de l'Agence Nationale de Radioprotection (ANRP) au Cameroun et du Laboratoire de Spectroscopie atomique et nucléaire, archéométrie de l'Université de Liège ont été utilisés pour les mesures expérimentales. La caractérisation élémentaire des échantillons de sol, la détermination de l'origine et la provenance géologique ont été effectuées par spectroscopie à fluorescence X. En comparant les résultats de deux détecteurs et les techniques utilisées selon le type de détecteur, des améliorations ont été apportées sur la méthodologie. L'incertitude relative sur les concentrations d'activité a été calculée pour le ^{226}Ra , ^{232}Th et ^{40}K . Le rapport moyen entre le modèle de détecteur GC0818-7600SL et le modèle BEGe-6530 a été le principal résultat suggérant une réelle attention à accorder lors de la sélection du radionucléide à étudier sur un type de détecteur spécifique. Le détecteur BEGe s'est avéré plus approprié pour la mesure d'émetteurs γ de faible énergie, par rapport au modèle GC0818-7600SL, jugé plus efficace pour les émetteurs γ à haute énergie.

Les paramètres de risques radiologiques ont été évalués en calculant successivement les paramètres suivants : activité équivalente radium (Ra_{eq}), débit de dose γ absorbé à l'extérieur (D_{out}), débit de dose efficace annuel, Les indices de danger interne (H_{in}) et de danger externe (h_{ex}) et les indices α et γ pour les échantillons de sable utilisés comme matériaux de construction. Les résultats obtenus montrent que la dose efficace annuelle absorbée par les habitants en raison de l'utilisation du sable étudié comme matériaux de construction s'est avérée inférieure à $1,0 \text{ mSv y}^{-1}$. Par conséquent, le sable utilisé comme matériau de construction des carrières étudiées semble être radiologiquement sans danger pour la construction de bâtiments et pour l'environnement (plages, maisons construites, ...) où les gens pourraient passer du temps en toute sécurité. La caractérisation du sol dans la présente étude a donné un aperçu de l'origine géologique ou de la provenance de la zone étudiée. En conséquence, les échantillons de sol analysés pourraient être classés chimiquement comme des sols ferrallitiques et sont des résidus illustratifs de la marge continentale en raison de la forte concentration de Fe dans tous les échantillons étudiés. Ces données pourraient servir de base de données de référence dans la région, au Cameroun ainsi que pour les données du golfe de Guinée.

La modélisation Monte Carlo basée sur la boîte à outils GEANT4 a été utilisée pour valider l'étalonnage de l'efficacité du système, et il a été remarqué que la combinaison de la spectrométrie γ , le développement des méthodes Monte Carlo associées et l'outil GEANT4 (GEometry ANd Tracking) est une méthode convaincante et utile pour la caractérisation des détecteurs au germanium. On peut alors conclure que la simulation Monte Carlo donne une adaptabilité plus importante, une plus grande flexibilité, un gain de temps, de précision et d'exactitude lors de la détermination de la réponse et de l'efficacité du détecteur dans le domaine de la surveillance de la radioactivité environnementale.

Mots clés : radionucléides naturels ; Simulation de Monte Carlo ; GEANT4 ; Spectrométrie- γ ; XRF ; HPGe.

Thesis Outline

After a brief general introduction and background of the research in the chapter 1, chapter 2 presents the interaction of ionizing rays with matter. The description of direct and indirect ionizing rays has been developed in this section. Since γ ray are used for qualitative and quantitative characterization of the samples in γ spectrometry, it has been a subject of particular attention in this chapter. Different processes of γ -ray interaction with matter have been developed to show the physics processes involved during their interaction and used later for GEANT4 simulations.

In chapter 3 we present the γ -ray spectrometry method used for radiological characterization of the samples investigated in this thesis. The study is based on semi-conductor detector and for this reason, only HPGe detectors characterization was presented in this section. The process is based on methodology description including sampling and sample preparation, detector calibration, experimental protocol, and result analysis and interpretation for both model of detectors used in this thesis. The following chapter (Chapter 4) presents the results of γ -ray spectrometry analysis and the discussion. The campuses of the University of Douala, and the quarries of the city of Douala and surrounding are the area of experimentation and the results from both sites have been presented.

Chapter 5 contains a complete characterization of X-Ray Fluorescence spectrometry using the same samples as those used in γ spectrometry. Two methods have been using: Energy Dispersive X-Ray Fluorescence (EDXRF) and Wavelength Dispersive X-Ray Fluorescence (WDXRF). The description of the methodology and the results obtained are presented in this chapter. Nevertheless, perspectives on the characterization of the same samples using PIXE and PIGE are expected soon. In chapter 6 we present a wide description of Monte Carlo method used for simulation in the validation process during this thesis. The principle of the Monte Carlo Method Applied to the Particle Transport and its application for Semi-Conductor Detectors calibration is presented in principle. In addition, the GEANT4 toolkit useful aspects for the present study is presented at the middle of the chapter and its implementation in γ -rays spectrometry concluded the chapter.

Chapter 7 presents the result of Monte Carlo simulation of the BEGe detector (BE6530 model) based on GEANT4 toolkit. Basic concepts of geometry definition and material definition are presented with a wide range of geometry constructed in this research. After the presentation of the geometries built in this thesis, the process of efficiency simulation and the results for our detector are presented. This chapter end up with the validation of the GEANT4 simulation which uses Monte Carlo equation and C++ language code. The last chapter presents the conclusion and future work that will be implemented in the future. At the end of this manuscript, we present the general conclusions of this thesis and the scientific communications derived from the work. Appendixes and references are the last part of the document.

Dedication

“The more you learn, the more you have come to the conclusion: *I don't know anything*”

So, as long as I'm alive, I'll never stop asking, knocking, and searching

“The one who watches the wind will not sow seed, and the one who looks at the clouds will not reap”

(Proverbs 11:4, from King Solomon)

Contents

Acknowledgements.....	v
Abstract.....	vii
Résumé.....	ix
Thesis Outline.....	xi
Dedication.....	xiii
Contents.....	xv
List of Figures.....	xix
List of Tables.....	xxv
Abbreviations and symbols.....	xxvii
Constants and Units.....	xxix
CHAPTER 1. GENERAL INTRODUCTION AND BACKGROUND.....	1
1.1. Introduction.....	1
1.2. Natural sources of ionizing radiation.....	3
1.3. Importance of the Monte Carlo Simulation.....	3
1.4. Relevance and justifications of the study.....	4
1.5. Description of the environment of work.....	5
1.6. Overview of the research.....	7
1.7. Aims of the research.....	8
CHAPTER 2. INTERACTION OF RADIATION WITH MATTER - PHOTON.....	9
2.1. Particulate Radiation.....	9
2.2. Electromagnetic Radiation – Photons.....	15
2.3. Interaction of Electromagnetic radiation with matter.....	15
2.4. Particle Transport and Linear Energy Transfer (LET).....	23
2.5. Conclusion.....	26
CHAPTER 3. γ SPECTROMETRY AND RADIATION MEASUREMENT.....	27
3.1. Introduction.....	27
3.2. HPGe Detectors Characterization.....	27

Contents

3.3.	Experimental Protocol in γ -ray spectrometry	36
3.4.	Measurements of Activity concentration.	48
3.5.	Assessment of radiation hazard and radiological parameters.....	49
3.6.	Conclusion.....	51
CHAPTER 4. γ SPECTROMETRY RESULT AND DISCUSSION		53
A.	<i>Campuses of the University of Douala (Campus 1 and 2)</i>	53
4.1.	The concentration of natural radionuclides.....	53
4.2.	Comparison between the two detectors.....	58
B.	<i>Quarries in Douala and Surroundings</i>	64
4.3.	Activity concentration in the Extending Area	64
4.4.	Radium equivalent activity (Ra_{eq}).....	67
4.5.	Radiological parameters and radiation hazard.....	68
4.6.	Conclusion.....	73
CHAPTER 5. X-RAY FLUORESCENCE ANALYSIS		75
5.1.	Interest of XRF Analysis.....	75
5.2.	XRF Protocol and Experiment.....	76
5.3.	XRF-Results and Discussion: Elemental composition	83
5.4.	Sample Classification and geological provenance.....	95
5.5.	Conclusion.....	101
CHAPTER 6. MONTE CARLO METHOD AND GEANT4 TOOLKIT		103
6.1.	Introduction.....	103
6.2.	State of the art	104
6.3.	Monte Carlo Method	106
6.4.	Geant4 Toolkit overview	115
6.5.	GEANT4 for γ -ray spectrometry.....	119
6.6.	Experimental Setup for GEANT4.....	125
6.7.	Conclusions	127
CHAPTER 7. GEANT4 VALIDATION STUDIES		129
7.1.	Geometry and material definitions	129

Contents

7.2. Geometry built in this thesis	132
7.3. Efficiency Simulation	140
CHAPTER 8. CONCLUSIONS AND OUTLOOK	149
8.1. General conclusions	149
8.2. Specific Conclusions.....	150
8.3. Future Work.....	154
Appendix A: Decay Chains.....	157
A.1. The ²³² Th decay chain.....	157
A.2. The ²³⁵ U decay chain	158
A.3. The ²³⁸ U decay chain.....	159
Appendix B: HPGe and EDXRF methodology	161
I. γ - & X-ray spectrometry	161
Appendix C: List of Scientific Contribution	164
Scientific Publications as first or corresponding author	164
Additional Publications.....	165
Scientific congresses, seminars and symposia	166
REFERENCES.....	169

Contents

List of Figures

Figure 1-1: Sampling site-geographic localizations: the first studied site selected, the campuses of the University of Douala-Cameroon.....	6
Figure 1-2: Sampling site-geographic localizations, the second studied sites. Sand Building material used in Douala and its surrounding. Map of the seven big sand quarries in Douala-Cameroon.....	6
Figure 1-3: CANBERRA high purity germanium detectors used in Cameroon’s spectrometry laboratory (left: BEGe 6530).	6
Figure 2-1: A polar plot of the intensity of Compton scattered radiation as a function of scattering angle, θ . Higher energy photons tend to be forward scattered, while lower energy γ -ray tends to be more evenly distributed [34, 53, 66].	17
Figure 2-2: The photon absorption coefficient for a material (lead in this case) at different photon energies.	20
Figure 2-3: The photon absorption coefficient through germanium material at different photon energy.....	21
Figure 2-4: The three main interactions of photon with matter considered in the rest of the manuscript for computational work: photoelectric effect, Compton scattering, and pair production from right to left. Rayleigh scattering (or elastic scattering) is neglected in the rest of the project as its contribution is negligible in the framework of the present research.	21
Figure 2-5: Relative predominance of photon interaction processes [64]. Only the main processes described in this section are presented.....	22
Figure 2-6: Exponential law of attenuation of photon when interacting with matter (x denotes the thickness of the medium).	22
Figure 3-1: Representation of HPGe as reverse biased semiconductor diode: principle of semiconductor detector counting system.	28
Figure 3-2: Broad Energy Germanium detector (BE 6540 model) used in Cameroon	30
Figure 3-3: Band structure of the high purity germanium detector based on semi-conductor technology.....	31
Figure 3-4: On the left side: closed-ended coaxial BEGe 6530 in N-type configuration. Right side: dimensions of the HPGe crystal as provided by CANBERRA firm.	31
Figure 3-5: Diagram of high purity germanium detector system, including its major components.....	34
Figure 3-6: Scheme of preamplifier (electronic representation), FET, and capacitor inside the Pop-Top capsule.	35
Figure 3-7: Canberra Amplifier - Nuclear Instrument Module (NIM) of the detection system used... ..	35
Figure 3-8: First - The Study Area consisting Douala Bassa area and second - Geographic location map with sample sites (the seven queries were presented here).....	37
Figure 3-9: Composite sample collection methodology within the Sampling Sites.....	38
Figure 3-10. Energy calibration curves (Linear and Polynomial fitting) of the high purity germanium detector (HPGe).....	44

List of Figures

Figure 3-11. Nomenclature of the spectra of Na-22 and Cs-137 when taking into account the Compton Edge during analysis measured from NaI detector.	45
Figure 3-12. Spectra comparison between HPGe and NaI detectors. Large Gaussian distribution of picks from NaI detector than from HPGe detector (left: Normal scale. Right: Log scale).	47
Figure 4-1: Standard deviation between the two measurements using BEGe-6530 and GC0818-7600SL HPGe detectors: (a) deviation for ^{226}Ra , (b) deviation for ^{232}Th , and (c) deviation for ^{40}K . The blue curve is the characteristic of the BEGe while the red one is for the GC0818-7600SL detector. Fluctuation represent the inability of a particular detector to perform accurate measurements at a given energy range.	61
Figure 4-2: Relative error related to the radium equivalent activity for measurements from both detectors. As displayed, the BEGe detector result in blue chart, is three times smaller than that of the GC0818-7600SL in red chart.	64
Figure 4-3: Mean values of specific activities of sand samples from seven big quarries investigated in Douala Littoral Region as additional studied site. This site was added along the project and the obtained data show non-uniform distribution of radionuclides in Earth crust.	67
Figure 4-4: Frequency distribution of the specific activities of ^{226}Ra (a), ^{232}Th (b), and ^{40}K (c) in the sand samples investigated in different quarries in Douala and surroundings.	67
Figure 4-5: Calculated mean values of Radium equivalent activity (Ra_{eq}) of sand from Douala Littoral Region. The results are from the seven quarries investigated.	68
Figure 4-6: Triple representative diagrams of radionuclides investigated in the samples from Douala. The diagram correlated the activity concentrations of ^{226}Ra , ^{232}Th , and ^{40}K . The left diagram shows three axis representation while the right one is a 2D with point surface for Th-232 (presented as Ac-228 on in the figure). Erreur ! Signet non défini.	
Figure 4-7: Activity concentrations of measured radionuclides and radiological parameters as presented in previous paragraphs. Statistical representation of obtained data after investigation, the x-axis is in %.....	72
Figure 5-1: Descriptive principle of X-ray Fluorescence spectrometry. The incident photon is either γ - or X (in most cases)-ray in this case, even though it is not the only representative case found in Physics.....	76
Figure 5-2: Glass disk preparation for major and minor elemental characterization of the investigated samples. On the top left, the sensitive balance is presented, as it is used for quantity (mass) measurement. It is followed by the porcelain crucible used to dry samples at melting temperature. Bottom left, is presented different samples in a desiccator, used to desiccating samples prior to the second melting process and quick cooling down for glass disk making. The last picture displays glass disks made in our laboratory for WDXRF analysis.	78
Figure 5-3: Pressed pellet preparation process for EDXRF measurement. All samples were labelled and the labelling process took place at each step of the preparation as well. The measurement (irradiation) was performed on the sample side facing the ground without any labelling mark. Different colors of the pressed pellet represent the color of the sample (sand present in chapter 4).	79
Figure 5-4: Detection system used for EDXRF measurement (x-ray incident beam and the geometry). The system is from the Silicon Drift Detector X-123SDD design: θ varies in different measurement but in our experiment, $\theta=45^\circ$ [238].	82

List of Figures

Figure 5-5: Schematic description of the complete X-Ray Spectrometer with Silicon Drift Detector X-123 SDD	83
Figure 5-6. EDXRF Spectra of the reference material used for calibration and result validation. Four elements used in this process included NIST-SRM 610, PACS-2, MESS-3, and BE-N.	85
Figure 5-7. Spectra of different samples (UD1 to UD7) from Campus 1. Labelled spectra for campus 1 investigation. This labelling and annotation is valid for spectra from both campuses as the elements and compounds assessed are similar. Detailed views are presented in the following figures.	85
Figure 5-8: Color graphs of major compounds, minor and trace elements found in the investigated samples. The color graph displays the elemental concentration while the y-axis lists the sampling site of sample Id.....	86
Figure 5-9: Spectra of different samples (UD-1 to UD-7) from campus 1. (a) All picks (related to major compounds and trace and minor elements concentration) are presented in the same graph. (b) Zoom of the Fe and another surrounding representative picks.....	90
Figure 5-10: Spectra of different samples (UD-8 to UD-18) from campus 2. (a) All picks (related to major compounds and trace and minor elements concentration) are presented in the same graph. (b) Zoom of the Fe and another surrounding representative picks.....	91
Figure 5-11: Spectra of all investigated samples (UD-1 to UD-18) from both campuses. Energy in deV (2000 deV = 20 keV): (a) All picks (related to major compounds and trace and minor elements concentration) are presented in the same graph. (b) Zoom on the Ar, Ni, Sr, and Ag and other closed representative picks (c) Zoom of the As, Zr, Sr, Kr, Rb, and other surrounding representative picks. (d) Zoom on the S, Ar, and Si k-lines.	91
Figure 5-12: Elemental composition of major and minor compounds from XRF-measurement of all investigated sand samples: (a) Correspond to major compounds assessed measured (all compounds have their maximum detected concentration higher than the unity) and (b) Correspond to minor compound concentrations (all compounds have their maximum detected concentration less than the unity) [209, 232].....	92
Figure 5-13: The positive correlation trend between K_2O and Al_2O_3 for the 18 investigated samples from the campuses of the University of Douala.	95
Figure 5-14. Diagram of chemical classification of the investigated samples from Douala – Bassa area based on binary diagrams; $\log(SiO_2/Al_2O_3)$ as a function of $\log(Fe_2O_3/K_2O)$ diagram of Herron. Among the nine types displayed, the investigated samples are from two main types and the majority from Fe-sand type.....	97
Figure 5-15. Al_2O_3/SiO_2 concentration ratio as a function of Fe_2O_3 and MgO concentration (%) for investigated samples from Douala – Bassa area (the so-called discrimination diagram of tectonic for the determination of sediment provenance).	97
Figure 5-16: Positive correlation between K_2O and Al_2O_3 . The trend shows a regression line that implies relevant correlation between concentrations of both compounds.....	98
Figure 5-17: Chemical classification of analyzed geological samples from Douala and surrounding areas based on binary diagrams; discrimination plot of $\log(SiO_2/Al_2O_3)$ as a function of $\log(Fe_2O_3/K_2O)$ diagram of Herron [271, 272]. Evidence of the 04 classifications of analyzed sand samples from a total of nine different types.	99

List of Figures

Figure 5-18: Diagram of Heron for the classification of different sample (in term of frequency), based on the only four types assessed in this project.....	100
Figure 5-19: TiO ₂ (%) as a function of Fe ₂ O ₃ and MgO (%) for all investigated samples: (a) Normal scale for overall view; (b) high scale visualization with labelling display.....	100
Figure 5-20: The diagram for the tectonic discrimination of sediment provenance based on Al ₂ O ₃ /SiO ₂ concentration ratio as a function of Fe ₂ O ₃ and MgO concentration (%) for all investigated samples points: (a) Normal scale for overall view; (b) high scale visualization for labelling display.....	100
Figure 6-1: Monte Carlo method applied to approximating the value of π (real value is given by $\pi = 3.1415926535897932384626433832$ with 28 decimal characters). As a statistical method, the accuracy of the result obtained depends on the number of particles generated and tracked.	106
Figure 6-2: Monte Carlo based algorithm for particle tracking in a system to be assessed. The particle track starts at particle generation or emission to its death (total absorption) or escape from the system [103, 302–304].....	108
Figure 6-3: (a) Representation of probability of interaction for the photoelectric effect, Compton scattering, and pair production described previously (b) Representation of the cumulative probability distribution for the same case as in (a) [95, 305].	113
Figure 6-4: Geant4 class categories (Geant4 Collaboration 2017). GEANT4 classes overall functioning diagram for radiation simulation.	116
Figure 6-5: Recent geometrical primitives added in Geant4 by Alison et al. [33, 311]: generic trapezoid (A,B), extruded solid (C), parabolic solid (D), and cut tube (E), for the end-users simulation purposes.	121
Figure 6-6: Simplified diagram representing the multithreaded Geant4 application: the <i>master</i> thread plans simulation setups for geometry and physics, and the <i>worker</i> threads complete events to be simulated; otherwise they are separate [33].....	123
Figure 6-7: Main user interfaces' class diagram used in GEANT4 computer code. User initializations, including geometry and physics list, are distributed between threads and allocated to G4MTRunManager's single instance, while user actions are generated for each thread through G4VUserActionInitialization class, and assigned to G4WorkerRunManager's private thread [33]...	124
Figure 6-8: Schematic view of the BEGe detector (BE6530) with real dimension needed for GEANT4 simulations. Precise dimensions and geometry shapes are needed for accurate simulation and meaningful comparison of computer data with experimental ones.	126
Figure 7-1: A simulated cross-section of the experimental setup used in real experiment (cross-section of germanium crystal and lead shield compartment). The detector is defined in the center (green color on the last graph). The surrounding lead shield contours are described with yellow (in the left graph) and blue (in the two others). Some details are missing from the electrodes and other background protection in this representation, and the dead layers in the Germanium crystal detector are not shown.	135
Figure 7-2: A 3D view of the simulated geometry cross-section of the experimental setup. The crystal of Germanium detector is not visible in the first picture (a), but is shown in the center (purple color on the (b to f) graphs). The surrounding lead shield and liners are also simulated in this case and shoewn in yellow color corresponding to lead. Some details are missing from the electrodes and other background protection in this representation, and the dead layers in the	

Germanium crystal detector are not shown. An example of source or sample to be assessed is presented on the top of the detector (the white cylinder). The distance between detector and sample varies depending on experimenter and experimental design..... 136

Figure 7-3: Geometry design of the detector for BEGe detector (model BE6530). The system's design has a lead shielding enclosure with 10 cm thickness (presented here in white color) and is jacketed by an external metal cask of 9.5 mm thickness. The graded lining is made up of a Tin (Sn) 1 mm thick surface and a 1.5 mm thick copper sheet (the part represented in yellow color). ... 138

Figure 7-4: Specific geometric layout of the simulated system in 2D and 3D views: (a) two-dimensional top view of the planar representation. (b) Bottom view-three-dimensional representation resulting from (a) with small angle transformation. (c) 3D 45 ° inclined perspective geometry view using rotational transformation. The bulk of the lead shielding cask is open. (d) The lead cask cover is on the top of the detector in position ready for an acquisition. (c and d) 3D views without and with the cover on the top of the detector (lead shield capsule), respectively. 139

Figure 7-5: Energy spectra from experimental measurements and from the simulation using the full GEANT4 decay library. Both spectra of the following radionuclides are displayed: ¹³⁷Cs, ¹⁵²Eu and ⁵⁷Co source in both the convenient real and simulated geometry. The events were generated at a randomized coordinate within the source geometry, uniformly throughout the total source geometry, and sum peaks where photons (γ) were recorded could be clearly seen on the plotted spectra. Accordance is observed in the peak areas compared to the background area where the GEANT4 background is lower than experimental data. The last graph is for a reference sample named SS1..... 143

Figure 7-6: Simulated and experimental efficiency calibration curves for BEGe detector (BE6530 model). Red curve represents results obtained by GEANT4 and black represent experimental results in all presented graphs. (a) ¹⁵²Eu as single source. No comparison for single source for the efficiency purposes; (b and c) are results from 2nd sample of multi-γ source containing the following radionuclides: ²⁴¹Am, ¹⁵²Eu, ¹³⁷Cs, ¹⁰⁹Cd, and ^{60, 57}Co; (d and e) data from 120 ml cylindrical container of PET containing 320 Bq of soil sample (with the following chemical composition of material in percentage: SiO₂=91±5; Al₂O₃=4.9±0.4; K₂O=2.0±0.1; Fe₂O₃=0.9±0.1; TiO₂=0.2±0; Na₂O=0.4±0; MgO= 0.01±0; CaO=0.3±0; MnO=0.01±0; P₂O₅=0.01±0). (C₁₀H₈O₄)_n is the chemical formula of PET used with n = 5 in GEANT4 code. This sample code was described in Table 7-2..... 145

Figure 7-7: Ratio of the simulated and experimental efficiencies depending on γ energy. The average fluctuation ration between both experimental and simulated values is less than 2 %. 147

List of Figures

List of Tables

Table 2-1: Linear range of 5.5 MeV α particles in various absorber in units of cm [54].	10
Table 2-2: Range of 2.3 and 1.1 Mev electron radiation in some medium. The range depends on the medium density absorbers.	13
Table 2-3: Categorization of Neutrons according to their energy	13
Table 3-1: Specifications of both HPGe detectors used for γ assessment, BEGe-6530 model and GC0818-7600SL model [22, 101].	29
Table 3-2. Samples description for the second sampling campaign. Quarry's description and location are given within the vicinity of the Douala basin (Rio Del Rey basin on the Atlantic Ocean cost) [2].	39
Table 3-3: Spectra resolution comparison between HPGe and NaI (Tl)	46
Table 4-1: Specific activities of ^{137}Cs , ^{226}Ra , ^{232}Th , and ^{40}K in soil samples from Campus 1 and 2 of the University of Douala measured using BEGe-6530 (Douala) and GC0818-7600SL (Liege) high purity germanium detectors. The uncertainty was given at the 95 % confidence level	55
Table 4-2: Comparison of activity concentrations (Bq/kg) of U-238, Th-232, Cs-137, and K-40 measured in the investigated soil samples with that of other countries.	57
Table 4-3: Errors related to Specific activities (in %) of ^{226}Ra , ^{232}Th , and ^{40}K and standard deviation in soil samples from Campus 1 and 2 using both detectors. The uncertainty was given at the 95 % confidence level.	59
Table 4-4: Errors related to radium equivalent activity computed based on activity concentrations of ^{226}Ra , ^{232}Th , and ^{40}K and standard deviation in soil samples from Campuses 1 and 2 using both detectors. The last column shows the ratio between both detectors in the case of detector selection for measurements based on γ energy range. The uncertainty was given at the 95 % confidence level.	63
Table 4-5: Specific activities of ^{226}Ra , ^{232}Th , and ^{40}K and the Radium equivalent activity (Ra_{eq}) of sand samples from different quarries (Douala Littoral region of Cameroon and surroundings). Data of sand samples from the seven big quarries studied.	66
Table 4-6: Inter-comparison of specific activities and Ra_{eq} from Douala Littoral Region sand samples with other areas of the world. The comparison is defined for primordial radionuclides activity concentration and the radium equivalent activity.	68
Table 4-7: Mean values of γ Dose rate, Annual Effective Dose rate, and Hazard indexes for sand samples. External and internal indices, and α and γ indexes calculated are reported in the last columns of the table. All the equations used for computation are presented in the previous chapter.	71
Table 5-1: Certified reference materials used for the calibration of the instrumental setup (GeoReM material. Additional details can be found on the web site: http://georem.mpch-mainz.gwdg.de/sample_query.asp).	80
Table 5-2: Confidence about the XRF reported values. Validation of the XRF measurements based on comparison between reported value by the standard sample's manufacturer and the data obtained in our laboratory.	81
Table 5-3: Concentrations of major elements and their standard deviation (s) in terms of	

List of Tables

percentage (%) of all soil samples from the two campuses (07 samples from Campus 1 and 11 from Campus 2).	87
Table 5-4: Concentrations of minor and trace elements and their standard deviation (s) in term of ppm of all the investigated soil samples from the two campuses. The concentrations are presented following by the standard deviation of the measurement (denoted “s”).	88
Table 5-5: Summary of the elemental concentrations of major elements and their standard deviation (s) in term of percentage (%): Range and averaged concentration of samples from the two campuses.	88
Table 5-6: Concentrations of minor and trace elements and their standard deviation (s) expressed in ppm: range and averaged concentration of samples from the two campuses.	89
Table 5-7: Concentrations (in term of percentage %) of major and minor elements in sand samples from the seven investigated quarries. Result obtained using WDXRF	93
Table 6-1: Evaluation of the value of π and the precision and accuracy of MC methods used for its evaluation.....	111
Table 6-2: Specifications of the BEGe detector used in the laboratory for experimental study (BE6530) and used for MC based GEANT4 toolkit simulation. Some parameters as voltage related ones are for experimental understanding.	125
Table 7-1: G4VProcess classes and methods implemented and used in the GEANT4 simulation	132
Table 7-2: Simulated elements (material that the geometry was built with) in the geometry of the detection system. Mat. Name stands for material name; NComp for number of chemical component in the defined material. Some are predefined in the GEANT4 data base while other (the sample simulated) were created in this project and include in our GEANT4 application.	134
Table 7-3: Simulated and experimental values of the activity concentration obtained with the mix γ standard source SS1. Simulated activity concentration values are obtained with efficiency curve from GEANT4 simulation presented in Figure 7-6.....	147

Abbreviations and symbols

AD	: Absorbed Dose Rate
ADC	: Analog-to-Digital Converter
AED	: Annual Effective Dose
BEGe	: Broad Energy Germanium detector
CPCS	: Centre Pedologique de Classification des Sols
CRM	: Certified Reference Material
DSA	: Digital Signal Analyser
ECC	: Efficiency Calibration Curve
EEC	: Equilibrium Equivalent Concentration
FWHM	: Full Width at Half Maximum
FWTM	: Full Width at Tenth Maximum
GEANT4	: GEometry ANd Tracking versus 4
GPS	: Global Positioning System
HPGe	: High Purity Germanium detector
HVPS	: High Voltage Power Supply
IAEA	: International Atomic Energy Agency
ICRP	: International Commission on Radiological Protection
ICRU	: International Commission on Radiation Units and Measurements
IEDE	: Indoor Effective Dose Equivalent
LabSOCS	: Laboratory Sourceless Calibration Software
LEGe	: Low Energy Germanium detector
LN2	: Liquid Nitrogen
MC	: Monte Carlo methods
MCA	: Multi-Channel Analyzer
MCNP	: Monte Carlo N-Particle Transport Code
MDA	: Minimum Detectable Activity
NaI	: Sodium Iodide detector
NID	: (Tentative) Nuclide Identification
NIST	: National Institute of Standards and Technologies
NORM	: Naturally Occurring Radioactive Materials
NRPA	: National Radiation Protection Agency of Cameroon

Abbreviations and symbols

OEDE	: Outdoor Effective Dose Equivalent
ROI	: Region of Interest
SD	: Semiconductor Detectors
SRMs	: Standard Reference Materials
TENORM	: Technologically Enhance Naturally Occurring Radioactive Materials
UNSCEAR	: United Nations Scientific Committee on the Effect of Atomic Radiation

Constants and Units

Speed of light	c	$2.9979 \times 10^8 \text{ m/s}$
Fundamental Charge	e	$1.6022 \times 10^{-19} \text{ C}$
Avogadro's number	N_A	$6.0221 \times 10^{23} / \text{mol}$
Electron mass	m_e	$9.1094 \times 10^{-31} \text{ kg} = 511.00 \text{ keV}/c^2$
Proton mass	m_p	$1.6726 \times 10^{-27} \text{ kg} = 938.27 \text{ MeV}/c^2$
Neutron mass	m_n	$1.6749 \times 10^{-27} \text{ kg} = 939.56 \text{ MeV}/c^2$
Boltzmann's Constant	k_B	$1.3807 \times 10^{-23} \text{ J/K} = 8.6173 \times 10^{-5} \text{ eV/K}$
Planck's Constant	h	$6.6261 \times 10^{-34} \text{ J}\cdot\text{s} = 4.1357 \times 10^{-15} \text{ eV}\cdot\text{s}$
Planck's Reduced Constant	\hbar	$1.0546 \times 10^{-34} \text{ J}\cdot\text{s} = 6.5821 \times 10^{-16} \text{ eV}\cdot\text{s}$
Coulomb's Constant	k	$8.9876 \times 10^9 \text{ N}\cdot\text{m}^2 / \text{C}^2$
Magnetic permeability of a vacuum	μ_0	$4\pi \times 10^{-7} \text{ N s}^2 / \text{C}^2$
Stephan-Boltzman constant	σ	$5.67 \times 10^{-8} \text{ W m}^{-2} \text{K}^{-4}$
Gravitational constant	G	$6.67 \times 10^{-11} \text{ N m}^2 / \text{kg}^2$

CHAPTER 1. GENERAL INTRODUCTION AND BACKGROUND

1.1. Introduction

The binding of nucleons in a nucleus is stronger for some isotopes than others, for the hundreds of elements known. Some nuclei are sufficiently tightly-bound that they are stable (as the case of the elements as hydrogen, carbon-12, nitrogen-14, lead-210, iron, aluminum...), others have weaker binding. This later group would be in a more tightly-bound configuration if they changed their form by different processes as emission or capture: these are the unstable isotopes, which undergo radioactive decay. When they undergo decay naturally, they are called natural radionuclides (U-238, Th-232, K-40 γ) and when it is from manmade reaction or activities, they are artificial radionuclides (Cs-137). When we have a group of unstable nuclei of the same type, they will tend to decay, and it is useful to think of the half-life, which is the time taken for half of the nuclei to decay. The half-life is one of the most important characteristics of a radionuclide and is related to its decay constant. Natural radionuclides are present everywhere on the Earth since its creation and most of the remaining are products of reaction chain of the measured ones. Artificial radionuclides from Chernobyl and Fukushima accidents have been transported through natural air and water circulations. It is therefore obvious that humans are exposed to both natural and artificial radiation since the discovery of radioactivity and its exploration for human applications (industrial, medical, or research).

Human beings are continuously exposed to ionizing radiation from natural sources. There are three main contributors to natural radiation exposures: Primordial (from the origin of the Earth), cosmogenic (cosmic-rays from the universe and solar winds), and human produced [1, 2]. The presence of natural radioactivity in our living environment can result to internal and external exposures. The most commonly encountered radionuclides that irradiated the human body through external exposure from geological material such as soils and rocks (primarily by γ radiation) are $^{235, 8}\text{U}$ and ^{232}Th and their subsequent radioactive decay products, and ^{40}K . Different elements in the natural environment as soil, rocks, building material, water, air, foodstuff (vegetable and meat) contains natural radioactivity. Naturally Occurring Radioactive Materials (NORMs), under certain conditions, can reach radiologically hazardous levels. In addition, the human life environment is subjected to NORM in all its existence. The radiological implication of these radionuclides is external radiation exposure by γ -rays and internal exposure due to inhalation of radon and its daughters [1]. Measurements of radiation exposure by γ -rays from NORMs, and consequently the determination of the respective dose rate are needed to implement radiation safety measures. Human activities that enhance the exposure to NORM are defined as Technologically Enhance NORMs (TNORMs).

The knowledge of the natural radioactivity level is useful in order to set standards and national guidelines in the light of national and international regulations. Social concern on public exposition has recently encouraged many researchers to be involved in work that evaluated the natural background radioactivity in different countries and worldwide [2–5]. The measurement of the radioactivity level and the radiological characterization of an area is a technical work that implies the knowledge of different parameters, economic and societal factors. The used of γ -ray spectrometry method for samples characterization as well as sampling method are the first steps of this technical work. Its use has been increased recently in different countries, especially on assessing natural radioactivity and associated radiation exposure in different soils, building materials, and sediments [4, 6, 15, 7–14]. The calibration of the detection system is a subject of importance during the assessment of natural radioactivity in environmental samples since the γ -ray emission of the samples is generally low.

Long-lived radionuclides such as ^{238}U , ^{232}Th , and ^{40}K in soil, building material, water resource, foodstuff, and their corresponding decay products are of special interest in this context. Detailed information about their distribution in our environment is one of the major interests of national and international organizations. The determination of the activity concentrations of natural radionuclides in soil with acceptable accuracy is important in the assessment of radiation dose by these radionuclides, observing the behavior of natural radioactivity in the eco-system, and monitoring the natural background. The monitoring task has been carried out in developed countries in the early 1990 s while in developing countries, the methodology is novel. Its novelty in such countries is probably justified by the advanced technology needed for nuclear detection systems. Its combination with X-ray fluorescence measurement could provide complete environmental assessment in term of health protection. XRF method provides elemental characterization of the investigated area and from the output results, heavy metal concentration can be determined. It is also a subject of great importance to assess heavy metal composition in natural resource, and in human environment (water, foodstuff) to provide useful recommendations to governments and regulators in charge of the protection of people and goods. Elements as Au, Pb, Cu, Cr, Mn, Fe, Ni, Co, and elements 113-118 are subjected to investigation in XRF analysis in general.

Soil and sand are mineral deposits formed through the weathering and erosion of rocks. Sand is usually a subject of advance degradation and transportation processes. The deposits found at different levels within the soil generally contain natural radionuclides that contribute to external γ radiation. The distributions of these radionuclides in various soils are related to the nature of the parent rock from which the soils are derived and the processes through which the soils are concentrated [16–18]. For this reason, there are some areas in the world where the natural background is high compared to other. In some countries as Iran, Brazil, China, Australia, and India, the background level is more than a magnitude higher compared to what has been measured in other countries [19]. In addition to the natural sources, soil radioactivity may also be affected by man-made radionuclides such as ^{137}Cs , ^{134}Cs , ^{90}Sr etc..., resulting from nuclear weapon, atmospheric weapons testing conducted in the past century, and nuclear accidents such as Chernobyl and Fukushima [5]. External exposure to high level of these non-natural radionuclides can result in malignant tumors and shortening of life. Internal exposure is not excluded as the contamination can be involved in the alimentation chain. Nonetheless, NORM concentration in environment can also be increased above average natural background level through specific industrial activities, including waste products from companies.

Radioactivity assessment is a complex task as the counting system needs calibration prior to an acquisition. Since equipment calibration requires the use of calibration samples or standards with the same geometry as the samples, computational method can be really useful in environmental monitoring assessment. With a wide variety of sample matrices and geometries, scientists proposed different codes for equipment calibration based on Monte Carlo algorithms [20, 21, 30–32, 22–29]. GEANT4, MCNP, FLUKA, PENELOPE, PHITS, and several codes had been used for efficiency calibration of different detectors. Since the simulation methods improve the advancement of science as well as reduce the cost and time consumed for the fabrication and used of calibration sources, the GEANT4 toolkit based on Monte Carlo algorithms is used in this research project in the view of the validation of calibration of the γ detector [20, 31–34]. This toolkit is one of the most used in nuclear technology for national defense and generation of power, and the applications of radionuclides in medicine, industrial research, consumer products resulted in the release of radioactive material into the environment, and astrophysics research. The main advantage of GEANT4 is that it is not a software as MCNP, PHITS, EGS, and so on, but GEANT4 is a Toolkit that provides tools to build one personal application.

In Monte Carlo methods, quantities of interest for the application are calculated through statistical sampling of interaction processes and are based on random numbers. The Monte Carlo algorithm implies that the physical system is described by the probability density function which allows generating random figures and the result is taken as an average of numbers which were observed [26, 35]. γ -ray spectroscopy has been widely used in environmental radioactivity monitoring, nuclear industry, geochemical investigation, and astrophysics. Most radioactive sources produce γ rays, which are of various energies and intensities, and their use is subjected to exposure risk in the laboratory and in-situ. Geant4 (for GEometry ANd Tracking), a platform for the simulation of the passage of particles through matter using Monte Carlo methods, was used in the present project for simulation of the Broad Energy Germanium detector (BEGe model BE6530) [31–38]. The GEANT4 toolkit allows the simulation of the electromagnetic processes. In the related chapter, we presented the Monte Carlo equations used in γ spectrometry and implemented in Geant4 for our simulations. The present chapter describes an overview of the present thesis project.

1.2. Natural sources of ionizing radiation

As previously highlighted, cosmic radiation, cosmogenic radionuclides, and terrestrial radiation due to the primordial radionuclides are the main natural sources of ionizing radiation. The variation of the magnitude of exposure varies depending on different parameters as the region of the exposition and the composition and origin of the geological formation. For example, the exposure to cosmic ray obeys to the principle of “the higher is the altitude, the higher is the exposure” and increases with the latitude with minimum exposure at equatorial regions [1]. Cosmogenic radionuclides are those formed as a result of interaction of the primary cosmic ray with earth’s atmospheric (C-14, H-3, and Be-7). Primordial radionuclides characterized by long half-life are those that are thought to have occurred since the creation of the earth (U-235, U-238, Th-232, and K-40).

In another hand, we distinguish TENORM for Technologically Enhanced Natural Exposure which are exposures to natural radiation technologically enhanced by human activities. For instance, the exposure to cosmic rays during air travel and special exploration are considered as TENORM [1, 39, 40]. Additional cases of enhanced exposures include mining activities in phosphate industry, processing of monazite sands for rare earths extraction, oil and gas industry, radon in subway station, radon and thoron in closed culture with CO₂, and coal-fired workstations. Significant exposure in some agricultural facilities, especially in case of vinyl greenhouse in radon prone area as large-scale agricultural facilities which used underground air for air -conditioning and CO₂ supply is a TENORM.

1.3. Importance of the Monte Carlo Simulation

The Monte Carlo simulations have two contributions to this project. First, we characterized the efficiency and the calibration of the spectrometry chain: this is directly applicable to the calibration of the γ detectors of our laboratories. Several parameters related to the efficiency of the detector are at the origin of the inaccuracies during the measurement: the detection and sample geometry, the shielding of the measurement system, the solid angle of detection, and the statistical and counting times that can be easily profiled by simulation. This simulation has not only academic but also industrial inputs as it could enable detector manufacturers such as CANBERRA to refine the characteristics of the germanium crystal in order to further optimize the detection efficiency of the system. On a second point, the laboratory measurement results must be resumed by simulation in order to identify and reduce the error on the measurement. This was achieved by the following steps [10, 11]:

- Understanding and correction of complex effects that plague coincidence systems, including cascade summing and the low-energy time-walk of coincident events;

- Developing expertise in the Geant4 toolkit and Monte-Carlo methods for metrology, allowing the creation of detector system simulations which could be utilized to optimize the geometries and efficiencies of the proposed system.

As GEANT4 is an object-oriented toolkit for simulating the passage of particles through matter in different disciplines as Nuclear, Medical, Applied Physics, and Astrophysics, it provides a wide range of classes to be implemented for our personal simulation. Originally it was used to model particle and nuclear physics experiments, however Geant4 is now used in a wide range of fields including nuclear medicine and radiation protection. The GEANT4 toolkit encompasses an ample set of physics models, specialized for particle type, energy range and detector applications, and functionality, ranging from geometry to tracking, visualization and event biasing [31, 32, 41]. Relevant classes edited by programmers are usually related to the geometry, the physics processes, and the primary particle generator. When correctly adjusted, one can develop appropriate MC code for reproduction of a real physical phenomenon. The Monte Carlo methods based GEANT4 simulations developed in the present study were used to validate the obtained experimental result.

1.4. Relevance and justifications of the study

According to the literature, few studies have been carried out in Cameroon on assessment of the public exposure due to natural radioactivity from soils and building material such as sand and data on radionuclides concentrations in materials from mining areas are scanty. Consequently, there is a general lack of awareness and knowledge of radiological hazards and exposure levels by legislators, regulators, and operators. Some studies conducted on two suspected uranium mining in Lolodorf and Poli by Beyala and Saidou [5] [16] have reported average annual effective dose of 0.307 mSv/year and 0.31 mSv/year, respectively. The expected results obtained in this work will be additional information on natural radioactivity from NORM industries in Cameroon and may be used to set a national global system of NORM in the light of global recommendations. They can also be used in Validating Geant4 detector models in comparison to existing detector systems, including HPGe detectors. Using Geant4 models to optimize the HPGe primary crystal and Extending Geant4 detector system models to identify areas where current systems can be improved and contributed to the novelty of this study were set as additional objectives.

The used of Monte Carlo simulations is a real challenge in a context which involved manipulation in the laboratory and simulation by coding or programming at the same time. In Cameroon, the number of researchers knowing as expert in Monte Carlo methods and using GEANT4 toolkit is almost null. It is, therefore, a priority to implement MC methods based GEANT4 toolkit and extend the research application to XRF, medical application, and other detection systems. It is also a new opportunity to invest in this new research field in view to share the knowledge with the future generation and implement the results of the present work with another researcher in the field and everywhere it can be useful.

This study will be important especially to the Radiation Protection Board in designing radiation protection control guidelines. It is therefore of primary importance that radioactivity data that is collected for the investigated areas, forms a basis for protection guidelines. The results obtained in this study, together with data from other studies performed earlier, will enable projections on the possible levels of radioactivity enhancement due to radioactive soils and sands in Cameroon due to human actions. Having a baseline is always a matter of monitoring as the background could be contaminated by manmade actions and accidents as Fukushima. After such accident, monitoring the contamination knowing the background is appropriate and could easily lead to valuable conclusions as the situation without background data could be difficult to manage. The main contribution is the drawing of radio-

logical map of the country as well as the introduction of Monte Carlo methods based GEANT4 code. The useful value of GEANT4 might be proven by extending its use in different medical centers for cancer's treatment as the use of Radiotherapy, Cobalt-therapy, and linear accelerator in the sub-region (Central Africa Zone).

1.5. Description of the environment of work

A PhD thesis requires to some extent, intervening parties, an organization, an internal and external collaboration, and capabilities (intellectual, material, and technical) for its achievement. By the active participation to the national and international communication on the research domain, the present work is partially the continuity of the Master's study concerning environmental monitoring assessment on the one hand, and is a new project concerning Monte Carlo simulation, Geant4 toolkit, and other nuclear methods used (XRF) on the other hand. The understanding of γ spectrometry's principles was acquired during Master thesis. Concerning Geant4 toolkit and Monte Carlo simulation based on C++ programming, the laboratory provided a framework where the attendance to different international programming summer schools was possible. Two summer's schools had then been attended in the field of Monte Carlo simulation based GEANT4 toolkit, in 2015 and 2016. The Atomic and Nuclear Spectroscopy, Archeometry laboratory of the University of Liege, the host University is equipped with many High Purity Germanium detectors and Silicon Drift Detectors as well as Sodium Iodine (NaI) detectors. The laboratory is also equipped with servers (NIC4); a cluster dedicates to intense scientific calculations. This equipment was used as experimental setups and computational resources. Several detectors used for experimental part of the project are presented in Figure 1-3 a and b.

Resource for computational work consisted of laptops and desktops as well as the GEANT4 toolkit. GEANT4 toolkit [32, 34, 42] is a publicly available Monte-Carlo toolkit developed at CERN, which enables us to create accurate simulations of particle propagation through interactions with matter. As the cost of computing facilities decreases (the main limitation for computer-based modelling), Monte Carlo simulations have become essential when developing new equipment, providing substantial cost savings on prototyping and designing complex works. Our personal computers are equipped with Geant4 code for test during computational assay.

The experiment was carried out at the campuses of the University of Douala Cameroon (04° 03'14.8" - 04° 03'29.7" N and 09° 44'00.1" - 09° 44'45.2" W). The map of the area is presented in Figure 1-1. This study site was extended to the Littoral region of Cameroon (concerning building material, especially sand from seven largest quarries). The first studied sites are located within the Douala-Bassa zone where the geology is compromised by sedimentary rocks namely by the tertiary to quaternary sediments. The second Field of experiment was formed by seven largest quarries namely:

- Bonaberi Bonamikano;
- Northern Akwa;
- Bois-de-Singe;
- Youpoue;
- Youpoue-Bamenda;
- Dibamba; and
- Village.

They are all located around the Douala town as can be seen in Figure 1-2. It is located within a humid equatorial climatic zone. Annual rainfall ranges between 3000 and 5000 mm, and the annual average temperature is 26 °C. The hydrogeology is modelling by the Wouri, Dibamba, Mungo, and Docteur Anse rivers and the Atlantic sea [43–45]. The site is located in and around the most industrial

city in Cameroon as well as in Central Africa Sub-region.

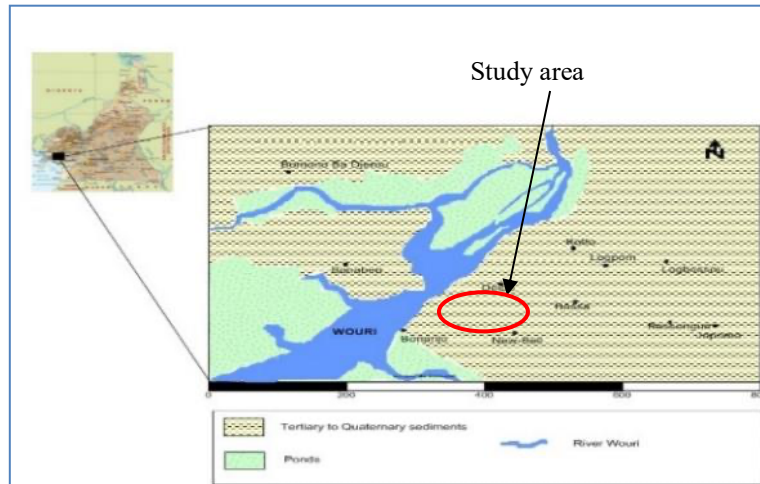


Figure 1-1: Sampling site-geographic localizations: the first studied site selected, the campuses of the University of Douala-Cameroon.

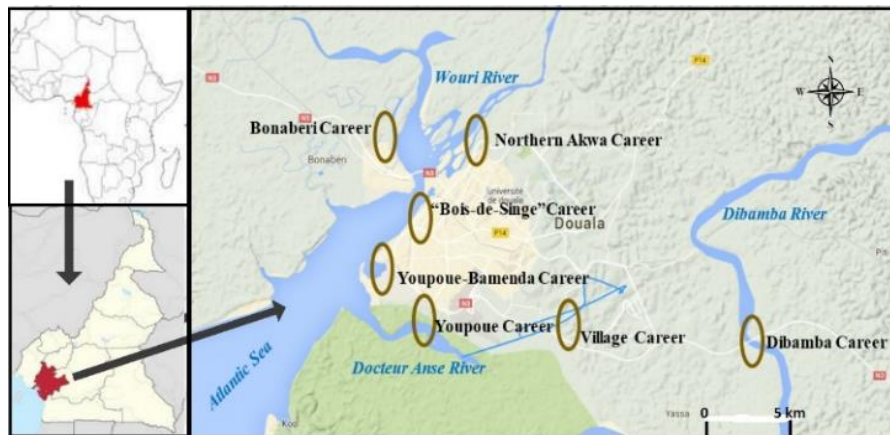


Figure 1-2: Sampling site-geographic localizations, the second studied sites. Sand Building material used in Douala and its surrounding. Map of the seven big sand quarries in Douala-Cameroon.



BEGe6530 at the NRPA laboratory

Figure 1-3: CANBERRA high purity germanium detectors used in Cameroon’s spectrometry laboratory (left: BEGe 6530).

1.6. Overview of the research

Various studies are being carried out all over the world to determine the exposure of humans to ionizing radiation by γ -ray spectrometry. In Cameroon, little works had been done to date. According to the literature, very few studies have been carried out on the assessment of public exposure due to natural and artificial radioactivity and data are scarce even for mining areas. Preliminary studies have been conducted in Fongo Tongo in the western region of Cameroon [46], Poli in the north [5], Lolodorf in the south [16], and Douala in the Littoral [47]. These studies [4, 5, 16, 47] done by Nguelem et al. (in 2014), Saidou et al. (2008), Ben Bolie et al. (2010), and Ndontchueng et al. (in 2013 and 2014) revealed exposure doses Non-negligible and in some investigated sites, the presence of non-natural radioisotopes such as ^{133}Xe and ^{137}Cs . Some studies conducted at two sites of uranium Lolodorf and Poli by Saidou et al. [5] and Beyala et al. [16] reported the mean annual effective dose of 0.307 mSv / year and 0.31 mSv / year, respectively. Even if these values are lower than the recommended values set by the IAEA [48] and UNSCEAR [1, 49], it is necessary and urgent to determine the NORM levels in the environment where the population live, especially for other high density (population) sites.

Recently, the activity concentration of primordial and anthropogenic radionuclides of top surface soil samples collected in bauxite ore deposit in the Western Region of Cameroon was determined using γ -ray spectrometry based Broad Energy Germanium (BEGe 6350) detector by Nguelem et al. [13]. The observed average activity concentration values of ^{226}Ra , ^{232}Th , and ^{40}K are comparably higher than the recommended limit of normal areas by UNSCEAR but lower than the reported safe limit of mineral bauxite ore deposit zone reported in the IAEA technical report. This investigation also presents trace amounts of ^{137}Cs (that is not naturally occurring material) and ^{235}U in some few soil samples. From the obtained values of radiological parameters such as radium equivalent activity and external hazard indexes, using soils in the investigated area as building materials might increase radiation risk exposure to the population. Additional investigation based on radon exposure and its daughters was recommended for further recommendations to the regulatory authority and inhabitants of the locality.

The Monte Carlo simulation was born (firstly developed) in 1947 at the Casino Los Alamos where games of chance inspired Nicholas Metropolis, who published for the first time in 1949 in an article co-written with Stanislaw Ulam, [50, 51] the principle of this method. In this area too, very few studies are undertaken in combination with γ -ray spectroscopy in Cameroon [52]. Work has been done to compare the theoretical and experimental results but very little to improve the construction of γ detectors [24]. In addition, the simulation code Geant4 is itself a new research domain in developing countries as Cameroon [24, 31, 32, 34]. It is much more used in the fields of space, medicine, and high energy enabling international collaboration. One of the best recent PhD thesis on Monte Carlo methods based on Geant4 toolkit and γ -ray spectrometry was done by Richard Britton in 2014 [53]. He used a combination of secondary detectors to optimize a Compton suppression system for the primary detector, which could improve the performance of the Compton Suppression system by an order of magnitude. For the detector systems themselves, he also used a combination of experimental work and Monte-Carlo simulations to develop and validate computer models of the laboratory systems, which have then been utilized to improve the performance of all system components. Monte-Carlo models (using the Geant4 toolkit) were initially used to reproduce the detector response of a HPGe detector system, with the geometry parameters tuned to reproduce the peak efficiencies for a range of photon energies. These models were then extended to accurately reproduce more complex HPGe detector systems, with all detector components, interaction effects, and source matrices fully simulated.

Obviously, the expected results of this thesis will not only have a contribution to the international literature, but also applications in human society with regard to protection against ionizing radiations, the benchmark definition of natural radioactivity, and especially in the field of construction of γ detectors with wide energy range. Improvement would be the benefit of Cameroonian society first in the sense that the data to be generated are related to the country directly. For experimental γ and X-rays spectrometry, the samples analyzed came from the Littoral region of Cameroon. Monte Carlo simulation can be really useful internationally since the used of Germanium detector for radioactivity assessment is a worldwide activity. In every laboratory (using γ spectrometry with HPGe) in the world, the efficiency calibration of the equipment is an important step that could be achieved and improved using the outcome of this thesis (GEANT4 simulation results).

1.7. Aims of the research

The research tends to conduct a comprehensive assessment and evaluation of public exposure to natural radiation from a selected area in Cameroon using nuclear analytical techniques. As a result of mining or undergoing mining process, the release of radioactive elements in the environment may result into contamination and enhancement of the background radioactivity in different areas. As the measure city in Cameroon, Douala is the economic capital of the country and the most popular with more than three million inhabitants. Campuses of the university of Douala were selected as the primary study zone. From being a student at the University, interest was shown as to figure out if the temple of knowledge is radiologically safe enough or not. The studied site was extended to the largest quarries in and surrounding the city of Douala. Objectives consisted of to obtain reliable exposure data from natural radionuclides. This will establish a baseline map of radioactivity levels and the radiation dose levels within the vicinity of the investigated areas (both campuses 1 and 2 of the University of Douala and the seven big sand quarries in and around the city of Douala - Cameroon). Secondly, the research also tends to study the pathways of exposure to radioelement from soils and evaluate the radiological risk to the population by determining the activity concentration of ^{235}U , ^{238}U , ^{232}Th , ^{40}K using high purity germanium (HPGe) detector and measuring of dose rate of the soil/sand samples obtained from two campuses of University of Douala-Cameroon and the big quarries. Thirdly, the study uses the combination between γ spectrometry, development of related Monte Carlo methods, and the GEANT4 toolkit for γ -ray spectrometry simulation (simulation of the interaction of photon through matter) for the validation of the experimental results. The simulation was focused on Broad Energy Germanium detector using in our laboratory.

The evaluation of the exposure due to natural radionuclides in the campuses of the university of Douala and surroundings (sand's quarries) using High Purity Germanium (HPGe) detector is then one of the major outcomes of the present reseach. As the study was going on, the area of research was extended to the surrounding of the campuses (the city of Douala) and the validation based on Monte Carlo simulation using GEANT4 code was implemented. Extensive characterization of the investigation area based EDXRF and WDXRF provided valuable insights for environmental resource assessment. Classification of the studied area is one of the major topics in geology to control the weathering process and erosion. This allows the provenance determination of the investigated areas and could guide in historical reconstitution or classification. Information collected from this part could be also explored by geologist and government for resource management.

CHAPTER 2. INTERACTION OF RADIATION WITH MATTER - PHOTON

Radioactive decay is defined as a statistical process that characterizes unstable nuclei by emitting radiation that changes the state of the nucleus. Unstable nuclei are typically defined as those that have an excess of energy, and therefore decay to a lower energy state via a variety of energy-loss mechanisms [53]. An isotope that is radioactive is then called a radioisotope and this nomenclature will be used in the remaining document. Each radioisotope may decay using one or many modes of disintegration depending on different parameters as probability of existence of a nuclear state and transition. Each mode of decay for every nucleus has a characteristic decay half-life ($t_{1/2}$) which is a fundamental characteristic of radionuclides. These half-lives depend on the amount of excess energy, the disintegration mode, and the underlying structure of the nucleus. The primordial radionuclides have a half-life in the order of the Earth age. The common energy loss mechanisms relevant to the interaction of radiation with matter that have been subjects of the present thesis are α decay, β decay, and γ decay (which is the main topic of the research).

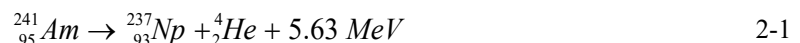
2.1. Particulate Radiation

Nuclear radiation can occur in various categories, percent abundances (branch ratio), and energies and this is a challenging field when performing radioactivity analysis. Also, a given radionuclide may have more than one mode of decay, instead of been mono-energetic emitter, it could be dual energy or multi-energy emitter (Eu-152) [54]. It is then important to differentiate radiation by their properties. In this section, the attention is brought to the particulate radiation including α particle and electron.

Particulate radiations are those made of particles of matter. Particle radiation is referred to as a particle beam if the particles are all moving in the same direction, similar to a light beam. This notion was explained by De Broglie in early starting of applied nuclear physics (light properties) [55–57]. Due to the wave–particle duality, all moving particles also have wave character. But the reason why we separated these radiations to electromagnetic radiations is the detection method and equipment that will be presented in chapter 3 and their nature as massif radiation. There are many particulate radiation as α particles, Negatrons, Positrons, β particle, Auger electrons, and Neutron radiations. This section presents only α , β , and Neutron radiation for consideration of interest.

2.1.1. α radiation

The α particle, structurally equivalent to the nucleus of a helium atom without two electrons, is denoted by the Greek letter α , and consists of two protons and two neutrons. α decay is a radioactive decay that often occurs in heavy nuclei with an atomic mass higher than 82 ($Z > 82$) and results with a Helium nucleus emission (helium nucleus instead of helium atom as mentioned in some references). For example, the radionuclide americium-241 decays by α particle emission to yield the daughter nuclide ^{237}Np according to the following equation [34, 53, 54, 58]:



Since both proton and neutron numbers must be conserved in this process, α decay changes the isotope of the parent nucleus according to the general equation (2.2). α decay series can be seen in Appendix A.



The energy liberated is shared between the daughter nucleus and the α particle, and the conservation law of energy and momentum are respected in this process. α particles are less penetrative and can be easily stop by a small layer of paper. For example, the Table 2.1 presents the linear range of 5.5 MeV α particles in various absorber in units of cm.

Table 2-1: Linear range of 5.5 MeV α particles in various absorber in units of cm [54].

Air	Water	Mylar	Paper	Aluminum	Copper	Gold
4	0.0048	0.0036	0.0034	0.0024	0.001	0.00075

It was observed that the range of α particle range depends on several variables including:

- (i) the energy of the α particle,
- (ii) the atomic number and atomic weight of the absorber, and
- (iii) the density of the absorber.

All these parameters are taking into account during a reaction to determine different products. As the α particle cannot easily penetrate the human skin, the external exposure is usually neglected compared to external exposure from other radiation type. But the internal radiation from α particle is a real concern as the energy of α particle is usually around 5 MeV or more.

2.1.2. Electron Radiation

Electron radiation, also called β radiation, is usually known as the free electron / negatron and its antiparticle, called positron or positon. Electron family is composed of positive and negative charged electron. Electron is considered as radiation only when it is free and in movement. The precision will not be always repeated in the rest of the manuscript, but we will consider this notion as fundamental for radiation definition.

- Negatron

A negatron or negative β particle (β^-) is a free electron emitted from the nucleus of a decaying radionuclide that possesses an excess of neutrons or, in other words, a neutron/proton (n/p) imbalance. A negatron bound to a nucleus is not radiation, but only free negatron when propagates, is consider as radiation. The nuclear disequilibrium caused by the n/p imbalance results in the decaying of a neutron to a proton within the nucleus, where the balance of charge is conserved by the simultaneous formation of an electron (negatron) according to the equation below (mass energy balance is conserved):



An anti-neutrino accompanies β -particle emission. Neutrino in this reaction as always is a particle of zero charge and zero mass. Like the α particle, the β particle interacts with matter via:

- (i) Ionization; and
- (ii) electron orbital excitation as it dissipates its kinetic energy.

A third mechanism of interaction with matter, which distinguishes the β particle, is radiative energy dissipation via Bremsstrahlung production [54].

- Positrons

In contrast to negatron emission from nuclei having neutron/proton (n/p) ratios too large for stability, positrons, which consist of positively charged electrons (positive β particles), are emitted from

nuclei having n/p ratios too small for stability, that is, those which have an excess of protons. Usually, the number of proton in the nucleus is larger than the required number for stability, and the proton number should be reduced by proton decay. To attain nuclear stability, the n/p ratio is increased. This is realized by a transformation of a proton to a neutron within the nucleus. The following equation illustrates such a transformation that can transform Co-58 to Fe-58, N-12 to C-12, and B-12 to C-12:



Positrons dissipate their energy in matter via the same mechanisms as previously described for negatrons, which is understandable, as both are electrons. But since the positron is an antiparticle of electron, the emission of neutrino is needed: particle + antineutrinos as products or antiparticle + neutrinos. The stopping powers and ranges of positrons are virtually identical to negatrons and electrons over the broad energy range of 0.03–103 MeV as both particles have the same properties except that they are particle-antiparticle one another [54].

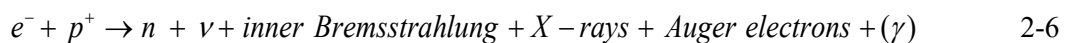
The stopping power for β particles (β^+ or β^-) is the sum of the collisional and radiative contributions as shown by the following equation:

$$\left(-\frac{dE}{dx}\right)_{tot}^{\pm} = \left(-\frac{dE}{dx}\right)_{col}^{\pm} + \left(-\frac{dE}{dx}\right)_{rad}^{\pm} \quad 2-5$$

where the superscript \pm refers to positively or negatively charged electrons. β particles are more penetrative than α radiations and could be shield by composition of metal as aluminum and low atomic weight materials as plastic, wood, water or acrylic glass.

- **Electron Capture**

Sometimes, instead of converting a proton into a neutron internally, a nucleus is likely to capture an electron to create a neutron after electron-proton combination. The mechanism by which an unstable nucleus can increase its n/p ratio is via the capture by the nucleus of a proximate atomic electron (e.g., K- or L-shell electron). The combination of electron and proton is done via the following equation [59–61]:



The electron capture (EC) process is sometimes referred to as K capture, because most of the electrons are captured from the K shell, which is the closest to the nucleus. This process is regulated by mass-energy conservation as the most conservative process will be likely to occur. A ν is emitted and this emission is accompanied by another emission of internal bremsstrahlung. In this situation, the bremsstrahlung is a continuous spectrum of electromagnetic radiation that originates from the atomic electron as it undergoes acceleration toward the nucleus. An example of a nucleus that undergoes this process is the transformation of Na-22 to Ne-22: the process is possible by β^+ decay at 90% and Electron Capture at 10% while the transformation of Zn-65 to Cu-65 is possible by β^+ at 1.5% and by EC at ~98%.

- **Internal Conversion Electrons (IC)**

Decay by internal conversion (IC) results in the emission of an atomic electron. In general situation, when an atom absorbs the excited energy of a nucleus, it emits an electron called the internal conversion electron. The process is known as internal conversion. It is accompanied with the emission of γ -rays. This mode of decay even competes with γ -ray emission as a de-excitation process of unsta-

ble nuclei. The kinetic energy of the electron emitted is equivalent to the energy lost by the nucleus (energy of transition of the excited nucleus to its ground or lower energy state) less the binding energy of the electron as illustrated by the following equation:

$$E_e = (E_i - E_f) - E_b \quad 2-7$$

where E_e is the kinetic energy of the internal conversion electron as it is propagated. This value could be positively limited to zero as the process is likely to occur,

$(E_i - E_f)$ is the energy of transition between the initial, E_i , and the final, E_f , nuclear energies normally associated with γ ray emission, and

E_b is the binding energy of the atomic electron.

Internal-conversion electrons may be emitted from specific electron shells of atoms. The energy involved for the possible process may be expressed in terms of internal-conversion electrons and γ -rays of the same energy less the energy difference resulting from the binding energy of the electron [34, 54]. The process is useful in spectrometry to analyze 243/244 Cm mixture. It also helps in dealing with safeguards verification with IAEA system of verification of Nuclear material [62]. In the electron-capture (EC) decay processes, vacancies are left in electron shells (K, L, M . . .) that can be filled by atomic electrons from higher energy levels.

- Auger Electrons

An Auger electron can be considered as the atomic analogue of the internal conversion electron. In the internal conversion process, the energy absorbed is from nuclear origin while in the Auger process, it is from atomic origin. In the process of falling to a lower energy shell to fill a vacancy, electron energy is lost as a photon of x-radiation emission. This x-radiation may either travel on to be emitted from the atom or it may collide with an atomic electron, resulting in the emission of the electron referred to as an Auger electron [34, 63–65]. The application of Auger electron is generally the Auger electron spectroscopy that is used as a valence – band spectroscopy. It is a surface sensitive analytical technique because the Auger electrons have an escape depth of only few tens of angstroms.

$$\varepsilon_{Auger} = (E_L - E_K) - E_b = h\nu - E_b \quad 2-8$$

- β particle absorption and Transmission

On the basis of the exponential character of β -particle absorption we can describe the transmission of β particles through the absorber as the exponential decay law. It is shown in the equation 2.9 below:

$$I = I_0 e^{-\mu x} \quad 2-9$$

where I is the intensity of the β particles transmitted through the absorber,

I_0 is the initial intensity of β particles incident on the absorber,

μ is the linear absorption coefficient in units of cm^{-1} , and

x is the absorber thickness in cm (or in inverse unit of the linear absorption coefficient).

This expression can also be given in mass absorption coefficient [53, 58, 66, 67]. In that case, the

density is considered in the formula in the exponential argument. The average range of electron depending on the density of the medium for different materials is given in **Table 2-2**.

Table 2-2: Range of 2.3 and 1.1 Mev electron radiation in some medium. The range depends on the medium density absorbers.

Material	Density	Maximum β range (energy dependence)	
		(2.3 MeV)	(1.1 MeV)
Air	1.2 mg/cm ³	8.8 m	3.8 m
Water (soft tissue)	1.0 g/cm ³	11 mm	4.6 mm
Plastic (acrylic)	1.2	9.6	4
Glass (Pyrex)	2.2	5.6	2.2
Aluminum	2.7	4.2	2
Copper	8.9	1.2	0.5
Lead	11.3	1	0.4

2.1.3. Neutron radiation

The neutron is a neutral particle, which is stable only in the confines of the nucleus of the atom. A free neutron is not stable and especially when moving with high speed, becomes subject of interest. Its mass, like that of the proton, is approximately equivalent (superior equivalence) to 1 u (atomic mass unit). Unlike the particulate α and β nuclear radiation previously discussed, neutron radiation is not emitted in any significant quantities from radionuclides that undergo the traditional nuclear decay processes with the exception of a few radionuclides such as ²⁵²Cf and ²⁴⁸Cm, which decay to a significant extent by spontaneous fission. For Cf-252, the average neutron ratio per fission is 3.75, which is high enough to give this radionuclide the attention to be used in industrial radiography.

Neutrons are generally classified according to their speed which determines their kinetic energies. There is no sharp division or energy line of demarcation between the various classes of neutrons as it is the case for other radiation with characteristic energy; however, the following table (Table 2-3) is an approximate categorization according to neutron energy [67–71]:

Table 2-3: Categorization of Neutrons according to their energy

Class of Neutron	Energy range
Cold Neutron	<0.003 eV
Slow or Thermal Neutrons	0.003 – 0.4 eV
Slow or Epithermal Neutrons	0.4 – 100 eV
Intermediate Neutrons	100 eV – 200 keV
Fast Neutrons	200 keV – 10 MeV
High energy or relativistic Neutrons	>10 MeV

Until late 1932, the neutron discovered had eluded scientist all over the world as the particle is neutral charged and its penetration power is too high compared to particles discovered at that time. The evidence of the existence of neutron was provided in 1932 by J. Chadwick during an experiment. When he placed a source of α particle-radiation in close proximity to beryllium, a particle with high penetration power was emitted contrary to the expectation: the particle was neutron. It was known that bombarding beryllium with α radiation would produce another source of radiation, which had a pene-

tration power through matter even greater than that of γ radiation (especially for high Z materials). Nowadays, americium / beryllium neutron sources are still used in non-destructive tests (NDT).

The discovery of neutron had been one subject of real importance in the human history since nuclear fission, fusion, and accelerator sources are based on neutron technology. The absolute use of neutron in nuclear reactors without any other possibility shows how important neutrons are in nuclear physics. Neutron has many channels of interaction with matter as elastic scattering also known as collision with an atomic nucleus, inelastic scattering (generally occurs when a fast neutron collides with nuclei of large atomic number), neutron capture, and nuclear fission [60, 61, 67, 72–74].

The most simplified expression for the calculated beam intensity (I) after passing through an absorber of thickness (x) when the absorber material consists of only one pure (when there is a mixture, the order and arrangement of material should be taken into account) nuclide and only one type of reaction between the neutron beam and nuclei is the following equation:

$$I = I_0 e^{-n \sigma x} \quad 2-10$$

where $n \cdot \sigma$ is the number of nuclei per unit volume (cm^3) and

σ the neutron cross section in cm^2 .

The neutron cross section σ can be defined as the area, usually in cm^2 or barn, for which the number of nuclei–neutron reactions taking place is equal to the product of the number of incident neutrons that would pass through the area and the number of target nuclei. This concept is the most important in neutron physics or reactor physics as the neutron is not characterized by a specific radionuclide or a characteristic spectrum. The-cross section is defined in units of 10^{-24} cm^2 (one barn) on the basis of the radius of atomic nuclei being about 10^{-12} cm . The question on what would happen to a free neutron that is not absorbed by any atomic nucleus remains. The free neutron is not stable and will not remain longer. It decays according to the following scheme:



The 0.782 MeV of energy released in the neutron decay corresponds to the difference in mass of the neutron (1.0086649 u) and the sum of the masses of the products of the neutron decay, that includes the proton mass (1.0072765 u) plus the electron mass (0.0005485 u), or 1.0078250 u. Referring to Einstein's equation of mass and energy equivalence, this mass difference of 0.0008399 u can be converted to the equivalent of 0.782 MeV of energy [54]. For this reason, a free neutron at rest will always undergo the previous reaction with the production of 0.782 MeV.

In summary, we can state that the principal mechanisms of interaction of charged particles as α particles, protons, deuterons, and electrons or β particles with matter, which result in significant charged-particle energy loss are:

- (i) ionization via coulombic interactions of the charged particles with atomic electrons of the absorbing medium,
- (ii) electron orbital excitation of the medium, which occurs when the energy transfer through coulombic interaction is not sufficient to actually eject an electron from an atom, and
- (iii) the radial emission of energy as bremsstrahlung (x-radiation) when an electron or β particle decelerates as it approaches an atomic nucleus.

2.2. Electromagnetic Radiation – Photons

Nuclei in an excited state can decay to the ground state through the emission of one or more γ -rays. Each γ decay is mono-energetic and consists of a photon with the energy (ΔE) of the difference between the parent E_i and daughter E_f states (minus an often negligible correction for the recoil energy of the emitting nucleus). Photons have an intrinsic spin of $1\hbar$, and therefore transitions between 0^+ or 0^- states (where $\Delta L = 0$) are forbidden. These transitions do not violate quantum mechanics rules, instead occur via internal pair production or internal conversion. In the majority of cases, γ decay typically occurs after α or β decay in unstable nuclei, as for equilibrium or exceeding energy, where the initial decay leaves the daughter nucleus in an excited state. Subsequent γ emission allows the nucleus to reach the ground state, via a single emission (mono energetic γ emitter) or multiple decays (dual energy emitter or multi-energy γ emitter). These emissions are often prompt (emission time $< 10^{-10}$ sec) in comparison to the half-lives of the parent nuclei, and some are observed as a cascade of radiation [64, 68, 82, 83, 72, 75–81].

Among electromagnetic radiation, we distinguish:

- Γ radiation: usually radionuclide decay processes. It often occurs when the decayed products leave the nuclide in an excited energy state, that is an unstable state. The remaining nuclide in such excited state will likely fall either into the ground state or will descend in steps to lower energy states. This process liberates the energy in the form of γ radiation;
- Annihilation Radiation;
- Cherenkov Radiation;
- X-Radiation: during the electron capture decay process, the vacancy left by the electron from the K shell is filled by an electron from an outer shell (generally the adjacent L shell). This transition is not without disturbance in the atom, even if it is really small. Transitions produced in electron shell energy levels result in the emission of energy as x-radiation [54]. When naturally occur, the energy is generally not greater than tens of keV, compared to energy from γ radiation that can easily reach few MeV;
- Bremsstrahlung: Bremsstrahlung is electromagnetic radiation like x-rays. It is radiated by a charged particle as it decelerates in a sequence of collisional impacts with atomic particles.

There are different means by which photon can interact with matter. Different processes of interaction of photons are listed below (these four processes are the main well-known and subject of interest in this project):

- Photoelectric effect;
- Compton scattering;
- Pair production; and / or
- Rayleigh scattering.

And the probability of each interaction type is energy-dependent. For environmental investigations, the energy scope of interest is between 3 keV - 3 MeV , thus Compton scattering is the overwhelming interaction processes. Choice of a high- Z material will hence enhance both the full photopeak efficiency and the extent of photons interaction with the sensible detector [36–38, 64, 82, 84, 85].

2.3. Interaction of Electromagnetic radiation with matter

2.3.1. Photoelectric effect

The incident photon interacts with a highly bonded atomic electron, ejecting it with a kinetic energy equal to the difference between the incident photons energy and the binding energy of the elec-

tron. The resulting electron shell vacancy can be filled by either capturing a free electron or via rearrangement of the electrons in other shells, resulting in the emission of a characteristic X-ray or Auger electron. One of the case result in energy – mass conservation according to quantum mechanics principles. This is the dominant mechanism at low energies ($< \sim 100 \text{ keV}$), and the probability for full absorption decreases rapidly with increasing photon energy ($\propto E_\gamma^{-3}$). The photo-absorption parameterization cross-section proposed by Biggs et al. [59] is shown in the following eq.

$$\sigma(Z, E_\gamma) = \frac{a(Z, E_\gamma)}{E_\gamma} + \frac{b(Z, E_\gamma)}{E_\gamma^2} + \frac{c(Z, E_\gamma)}{E_\gamma^3} + \frac{d(Z, E_\gamma)}{E_\gamma^4} \quad 2-12$$

A separate fit of each of the coefficients a, b, c, and d to the explore information was determined in several energy intervals using the least-squares method [38]. In the event that photon energy is underneath the lowest Sandia energy for the material, the cross section is processed for this lowest energy, so γ is absorbed by photo absorption at any energy. This approach is coherently implemented for models of photoelectric effect of Geant4. The physics of photoelectric effect is then well described and implemented in GEANT4 as well as other MC code for calculations. Thus, any medium becomes not transparent for low-energy γ -ray. For example, the Ra-226 and U-235 have characteristic γ -ray at around 186 keV and implementing model for photoelectric absorption in this case is quite challenging because of the appearance of both peaks at approximately the same energy levels.

The binding energies of the shells rely on the atomic number Z of the material for single element material. In compound materials the i^{th} element is picked arbitrarily according to the probability described in the following equation:

$$\text{Prob}(Z_i, E_\gamma) = \frac{n_{\text{at}} \sigma(Z_i, E_\gamma)}{\sum_i [n_{\text{at}} \sigma_i(E_\gamma)]} \quad 2-13$$

Theta distribution of the Photoelectron: it is though important to evaluate the variation and change in distribution of photoelectron since such parameters will be useful for detection systems. The polar angle of the photoelectron is accessed from the Sauter-Gavrila distribution [76]:

$$\frac{d\sigma}{d(\cos\theta)} \sim \frac{\sin^2\theta}{(1-\beta\cos\theta)^4} \left\{ 1 + \frac{1}{2} \gamma(\gamma-1)(\gamma-2)(1-\beta\cos\theta) \right\} \quad 2-14$$

β and γ in this case are not the β and γ decays, but the Lorentz factors of the photoelectron. $\cos\theta$ is related to the probability density function as described in the following equation:

$$f(\cos\theta) = \frac{1-\beta^2}{2\beta} \frac{1}{(1-\beta\cos\theta)^2} \Rightarrow \cos\theta = \frac{(1-2r)+\beta}{(1-2r)\beta+1} \quad 2-15$$

The rejection function is expressed as:

$$g(\cos\theta) = \frac{1-\cos^2\theta}{(1-\beta\cos\theta)^2} [1 + b(1-\beta\cos\theta)] \quad 2-16$$

$$b = \gamma(\gamma-1)(\gamma-2) / 2 \quad 2-17$$

2.3.2. Compton Scattering

Compton Scattering is the process whereby an incident photon scatters off of an atomic electron, resulting in a photon with reduced energy, and an electron carrying the energy lost from the photon [66]. The energy of the photon and electron is angular interaction-dependent. The energy conservation for Compton scattering process is described by the following equation (assuming that the electron is free and at rest):

$$E'_\gamma = \frac{E_\gamma}{1 + \frac{E_\gamma}{m_0 c^2} (1 - \cos\theta)} \quad 2-18$$

where E_γ = energy of the incident photon,

$m_0 c^2$ = rest mass energy of the electron, and

θ = angle through which the photon is scattered [53].

When $\theta = 0$, the photon is forward scattered (or not scattered at all), and the following equation reduces to $E'_\gamma = E_\gamma$ (as expected). For high energy photons that are completely back scattered ($\theta = 180^\circ$), equation reduces to $E'_\gamma \approx \frac{m_0 c^2}{2}$. The angle dependence of the scattered photon is shown by the polar plot of the intensity of Compton scattered radiation in Figure 2-1.

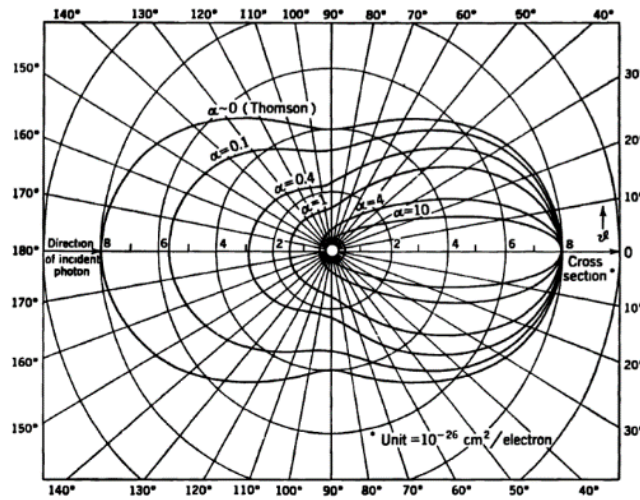


Figure 2-1: A polar plot of the intensity of Compton scattered radiation as a function of scattering angle, θ . Higher energy photons tend to be forward scattered, while lower energy γ -ray tends to be more evenly distributed [34, 53, 66].

An empirical cross-section equation is utilised, which similarities with the cross-section data down to 10 keV are observed:

$$\sigma(Z, E_\gamma) = \left[P_1(Z) \frac{\log(1+2X)}{X} + \frac{P_2(Z) + P_3(Z)X + P_4(Z)X^2}{1+aX+bX^2+cX^3} \right] \quad 2-19$$

$P_i(Z) = Z (d_i + e_i Z + f_i Z^2)$. The probability of a Compton scattered photon at an angle θ is described by the following *Klein-Nishina* formula:

$$\frac{d\sigma_c}{d\Omega} = r_0^2 \left[\frac{1}{1-\alpha(1-\cos\theta)} \right]^3 \left[\frac{1+\cos\theta}{2} \right] \left[1 + \frac{\alpha^2(1-\cos\theta)^2}{(1+\cos^2\theta)[1+\alpha(1-\cos\theta)]} \right] \quad 2-20$$

Here $\alpha = E_\gamma/mc^2$, $r_0 = e^2/4\pi\epsilon_0 mc^2 \cong 2.818 \text{ fm}$, the classical electron radius. The value of ϵ corresponding to the minimum photon energy (in the case of backward scattering, $\theta = \pi$) is given by:

$$\epsilon_0 = \frac{m_0 c^2}{m_0 c^2 + 2E_0} \quad 2-21$$

hence $\varepsilon \in [\varepsilon_0, 1]$. Combining composition and rejection MC methods described in the literature [34, 82–84, 86, 87], one may set the following function for simplification:

$$\varphi(\varepsilon) \cong \left[\frac{1}{\varepsilon} + \varepsilon \right] \left[1 - \frac{\varepsilon \sin^2 \theta}{1 + \varepsilon^2} \right] = f(\varepsilon).g(\varepsilon) = [\alpha_1 f_1(\varepsilon) + \alpha_2 f_2(\varepsilon)] g(\varepsilon) \quad 2-22$$

where $\alpha_1 = \ln\left(\frac{1}{\varepsilon_0}\right)$; $\alpha_2 = \frac{1 - \varepsilon_0^2}{2}$; $f_1(\varepsilon) = \frac{1}{\alpha_1 \varepsilon}$; $f_2(\varepsilon) = \frac{\varepsilon}{\alpha_2}$

f_1 and f_2 represent the probability density functions defined on the interval $[\varepsilon_0, 1]$, and

$$g(\varepsilon) = \left[1 - \frac{\varepsilon \sin^2 \theta}{1 - \varepsilon^2} \right] \quad 2-23$$

Described the rejection function as explained previously, $\forall \varepsilon \in [\varepsilon_0, 1] \Rightarrow 0 < g(\varepsilon) \leq 1$.

2.3.3. Γ conversion into e^+e^- pair

During pair-production the impinging photon creates an e^-e^+ pair with kinetic energies T_- & T_+ respectively. An atom must be present nearby for momentum conservation, and the energy transported by the incident photon must be greater than the rest masses of the electron and positron combined:

$$E_\gamma = 2mc^2 + T_- + T_+ \quad 2-24$$

Pair-production only contributes significantly at higher energies and becomes the dominant interaction mechanism at $E_\gamma > 5 \text{ MeV}$. In comparison to Compton scattering and photoelectric effect, pair production has a cut-off energy and occur at high γ -ray energy. The total cross-section per atom for an (e^+ , e^-) pair production has been parameterized as presented in the following equation [78, 88]:

$$\sigma(Z, E_\gamma) = Z(Z+1) \left[F_1(X) + F_2(X) Z + \frac{F_3(X)}{Z} \right] \quad 2-25$$

E_γ is the incident γ energy and $X = \ln(E_\gamma/m_e c^2)$. The functions F_n can be written as:

$$\begin{cases} F_1(X) = a_0 + a_1 X + a_2 X^2 + a_3 X^3 + a_4 X^4 + a_5 X^5 \\ F_2(X) = b_0 + b_1 X + b_2 X^2 + b_3 X^3 + b_4 X^4 + b_5 X^5 \\ F_3(X) = c_0 + c_1 X + c_2 X^2 + c_3 X^3 + c_4 X^4 + c_5 X^5 \end{cases} \quad 2-26$$

Parameters a_i , b_i , c_i can be found in a least-squares fit to the data [78]. This parameterization explains the data in the range $1 \leq Z \leq 100$ and $E_\gamma \in [1.5 \text{ MeV}, 100.0 \text{ GeV}]$ (because for energies lower than 1.5 MeV, the likelihood of pair production is almost null). The mean free path, λ , for a photon to convert into an (e^+ , e^-) pair in a given material can be written as:

$$\lambda(E_\gamma) = \left(\sum_i (n_{at})_i \cdot \sigma(Z_i, E_\gamma) \right)^{-1} \quad 2-27$$

$(n_{at})_i$ represents the atomic density of the i^{th} element of the material. The Bethe-Heitler formula corrected for various effects is written as [34, 88]:

$$\frac{d\sigma(Z, \varepsilon)}{d\varepsilon} = \alpha r_e^2 Z [Z + \zeta(Z)] \left\{ \left[\varepsilon^2 + (1 + \varepsilon)^2 \right] \left[\phi_1(\delta(\varepsilon)) - \frac{F(Z)}{2} \right] + \frac{2}{3} \varepsilon (1 - \varepsilon) \left[\phi_2(\delta(\varepsilon)) - \frac{F(Z)}{2} \right] \right\} \quad 2-28$$

α define the fine-structure constant (approximately 1/137). Here $\varepsilon = E/E_\gamma$, the total energy carried by

one particle of the (e^+, e^-) pair is E . Therefore, $\frac{m_e c^2}{E_\gamma} = \varepsilon_0 \leq \varepsilon \leq 1 - \varepsilon_0$ are the kinematical limits of ε .

The screening variable, δ , can be expressed as $\delta(\varepsilon) = \frac{136}{Z^{1/3}} \frac{\varepsilon_0}{\varepsilon(1-\varepsilon)}$ and explain the ‘‘impact parameter’’ of the projectile. According to some conditions, two screening functions are introduced in the Bethe-Heitler formula:

$$\text{for } \delta \leq 1 \quad \phi_1(\delta) = 20.867 - 3.242\delta + 0.625\delta^2 \quad 2-29$$

$$\phi_2(\delta) = 20.209 - 1.930\delta + 0.086\delta^2 \quad 2-30$$

$$\text{for } \delta > 1 \quad \phi_1(\delta) = \phi_2(\delta) = 21.12 - 4.184 \ln(\delta + 0.952) \quad 2-31$$

Due to the symmetry under the exchange $\varepsilon \leftrightarrow (1 - \varepsilon)$, the range of ε can be restricted to $\varepsilon \in [\varepsilon_0, 1/2]$.

The Bethe-Heitler was applicable with plane waves, but Coulomb waves should be used instead. This approximation in the field of detection is justified by the conversion process that takes place in the detection system: a photon is not directly measure as it transports no charge and no mass. A Coulomb correction function is introduced in the Bethe-Heitler equation: this is called *Born Approximation*. In γ spectrometry, energy range hardly ever exceed 5 MeV and we have the following formula [89, 90]:

$$F(z) = 8/3 \ln Z + 8f_c(Z) \quad 2-32$$

with

$$f_c(Z) = (\alpha Z)^2 \left[\frac{1}{1 + (\alpha Z)^2} + 0.20206 - 0.0369 (\alpha Z)^2 + 0.0083 (\alpha Z)^4 - 0.0020 (\alpha Z)^6 + \dots \right] \quad 2-33$$

The electron cloud gives another contribution to pair creation taken into account through the expression:

$$\zeta(Z) = \frac{\ln(1440/Z^{2/3})}{\ln(183/Z^{1/3}) - f_c(Z)} \quad 2-34$$

2.3.4. Rayleigh scattering

From the name of the physicist who discovered it, it is a predominant elastic scattering of electromagnetic radiation in the nuclear field. The total cross-section of the Rayleigh scattering process was resolved from an analytical parameterization. M. Born give the approximately atomic cross section for this process [34, 67, 68]:

$$\sigma(E) = \pi \cdot r_e^2 \int_{-1}^1 \frac{1 + \cos^2 \theta}{2} [F(q, Z)]^2 d \cos \theta \quad 2-35$$

$F(q, Z)$ referred to the atomic form factor, Z the atomic number, and q the magnitude of the momentum transfer, that can be defined by the following equation:

$$q = 2 \frac{E}{c} \sin\left(\frac{\theta}{2}\right) \quad 2-36$$

The following analytical approximations are justified and used for the form factor:

$$F(q, Z) = f(x, Z) = Z \frac{1 + a_1 x^2 + a_2 x^3 + a_3 x^4}{(1 + a_4 x^2 + a_5 x^4)^2} \quad \text{or} \quad \max[f(x, Z), F_K(x, Z)] \quad \text{if } Z > 10 \text{ and } f(x, Z) < 2 \quad 2-37$$

$$F_K(x, Z) = \frac{\sin(2b \arctan Q)}{bQ(1+Q^2)^b} \quad \text{with } x = 20.6074 \frac{q}{m_e c}, \quad Q = \frac{q}{2m_e c a}, \quad b = \sqrt{1-a^2}, \quad a = \alpha(Z - \frac{5}{16}) \quad 2-38$$

where α referred to the fine-structure constant,

$F_K(x, Z)$ describes the contribution to the atomic form factor due to the two K-shell electrons,

$f(x, Z)$ have been assessed by Baro for $Z = 1$ to 92 by numerically fitting the atomic form factors classified by Hubbel.

The integration of cross-section equation is performed numerically utilizing the 20-point Gaussian method [67, 75, 85]. Examples of photon cross sections for lead and germanium (the semiconductor used as crystal detector for our system) are shown in Figure 2-2 and Figure 2-3 below.

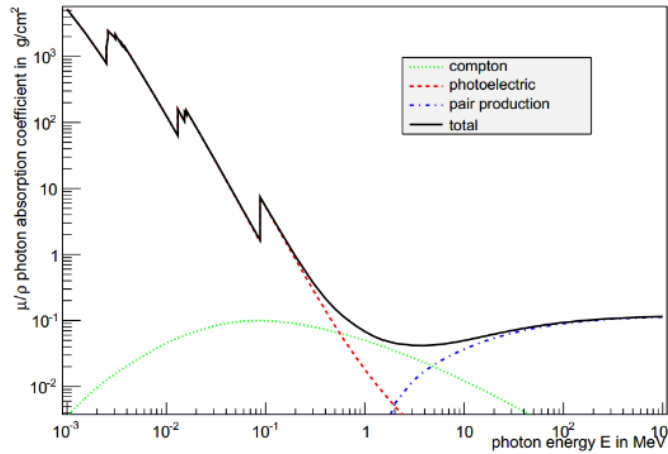


Figure 2-2: The photon absorption coefficient for a material (lead in this case) at different photon energies.

In the case we use germanium detector (HPGe) in our laboratory, we get the photon absorption coefficient as showed by the following figure.

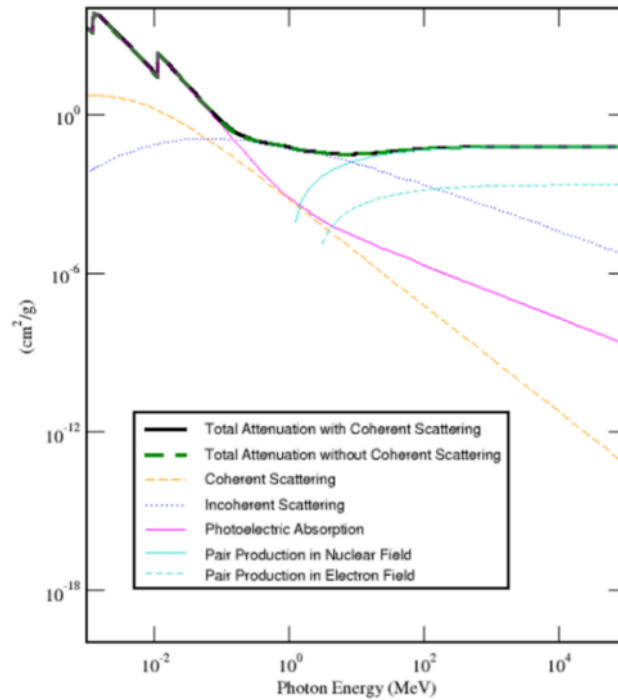


Figure 2-3: The photon absorption coefficient through germanium material at different photon energy.

The three main processes described in this sub-section, including photoelectric effect, Compton effect, and pair production are illustrated in Figure 2-4. These three physical processes are those considered in the rest of the manuscript and taking into account in physical model in GEANT4 for MC simulations.

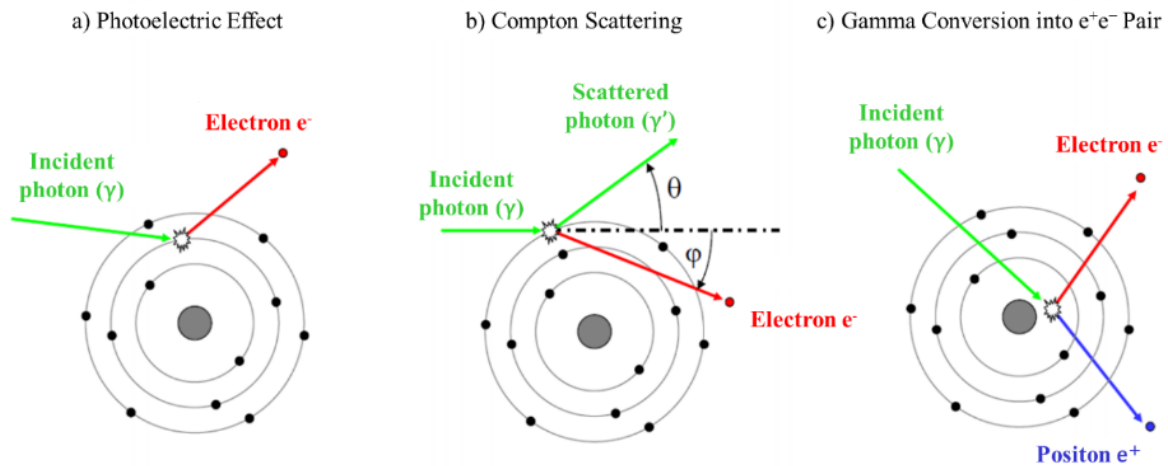


Figure 2-4: The three main interactions of photon with matter considered in the rest of the manuscript for computational work: photoelectric effect, Compton scattering, and pair production from right to left. Rayleigh scattering (or elastic scattering) is neglected in the rest of the project as its contribution is negligible in the framework of the present research.

Different processes have their occurrence likelihood depending on the energy of the γ -ray and the atomic number, Z of the material. Figure 2-5 shows the relative predominance of the three processes considered as contributors for work done, taking into account the photon energy and the atomic number of the material involved in the interaction. Photoelectric effect is predominant for low energy photons and high- Z materials while pair-production is predominant for high energy photons and high Z

materials. Compton scattering is dominant for the intermediate energy range.

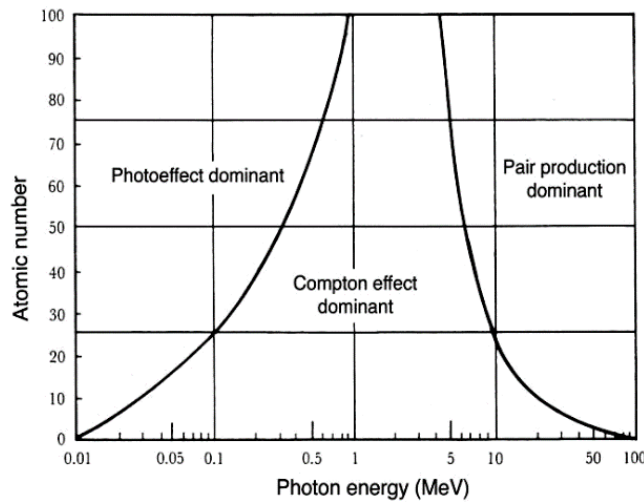


Figure 2-5: Relative predominance of photon interaction processes [64]. Only the main processes described in this section are presented

Because of its zero rest mass and zero charge, γ radiation has an extremely high penetration power in matter. Compared to α and β particles, γ penetration is more than an order of magnitude higher. Materials of high density and atomic number (such as lead or concrete) are most often used as absorbers to reduce X- or γ -radiation intensity. Radiation intensity is defined as the number of photons of a radiation beam that crosses a given area per second. Its attenuation when passing through a medium is governed by the decrease exponential law as shown in Figure 2-6 and in the following equation [80, 91]:

$$I = I_0 e^{-\mu x} \tag{2-39}$$

which is similar to the exponential attenuation of neutrons discussed earlier in this chapter. But attention must be paid that for multilayer compound material, the attenuation of photon does not change with the arrangement of elements in the material as it does for neutrons. For example, for 10 cm lead and 1 cm water, the photon attenuation is the same whether it crosses water first of lead first. That is not the case for neutron in general, because some materials are moderators, others are absorbers, and the attenuation power depends on the neutron energy absorbed or moderated.

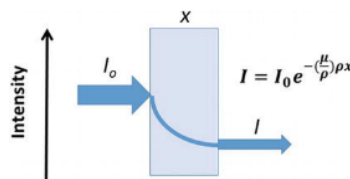


Figure 2-6: Exponential law of attenuation of photon when interacting with matter (x denotes the thickness of the medium).

In summary, electromagnetic radiation dissipates its energy in matter via three main mechanisms, that are the photoelectric effect, the Compton scattering, and the pair production. The photoelectric effect and Compton scattering generate ion pairs directly within the absorbing medium, even though they are not directly ionizing particles as charged particles (α , electron, proton, heavy charged particle), whereas, pair-production results in the creation of charged particles (positrons and negatrons) that will subsequently dissipate their energy via ionization, electron excitation, and annihilation (for

positrons only) [64, 92–96]. Annihilation will always occur when the positron lost its kinetic energy, and come to rest. Γ -rays interact primarily with atomic electrons; therefore, the attenuation coefficient must be proportional to the electron density P , which is proportional to the bulk density of the absorbing material. Thus, γ -ray interaction with matter is an important tool to measure and evaluate the behavior of atoms and nucleus [64, 89].

2.4. Particle Transport and Linear Energy Transfer (LET)

The radiation properties as their charge, mass, and energy and mechanisms of interaction previously described are important parameters considered in particle transport. They govern the rate of dissipation of energy and consequently the range of travel of the nuclear radiation in a medium. In this regard, two concepts are considered to describe the behavior of particles during their propagation in a medium and the behavior of the medium when crossed by radiation: the stopping power and linear energy transfer (LET) are those two descriptive parameters described subsequently [64, 75, 89, 91, 92].

2.4.1. The Interaction Length or Mean Free Path

The mean free path is one important parameter used to describe the depth at which a particle / radiation could travel into a particular medium (material). Computation of mean free path of a particle in a media is performed using cross-section. As the cross-sections are physical processes and atom density-dependent, the mean free path is usually given as a table of values depending on radiation energy and material characteristics (atom density). In a simple material the number of atoms per volume is given by the following formula:

$$n = \frac{N_A \rho}{A} \quad 2-40$$

where N_A = Avogadro's number;

ρ = density of the medium;

A = mass of a mole.

This formula differs in multiplicity when the medium is composed of multiple elements. In a compound material the number of atoms per volume of the i^{th} element is given by:

$$n = \sum_i \frac{N_A \rho w_i}{A_i} \quad 2-41$$

where w_i = proportion by mass of the i^{th} element;

A_i = mass of a mole of the i^{th} element.

The mean free path of a process, λ , also called the *interaction length*, that is used in computational physics, can be given in terms of the total cross-section as shown by the following equation:

$$\lambda(E) = \frac{1}{\sum_i [n_i \cdot \sigma(Z_i, E)]} = \left(\sum_i [n_i \cdot \sigma(Z_i, E)] \right)^{-1} \quad 2-42$$

where $\sigma(Z, E)$ is the total cross section per atom of the process and;

\sum_i the sum over all elements composing the material;

$\sum_i [n_i \cdot \sigma(Z_i, E)]$ is also called the macroscopic cross section. It is the summation of all microscopic cross-sections averaging the atom density in the medium. Simply stated, the mean free path is the inverse of the macroscopic cross-section [34, 64, 80–83, 89, 90, 97].

2.4.2. Stopping Power

The average linear rate of energy loss of a heavy charged particle in a medium (MeV cm^{-1}) is of fundamental importance in radiation physics, dosimetry, and radiation biology. It is the main characteristic of ionization process in the tissue, which constitutes the damage in human body during irradiation or exposure to such rays. This quantity, designated $[-dE/dx]$, is called the stopping power of the medium for the particle. It is also referred to as the linear energy transfer (LET) of the particle, usually expressed as $\text{keV } \mu\text{m}^{-1}$ in water. Stopping power and LET are closely associated with the dose and with the biological effectiveness of different kinds of radiation. These parameters are correlated to the biological effects of radiation in human body and are subject to investigation in radiobiology.

In 1913, Niels Bohr derived an explicit formula for the stopping power of heavy charged particles. His calculations were based on simple and valuable approximations as: the energy loss of a heavy charged particle in a collision with an electron could be averaged over all possible distances and energies to determine the stopping power [37], [38], [45]. Using relativistic quantum mechanics, Bethe derived the following expression (accurate even using some approximations) for the stopping power of a uniform medium for a heavy charged particle:

$$-\frac{dE}{dx} = \frac{4\pi k_0^2 z^2 e^4 n}{m c^2 \beta^2} \left[\ln \left(\frac{2 m c^2 \beta^2}{I(1-\beta^2)} \right) - \beta^2 \right] \quad 2-43$$

where $k_0 = 8.99 \times 10^9 \text{ N m}^2 \text{ C}^{-2}$ is the Boltzman constant given in constants definition at the beginning of this report;

z = atomic number of the heavy particle (fundamental parameter for atom definition);

e = magnitude of the electron charge as defined in constants section;

n = number of electrons per unit volume in the medium;

m = electron rest mass usually denoted m_0 ;

c = speed of light in vacuum and usually accept for the medium as air also;

$\beta = V/c$ = speed of the particle relative to c ;

I = mean excitation energy of the medium.

Only the total charge ze and velocity V of the heavy charged particle enter the expression for stopping power. For a given medium, only the electron density n is important. For simplification, the stopping power should be derived from the previous formula. If the constants in the Bethe equation for stopping power, dE/dX , are combined, the previous equation can be reduced to the following form:

$$-\frac{dE}{dx} = \frac{5.08 \times 10^{-31} z^2 n}{\beta^2} [F(\beta) - \ln I_{ev}] \text{ in MeV cm}^{-1} \quad 2-44$$

where

$$F(\beta) = \ln\left(\frac{1.02 \times 10^{-6} \beta^2}{1 - \beta^2}\right) - \beta^2 \quad 2-45$$

At low energy range, the factor in front of the bracket of equation 2.44, $(\frac{5.08 \times 10^{-31} z^2 n}{\beta^2})$, increases as $\beta \rightarrow 0$, causing a peak to occur. That peak is called the *Bragg peak* and is one important parameter of the heavy charged particle applications (because of the Bragg peak, the proton therapy, and other form of its exploration are possible in nuclear medicine). The linear rate of energy loss is a maximum as the particle energy approaches zero (0) [68, 72, 78, 82, 88].

Energy loss along an α particle track: For the majority of α particle track, the charge on the α is two electron charges. In addition, the rate of energy loss increases roughly as $1/E$. This is from the prediction from the equation of stopping power. Near the end of the track, the charge is reduced through electron pickup and the curve falls off. This falling off is the principal description of the Bragg pick.

Mass Stopping Power: The mass stopping power of a material is obtained by dividing the stopping power by the density ρ . It thus expresses the rate of energy loss of a charged particle when crossing a medium. It is useful to express the mass stopping power, $-dE/\rho dx$, in $\text{MeV cm}^2 \text{g}^{-1}$. Attention should be paid when dealing with medium formed by matter in different states. In a gas, for example, $-dE/dx$ depends on pressure, but $-dE/\rho dx$ does not, because dividing by the density exactly compensates for the pressure. Mass stopping powers for water can be scaled by density and used for tissues, plastics, hydrocarbons, and other materials that consist primarily of light elements. As a result, its values are similar for medium with similar density and heavy atoms are less efficient on a g cm^{-2} basis for slowing down heavy charged particles in general. It is because many of their electrons are too tightly bound in the inner shells to participate effectively in the absorption of energy [34, 80].

The modified Bethe–Bloch formula for the energy loss reads as follows

$$\frac{dE}{dx} = \frac{4\pi N e^4}{m c^2} \frac{1}{\beta^2} z^2 \left[\ln\left(\frac{\sqrt{2 m c^2 E_{\max}} \beta \gamma}{I}\right) - \frac{\beta^2}{2} - \frac{\delta(\beta)}{2} \right] \quad 2-46$$

Equation (2.46) holds for the range of $\beta\gamma$ where E_{\max} is smaller than the kinematic limit, and for $\gamma^2 \gg E_{\max}/m c^2$. The restricted energy loss could be applied for electrons as the different kinematic limits have been replaced by the common cut-off E_{\max} . The cut-off energy applied in this case is characteristic of all charged particles, included electron radiation. In the limit $\beta \rightarrow 1$, we now have complete the elimination of the γ dependency, and the restricted energy loss reaches the Fermi plateau [82]. The description is given by the following equation:

$$\left(\frac{dE}{dx}\right)_{\beta=1} = \frac{4\pi N e^4}{m c^2} z^2 \ln\left(\frac{\sqrt{2 m c^2 E_{\max}}}{\hbar \omega_p}\right) \quad 2-47$$

2.4.3. Determination of the interaction point

The interaction point in this section differs from interaction point in an accelerator, which is defined as the place where particles collide in an accelerator experiment. It describes the number of mean free path the particle travel during its existence, in average. The number of mean free paths which a particle travels is shown by the following equation:

$$n_{\lambda} = \int_{x_1}^{x_2} \frac{dx}{\lambda(x)} \quad 2-48$$

Its value is independent of the material crossed by radiation. In general, it depends on generic parameters. If n_r is a random variable referring to the number of mean free paths from a given point to the point of interaction, it can be shown that n_r has the distribution function of probability density:

$$P(n_r < n_{\lambda}) = 1 - e^{-n_{\lambda}} \quad 2-49$$

The total number of mean free paths the particle travels before reaching the interaction point, n_{λ} , is sampled at the beginning of the trajectory as:

$$n_{\lambda} = -\log(\eta) \quad 2-50$$

where η is a random number uniformly distributed in the range (0, 1). The definition of this number is much clearer in the chapter related to MC and GEANT4 simulation. n_{λ} is updated after each step Δx according to the formula presented in eq. 2-48 until the step originating from $s(x) = n_{\lambda} \cdot \lambda(x)$ is the shortest and this triggers the specific process [34, 81, 95, 96]. This formulation is used for computation in the rest of the manuscript.

$$n_{\lambda}^i = n_{\lambda} - \frac{\Delta x}{\lambda(x)} \quad 22-51$$

2.5. Conclusion

This chapter is the basement of the physics used in the next chapter for detection and simulation. It is then important to illustrate such interaction of radiation with matter before introducing the experimental method used in this work: the γ spectrometry method. Three processes are usually considered in γ -ray spectrometry as the processes by which the γ -ray interacts with matter. The photoelectric effect, the Compton scattering, and the pair-production are the phenomena described in this chapter. An overview of other particle types was presented. Other parameters were discussed in *Particle Transport and Linear Energy Transfer (LET)* sections. Those include the Interaction Length or Mean Free Path, the Stopping Power, and the Interaction Point. These parameters are subjects of importance in γ -ray spectrometry and especially when certain detector parameters could vary during an experiment.

The following chapter is based on the description of the experimental γ spectrometry, from sampling method to the data published and comparison with the result obtained in different other countries in the world. As radiation measurement is one of the most innovative topics in physics, enhancing detection method is a topic of international concern. International organization as IAEA used detection for safeguards verification processes. Understanding first and improving the method could lead to important advancement in the field. The following chapter deals with γ -ray spectrometry principles and radiation measurements in practice as implemented from the sampling sites to the laboratory.

CHAPTER 3. γ SPECTROMETRY AND RADIATION MEASUREMENT

3.1. Introduction

γ -ray spectrometry is a non-destructive quantitative and qualitative technique used to gauge electromagnetic radiation in the γ -ray spectrum of radioactive sources. It is performed through a procedure consisting of counting the number and measuring the energy of photons emitted from different elements (radionuclide) present in a sample. The main advantage of the technique resides in the use of high resolution germanium detectors. These high resolution γ detectors are usually based on semiconductor technology and scintillator, that is the secret of high resolution γ -ray spectrometry [2, 98, 99]. The assess of γ -rays is valuable for the public exposure assessment to radiation and has been widely used especially for natural radiation. Since the energy spectrum of a radionuclide is specific as a fingerprint, the measured energy of a γ -ray corresponds to the type of element and its isotope, while the number of counts corresponds to the abundance of the radioactive source present in the measured sample with some little considerations. The principle is then based on natural characteristics of γ radiation.

The process of measuring γ -rays begins at the radioactive source, which emits high energy photons during its unstable radioactive decay [100]. This spectrometry technique requires advanced understanding of the photo-peak efficiency of the detector in the counting geometry for each photon energy. The use of High Purity Germanium detectors has been increasing in the 21st century so that it is necessary to know every step involved in the method by a researcher in the field. That is the framework in which this chapter is part, which consists of a presentation of γ spectrometry methodology, HPGe detectors used for this thesis and their functioning principles. Two HPGe detectors were used in this study, one in Cameroon: a Broad Energy Germanium detector (BEGE-6530 model) and a second one at the Laboratory of Nuclear Physics of the University of Liege in Belgium: a HPGe (GC0818-7600SL model) [2, 101, 102].

3.2. HPGe Detectors Characterization

The ionization process in crystalline solids is the principle that allows electrons and holes movement and is the basis of detection systems. Simply states, an electron raises from the valence band to the conduction band during the ionization process. When electrons leave the valence band, an equal number of positive holes are created in that band. The length of the band between the valence and conduction bands, known as the gap, is the most important part to be explored for γ spectrometry technique. For example, materials with a small band gap are useful for electron transport and amplification, that is involved in the detection process. Germanium (with 0.7 eV gap) and silicon (with 1.1 eV gap) require an average of 3.0 eV and 3.6 eV, respectively, to be expended in creating a hole-electron pair, and so the amount of primary charge released is about ten times that in a gas filled detectors [3, 53, 75, 103–106]. This provides a real advantage for using semiconductor detectors compared to gas filled detectors for γ -ray spectrometry assessment and environmental monitoring.

Hyper-Pure Germanium (HPGe) detectors are essential instruments in high-resolution γ spectroscopy applications. As mentioned previously, germanium material has a small gap compared to silicon and other materials. In order to study low-level γ sources and internal activity of scintillators, a detector capable to detect low energy, separation of the closest picks in the spectrum is necessary: usually, it is said high energy resolution and good efficiency detectors for low energy γ - and X-rays. High purity germanium detectors are the best suited for this purpose, if one goal is to achieve measurement with high resolution and efficiency for low energy γ rays. Recent developments in semiconductor

growth technology have allowed the silicon and semiconductor companies to manufacture very high purity germanium (HPGe) with impurity concentrations of less than 10^{10} atoms/cm³. With this ongoing progress, the best detection techniques are for the future, but in the meantime, germanium is one of the most important detection crystals used in the world nowadays.

HPGe detectors operate as reverse-biased semiconductor diodes. This operational principle is shown in the following figure. When the incoming radiation passes through the semiconductor crystal, it produces electron-hole pairs. These phenomena release charges. When an electrostatic field is applied to the junction, charges are collected at electrodes in the surfaces of the crystal. The accounting process is then mathematically solvable as the number of electron-hole pairs created, and the magnitude of the resulting electrical signal is proportional to the amount of energy deposited in the detector by the incoming radiation [104, 107]. A reverse-biased semiconductor representation, as that used for high purity germanium detectors, is shown in the **Figure 3.1**.

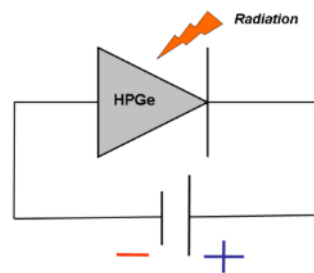


Figure 3-1: Representation of HPGe as reverse biased semiconductor diode: principle of semiconductor detector counting system.

The γ detector used to analyze the collected samples the first PhD year was a Broad Energy Germanium (BEGe) detector. It presents several advantages than other HPGe detectors such as:

- Its energy range, about of 3 keV to 3 MeV like no other type of detector;
- The resolution at low energies, equivalent to that of a Low Energy Ge (LEGe) detector;
- The resolution at high energy, comparable to that of good quality coaxial detectors; and
- Its short fat Sharpe which greatly enhances the efficiency at 1 MeV for typical sample geometries... etc.

Another HPGe detector used in the Atomic and Nuclear Spectroscopy laboratory of the University of Liege was the GC0818-7600SL model. The spectra displayed for BEGe detector is characterised by a high energy resolution. The GC0818-7600SL model is known for its ability to detect γ -rays with high energy as artificial radiation from irradiators. Specifications of both detectors used are presented in **Table 3-1** [102].

Both detectors are HPGe and have the same construction structure as described below:

- Broad energy germanium detector (including germanium crystal and all protection material consisting of lead shield). The germanium crystal is usually known as the central part of the detector, the heart around what all other parts are built;
- High voltage supply (for electron-hole pair transport or acceleration);
- Analog-to-digital converter (ADC);
- Pre-amplifiers in direct contact with the crystal detector;
- Amplifier as the signal output should be measured and quantified in understandable scales;
- Nuclear Instrumentation Material (NIM or the NIM-bin electronic system);
- Multichannel Analyzer as the sieve of the energy-system (MCA);

- Sample in cylindrical barker or other appropriate geometry depending on the measurement (Including all materials used during sampling campaign, the transfer of samples to the laboratory, and their preparation);
- Global positioning system (GPS used to mark site during sampling campaign) just in case of the necessity of re-sampling for a specific sampling point;
- Nitrogen cooling system for the GC0818-7600SL model in Belgium and a permanent electric system of electric cooling for the BEGe 6530 model in Cameroon;
- Computers including Genie 2000 software installed and LabSocs mathematics simulation software for calibration as well as other MCA software;
- Calibration sources in different varieties as point sources, volumetric sources, ...

Table 3-1: Specifications of both HPGe detectors used for γ assessment, BEGE-6530 model and GC0818-7600SL model [22, 101].

Descriptions	Detector	
	GC0818-7600SL	BEGe-6530
Detector type (Canberra)	GC0818-7600SL	BEGe-6530
Detector geometry	Plan (coaxial one open end, closed and facing window)	Plan
Detector active area-facing window	/	6500
Active diameter (mm)	43	91.5
Thickness (mm)	32	31.5
Distance from window (outside) (mm)	5	5
Window thickness (mm)	/	0.6
Detector end-cup type	/	Carbon epoxy
Relative efficiency at 1332.5 of ⁶⁰ Co (%)	30	60
Full Width Half Maximum (FWHM) Resolution (keV) at 5.9KeV	/	0.478
Full Width Half Maximum (FWHM) Resolution (keV) at 122KeV	0.825	0.695
Full Width Half Maximum (FWHM) Resolution (keV) at 1332.5KeV	1.88	1.785
Peak/Compton	38	/
Cryostat description / electrical cooling	Horizontal dipstick (Electrical cooling)	Vertical dipstick (LN2 cooling system)
Peak shape (FWTM/FWHM) for ⁶⁰ Co	1.71	1.88
Operational High Voltage supply (Volts)	3500	4500

The detector used for investigation was a commercial p-type BEGe detector (Model BE6530) produced by Canberra Ltd and companies. A schematic view of the detector configuration and its disposition in the laboratory is shown in Figure 3-2. The small boron-implanted p+ electrode is 13.5 mm in diameter and serves as the signal contact. Most of the residual surface of the detector is covered by the lithium-diffused n+ electrode which also serves as the high voltage contact and is separated from the p+ electrode by an annular groove. Different materials protect the detector crystal, that is held by a copper cup in a 1.6 mm-thick aluminum endcap placed at 8 mm from the front window. The window front protection is a very thin layer that should allow low-energy particles to penetrate the system

without filtering them. The front window is made of 0.6 mm-thick carbon epoxy to enhance the detection efficiencies of low-energy γ -rays that penetrate from the front. The recommended bias voltage is +4500 V. Data acquisition systems in this work involves a charge-sensitive pre-amplifier, an integrated digital signal analyzer, and the Genie-2000 software v3.2. All components cited previously are included in the detection chain. The pre-amplifier is integrated with the detector crystal directly and pre-amplifies the charge signal from the p+ electrode [108–110].

The digital signal analyzer (DSA) meshes functions of the high-voltage module, main amplifier module and MCA module in an analog electronics system. The record of the signal pulse shapes is done by the DSA. It extracts energy information and finally sends the information to the Genie-2000 software, which addresses the production and stores the energy spectra [105]. This is done in term of Nano or Pico second as one billion or more particles could be counted per second.



Figure 3-2: Broad Energy Germanium detector (BE 6540 model) used in Cameroon

3.2.1. Germanium crystal detector

The N-type crystal High Purity Germanium (HPGe) operational system is based on a semiconductor diode. Its operation is based on the electronic band structure in crystalline material with a valence band in which electrons cannot move, and a conduction band in which the electrons can move. As the forbidden gap for HPGe is low (0.7 eV), it is evident that those detectors are the most important used with semiconductor. After the creation of electron-holes pairs, the movement of electrons in the conduction band are influenced by the applied electric field. Even, before electrons are cached, the charges release more charges because of the acceleration due to the applied electric field. In counting system, the proportionality between the number of electron-hole pairs created and the energy deposited in the system by γ radiation is explored [104, 111–113]. Nevertheless, the correspondence is not perfect as some photons undergo scattering in the system before their capture or escalation. An approximation usually used consists of neglecting the scattering from specific γ compared to the total absorption of another γ that the energy corresponds to the absorption of another.

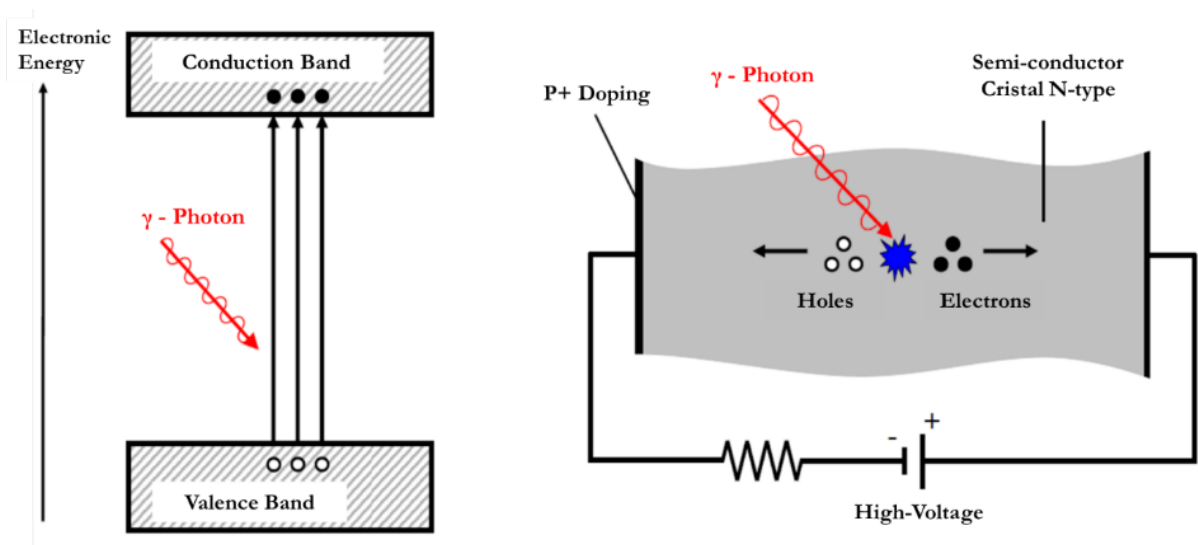


Figure 3-3: Band structure of the high purity germanium detector based on semi-conductor technology.

For semiconductor diode detectors, a reverse bias is applied over a p-n junction. The bias dimension should be as to deplete the detector and to saturate the drift velocity of electrons and holes [100, 113–115]. With an N-type germanium detector configuration, the contact material can be reversed, and the thin contact (minus terminal) can be put on the outside of the crystal while the thick contact (plus terminal) on the inside, as shown in Figure 3-3 and Figure 3-4. To avoid repetition of concept, the Figure 3-3 combines P-type and the principle and the Figure 3-4 implements details of the overall system. This junction is still maintained near the inner contact by this type of configuration. Important parameter taking into account for accuracy of the measurement in γ spectrometry is the dead layer of the detection system. Furthermore, the low energy efficiency increases due to the reduction of the thickness of the dead layer, as it could be reduced as smaller as possible [76, 104, 116].

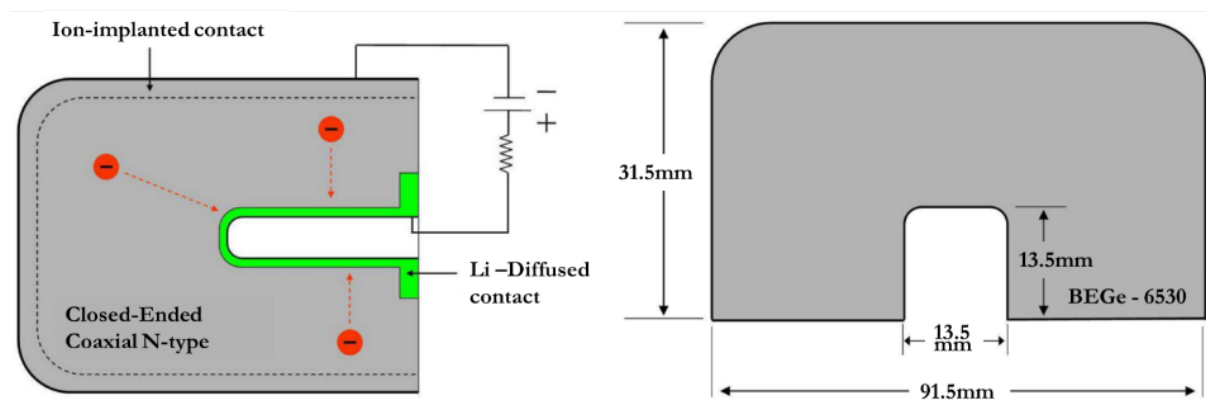


Figure 3-4: On the left side: closed-ended coaxial BEGe 6530 in N-type configuration. Right side: dimensions of the HPGe crystal as provided by CANBERRA firm.

The γ detector used to analyze the collected samples during the first PhD year was a Broad Energy Germanium (BEGe 6530 model) detector. It presents several advantages than other HPGe detectors such as: Its energy range about of 3 keV to 3 MeV; its resolution at low energies equivalent to that of a Low Energy Ge (LEGe). The second HPGe detector type was the GC0818-7600SL model. The spectra displayed for BEGe detector is characterized by a high energy resolution [101]. Another

important feature of the HPGe detector used in this project is its geometry. As previously shown in Table 3-1, the detector belongs to the closed-ended type of coaxial detectors. This means that this detector allows overcoming the leakage current problem at the front and the transmission of low energy radiation through the front surface. This second condition is achievable only if it is made with a thin contact, that was the case with the detectors used for this study.

The resolution of the CANBERRA Broad Energy Ge (BEGe) detector at low energies is equivalent to that of our Low Energy Ge Detector and the resolution at high energy is comparable to that of good quality coaxial detectors. The Co-60 relative efficiency for specific BEGe geometry displays its difference with other coaxial type detector or with NaI scintillator. The detector efficiency approximately ranges between 20-50 % [102, 105, 108]. In addition to higher efficiency for typical samples' geometry, the BEGe is characterized by lower background than typical coaxial detectors because it is more transparent to high energy cosmogenic background radiation that permeates above ground laboratories and to high energy γ from naturally occurring radioisotopes such as ^{40}K and ^{208}Tl (thorium) [104, 107, 117]. In general, most of the low energy γ detectors have good resolution at higher energies, but the resolution is not usually specified above 122keV. In this case, the Broad energy germanium detector represents a breakthrough of this common observable rule as it is able to detect γ -rays up to 30 keV and could easily separate ~ 86 keV of Ra-226 and U-235. This performance finds its secret in the design process of BEGe: the design includes an electrode structure that enhances low energy resolution and is fabricated from selecting germanium with an impurity profile that improves charge collection at high energies. This performance allows the use of BEGe in different applications. But for certain nuclear waste assay systems, particularly those involving special nuclear materials verification, Germanium detector needs cooling system that limits its practical management [92, 95, 104, 107]. A set of different parts of the detector and their functions is listed below:

- **Carbon Window**

The carbon window is used in the detection system in order to reduce attenuation of γ -rays before they interact with the detector. The layer of the end window located close to the detector is very thin. Another advantage to use a thin carbon window is that it increases the transmission of lower energy γ s than normal aluminum housing used in old systems or different ones [100]. Usually for HPGe this end cap consists of a beryllium or carbon filter. As both have a smaller Z compared to the aluminum, they are likely to be more effective as the lower Z material allows the reduction of the MDA (lower Minimum Detectable Activity) for a specific counting time. This reduction also provides another step in increasing sample throughput in low background counting applications as environmental assessment, especially in the region where activity is in a level comparable to the background.

- **Lead Shielding**

One major concern in γ spectrometry is the shielding against cosmic radiation and other radiation from environment of the measurement laboratory. The solution is usually provided by surrounding the detector material by thick shielding material as lead for γ radiation measurement. Lead, steel, concrete, or depleted uranium are usually used because high atomic number materials (Z) are good γ shielding systems. Lead has advantages with its high density, malleability, and large atomic number, and is the most used element to shield γ radiations [66, 100, 118]. As the detector in NRPA (Cameroon) was a cylindrical shape type, a cylindrical shielding made of Pb (lead castle) was used to remove γ -rays coming from natural and artificial sources, and so to shield the γ background. The shielding covers the detector region and let some space to put the sample to be characterized as it was shown in Figure 3-2 [104]. The shielding system of the detector used in Belgium was made with lead plates adjusted ac-

ording to the experiment and to the sample dimensions. The shielding system was built on the top of the detector and sample location.

Additional design requirements are needed for lead shielding as the interaction with Pb can increase the generation of X-rays. X-rays are released by the lead because some cosmic rays and γ s coming from the samples interact with the shielding. These X-rays should be shielded by additional material in the shielding enclosures, otherwise they could enter to the detector and increase the background. For this reason, this effect has to be taken into account during the design and analysis, this means the contributions of X-rays from Pb have to be subtracted from the spectra [90, 94, 100, 104, 112]. The detection system used for experiment in this project has a complete shielding. The lead castle includes an outer jacket made of ~ 9 mm thick carbon steel. The internal of the lead shield (bulk shield) is surrounding by 1 mm low background tin and ~ 1.5 mm high purity low background copper material. The copper as internal cover reduced the X-rays production from lead interaction with γ -rays.

3.2.2. Cooling System: Liquid Nitrogen and electric cooling.

HPGe detectors are known for their high resolution. Its large value finds its principle in the small value of the forbidden energy gap of 0.7 eV for germanium semiconductor. However, the resolution of the semiconductor detectors is not as good as that of the scintillators because of its strong dependence to the temperature. If the temperature of the HPGe is not maintained lower enough, the resolution deteriorates due to several parameters as:

- The increase of the forbidden energy gap,
- The thermal noise, and
- The leakage current.

It is only at sufficiently low temperature that thermal generation of intrinsic carriers (electrons and holes) in the germanium crystal becomes negligible, the forbidden energy gap is optimized and the leakage current decreases to the low value that is required for good performance of the detector [119, 120, 90, 100, 104, 112]. Liquid nitrogen is the cooler for many purposes including detector coolant. Therefore, the germanium crystal of the detector should be kept at very low temperature. The customary procedure to achieve the cooling objectives is the use of liquid nitrogen, although an alternative use of the electrical cooling is commercially developed and available in case LN2 technology is unavailable.

- GC0818-7600SL

The detector is usually housed in a vacuum-tight cryostat to reduce potential condensation of impurity gases on the detector surface and to inhibit thermal conductivity between the crystal and the surroundings [100, 104, 119]. The detector used in the IPNAS laboratory in Belgium was cooled using Liquid Nitrogen (LN2). It was designed as the cryostat is mounted on the Liquid Nitrogen Dewar. This configuration allows the cooling of the cryostat by thermal conductivity with connector in contact with LN2. The lifetime of the germanium detector thus depends on the constant maintaining of its temperature. Its thermal variations occur over the lifetime of the detector and cause the reduction of its performance and the detector does not last longer [120]. In fact, to prevent serious damage, high voltage can be applied to the diode only when the crystal temperature is sufficiently low to make reverse current negligible. Protection systems are connected to the detector to assure that high voltage activation is available only at the required temperature. The Dewar used was about 40 liters capacity and was equipped with a light signal that shows the level of LN2 in the tank. This control system allows the technician to constantly refill the Dewar manually with liquid nitrogen and conserve the

good functioning state of the system [121].

- BEGe-6530 cooling

The broad energy germanium detector's cooling system used in the laboratory of the National Radiation Protection Agency of Cameroon consisted of an electric cooling. This is a useful option provided by CANBERRA to developing countries where LN₂ technology can pose serious problems of availability. The electric system was connected to a power generator for alternative power supply in the case of emergency (usually due to power outage). The starting of the generator was automatically controlled in the case of power outage [122].

3.2.3. Electronic Devices

Signal processing is a meaningful part of the γ spectrometry assessment. It plays a relevant role in extracting useful information from the acquisition system. The description of the processing system is though important while characterizing all the electronic devices that shape the spectrometric system. Considering similitude between both detectors, we should optimize the parameters in the charge that includes sensitive preamplifier, HV power supply, amplifier, and multichannel analyzer (MCA). In the Figure 3-5 a schematic view of the set-up is shown [9, 104, 123].

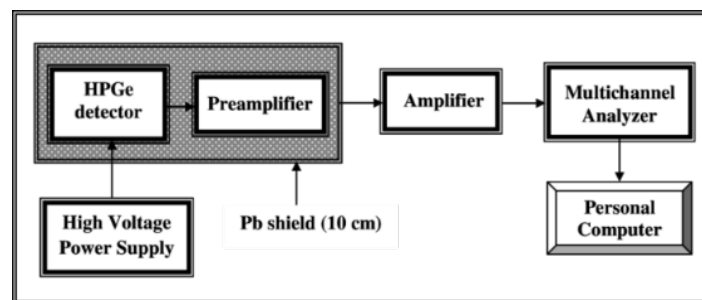


Figure 3-5: Diagram of high purity germanium detector system, including its major components.

- Preamplifier

The signal pulse produced as a result of the interaction of a γ in the detection system cannot be directly digitized or counted. The pulse has a very narrow width, short lifetime, noise, and small amplitude. For these reasons a pre-amplification stage is necessary before any further treatment of the signal [124]. Thereby, the preamplifier plays the following main roles:

- provide an optimum coupling between the detector crystal and the rest of the electronic system,
- shape the pulse, minimize the noise by filtering, and increase the amplitude of the pulses [125].

Changes in the capacitance of the detector and from cables must be regulated by the preamplifier in order to reduce the noise. It should be mounted as close as possible to the germanium crystal to reduce the capacitance effect from wires. Direct coupling between germanium crystal and preamplifier is the best solution as it additionally minimizes the input capacitance and allows the monitoring of the leakage current. Another function of the preamplifier, instead of directly amplifying the voltage or converting the current to voltage, is to integrate the accumulated charge on the detector capacitance in another capacitor [104, 123, 124].

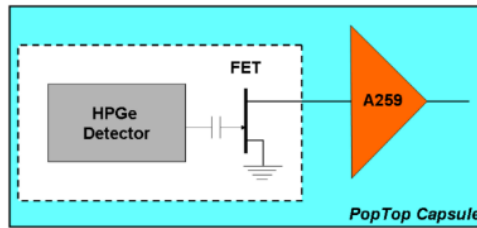


Figure 3-6: Scheme of preamplifier (electronic representation), FET, and capacitor inside the Pop-Top capsule.

- Amplifier

From the Pop-Top of the HPGe comes out two duplicated pre-amplified signals, called Energy and Time signals. From the preamplifier, the signal course continues in the amplifier. The main functions of the amplifier are to:

- fix the gain of the signals (increase the amplitude),
- restore the baseline,
- filter the noise,
- provide a (near-) Gaussian shaping and cancel the pole-zero [100].

In the case of the BEGe detector, the amplifier is coupled with the Nuclear Instrument Module (NIM) provided by Canberra connected to the MCA. Usually from the two signal outputs of the pre-amplifier, the unipolar (with positive lobe) is used in γ -ray spectroscopy. It is carried to the MCA whereas the bipolar with a positive lobe is used for timing applications. In spectrometry treatment, an amplifier should have a constant amplification for pulses of all amplitudes without distorting any of them to conserve information transmission and signal data [66, 100, 105].



Figure 3-7: Canberra Amplifier - Nuclear Instrument Module (NIM) of the detection system used.

- High voltage power supply

The bias voltage value has to be set in a way that it stabilizes coupling between devices and reduces thermal noise [104, 118]. HV should be regularly controlled also as the number of fully stopped radiation and the pulse height depends on its value. Adjustment should be made consequently to the design requirement and experimental condition. For example, when the bias voltage and electric field are low, the collection of charge carriers is incomplete because of trapping or recombination along the track of the incident particles. Charges are created but are not transported up to the conduction band for acceleration by electric field. The fraction that escapes to the collection will decrease as the elec-

tric field is increased. It is though important to set the saturation region as the charge collection becomes complete and constant at that value [104, 126]. The safety of the detector should also be assured by applying the high voltage only when the system is cooled enough at LN2 temperature as stated before. Maintaining a slow ration of increasing voltage starting from 0 up to -4500 V is one condition to maintain the stability of the detector and its long-life reliability.

- **Multichannel Analyzer (MCA)**

The Multichannel Analyzer is a device which sorts out incoming pulses according to pulse height and keep counting the number at each height in a multichannel memory. As its name indicates, every γ -ray that interacts in the detector volume is analyzed by the MCA. The content of each channel can then be displayed on a screen or printed out to give a pulse height histogram (displaying the number of detected particle counted versus channel number) [118]. The MCA digitize the amplitude of the incoming pulses through of an analog-to-digital converter (ADC), which associates different values received according to the pulse height. As the output is counts versus channels, the energy calibration is needed to allocate different energies of the study scale to channels [100, 104]. Energy calibration is one of the most important steps in γ spectrometry measurement as well as in other nuclear counting systems (that the interest is qualitative and quantitative). Furthermore, the total number of channels settles the grid into which the voltage range is to be digitized. This grid is known as *conversion gain* and determines the resolution of the MCA, that is also an important parameter to be controlled in γ -ray spectrometry for energy resolution. Larger number of channels with a short range of energy implies improvement of energy resolution.

3.3. Experimental Protocol in γ -ray spectrometry

3.3.1. Field of experiment

- ***Campuses of the University of Douala.***

The field of the experiment covered the two campuses of the University of Douala – Cameroon, a site located within the basin of Douala, named “Douala – Bassa” zone. The geographic coordinates were measured between 04° 03'14.8" - 04° 03'29.7" N and 09° 44'00.1" - 09° 44'45.2" W. The geology of the site is characterized by sedimentary rocks from the tertiary to quaternary sediments as shown of Figure 3-8 left [44, 127]. Detailed descriptions of the study area are presented in research done by Guembou et al., [2, 101]. As the area of study cover a location in an important basin in the Littoral Region of Cameroon, its geology is well known. It is a part of the largest city of Cameroon and Central Africa Region where the annual average temperature fluctuated around the value of 27.0 °C (80.6 °F). The studied area sits on high hydrology with flowing rivers as Wouri and Dibamba and characterized by a tropical climate. The city of Douala is a coastal city with borders-shared with the Atlantic Ocean. It typically features warm and humid conditions with an average annual humidity of ~83% and the rainfall is a particularity of the area which experiencing around 3,600 millimeters (140 in) average of precipitation per year [2, 101]. The rainfall variability is observed between two main seasons: the raining season, usually from Mars to October and the dry season from November to February. sampling areas are presented in the following figures with sampling points (Figure 3-8).

- ***Extending area of study: quarries in the city of Douala and surrounding.***

For the second part of experimentation, the sites of experiment were the seven big quarries name-ly “Bonaberi Bonamikano, Northern Akwa, Bois-de-Singe, Youpoue, Youpoue-Bamenda, Dibamba and Village” around the Douala city as shown on Figure 3-8 (right). The hydrogeology is modeling by the Wouri, Dibamba, Mungo, and Docteur Anse rivers and the Atlantic sea, as it includes the sur-

roundings of the main city, not only the Bassa area as the site presented previously [43–45]. The sand of these different careers is caught in various rivers in the vicinity of the city of Douala and in the sea (Douala is a coastal city). We had different criteria to classify sand; by color (gray, black, red, and white) depending on the grain size (fine, small grain, medium grain, and coarse) and according to the need of construction (bricks, slab, beam, and plastering). All these types were analyzed and different characteristics are presented in Table 3-2. These detailed data were collected during sampling campaigns in collaboration with different category of people including masons, inhabitants, sandblasters, beach visitors, and representative communities. Additional data were collected from the data bank of studies done on the site published and non-published.

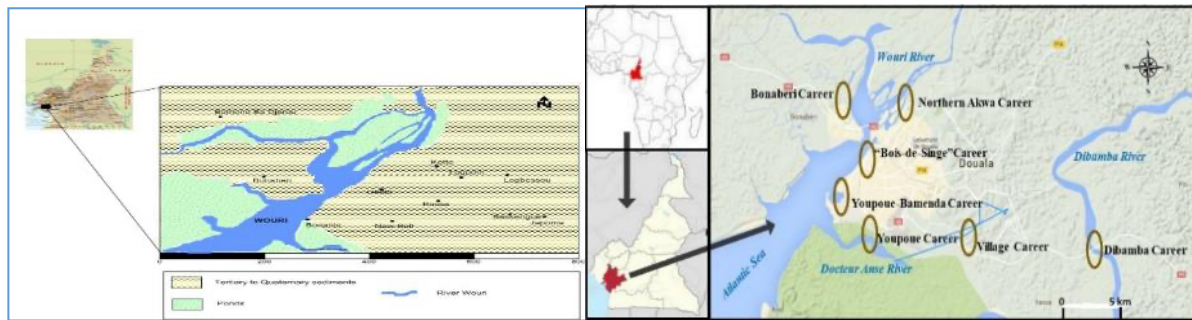


Figure 3-8: First - The Study Area consisting Douala Bassa area and second - Geographic location map with sample sites (the seven queries were presented here)

3.3.2. Sampling and sample preparation

- Sampling

For the first campaign: Composites of 18 soil samples were sampled from the 02 campuses, 07 from Campus 1 named ESSEC situated at Ange-Raphael and 11 from Campus 2 located at Ndong-Bong (Douala – Bassa area). The sampling method was a mixed sampling technique combining both simple sampling method (random selection of sites) and stratified sampling method using a representative well-defined distance between sampling points. The samples were labelled accordingly on-field and transferred to the laboratory for specific preparation and analysis. The vertical or near vertical surface was dressed to remove smeared soil before sampling. As human activities are ongoing in the study area (construction, agriculture, and waste deposit), the impact on the human being should not be neglected. This was necessary to minimize the effects of contaminant migration interferences due to smearing of material from other levels and activity. In addition, weathering and erosion processes are highly active processes in the area of study with high annual rainfall. Each composite sample was a mixture of five samples collected within an area of 6.25 m² separated from each other by a distance of 300 m to cover the study site and to observe a significant local spatial variation in terrestrial radioactivity as shown in Figure 3-9 [2, 47, 101]. This stratification and sampling process help displaying the result in an appropriate manner in case additional investigations are needed around a sample point. Each sampling point was marked using a global positioning system (GPS). Four samples were collected at the edges of a square of 2.5 m length and one at the center. These five sub-samples collected at a depth of approximately 20 to 25 cm from the top surface layer were mixed-up thoroughly to form a composite sample and packed into a polyethylene bag to avoid contamination between different samples taken at different points.

For the second sampling campaign: A total of 24 representative samples of sand building materials currently used in Douala, have been collected and labelled accordingly directly on site in the selected quarries thus to avoid contamination either during transportation and storage in the different sites

where work shall be done. The sampling method was based on site sampling instead of site-point sampling as in the previous case. This is due to the non-fixed point of study and the origin of the sand used as building material. In this case, sand is transported all over the city to be used as building material and the exposure is not on-site as the case of soil study. Mobility and mixture is on a high-level in the second sampling campaign compared to the first one. In the case of further investigations, site study is considered instead of sampling point and its surrounding, that is likely to be a little bit complex process because of large area to be assessed.

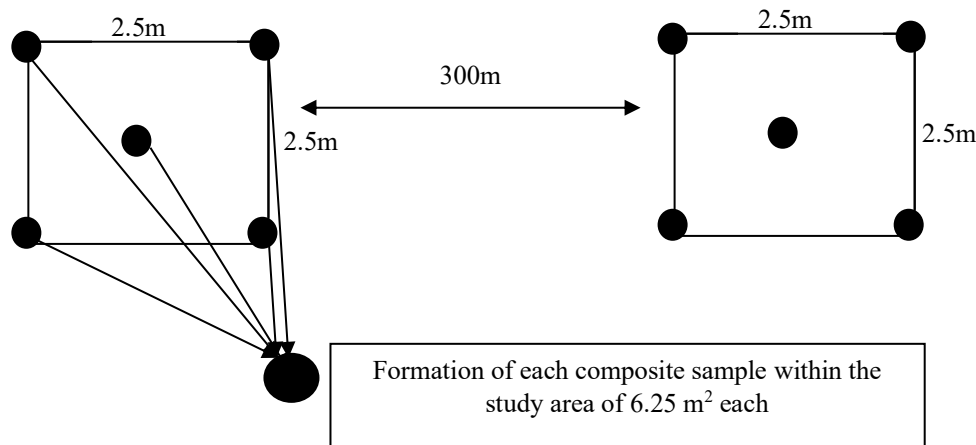


Figure 3-9: Composite sample collection methodology within the Sampling Sites

- Sample preparation

At the laboratory, samples were air-dried for a week then oven-dried at 105°C for 24 hours, as the moisture should be totally removed from the samples to avoid moisture effect. The dried samples were grinded into powder and sieved through a 2 mm wire mesh to obtain a uniform particles size. Homogeneity of the sample is an important factor in γ -ray spectrometry as it could influence the self-attenuation factor of the sample itself. One might make sure that the sample homogeneity is achievable at 90% at least during the sample preparation. Samples were then packed in a 120 mL air tight polyethylene cylindrical container, dry-weighed, and stored for a period of 30 ~ 32 days for secular equilibrium between the long-lived parent and daughter nuclides (For more details, see Ndontchueng et al. 2014 [2, 47]). One month was set in order to maintain radioactive equilibrium between ^{226}Ra and its daughters as 30 days' period is 10 times the 03 days' half-life period of the uranium daughters in the uranium series.

It is really important to achieve secular equilibrium since the radionuclides investigated includes Uranium and Thorium that the concentrations were evaluated using daughter radionuclides in the decay chain of Uranium and Thorium.

In both cases, the acquisition process of the measurement of samples consisted of counting the 120 ml container for 86,400 seconds. The main objective of the acquisition was the determination of activity concentrations of different radionuclides as ^{235}U , ^{226}Ra , ^{232}Th , and ^{40}K using appropriate γ -lines as stated by Ndontchueng et al. [4, 13, 47]. Interference or coincidence correction due to the pick at energy of 186.2 keV of ^{226}Ra (correction to Uranium γ -ray at around 185.7 keV) has been taken into account for the activity concentration assessment. Due to the high quality of the detection system and the long measurement time, the uncertainty was given at the 95 % confidence level. As γ -ray

spectrometry is a non-destructive passive analytical method, measurement time is usually set longer to achieve the desired statistic. In some cases, the measurement time might be adjusted (half day, two days or more) depending of the detection system characteristics and the activity of the sample [116, 128–133].

Three parameters were checked using a ⁶⁰Co and ¹⁵⁵Eu point sources located at 30 cm distance from the germanium detector crystal: these parameters are relative efficiency, resolution, and peak to Compton ratio. For the effectiveness of the radioactivity assessment, energy and efficiency calibrations should be done appropriately. Both calibrations determine the qualitative and quantitative measurements in nuclear applications, respectively.

Table 3-2. Samples description for the second sampling campaign. Quarry’s description and location are given within the vicinity of the Douala basin (Rio Del Rey basin on the Atlantic Ocean cost) [2].

Sampling site	Sample Id	Origin river/ Sea	Color of sample	Grain size	Need of construction
Akwa-Nord	AN_1	Wouri	Gray	Medium	Bricks, Beam, Plastering, Concrete Rambler, Slab
	AN_2	Wouri	Yellow	Coarse	Slab, Beam
	AN_3	Wouri	Yellow	Medium	All*
	AN_4	Wouri	Gray	Fine	Plastering
	AN_5	Wouri	Gray	Small	All
	AN_6	Wouri	Black	Small	Rambler
Dibamba	DI_1	Dibamba/soil	Black	Fine	Bricks, Slab, Beam
	DI_2	Dibamba/soil	Red	Small sticky	Plastering
Village	VI_1	Doctor Anse	White	Medium sticky	Bricks, Rambler
	VI_2	Doctor Anse	White	Fine	Slab, Beam
Bonaberi-Bonamikano	BB_1	Wouri	Yellow	Fine	Bricks, Beam
	BB_2	Wouri	White	Small	Slab, Beam
	BB_3	Wouri	Yellow	Small	All
	BB_4	Wouri	Yellow	Coarse	Bricks, Rambler
Bois-De-Singee	BS_1	Wouri/Sea	White	Coarse	Plastering
	BS_2	Wouri/Sea	Red	Medium	Plastering, Rambler
	BS_3	Wouri/Sea	White	Small sticky	Bricks, Beam
	BS_4	Wouri/Sea	Black	Medium	Bricks, Rambler
Youpoue	YO_1	Wouri/Sea	White	Fine	Rambler
	YO_2	Wouri/Sea	White	Medium	Bricks, Rambler
	YO_3	Wouri/Sea	Black	Coarse	Bricks, Slab, Beam
Youpoue-Bamendal	YB_1	Doctor Anse	Black	Small	Bricks, Beam
	YB_2	Doctor Anse	Gray	Coarse	Bricks, Beam
	YB_3	Doctor Anse	Yellow	Small	Bricks, Plastering

* Sand used for different purposes in general. It can be used in replacement of all other type studied in this work with high cost.

3.3.3. Steps for quality assurance during sampling and sample preparation

As to check whether the equipment is well calibrated and if the obtained results are in accordance with the reality, quality assurance should be done in the laboratory where measurements are under taken. The following measures were taken into consideration during the study;

- (i) During sampling, logs were kept with the details of sample site and sample number and location of the sampling point for information storage during the overall study;
- (ii) Samples were kept in sealed polythene bags to avoid cross contamination during transportation and with properly fixed unique labels on each bag. Appropriated plastic bags were used to make sure that additional chemical or physical processes are not likely to be occurred during their conservation;
- (iii) Three samples were obtained from each sampling site in order to achieve statistical representation of sampling in the case of sand analysis and five sub-samples to form the main sample in the case of soil study. Both sampling methods were proved to be statistically representative for the study area;
- (iv) All the necessary precautions were taken in the use of tools during sampling, drying, and crushing to avoid cross contamination of samples. For example, the sampling tools were cleaned after taking one sample and prior to the next sample, as a double bling check in case dust might be deposited on a tool during the movement from one point to another;
- (v) During the determination of intensity of the natural radionuclides, a careful selection of region of interest (ROI) on the spectrum and with consistent window for all samples was ensured. As picks could be closer and the analysis become more complex, pick separation need clear ROI definition.
- (vi) The standard reference materials prepared in the local laboratory or/and provided by IAEA were used for calibration of the γ -ray detector and calculation of activity of the samples provided a standard procedure for the analytical technique of measurements. Energy calibration is related to qualitative analysis, consisting of identifying energy-ray characteristic of a radionuclide while efficiency calibration allows quantitative measurement. The last one is used in activity evaluation to determine the activity concentration of a radionuclide present in a sample.

- Secular equilibrium

The rate of decay of any radionuclide is proportional to the number of atoms present in the source i.e., the activity A is directly proportional to the number of atoms, N of nuclides present [105, 134, 135]. Simply states, the activity is defined as the number of decay per unit time as in the case of γ , α , and β emissions (decay):

$$A = -\frac{dN}{dt} = \lambda N \quad 3-1$$

where λ is the decay constant in s^{-1} . Activity of radionuclide after time t is given by the following equation, which can be derived from the previous one by mathematical integration:

$$A = A_0 e^{-\lambda t} \quad 3-2$$

Where A_0 is the initial activity of the source. As the parent decay produces the daughter, the rate at which the daughter radionuclide depends on the parent instantaneous activity. As initially, there is not daughter radionuclide as considered in general cases, the relationship between parent and daughter activity is given by the following equation:

$$\frac{A_{\text{Daughter}}}{A_{\text{Parent}}} = \frac{\lambda_{\text{Daughter}}}{\lambda_{\text{Daughter}} - \lambda_{\text{Parent}}} \quad 3-3$$

This equation is the result of development and simplification of activity decay relation for parent and daughter radionuclide. If the daughter radionuclide's half-life is too lower than the parent's, $\lambda_D \gg \lambda_P$, this means the daughter's activity is approximately equal to the parent's activity. The corresponding state is referred to as secular equilibrium. This is normally achieved in a closed system hence secular equilibrium in the decay series of ^{238}U can be distorted by the escape of ^{222}Rn . For this reason, samples should be sealed and stored for a while before measurement. The amount of the daughter's radionuclide builds up until the number of daughter atoms decaying per unit time becomes equal to the number being produced per unit time [76, 104, 107, 111, 123, 136, 137].

- **Detector Energy Response**

In addition to detect the presence of radiation, most detectors can also provide radiation data: energy, time, etc. This follows as the quantity of ionization in a detector generated by radiation is proportional to the energy it loses in the sensitive volume. The dimension of the detector affects the measurement process and influences the result as the statistic could be adjusted based on the system. For example, if the detector is large (dimension) enough to fully absorb the radiation, the ionization process will give a measure of the energy of the radiation. The count rate will be larger than that of a small detector [118].

- **Energy Resolution**

The energy resolution is the most significant variable for detectors intended to assess the energy of incident radiation and to identify the emitter radionuclide. This is the extent to which two close energy-lines can be distinguished by the detector. The resolution can generally be evaluated by sending a mono-energetic radiation beam into the detector and observing and interpreting the resulting spectrum. The resolution is generally provided at full width half maximum of the peak (FWHM). Energy peaks closer than this interval are generally regarded as irresolvable, as the detector view them as one peak. There are several deconvolution methods to separate such close peaks in the spectrum, but in basic γ-ray spectrometry, it is almost impossible. Also, depending on the type of detector, the separation of the peaks is a difficult task if NaI scintillators are used compared to HPGe semiconductors. Deposition of energy in a detector is a stochastic process and is therefore linked to statistical fluctuations. A major restriction of energy resolution is the amount of basic procedures for which load is deposited (ionization, particle-hole formation, fluorescence excitation, and subsequent light emission) and the effectiveness of these additional procedures [104,105,115,140]. Thus, with increasing energy, these statistical fluctuations should be decreased in relative terms, roughly as: $E^{-1/2}$

- **Energy Linearity**

The linearity of the detector response is a highly desirable property. That is, the detector's output signal is proportional to the energy deposited on it. A detector may lose linearity at the high extreme of energies (saturation) or may be nonlinear in the low end [104]. When the linearity of the detector is assumed at the beginning of its life ($E = \alpha CN + \beta$), the linearity could not be fit after a certain period of use. The linearity previously expressed in the line equation is adjusted by a polynomial equation of the appropriate order ($E = \alpha_2 CN^2 + \alpha_1 CN + \alpha_0$). CN stands for channel.

- **Time resolution**

The time resolution is the capacity of a detector or experimental set-up to be used in time measurements to determine the exact moment an interaction occurred in the detector. Time resolution is expressed in terms of FWHM. Time histograms are generally achieved by measuring coincidence from one detector to another used as a reference [102–104, 123, 138]. Time resolution is a critical parameter in nuclear instrumentation as the signal treatment should be done in nano- or pico-second. Time scale is very low compared to what is usually measurable in human time scale.

- **Decay Time**

The decay time identifies the prompt scintillation yield of a material and its time of recovery before the material returns to its unexcited state and can undergo another scintillation event [66, 100, 104, 105]. It also describes the rate of decay for radioactive particles in a first order decay process as following the exponential decay relation.

- **Dead Time**

The dead time is the minimum amount of time necessary to separate two events to be recorded as two separate pulses. In other words, it is the detector's finite time to process an incident event that is generally associated with the pulse signal length (duration). Depending on the detector's type, during these phases, a detector may or may not remain sensitive to other occurrences. In some cases, the time limit may be set in the detector itself by process, and in other cases the time limit may arise in the related electronics [66, 100, 104]. Because of the random nature of radioactive decay, there is always some likelihood of losing a real event because it happens too rapidly after a previous event. These losses influence the observed count rates and distort the time distribution between events' arrivals. The counting rate of the detector must be kept sufficiently low to avoid large dead-time effects so that the likelihood of a second event occurring during a dead-time period is low. It is then possible to correct the residual impact.

3.3.4. Detector calibration procedure: energy and efficiency calibration

Both analyzes in Cameroon and in Belgium use similar methods for calibration of the detectors, but here we mentioned accuracy and deviance for each laboratory technics. There are few additional steps in each calibration procedure in each laboratory, depending on the geometry, the stability, and availability of the detection system.

In Cameroon, each sample was subjected to a coaxial γ -ray spectrometer consisting of Broad Energy Germanium detector (BEGe-6530 model) manufactured by Canberra Industries. The detector roomed at the spectrometry laboratory of the National Radiation Protection Agency of Cameroon. Excellent performance, routinely available in coaxial germanium detectors, and especially in the one used for this part of research. The energy resolution of the system (FWHM) at the experiment time was approximately 0.5 keV at 5.9 keV for ^{55}Fe , 2.2 keV at 1332 keV (^{60}Co), and approximately 0.75 keV at 122 keV (^{57}Co). For these higher efficiency detectors, "peak-to-Compton ratios" are usually quoted in the range of 25 to 40. These ratios are strong functions of resolution, efficiency, and exact detector crystal geometry, and no typical values can be given without knowledge of all of these parameters. The detector is placed in a low-level Canberra Model 747 lead shield with 10 cm thickness [2, 4, 13, 101, 139]. The energy distributions from radioactive samples to the nuclear instrumentation system were generated by the computer inbuilt Multiport II Multichannel Analyzer (MCA). Each sample was counted for 86400 seconds (24 hours). This counting time was set as the nuclear method used is a passive one and the samples were not highly radioactive, for effective peak area statistics of above 0.1%. Following the sample analysis process, the activity concentration in Becquerel

per kilogram ($\text{Bq}\cdot\text{kg}^{-1}$) for each radionuclide was calculated after background separation using the Genie-2000 software version v3.2. Prior to the activity calculation, the self-absorption and cascade summing correction were taken into account [108, 140, 141].

Assuming that the secular equilibrium between ^{238}U and ^{232}Th and their respective decay daughter products was reached after 32 days, the following relatively intense γ-ray transitions were used to measure the activity concentrations of the radium (Ra-226), thorium (Th-232), and potassium (K-40) above mentioned radionuclides [47, 53, 142].

- (a) ^{226}Ra concentration was calculated based on the assumption that it is a weighted mean of the activity concentrations of the γ-rays of ^{214}Pb (295.1 keV, 351.9 keV), ^{214}Bi (609.3 keV and 1120.29 keV), and its specific γ-ray at 186.2 keV. The 186.2 keV γ-ray line of ^{226}Ra was used only in the case the interference with the Uranium ray was resolved. Otherwise, the peak is likely to be the combination of the two's, including uranium surface.
- (b) The γ-ray photopeaks used for the determination of the ^{232}Th activity concentration contents were 338.4 keV, 911.2 keV, and 969.11 keV of ^{228}Ac and 238.6 keV of ^{212}Pb . They were weighted accordingly during the activity calculation step.
- (c) ^{40}K activity concentration was directly determined using its γ-ray at 1460.8 (with 10.7% branch ratio) γ-ray [47].

In Liege, each sample was measured with a γ-ray spectrometer consisting of a high purity germanium detector setup (GC0818-7600SL model) and multichannel analyzer 8192 channel. The system was consisted of a Canberra germanium detector with active diameter of 43 mm, relative efficiency of 30% at 1.33MeV ^{60}Co line and a resolution of 1.88 keV at the same line. The shielding enclosure of the detector was an in-laboratory built system, compare to the BEGe system which the lead shield was a complete Canberra system. The selected samples were subjected to γ spectral analysis with a counting time of 86,400 s (24 hours). The absolute photopeak energy calibration of the system was carried out using standard multi-γ emitter ^{152}Eu source. The sources were placed in the dedicated space on the top of the germanium detector with the radionuclides dispersed in gel matrices within planar beakers of geometries identical to that of the evaluated samples for efficiency calibration step. The calibration spectra were also acquired for 7,200 s (2h) [6, 13, 47, 101, 140]. For background subtraction, background spectra were acquired for 48 hours prior to the measurement. The background spectra measured after the measurement of the last sample was compared to the first background spectrum in order to verify that the experimental conditions remain the same during sample acquisition (assurance quality).

Detector calibration.

The pulse height scale must be calibrated in terms of absolute γ-ray energy in γ-ray spectroscopy with germanium detectors. It is essential to correctly identify the centroid of some recognized energy peaks in order to calibrate any γ instrument, and then a calibration curve can be carried out to convert channels to energy units. Once the energy calibration points are created throughout the entire energy range of interest, a calibration curve relating energy to channel number is normally derived. Common techniques involve the least-square fitting of a polynomial of the following form:

$$E_i = \sum_{n=0}^N a_n \cdot C_i^n \tag{3-4}$$

Where E_i is the energy of the channel (C) number i (C_i). The calibration curve for a standard HPGe is usually linear, but in some cases the nonlinearity compels a polynomial fitting of order greater than 3 or 4 [22, 100].

Any measurement of absolute γ-ray emission rates needs detector efficiency understanding. The emission rate for a point source can then be calculated by evaluating the full-energy peak region over a specified time period and determining the solid angle of the detector from its size and the source-detector distance. However, the dimensions of these detectors are not standardized to any degree, and the accuracy of their active volume is very difficult to determine. Efficiency calibration is usually reported as an assortment of γ-ray energies covering the interest range to allow an empirical efficiency versus energy curve to be constructed.

Energy calibration is a procedure consisting to assign of channel number to energy values: The details are depending on the system used. Minima 2 energy lines are needed; ideal are 3 to 5 lines. We derived the polynomial (02 order) relationship because the fitting $Energy=Cst \times Channel$ was not as accuracy as possible and could lead to higher standard deviation values.

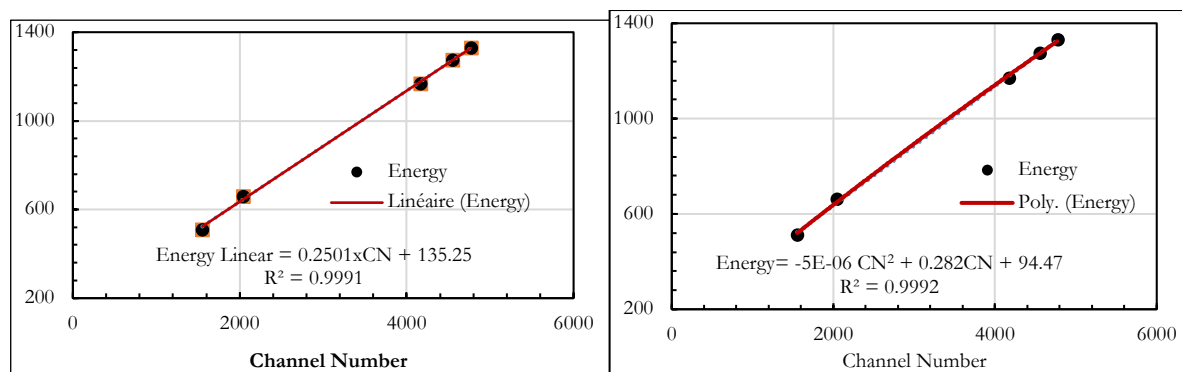


Figure 3-10. Energy calibration curves (Linear and Polynomial fitting) of the high purity germanium detector (HPGe)

The following equations

$$Energy\ Linear = 0.2501 \times CN + 135.25 \quad \text{with} \quad R^2 = 0.9991$$

$$Energy\ Poly = -5 \times 10^{-06} CN^2 + 0.282 \times CN + 94.47 \quad \text{with} \quad R^2 = 0.9992$$

are the best equations to fit the energy calibration curve.

Experimentally, the full energy peak efficiency for a particular sample-to-detector geometry is obtained by measuring the net counts under the photo-peak energy of interest, and using the following equation:

$$\epsilon = \frac{N_\gamma}{N_s} = \frac{N_\gamma}{t_\gamma P A_0 e^{-\lambda \Delta t}} \tag{3-5}$$

where: N_γ is the number of counts in the photo-peak, corrected for dead-time and pile-up losses and N_s is the number of photons emitted from the source. The other terms as ΔT describes the time elapsed since calibration up to measurement, A_0 the activity of the source on the reference date, P the branching ratio corresponding to the energy E_γ , λ the decay constant, and t_γ the real time taken for the

data run [2, 4, 6, 129, 143]. The experimental procedure follows the listed steps:

- Connect the detector to computer;
- Acquire background spectrum for 5 min or 2 hours;
- Put γ source in front of the detector;
- From start menu on the computer go to programs menu and then acquire a spectrum;
- Start detecting radiations;
- After 5 min (or two hours respectively), press stop;
- By right click on mouse and choose set ROI and then shade the area under the peak;
- Go to setting choice energy calibration and then choose 2 points;
- Move the pointer to the maximum count of the peak;
- Record the value of channel number (CH₀) at the maximum counts and the energy calibration (E₀);
- Repeat the same steps for the second and third source and unknown source;
- Plot a graph between CH₀ and E₀ to find the slope.

The Compton edge was considered in the evaluation of the spectra. In addition the process of accounting this process is given in the following figure (Figure 3-10). The calculation was done using the following formula:

$$E_{\gamma'} = \frac{E_{\gamma}}{1 + \frac{mc^2}{2E_{\gamma}}} \text{ derived from } E_{\gamma'} = \frac{E_{\gamma}}{1 + \frac{E_{\gamma}}{mc^2}(1 - \cos\theta)} \quad 3-6$$

The uncertainties can be calculated by the propagation of error equation and assuming the time t_{γ} is known precisely:

$$(\Delta\varepsilon)^2 = \left[\left(\frac{\partial\varepsilon}{\partial N_{\gamma}} \right)^2 (\Delta N_{\gamma})^2 + \left(\frac{\partial\varepsilon}{\partial A_0} \right)^2 (\Delta A_0)^2 + \left(\frac{\partial\varepsilon}{\partial P} \right)^2 (\Delta P)^2 + \left(\frac{\partial\varepsilon}{\partial \lambda} \right)^2 (\Delta \lambda)^2 \right] \quad 3-7$$

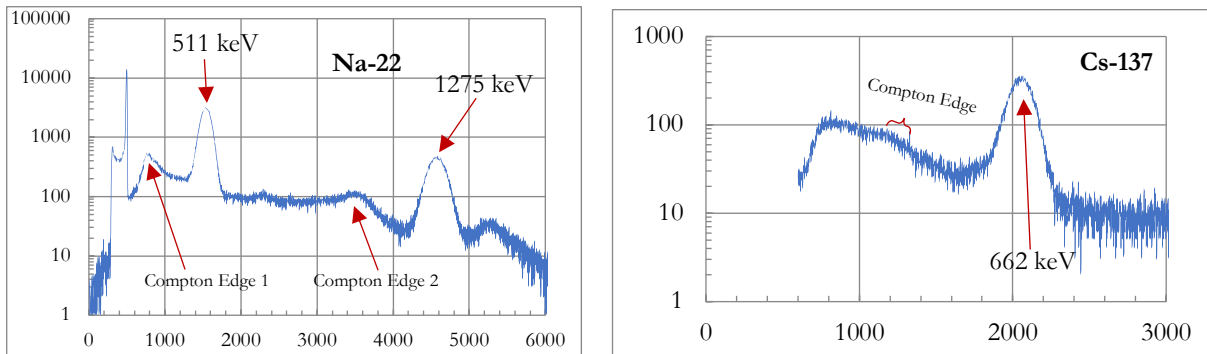


Figure 3-11. Nomenclature of the spectra of Na-22 and Cs-137 when considering the Compton Edge during analysis measured from NaI detector.

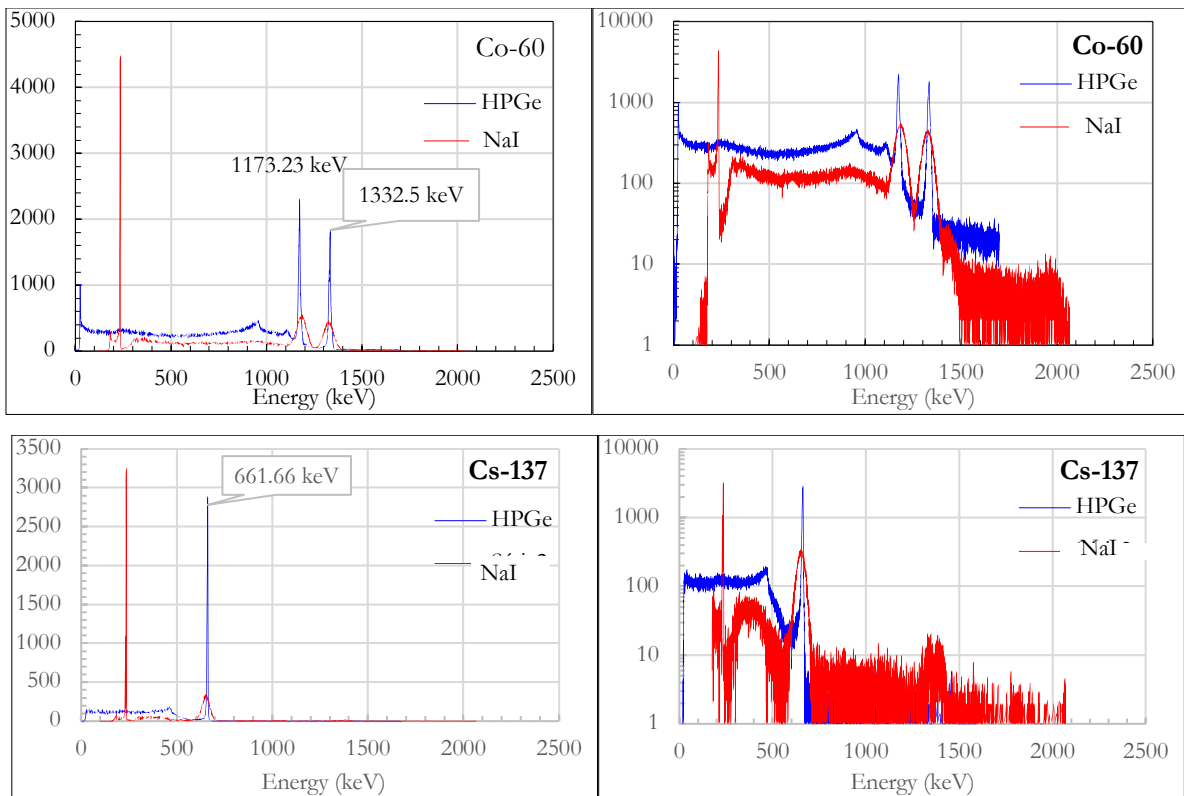
Thus,

$$\Delta\varepsilon = \left(\frac{N_{\gamma}}{t_{\gamma} P A_0 e^{-\lambda \Delta t}} \right) \left[\left(\frac{\Delta N_{\gamma}}{N_{\gamma}} \right)^2 + \left(\frac{-\Delta A_0}{A_0} \right)^2 + \left(\frac{-\Delta P}{P} \right)^2 + (\Delta t \cdot \Delta \lambda)^2 \right] \quad 3-8$$

Spectra from different radionuclide measure are presented below. The figures highlight (Figure 3.12) the high resolution of the HPGe compared to the NaI detector. This comparison shows best spectra resolution for HPGe detector as highlighted bellow.

Table 3-3: Spectra resolution comparison between HPGe and NaI (Tl)

Nuclide	Energy (keV)	HPGe	NaI (Tl)	Ratio NaI/ HPGe
		$\Delta E * 100 / E$		
Co-60	1173	0.865541	5.73%	6.620134
	1332.5	0.777486	4.70%	6.045125
Cs-137	662	0.782477	7.07%	9.035405
Na-22	511.22	1.175384	7.73%	6.576572
	1275	0.780047	5.26%	6.743183



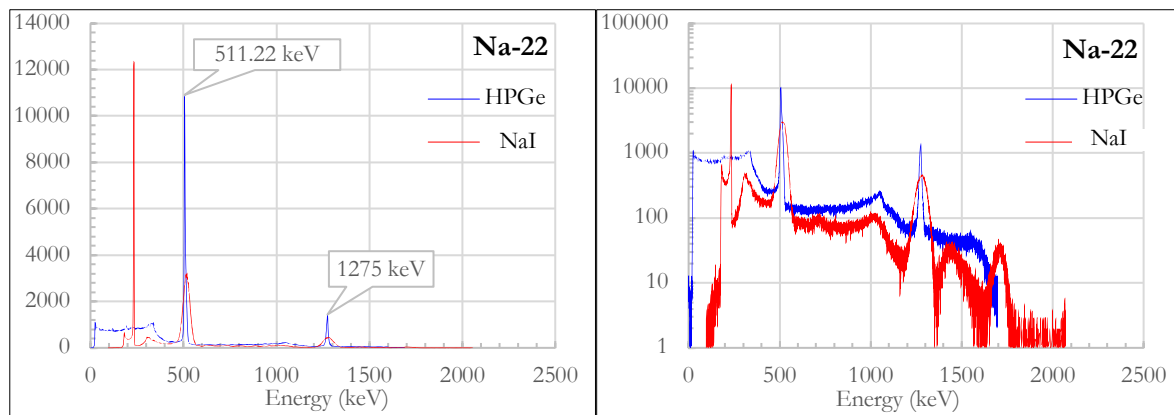


Figure 3-12. Spectra comparison between HPGe and NaI detectors. Large Gaussian distribution of picks from NaI detector than from HPGe detector (left: Normal scale. Right: Log scale).

The average value of full width at half maximum, FWHM, corresponds to the resolution of the high purity germanium (HPGe) and sodium iodide (NaI (TI)) detector. It describes how the detector can separate two adjacent energy peaks and hence, for unambiguous nuclide identification. Figure 3-12 indicates FWHM as a function of γ -ray energies for NaI(Tl) and HPGe detectors, provide useful information. It is shown that resolution is directly proportional to the γ -rays energies. But FWHM is much smaller in Germanium detector compared to the NaI(Tl) detector. Therefore, HPGe offers very good resolution and is a good instrument for nuclide identification compared to the NaI (TI) detector. In conclusion, high purity germanium detector has better resolution compared to the scintillation type of detector, sodium iodide (NaI). The HPGe detector offers the advantage of resolving two closely located energy points and has the ability to detect a mixture of nuclear material.

The ratio between resolution of NaI detector and High Purity germanium detector shows that the HPGe detector have about 9-time better resolution than Sodium Iodine detector for Cesium-137 with energy of 662 keV; about 6.6-time better for the first pick of sodium-22 with 511 keV energy and about 6.7-time better for its second pick with 1275 keV energy; about 6-time better resolution for the two picks of Cobalt-60 at 1173 keV and 1332.5 keV energies. HPGe detector has better resolution than NaI(Tl) detector

The detector's absolute efficiency calibration curve was determined using different calibration activity sources either prepared in our Spectrometry Laboratory, or produced by Areva Cerca Lea Company and supplied by Canberra. The system's efficiency calibration was performed using a classic ^{152}Eu multi- γ emitter source. The source was placed surrounding the germanium detector with the radionuclide dispersed in gel matrices within planar beakers of geometries identical to that of the evaluated samples. The ^{152}Eu source activity concentration was 3.24 kBq, for an active volume of 55 cl spread homogeneously in a gel matrix with a density of 1.6 g/cm^3 . This source was chosen to be comparable with the measured samples and therefore in the initial efficiency measurement using these planar housed sources, corrections for γ -ray self-attenuation within the samples are accounted for. The spectrum of calibration was also acquired for 7,200 s (2h). To compute the cascade summing correction, the (P/T) calibration curves were generated. Corrections were calculated after the sample geometry was established and specified in the software using the Geometry Composer Tool [13, 17, 47, 140, 144].

Once a detector's efficiency is evaluated using calibration sources at multiple energies, it is im-

portant to fit the obtained curve to these points to define the efficiency across the entire energy spectrum. Thus, for any energy value within the complete energy range, interpolation could be performed. Several empirical formulas have been defined in the literature to assess the efficiency of an HPGe, based on different software and tools. However, for one type of HPGe detector, whether planar or co-axial geometries, efficiency fits are optimized. One frequently used formula to cover broad energy ranges is a linear function relating the efficiency logarithm to the energy logarithm. The full energy peak (ϵ) of a high purity germanium detector (HPGe) can be demonstrated in the form of a γ -ray polynomial (E) as described in the following equation [103, 104, 123, 145–149]:

$$\ln(\epsilon) = \sum_{i=1}^N a_i \cdot (\ln E)^{i-1} \tag{3-9}$$

where E is the energy and a_i are the polynomial coefficients for different source-to detector distances (z). If a few data points are available or all are concentrated in a small energy region, the value of N could be limited to 2 or 3 terms to produce a stable oscillation-free solution [100]. An empty polystyrene container was counted in the same way as the samples to determine the background distribution owing to naturally occurring radionuclides in the surrounding environment around the detector. The levels of activity were calculated after measuring and subtracting the background.

3.4. Measurements of Activity concentration.

The activity of each sample was measured using a γ -ray spectrometer consisting of a shielded germanium detector supported by a classic electronic chain consisting of a multichannel analyzer, 8192 channels. The detector was a Canberra’s manufacturer product and contains a High Purity Germanium crystal with an active diameter of 91.5 mm. All the selected samples were subjected to γ counting or acquisition of 86,400 s (24 hours) and followed by the spectral analysis. γ Acquisition V.3.1 and Analysis Software from Canberra. Genie 2000 software was used for data acquisition and analysis. The spectra were evaluated using peak search, nuclide identification, activity and uncertainty calculation characteristics, and MDA calculation modules, all integrated in the software and relying on the following equation [2, 75, 104, 105, 111]:

$$A(Bq / kg) = \frac{\frac{N_S}{t_S} - \frac{N_B}{t_B}}{M_S \times \epsilon \times P_\gamma \times K_{SC} \times K_{SA} \times K_{DC}} \tag{3-10}$$

Where $A(Bq/kg)$ is the activity concentration of radionuclide,

$\frac{N_S}{t_S}$ the count rate of radionuclide in the sample,

$\frac{N_B}{t_B}$ the count rate of radionuclide in the background,

M_S mass of the sample,

ϵ the full energy peak efficiency,

P_γ the emission probability,

K_{SC} the cascade summing correction factor,

K_{SA} the correction factor for self-attenuation,

K_{DC} the decay correction factor for radionuclide.

The uncertainty of the activity concentration (ΔA) was calculated using the following equation and the result was expressed as relative uncertainties:

$$\frac{\Delta A}{A} = \sqrt{\left(\frac{\Delta N}{N}\right)^2 + \left(\frac{\Delta P_\gamma}{P_\gamma}\right)^2 + \left(\frac{\Delta \varepsilon}{\varepsilon}\right)^2 + \left(\frac{\Delta M}{M}\right)^2} \quad 3-11$$

Where ΔN is the count rate uncertainty,

ΔP_γ the emission probability uncertainty found in the nuclear data tables [150],

$\Delta \varepsilon$ the efficiency uncertainty, and

ΔM the weighing uncertainty [103].

The initial activity concentration of ^{226}Ra present in the samples was estimated using the γ -ray transition at ~ 186 keV. Several transitions from decays of shorter-lived radionuclides in the ^{238}U decay chain, such as ^{214}Pb and ^{214}Bi , were also used to estimate the activity concentration of ^{226}Ra , weighted as both radionuclides were taken into account in the activity evaluation. The activity concentration of ^{232}Th was determined using γ -ray transitions associated with the decay of ^{228}Ac , ^{212}Pb , and ^{208}Tl . Both radionuclides activity concentrations were weighted to the computation of the thorium activity as mentioned in the previous description [2, 101].

3.5. Assessment of radiation hazard and radiological parameters.

Radiation hazard

The radium-equivalent activity was assessed in order to evaluate the radiation hazard connected with construction materials used in dwellings. The radium equivalent activity is a weighted sum of activity of radionuclides ^{226}Ra , ^{232}Th , and ^{40}K based on the assumption that 370 Bq kg^{-1} of ^{226}Ra , 259 Bq kg^{-1} of ^{232}Th and 4810 Bq kg^{-1} of ^{40}K produce the same dose rate for γ -rays [47, 98, 129, 151]. Radium equivalent activity was computed from the following relation:

$$Ra_{eq} = A_{Ra} + 1.43 A_{Th} + 0.077 A_K = A_{Ra} + \frac{370}{259} A_{Th} + \frac{370}{4810} A_K \quad 3-12$$

Where A_{Ra} , A_{Th} , and A_K are the specific activities concentrations of ^{226}Ra , ^{232}Th , and ^{40}K expressed in Bq kg^{-1} , respectively and 1.0, 1.43, and 0.077 are weighted coefficients for the calculation.

Outdoor absorbed γ dose rate

γ dose rates in outdoor air at 1m above the ground surface were estimated using the activity concentrations of the ^{238}U , ^{232}Th , and ^{40}K measured previously in soil samples and using dose coefficients (in units of nGy h^{-1} per Bq kg^{-1}) 0.462, 0.604, and 0.0417 for ^{238}U series, ^{232}Th series, and ^{40}K , respectively [1, 49]. These values were proposed by Beretka and Mathew and implemented by many other authors [2, 129, 152]. The Outdoor absorbed γ dose rate (D_{out}) was assessed based on the following relation Eq. (14):

$$D_{out} (nGyh^{-1}) = 0.462 \times A_{Ra} + 0.604 A_{Th} + 0.0417 A_K \quad 3-13$$

where A_{Ra} , A_{Th} , and A_K are the activity concentrations of ^{226}Ra , ^{232}Th , and ^{40}K , respectively, expressed in the unit of Bq kg^{-1} .

Outdoor Annual effective dose (AED)

The conversion factor from the absorbed dose in air to the effective dose and the occupancy factor are essential in estimating the effective outdoor annual dose. A value of 0.7 Sv Gy^{-1} was used in the UNSCEAR report (2000) for the conversion factor from the absorbed dose in air to the effective dose received by adults and 0.2 for the factor of outdoor occupancy, implying that 20% of the time was spent outdoors. The coefficient 20% related to the fraction of time spent out is really fit with western countries with different climate. For example, in western countries, the winter season is one of the most contributors in reducing that factor as people are likely to stay indoors. In addition, the larger number of people involved in outdoor activities in developing countries increase the factor up to $OF = 0.4$. This value was not considered in this project but is under consideration for validation prior its use. The annual effective dose (AED) in units of mSv per year was estimated using the following formula [2, 4, 13, 47]:

$$AED(mSv/y) = D_{out} \times DCF \times OF \times FT \quad 3-14$$

Where AD, DCF, OF, and FT are absorbed dose rate in air (nGy/h), dose conversion factor (0.7 Sv/Gy), outdoor occupancy factor (0.2), and the time conversion factor (8760 h/y), respectively [49]. These factors are also expressed in UNSCEAR report [49].

External and internal Hazards indexes in sand samples

Krieger (1981) suggested the following conservative model based on the assumption of infinitely thick walls without windows and gates as a criterion for external hazard index (H_{ex}) calculations to limit the radiation dose from building material to 1.5 mGr y^{-1} . This criterion only reflects external exposure due to the γ -ray emitted and corresponds to a maximum radium equivalent activity value of 370 Bq kg^{-1} for the materials. The value of this index must be lower than unity for the radiation hazard to be negligible as recommended by UNSCEAR and IAEA [98, 153].

$$H_{ex} = \frac{A_{Ra}}{370} + \frac{A_{Th}}{259} + \frac{A_K}{4810} \leq 1 \quad 3-15$$

Internal exposure is caused by inhalation and ingestion of terrestrial radionuclides. Inhalation dose results from the presence of dust particles comprising ^{238}U and ^{232}Th decay chains radionuclides in the lower atmosphere in inhabitant environment. Radon's short-lived decay products (^{222}Rn) are the main contributors to inhalation exposure or internal exposure. They enter human (animal) body by inhalation through respiratory organs. To assess the internal exposure due to ^{222}Rn gas and its daughter products, the internal hazard index has been defined by Beretka and Mathew and validated by different other researchers in the field [129]. The calculation was based on the following equation:

$$H_{in} = \frac{A_{Ra}}{185} + \frac{A_{Th}}{259} + \frac{A_K}{4810} \leq 1 \quad 3-16$$

The European Commission (EC) suggested an index called the γ index (I_γ) to check compliance with EC rules for the use of building materials. I_γ was calculated using the formula below [154]:

$$I_{\gamma} = \frac{A_{Ra}}{300} + \frac{A_{Th}}{200} + \frac{A_K}{3000} \leq 1 \quad 3-17$$

EC introduced a two dose criteria for the γ dose related to the used of building materials: an exemption criterion of 0.3 mSv y^{-1} and an upper limit of 1 mSv y^{-1} . In general, countries in the European Union (UE) use these criteria as their guidelines. But some countries, depending on their own regulations, apply different rules. Therefore, most of the countries apply their control on the upper limit (1 mSv y^{-1}). If the exemption level of 0.3 mSv y^{-1} is considered, then the values of I_{γ} should be below 0.5 for materials used in bulk (like sand, cement, clay for concrete, ...); however, if the upper level of 1 mSv y^{-1} is considered then the values of I_{γ} should be below 1 for such materials. In Cameroon, the IAEA recommendations are applied by the regulatory body. For superficial building materials (covers, ornaments, and other material on surface with high likelihood of contact with inhabitants) with restricted use (tiles and board), the higher values of I_{γ} should be comprised between 2 and 6, supposing control values of 0.3 and 1 mSv y^{-1} , respectively. It is therefore a policy maker – decision making relation that is applied for each country. Attention should be paid on how the limits are set.

Excess α radiation caused by the inhalation of radon liberated from building materials can be estimated using the α index (I_{α}), which has been defined by the formula (3-18). The quantity I_{α} has been proposed by Krieger and Stoulos [2, 154–157]. The recommended values of I_{α} and I_{γ} are below 0.5 and 1, respectively [1, 2, 154, 158].

$$I_{\alpha} = \frac{A_{Ra}}{200} \quad 3-18$$

3.6. Conclusion

The present chapter depicted the basis of γ -ray spectrometry measurement. The description of different steps involved in γ -ray spectrometry measurement were detailed. Experimental procedures of the measurements of the energy resolution, the linearity, the efficiencies, the active volume size, and the dead layer thicknesses were described in detail as below [104]:

(a) **Energy resolution:** point-like sources of ^{241}Am , ^{133}Ba , ^{137}Cs , ^{60}Co and ^{152}Eu were located approximately above the top surface of the detector to measure its energy resolution. As to the point-like sources, the radioactive materials are sealed as a dot (1 mm diameter) in a thin plastic film. At first, the ^{60}Co source was measured alone to adjust the parameters of the system. Then the energy resolutions of more γ peaks with energies between 30 keV-3 MeV from the above radioisotopes were obtained to study their dependency to the γ peak energy.

(b) **Linearity:** the same sources as in Procedure (a) were measured and the peak locations of the corresponding γ -rays were recorded to check the linearity of the detector's response to the γ -ray energy deposition.

(c) **Efficiency:** a certified cylindrical volume mixed source made of filter medium (^{241}Am , ^{57}Co , ^{60}Co , ^{88}Y , ^{54}Mn , etc), was placed on the top surface of the detector to obtain the dependency of the absolute detection efficiency on the γ -ray energy. As for a concerned γ -ray, the net peak count was calculated and used to determine the corresponding detection efficiency, taking into consideration the measurement time, the emission intensity of the γ -ray, and the source radioactivity.

(d) **Dead layer thickness:** the same ^{241}Am source as in Procedure (a) was used to measure the front and side dead layer thicknesses. In certain measurements, the source was placed at a fixed posi-

tion and the full-energy-peak (FEP) detection efficiency of the 59.5 keV γ -ray was obtained experimentally (given the certified source activity).

As the application of nuclear methods are useful in industrialization, the world needs to keep developing new techniques and updating the existing ones. The present chapter focused on a technical overview of the γ spectrometry and the details used to obtain the results that are to be presented in the next chapter. From the sampling to data acquisition in the laboratory, different steps involved in the present project concerning γ detection are described in this chapter. They included:

- Investigated site description;
- Sampling method description;
- Sample collection and preparation;
- Detector calibration (in both energy and efficiency);
- Data acquisition and analysis;
- Activity concentrations calculation; and
- Radiation hazard parameters evaluation.

CHAPTER 4. γ SPECTROMETRY RESULT AND DISCUSSION

Since this study aim to contribute to the determination of natural radioactivity levels in the campuses of the University of Douala and surrounding, and to improve the γ spectrometry (Using High Purity Germanium detectors) methodology by Monte Carlo method, this chapter is complementary to the previous one. It presents the results of activity concentration measurements and radiological hazards from both studied areas. The soil and sand samples were analyzed by measuring the radioactivity concentration, the radiation absorbed dose rate, the annual effective dose rate, and hazard indexes. The quantities have been determined and the results presented in tables and graphs. The first section discusses the result obtained from campuses studied while the second part (section B) comments the result of the investigation of the queries in Douala and surrounding.

A. *Campuses of the University of Douala (Campus 1 and 2)*

4.1. The concentration of natural radionuclides

The activity concentrations of investigated primordial radionuclides ^{226}Ra , ^{232}Th , and ^{40}K in soil samples from the two campuses of the University of Douala-Cameroon, measured with both spectrometry instruments are presented in Table 4-1. Along the concentration are also presented the geological coordinates of each sampling point because this information was not presented in the previous chapter for the related site. As can be seen in the table, the average activity concentrations of ^{232}Th is higher than the worldwide value. As the thorium is the main contributor to the radiation exposure, attention should be paid to its level in soil samples, to deeply the investigated area. But the activity concentrations of ^{226}Ra and ^{40}K are lower than the world average values of 35 and 400 Bq kg^{-1} respectively. These average worldwide values found in the UNSCEAR report are not a limit or a target values, but specific value as comparisons are made with different other countries. The most abundant radionuclide found in the assessed sample was found to be potassium. Its concentration was about 66% and 70% of the total ($^{226}\text{Ra} + ^{232}\text{Th} + ^{40}\text{K}$), ^{226}Ra is 09% and 08%, and ^{232}Th is 25% and 22% in campus 1 and 2, respectively. These results were expected as the presence of potassium in soils, rocks, environment, and even in the human body is likely to be a natural process due to its high level. Potassium is also present in foodstuff as part of living being.

The radium equivalent activity was computed to evaluate the radioactivity in each sample weighted by the three natural radionuclides found. Ra_{eq} values ranged from 115.98 to 158.48 with an average value of 133.42 and from 116.63 to 159.77 with a mean of 136.53 in the unit of Bq kg^{-1} , in campus 1 and 2, respectively. Compared to the UNSCEAR recommended value of 370 Bq/kg , the average value of the radium equivalent activity was low. Therefore, the radiological analyses show that these two campuses are safe as recommended values were not exceeded. Extended analyses are needed to draw clear conclusions about the safety of people being exposed in the region, but in general when the radium equivalent activity is lower than 400 Bq/kg , other radiological parameters are lower than the recommended safe values. This applies to external exposure quantities.

As shown in Table 4-1, the activity concentration slightly varied from one sampling point to another and from one site to another. These differences observed in both locations may appear from the non-uniform distribution of radioactivity contents present under the crust of the Earth. Igneous rocks are usually regarded to have greater radioactivity concentrations than sedimentary rocks. The areas being studied are part of the Littoral Region, which is Cameroon's main sedimentary basin [2, 44, 101]. This formation has variation in sediments, limestone, shale, and clay. From the recorded activi-

ties concentration of the radionuclides found (^{226}Ra , ^{232}Th , and ^{40}K) in the present study, it can be noticed that the obtained average value of ^{232}Th in both locations was observed to be comparably higher (to the UNSCEAR value) than both of ^{226}Ra and ^{40}K in almost all the investigated soil samples probably due to the high content of thorium in sedimentary rocks.

We also evaluated the soil activity concentration using two both BEGe-6530 and GC0818-7600SL models HPGe detector. By comparing the results of the two detectors and the techniques used according to the detector type, results presented significant values as can be seen in Table 4-1 and Table 4-6 were displayed. The relative uncertainty activity concentration was calculated for ^{226}Ra , ^{232}Th , and ^{40}K . The average report between GC0818-7600SL model and BEGe-6530 model was calculated and the mean value of 3.36 was displayed as can be seen in Table 4.3.

As shown in Table 4-1, the measurement results of the activity concentration with the BEGe-6530 detector are very interesting. Indeed, the relative uncertainties are very small compared to the results obtained with the detector GC0818-7600SL regarding ^{226}Ra and ^{232}Th . It is important to notice that the Broad Energy Germanium Detector is very adaptable to low energies. The γ -ray of ^{226}Ra at 186.2 keV is detected with best resolution and minimal uncertainty while using the BEGe detector. However, for potassium which emits a line around 1461 keV, the ratio $\text{Err}(7600\text{SL})/\text{Err}(\text{BEGE-6530}) < 1$ is less than the unity. Therefore, the HPGe detector GC0818-7600SL model was found to be more suitable for high γ energy measurement and is not the best option for assessing radionuclides with low γ -ray energies. It can therefore be seen that BEGe measurement results are appropriate compared to other HPGe detector types and that we can really use 7600SL-model only to measure high energy γ emitters. As Broad Energy Germanium detector is designed for low background radioactivity measurement and low energy γ -ray, it was expected that the standard deviation for low γ emitter will be lower than that of the high γ energy emitter. When comparing potassium γ -ray line to those of radium and thorium, it is evident that the standard deviation for potassium measured by BEGe is expected to be higher. This is already checked through the computation of the minimum detection activity MDA [101]. These results were published by Guembou et al. (2017) [101].

In addition, Cs-137 concentrations measured with both detector models and the obtained results are displayed in Table 4.1. This radionuclide was not detected in few samples (ND) and its concentrations vary between 0.28 and 1.01 with an average value of 0.46 Bg/kg for campus 1, and from 0.17 to 0.95 with a mean of 0.30 Bq/kg for th samples from Campus 2, respectively. The origin of the measured cesium (non-natural Cs-137) was and is still subjected to further investigations as there are no nuclear power plants or nuclear reactors in operation in Cameroon or nearby the investigated area, to lead to the presence of such artificial radionuclide in the Campuses of the University of Douala. Its values measured with the BEGe detector model vary between 3.02 and 3.98 with an average value of 3.39 Bq/kg for samples from the campus 1, and from 0.72 to 3.79 with a mean of 3.02 for samples from the campus 2, respectively.

Table 4-1: Specific activities of ¹³⁷Cs, ²²⁶Ra, ²³²Th, and ⁴⁰K in soil samples from Campus 1 and 2 of the University of Douala measured using BEGe-6530 (Douala) and GC0818-7600SL (Liege) high purity germanium detectors. The uncertainty was given at the 95 % confidence level

Sampling sites	Sample ID	Latitude	Longitude	Activity concentration (Bq/kg)							
				¹³⁷ Cs		²²⁶ Ra		²³² Th		⁴⁰ K	
Laboratory of measurement				Dla* (BEGe)	7600SL	Dla (BEGe)	Lge# (7600SL)	Lge (7600SL)	Dla (BEGe)	Dla (BEGe)	Lge (7600SL)
Campus 1	UD01	04°03'20.8"N	09°43'57.6"W	4.0±0.3	0.6±0.1	26.7±0.8	11.2±1.9	65.9±1.6	35.7±0.5	32.6±3.2	117.9±3.8
	UD02	04°03'25.1"N	09°44'00.1"W	3.2±0.12	ND	29.0±0.8	31.51±2.2	80.0±1.9	54.9±0.6	13.9±2.9	195.7±4.1
	UD03	04°03'22.6"N	09°44'07.1"W	3.2±0.3	0.4±0.0	22.0±0.7	28.9±2.2	59.1±1.4	28.8±0.5	70.9±3.7	218.3±4.1
	UD04	04°03'19.7"N	09°44'04.1"W	3.0±0.3	0.3±0.1	25.4±0.8	28.4±2.5	63.3±1.5	27.4±0.4	38.0±3.4	170.1±3.9
	UD05	04°03'17.2"N	09°44'02.9"W	3.4±0.3	0.7±0.1	23.3±0.7	29.0±2.3	59.8±1.4	29.9±0.5	44.0±3.3	93.8±3.7
	UD06	04°03'14.8"N	09°44'08.0"W	3.7±0.3	1.0±0.1	29.2±0.9	21.5±2.3	71.1±1.7	45.4±0.6	21.8±3.1	188.0±4.1
	UD07	04°03'16.7"N	09°44'11.0"W	3.3±0.0	0.3±0.1	22.8±0.7	39.56±2.6	62.6±1.5	31.3±0.5	52.8±3.1	254.5±4.3
Minimum				3.0±0.3	ND	22.0±0.7	11.2±1.9	59.1±1.4	27.4±0.4	13.9±2.9	93.8±3.7
Maximum				4.0±0.3	1.01±0.1	29.2±0.9	39.6±2.6	65.9±1.6	54.9±0.6	70.9±3.7	254.5±4.3
Average values ± Standard Deviation				3.4±0.3	0.5±0.1	25.5±0.9	27.2±2.3	66.0±7.4	36.2±0.5	39.2±19.1	176.9±4.0
	UD08	04°03'29.7"N	09°44'26.5"W	0.7±0.4	ND	22.3±0.7	13.9±2.0	52.6±1.3	30.2±0.5	44.7±3.3	248.6±4.3
	UD09	04°03'31.0"N	09°44'30.3"W	3.8±0.3	0.2±0.1	27.7±0.8	41.6±2.2	62.8±1.5	32.5±0.5	16.8±3.1	47.4±3.6
	UD10	04°03'22.0"N	09°44'30.0"W	1.5±0.9	0.3±0.1	24.9±0.7	92.9±3.1	72.5±1.7	69.0±0.6	14.7±2.8	226.0±4.7
	UD11	04°03'25.1"N	09°44'36.8"W	2.8±0.2	0.5±0.1	22.0±0.7	11.8±2.6	63.9±1.5	76.0±0.7	11.9±2.7	172.6±4.2
	UD12	04°03'21.5"N	09°44'39.0"W	3.6±0.3	0.3±0.1	22.9±0.7	50.7±2.9	64.5±1.5	69.2±0.7	15.8±2.9	239.0±4.6

γ SPECTROMETRY RESULT AND DISCUSSION

The concentration of natural radionuclides

Campus 2	UD13	04°03'16.5"N	09°44'39.8"W	3.5±0.3	0.3±0.1	25.9±0.8	69.8±3.2	74.1±1.7	91.4±0.7	15.1±3.0	225.7±4.5
	UD14	04°03'18.4"N	09°44'37.5"W	3.2±0.3	0.3±0.1	23.8±0.7	41.5±2.9	63.2±1.5	78.1±0.8	80.8±2.8	198.2±4.4
	UD15	04°03'16.8"N	09°44'35.5"W	3.6±0.3	0.2±0.1	26.7±0.8	49.9±1.8	79.0±1.8	66.7±0.7	18.3±3.2	260.7±4.8
	UD16	04°03'24.9"N	09°44'42.2"W	2.9±0.3	0.2±0.1	24.6±0.8	62.9±2.5	71.7±1.7	73.9±0.6	29.9±3.2	245.0±4.6
	UD17	04°03'21.2"N	09°44'45.2"W	3.6±0.3	ND	25.0±0.7	23.5±2.2	72.4±1.7	76.3±0.6	19.8±1.8	240.2±4.6
	DU18	04°03'18.2"N	09°44'42.7"W	3.7±0.3	1.0±0.1	23.7±0.7	49.4±29	57.2±1.4	59.8±0.7	42.3±3.2	271.8±4.7
Minimum				0.7±0.4	ND	22.0±0.7	11.8±2.6	52.6±1.3	30.2±0.5	11.9±2.7	47.4±3.6
Maximum				3.8±0.3	1.0±0.1	27.7±0.8	92.9±3.1	79.0±1.8	91.4±0.7	80.8±2.8	271.8±4.7
Average values ± Standard Deviation				3.0±1.0	0.3±0.1	24.5±1.8	46.2±2.6	66.7±7.9	65.7±0.7	28.2±20.7	215.9±4.5
Worldwide	Range			-		17.00-60.00		11.00-68.00		140.00-850.00	
	Average			-		35.00		30.00		400.00	

*Dla means Measured at the laboratory of the University of Douala

#Lge means measured at the laboratory of the University of Liege

The observed similar variation in activity concentration of ²²⁶Ra and ⁴⁰K is due to the fact that both studied sites are closed one to another. In addition, investigated soils samples were from sites originated from the same geological formation and are likely to have similar properties. The slightly difference in average activity concentration value of ⁴⁰K from one sampling point to another is also due to the irregular distribution of uranium, thorium, and potassium contents present in the area under investigation. As radionuclides studied in the present project are natural long-life nuclides, their presence in an area could be constant or less variation could be observed if human activities have less effects. The measurements showed a comparatively low level of anthropogenic radionuclide ¹³⁷Cs activity levels. This could be interpreted as one of the consequences of the Chernobyl or Fukushima nuclear accidents. This conclusion was drawn since this radionuclide is not natural in the environment and is usually sprayed as nuclear power plant or bomb explosion product. Table 1 shows the activity concentration values of ¹³⁷Cs measured in soil specimens together with statistical uncertainty (1σ). The activity concentration of ¹³⁷Cs ranged from 0.28 to 1.01 Bq kg⁻¹ with a mean of 0.46 Bq kg⁻¹ (Campus 1) and from 0.17 to 0.95 Bq kg⁻¹ with a mean of 0.30 Bq kg⁻¹ (Campus 2). The highest mean activity concentrations of ¹³⁷Cs were measured in the soil samples from Campus 1. The altitude between both campuses varies from several meters to several tens of meters.

Table 4-2: Comparison of activity concentrations (Bq/kg) of U-238, Th-232, Cs-137, and K-40 measured in the investigated soil samples with that of other countries

Country	Activity concentration (Bq/kg)				References
	U-238	Th-232	Cs-137	K-40	
china (Xiaz-hung area)	40.2-442 (112)	32.6-88.1 (71.5)	-	440-913(672)	[159]
Botswana	6.1-97.4 (34.8)	7.4-110.0 (41.8)	-	33.5-1085.7 (432.7)	[160]
Ghana (Great Accra)	2.4-62.7	3.2-145.7	-	91.1-1395.9	[161]
Erçek Lake (Turkey)	8.6-42.6 (18.9)	11.6-53.2 (27.2)	0.7-24.4 (10.6)	254.1-771.9 (524.0)	[162]
India (Himwchal Pradesh)	42.09-79.63 (57.34)	52.83-135.75 (82.22)	-	95.33-160.30 (13 5.75)	[163]
Lebanon	5-73	5-50	2-113	57-554	[164]
Syria	6-69	3-50	1-143	87-750	[165]
Italy (Southern)	57-71	73-87	-	580-760	[166]
Jordan	-	-	8-573	-	[11]
Namibia	4.5-48(31)	3-38(32)	-	42-1100(480)	[167]
Nigeria Delta	11-40 (18±3.4)	12-40 (22±4.4)	-	69-530 (210±49)	[168]
Campus 1	25.48±0.92*	36.22±0.52	3.39±0.33	176.91±4.01	
Campus 2	24.50±1.80*	65.73±0.65	3.02±1.00	215.91±4.45	This work

() = average value / * average value of the activity concentration of ²²⁶Ra.

The observed activity concentrations of ²²⁶Ra, ²³²Th, and ⁴⁰K in the present work were compared with other published values obtained from the literature of radioactivity in soil by many authors as displayed in Table 4-2. Table 4-2 compares the activity concentrations of ²³⁸U, ²³²Th, ¹³⁷Cs and ⁴⁰K measured in the investigated soil samples from the present study with the values measured in different countries for the same material type. From the obtained data, the following remarks can be drawn: the

average activity concentrations of investigated radionuclides, ²³⁸U, ²³²Th, and ⁴⁰K measured in the study area are comparable with those reported by other studies. Activity concentrations ranged in the similar interval as that of different countries in the world. The mean activity concentration of ²³⁸U (²²⁶Ra by extension as they are parent and daughter radionuclides) and ⁴⁰K is lower than that of the worldwide mean (population weighted). Usually, potassium is the major radionuclide present in geological samples as soils, sediments, rocks, and sands. Even though its activity is lower than the average worldwide value generally measured and reported by UNSCEAR, it is much larger than that of radium and thorium. The average value of the activity concentration of ²³²Th activity is slightly higher than that of the world mean as reported by UNSCEAR [1, 47] for regular area. Here the comparison was not made with high natural background radioactive areas in the world as Ramsar (Iran), Brazil, China, and India, as the studied area is an inhabitable area with high population density and never been reported as high background area.

The observed average activity concentrations of ²³⁸U and ⁴⁰K in both studied sites were relatively lower than the values presented by other authors with the exception of the recorded values of ²²⁶Ra in Nigeria Delta published by Agbalagba and Onoja which were relatively low [2, 101, 168, 169]. Similar observations were seen for ²³²Th as recorded in the activity concentration in this work. It can be seen that the median ²³²Th values reported in this research were slightly smaller than those reported in China (Xiaz-hung region), Ghana (Greater Accra), and India [161][159, 161, 163, 170–172] and higher than the recorded and published average values in Namibia and Nigeria Delta [168, 169]. The present comparison shows similarities with material (sands) from different countries.

4.2. Comparison between the two detectors

4.2.1. Activity concentration validation

Results from comparison of the two HPGe detectors used in this research are presented below. It is clearly observed the importance of the selection of the equipment for γ spectrometry measurement or for any other metrology assessment. The energy gap of the radionuclides of interest must be taken into account in such situation. Table 4-3 presents the uncertainties on activity concentration measurement for both detectors. The standard deviation presented in this section indicated the extend of deviation for the whole measurement when choosing an apparatus for experiment.

Since in statistics, the standard deviation is a measure that is used to quantify the amount of variation or dispersion of a set of data values, it is important to highlight spectral analysis here. Great information is characterized as spectral data in which interested peaks are well shaped, molded all around, and have good "signal to noise." This is a key thought: simply having more data does not improve the data quality, as the deviation accuracy could be larger as well. One measure of a spectrum's quality is the detector system's minimum detectable activity (MDA) [131, 132]. The energy resolution, background, and efficiency of the detector are related parameter to the MDA. It is important to set the minimum detectable activity prior to the calculation of radiological parameter or activity calculation as it provides trustworthy data that the accuracy depends on. The MDA relationship might be essentially expressed as shown in the following equation:

$$MDA(E) \propto \frac{\sqrt{R(E).N(E)}}{\epsilon(E)} \tag{4-1}$$

Table 4-3: Errors related to Specific activities (in %) of ²²⁶Ra, ²³²Th, and ⁴⁰K and standard deviation in soil samples from Campus 1 and 2 using both detectors. The uncertainty was given at the 95 % confidence level

sample Id	Err _{Ra} /A _{Ra} (BEGe)	Err _{Ra} /A _{Ra} (7600SL)	Ra-7600S L/BEGe	Err _{Th} /A _{Th} (BEGe)	Err _{Th} /A _{Th} (7600SL)	Th-7600SL/ BEGe	Err _K /A _K (BEGe)	Err _K /A _K (7600SL)	K-7600SL/ B EGe
UD1	2.85	18.67	6.56	2.35	3.14	1.33	9.89	3.74	0.38
UD2	2.90	16.48	5.68	2.34	2.98	1.28	20.67	3.59	0.17
UD3	3.09	16.85	5.45	2.38	3.28	1.38	5.22	3.49	0.67
UD4	3.03	19.23	6.35	2.40	2.95	1.23	8.89	3.60	0.41
UD5	3.05	17.69	5.80	2.38	3.20	1.35	7.47	3.83	0.51
UD6	2.98	20.44	6.85	2.41	3.49	1.45	14.16	3.70	0.26
UD7	3.02	17.22	5.69	2.37	3.45	1.46	5.91	3.42	0.58
UD8	3.05	19.18	6.28	2.41	3.53	1.46	7.32	3.44	0.47
UD9	2.89	14.54	5.03	2.40	3.56	1.48	18.26	4.05	0.22
UD10	2.93	12.20	4.17	2.29	2.95	1.29	18.80	7.53	0.40
UD11	3.09	25.55	8.26	2.33	3.12	1.34	22.37	7.65	0.34
UD12	3.01	16.67	5.53	2.34	3.10	1.32	18.33	7.48	0.41
UD13	2.94	15.58	5.30	2.31	2.86	1.24	19.60	7.47	0.38
UD14	2.98	18.86	6.33	2.34	2.92	1.25	3.47	7.56	2.18
UD15	2.99	10.46	3.50	2.32	3.00	1.29	17.55	7.47	0.43
UD16	3.08	12.78	4.14	2.36	2.54	1.08	10.82	7.49	0.69
UD17	2.96	18.15	6.13	2.29	2.60	1.14	9.12	7.53	0.83
UD18	3.00	17.25	5.75	2.38	3.17	1.33	7.52	7.44	0.99
Min	2.85	10.46	3.50	2.29	2.54	1.08	3.47	3.42	0.17
Max	3.09	25.55	8.26	2.41	3.56	1.48	22.37	7.65	2.18
Average	2.99	17.10	5.71	2.36	3.10	1.32	12.52	5.58	0.57

The MDA changes with energy because energy changes the quantities it depends on. It separated all the variables in the MDA that depend solely on the detector itself. The γ-rays per decay, shield, and count time, for example, affect the MDA, but will do so for all detectors in the same way. From the previous equation, the followings are the description of different parameters used to describe the MDA:

R(E): the energy resolution of the detector which is a function of the photon energy;

N(E): the background counts per keV, in unit of energy, as a function of the photon energy; and

ε(E): the absolute efficiency of the detector. It depends on the γ (photon) energy.

Using γ-ray spectrometry, it is extremely strenuous task to select the correct detector for appropriate data assessment [173–175]. To reliably measure the γ-rays emitted from environmental samples (in this case water, air, rock, and soil), it is essential to attain as much far as possible, low uncertainties

by obtaining suitable photon counts with acceptable statistic. As the relative counting uncertainty is defined as reciprocal of the square root of the number of counts, it is important to have a large number of counted photon in the detector geometry to lower down the uncertainty related to.

$$\sigma = \sqrt{\frac{1}{n}} = 1/(n)^{1/2} \tag{4-2}$$

where n= number of counts

Despite the acceptable degree of relative uncertainty based on investigations, usually less than 3.2 percent of relative uncertainty is viewed as the minimum value to ensure the measurements ' un-wavering quality. The number of photon counts depends on measurement condition, sample quantity, sample geometry, and type of the detector. But as quality assurance of the laboratory is maintained, the measurement time has less influence on the result compared to other parameters [101, 173, 176].

As can be seen in Table 4-3, the relative uncertainty of specific activities is given for both types of detector used in the present project. For each detector, the ratio was computed for the two detectors to compared both for the perspective of detector selection based on energy range. The results from the table show a relatively larger error for the GC0818-7600SL for ²²⁶Ra and ²³²Th. The ratio values ranged from 3.50 to 8.26 with an average of 5.71 for ²²⁶Ra and from 1.08 to 1.48 with an average of 1.32 for ²³²Th, respectively. These observations demonstrate the interest in using the BEGe for these radioisotopes' activity concentration measurement. For potassium activity ratio calculation, this proportion is less than one for 17 samples (except for one sample, UD14), which shows that the use of GC0818-7600SL in high-energy measurement is more appropriate. As the γ-ray emission of the K-40 radioisotope is at an energy range larger than 1.4 MeV, this conclusion is worthy.

Figure 4-1 presents a comparison of uncertainties for the two detector type and distinct radioisotopes. The fluctuation with BEGe-6530 is almost imperceptible to the measurement of the ²²⁶Ra and ²³²Th activity concentration. But, because of the high γ-ray emitted at ~1461 Kev for potassium, stability for GC0818-7600SL is noticed for K-40 than for BEGe. This stability is reflected rather the extent GC0818-7600 detector regarding the values of ⁴⁰K or other artificial high energy γ-ray emitters. For the first two curves, a very stable uncertainty is noted for BEGe detector's result. The explanation emerges again from high and low γ-ray energies. This is expressed in Figure 4.2, in which both kinds of detectors compare the standard deviation of radium equal activity Ra_{eq}. It is evident that the BEGe is more appropriate for γ-ray spectrometry to measure natural low-background radioactivity [101]. For the blue curve representing the BEGe detector, the fluctuation is negligible for Ra-226 and for Th-232, compared to K-40 for the same detector. The fluctuation for K-40 is marked by many disturbances as it can be observed on the third part of the figure. Contrarily, the red curve shows irregular fluctuations for Ra-226 and Th-232, but for the K-40, the fluctuation is one order less than that of the blue curve. As the red curve characterizes the performances of the GC0818-7600SL detector, it is understandable that it is fit for high energy γ measurement as highlighted previously.

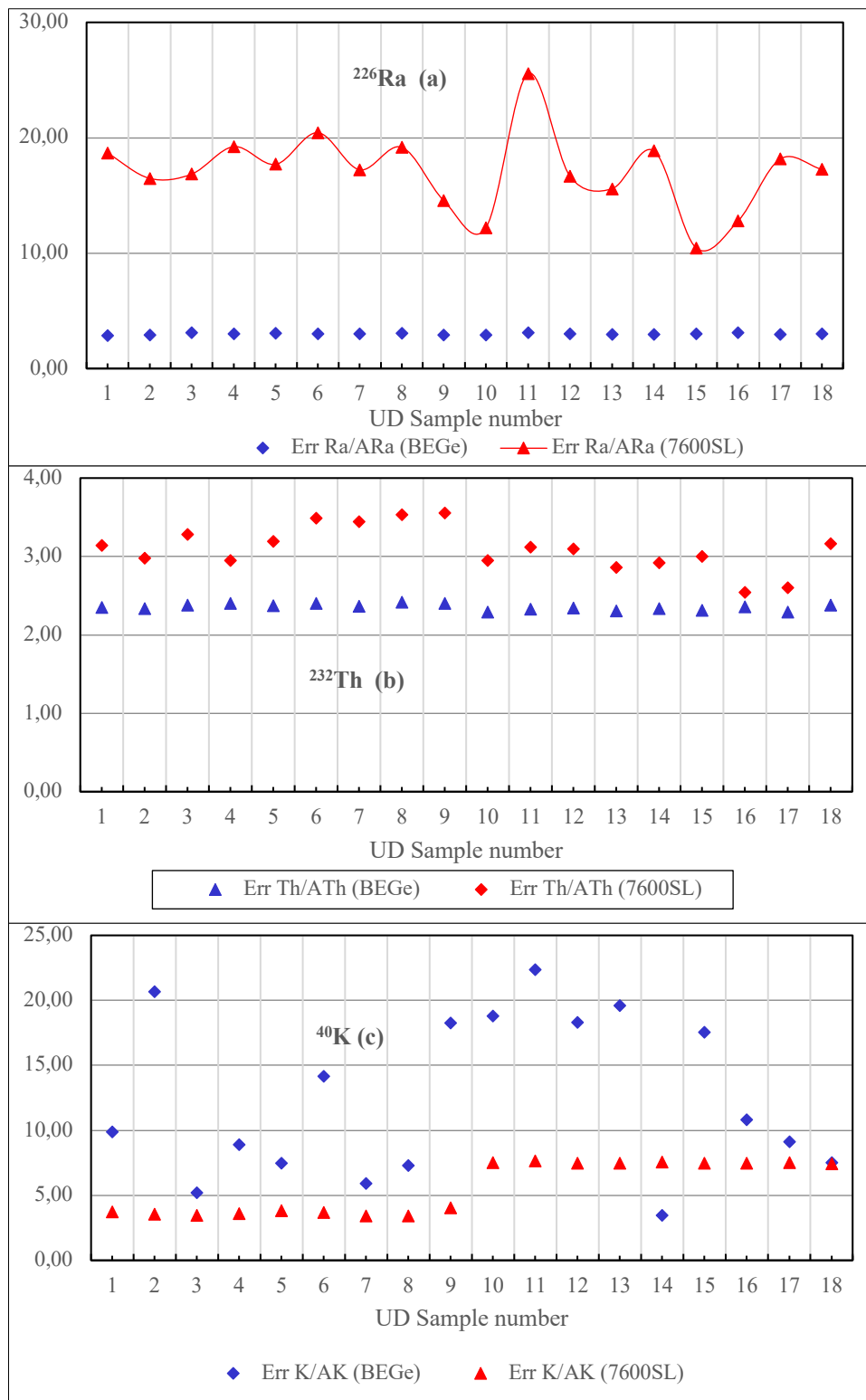


Figure 4-1: Standard deviation between the two measurements using BEGe-6530 and GC0818-7600SL HPGe detectors: (a) deviation for ^{226}Ra , (b) deviation for ^{232}Th , and (c) deviation for ^{40}K . The blue curve is the characteristic of the BEGe while the red one is for the GC0818-7600SL detector. Fluctuation represents the inability of a particular detector to perform accurate measurements at a given energy range.

The variation observed in both sites may result from the non-uniform distribution of the contents of radiation activity present under the crust of the Earth. As the studied sites show variable activity concentration for different radionuclides measured, it is important to recall that Igneous rocks are generally considered to have higher radioactivity levels than sedimentary rocks. The areas under study are part of the Littoral Region of Cameroon, observed to be the major sedimentary basin of Cameroon. The region falls into Douala Basin and well known as Rio Dell Rio basin that covers the region from the Gulf of Guinea to the coast of Brazil in South American continent. Because of the erosion and weathering process in the investigated area, the geological formation has variations in sediments, limestone, shale, and clay. From the recorded activities of ²²⁶Ra, ²³²Th, and ⁴⁰K in the present study, it can be noticed that the obtained average value of ²³²Th in both locations was observed to be comparably higher than the value usually measured and compared to both of ²²⁶Ra and ⁴⁰K in almost all the soil-sampling locations. This could be due to the high content of thorium present in sedimentary rocks as the area under investigation is part of the sedimentary basin of Douala [101, 177].

4.2.2. Radium equivalent calculation Validation

Table 4-4 shows the radium equivalent activity values and uncertainty on different values. The relative uncertainty ratio for both facilities calculated by the following equation can be seen in the last column:

$$T_{\frac{7600SL}{BEGe}} = \frac{(Err/R_{eq})_{7600SL}}{(Err/R_{eq})_{BEGe}} \tag{4-3}$$

The previous relation is simply an explanation of the comparison between both BEGe (6530 model) and GC0818-7600SL detector’s types. The average ratio, as expressed in the Table 4-4, ranged from 2.49 to 4.54 with an average value of 3.36; which means that the measurements made with the BEGe are generally more relevant and accurate. This variation is also seen in Figure 4-2: for 18 samples, uncertainties are higher for GC0818-7600SL, compare to BEGe 6530 model HPGe detector [101]. Consequently, the comparison shows clearly that the BEGe detector should be used for low background measurements.

In this case, the right detector is the detector that provides the most assessed information for the best statistical measurement in the shortest possible measurement time. With simple detectors (as NaI – Sodium Iodine detector), most spectrometry problems can be addressed, but for more precise and accurate measurements, improvements are needed. Exotic, intriguing, or excessively complicated detector designs are not needed for simple γ-ray spectrometry [103, 131, 132, 148, 178]. Most sophisticated detector are usually needed in applications as safeguards verification by IAEA, and there is a constant need to improve the quality of the detection.

Table 4-4: Errors related to radium equivalent activity computed based on activity concentrations of ²²⁶Ra, ²³²Th, and ⁴⁰K and standard deviation in soil samples from Campuses 1 and 2 using both detectors. The last column shows the ratio between both detectors in the case of detector selection for measurements based on γ energy range. The uncertainty was given at the 95 % confidence level

Sample Id	R _{eq} (Bq/kg)		Err R _{eq}		err/R _{eq}		T _{7600SL/BEGE}
	BEGe-6530	7600SL	BEGe-6530	7600SL	BEGe-6530	7600SL	
UD-1	145.98	41.02	3.22	2.88	0.02	0.07	3.18
UD-2	154.12	49.31	3.74	3.31	0.02	0.07	2.77
UD-3	161.15	43.40	2.98	3.20	0.02	0.07	3.98
UD-4	145.18	42.00	3.20	3.37	0.02	0.08	3.63
UD-5	142.66	42.61	2.99	3.32	0.02	0.08	3.71
UD-6	147.59	44.49	3.55	3.50	0.02	0.08	3.27
UD-7	152.95	46.41	3.05	3.64	0.02	0.08	3.93
UD-8	131.91	41.87	2.75	3.10	0.02	0.07	3.56
UD-9	130.37	43.95	3.19	3.24	0.02	0.07	3.01
UD-10	139.92	66.99	3.32	4.73	0.02	0.07	2.98
UD-11	122.57	51.01	3.02	4.21	0.02	0.08	3.36
UD-12	127.25	59.12	3.07	4.59	0.02	0.08	3.21
UD-13	143.49	67.10	3.43	4.94	0.02	0.07	3.08
UD-14	176.50	58.69	3.04	4.59	0.02	0.08	4.54
UD-15	153.78	57.47	3.66	3.41	0.02	0.06	2.49
UD-16	150.17	62.07	3.43	4.02	0.02	0.06	2.84
UD-17	143.77	54.37	3.25	3.75	0.02	0.07	3.04
UD-18	138.01	55.96	2.90	4.55	0.02	0.08	3.87
Min	122.57	41.02	2.75	2.88	0.02	0.06	2.49
Max	176.50	67.10	3.74	4.94	0.02	0.08	4.54
Average	144.85	51.55	3.21	3.80	0.02	0.07	3.36

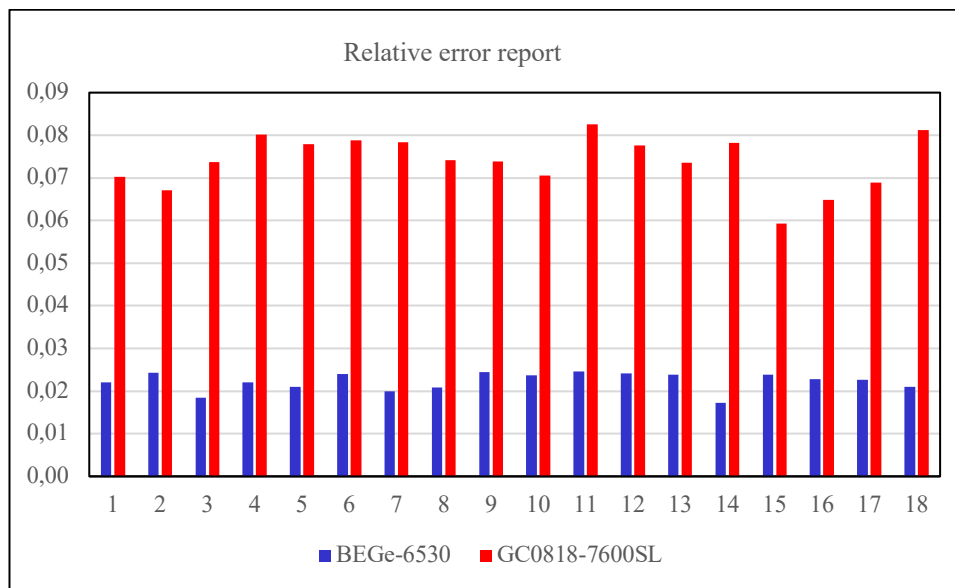


Figure 4-2: Relative error related to the radium equivalent activity for measurements from both detectors. As displayed, the BEGe detector result in blue chart, is three times smaller than that of the GC0818-7600SL in red chart.

B. Quarries in Douala and Surroundings

4.3. Activity concentration in the Extending Area

The investigated area was extended to the sand from different big quarries in the economic capital of Cameroon and its surroundings. Measurements of the sand samples from the quarries were done after the validation of the appropriate detector for measurement. All measurements were based on HPGe detector specified previously (only GC0818-7600SL model). The assessment method was the same as previously described in the chapter 3 of the present report. This section focuses on the presentation and discussion of the obtained results only. The methodology, assumed to be presented already, will not be discussed again. The specific activities of natural radionuclides in sand samples and the calculated Radium equivalent activity (R_{aeq}) are presented in Table 4-5. The Outdoor absorbed γ dose rate (D_{out}), the Annual Effective Dose rate (AED), both internal (H_{in}) and external (H_{ex}) hazard indices together with α and γ indexes are presented in Table 4-5. The results presented in this section were published by Guembou et al. (2017) [2].

Table 4-5 lists the mean values of the activity concentrations of ^{226}Ra , ^{232}Th , and ^{40}K for different types of sand building materials collected in Douala Littoral region of Cameroon. As seen in Table 4-5, the highest mean values of each investigated radionuclide, ^{226}Ra , ^{232}Th , and ^{40}K were 146.68, 102.93, and 927.82 Bq kg^{-1} in sand of Youpoue-Bamenda (YB_2), Village (VI_1), and Northern Akwa (AN_6), respectively. All these values are at least two times higher than the UNSCEAR reported values. As seen in Table 4-5, the lowest mean values of ^{40}K , ^{232}Th , and ^{226}Ra were 54.01, 7.96 and 11.79 Bq kg^{-1} for Youpoue (YO_2), Bonaberi-Bonamikano (BB_4), and Northern Akwa (AN_6) sands, respectively. The mean values are lower than the corresponding worldwide average value of 400 Bq kg^{-1} for ^{40}K but higher than worldwide average values, which are 35.00 and 30.00 for ^{226}Ra and ^{232}Th , respectively [1, 153]. The variation of the activity concentration in the investigated sand sample is quite large. This could be explained by the irregular repartition of radioisotopes in the Earth crust and non-uniform distribution of their concentration depending on soils type, human activity, manmade and natural processes as erosion and weathering.

By comparing the current study's particular radionuclide activity with worldwide average values (reported by UNSCEAR), ^{226}Ra concentration was greater by a factor of 1.14 whereas ^{232}Th activity was discovered to be greater by a factor of 1.43, and ^{40}K activity concentration was smaller by a factor of 0.85. As the investigated sand samples are formed after weathering processes and erosion, it was likely expected to found potassium concentration in higher proportion as it is easily transported by water erosion. In addition, the precipitation in the investigated zone is very high annually. So, the transportation of potassium used as fertilizer in cultivated soil in the region was expected, even though the radioisotope K-40 is in small proportion in the potassium used in fertilizer.

As shown in Figure 4-3, Activity concentration levels are relatively consistent for *northern Akwa*, *Bois de Singe*, *Youpoue* and *Dibamba* sand's quarries. This uniformity is seen by a slight difference in potassium activity between 698 and 938 Bq kg^{-1} for *Northern Akwa*, 70 and 100 Bq kg^{-1} for "*Bois de Singe*," 54 and 93 Bq kg^{-1} for "*Youpoue*", and 153 and 180 for *Dibamba*. The top level of specific activities of ^{40}K is observed in sand sample of Northern Akwa while the specific activities of ^{232}Th are the lowest. The high-level activities concentration of ^{226}Ra and ^{232}Th are observed in the sand from "*Bois de Singe*". As shown on the map, the variation of the activity concentration follows the closest trend: For example, the sand samples from *Youpoue* and *Youpoue Bamenda* quarries were sampled from the closest sampling sites. Their values are closely related in term of mean values and range of fluctuation.

Figure 4-4 shows the frequency distribution of ^{40}K , ^{226}Ra , and ^{232}Th activity concentrations in the sand samples. These frequency distributions are closely related to how the radionuclides in the investigated samples are distributed. Large number of samples in a range show approximation on how the fluctuation of radionuclides investigated are undergone. In addition, small trended value can show up the alert on a site that needs additional detailed investigations. The range of 11-38 Bq kg^{-1} and 54-228 Bq kg^{-1} measured for ^{226}Ra and ^{40}K , cover a percentage of 67 % for ^{226}Ra and 54 % for ^{40}K , respectively. This explained how radium activity measured in the samples is packed and the investigated area has similar geological characteristic. The activity concentrations of ^{232}Th measured in 38 % of the total soil samples are between 27 and 45 Bq kg^{-1} . These frequencies indicate relatively periodic and uniform radioactivity distribution for each sandpit of the quarry and mostly small range value (for the fluctuation relevant to the activity deviation) [2].

Table 4-5: Specific activities of ²²⁶Ra, ²³²Th, and ⁴⁰K and the Radium equivalent activity (Ra_{eq}) of sand samples from different quarries (Douala Littoral region of Cameroon and surroundings). Data of sand samples from the seven big quarries studied.

Quarry's name	Sample Id	Specific Activities (Bq.kg ⁻¹)			Ra _{eq} (Bq.kg ⁻¹)
		Ra-226	Th-232	K-40	
Northern Akwa	AN_1	37.70±1.28	40.58±2.57	726.23±32.36	151,64
	AN_2	31.31±1.11	45.19±1.84	698.06±35.19	149,69
	AN_3	36.29±0.66	52.05±2.15	702.54±39.80	164,82
	AN_4	38.37±2.55	41.89±0.15	706.43±30.82	152,66
	AN_5	54.06±2.86	22.54±1.23	782.18±35.79	146,52
	AN_6	11.79±1.00	69.11±2.46	927.82±46.70	182,05
Dibamba	DI_1	27.06±1.10	52.71±1.67	180.27±14.71	116,32
	DI_2	20.74±0.32	10.25±0.20	153.50±13.79	47,21
Village	VI_1	33.51±1.20	102.93±2.39	168.73±15.12	193,69
	VI_2	29.73±1.28	32.34±0.61	94.44±1.22	83,25
Bonaberi-Bonamikano	BB_1	57.77±1.72	95.20±2.33	285.84±22.48	215,92
	BB_2	31.26±1.18	10.87±0.05	617.38±34.37	94,35
	BB_3	17.64±1.06	30.49±1.13	523.30±17.93	101,53
	BB_4	36.17±1.31	7.96±0.10	439.35±6.87	81,38
Bois-De-Singe	BS_1	47.50±1.45	51.96±1.52	79.26±0.49	127,91
	BS_2	80.20±1.83	75.45±1.55	70.60±1.15	193,53
	BS_3	47.23±1.49	58.82±1.44	100.62±1.54	139,09
	BS_4	28.12±0.82	34.55±1.12	97.33±1.24	85,03
Youpoue	YO_1	24.43±0.89	43.68±1.35	91.24±0.92	93,91
	YO_2	49.43±1.03	39.84±1.51	54.01±0.16	110,56
	YO_3	20.31±0.49	34.12±1.19	93.09±0.05	76,27
Youpoue-Bamenda	YB_1	35.69±1.58	39.29±0.95	81.33±0.85	98,13
	YB_2	146.68±4.46	24.68±1.59	450.78±7.56	216,69
	YB_3	19.24±1.11	21.22±1.52	78.58±0.46	55,63
Min		11.79±1.00	7.96±0.10	54.01±0.16	47,21
Max		146.68±4.46	102.93±2.39	927.82±46.70	216,69
Average		40.09	43.24	341.79	128,24
Worldwide (UNSCEAR 2000)					
Range		17.00-60.00	11.00-68.00	140.00-850.00	-
Average		35.00	30.00	400.00	370.0

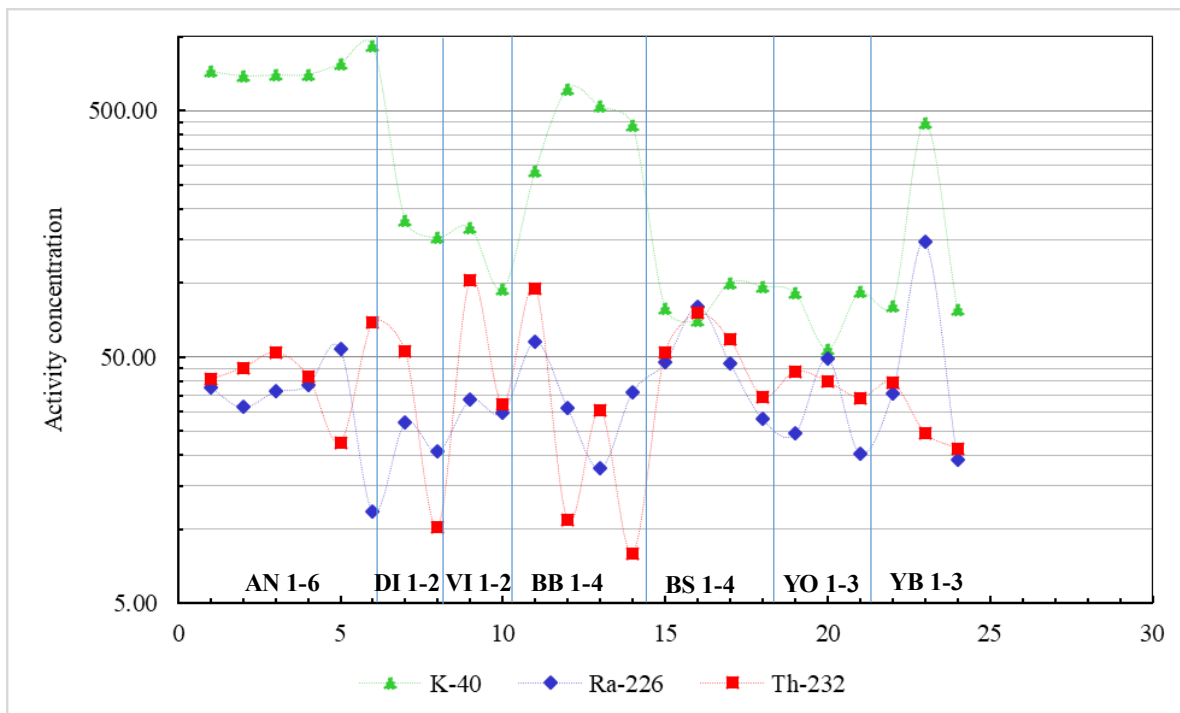


Figure 4-3: Mean values of specific activities of sand samples from seven big quarries investigated in Douala Littoral Region as additional studied site. This site was added along the project and the obtained data show non-uniform distribution of radionuclides in Earth crust.

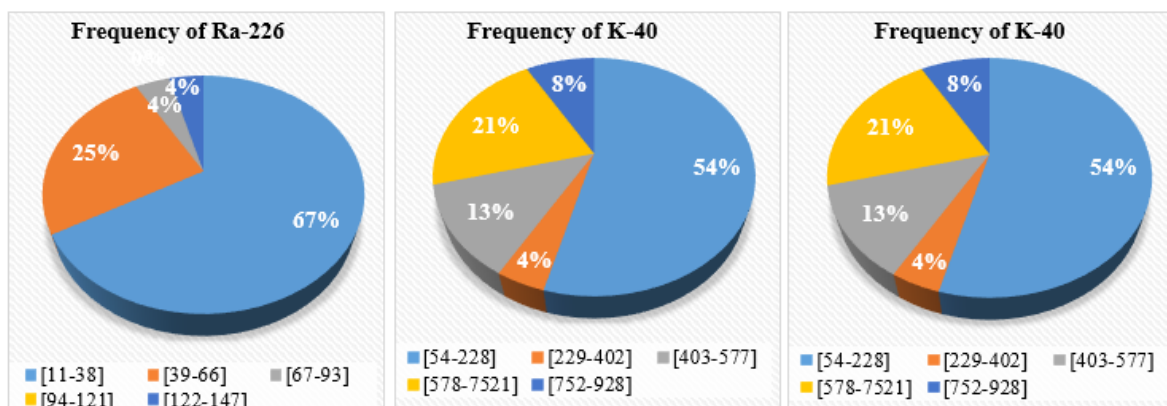


Figure 4-4: Frequency distribution of the specific activities of ²²⁶Ra (a), ²³²Th (b), and ⁴⁰K (c) in the sand samples investigated in different quarries in Douala and surroundings.

4.4. Radium equivalent activity (Ra_{eq})

The calculated mean values of the Radium equivalent activities of all sand samples of building materials are presented in the last column of Table 4-5. These calculated Ra_{eq} values range from 47.21 (*Dibamba 2*) to 216.69 (*Youpoue-Bamenda 2*) with an average of 128.24, in the unit of Bq kg⁻¹. The highest mean value of Ra_{eq} found in sand samples was 216.69 Bq kg⁻¹, which is significantly lower than the widely accepted upper limit of 370 Bq kg⁻¹ reported by UNSCEAR [48, 153, 179–181]. At these levels no radiological hazards are recorded when using the material from investigated area as building material. Also, no alarm should be addressed here as the level is insignificant to be the origin of overexposure of the inhabitants of the buildings built using sand from the quarries. Figure 4-5 shows the mean values of the Radium equivalent activity in different sand samples.

A comparison between the mean values of activities concentrations of ^{226}Ra , ^{232}Th , and ^{40}K and radium equivalent activity (Ra_{eq}) for sand from Douala Littoral Region and from other countries are given in Table 4-6. The mean values of the natural radionuclide concentration in building materials strongly differ from one country to another, depending on the sand and raw materials used for their formation while Ra_{eq} values are higher than the value of the corresponding material in different countries except the case of China, India, and Yemen. This table shows the result only for sand samples investigation while Table 4-2 shows the same (comparison) data for soil samples investigated in different countries and the present project.

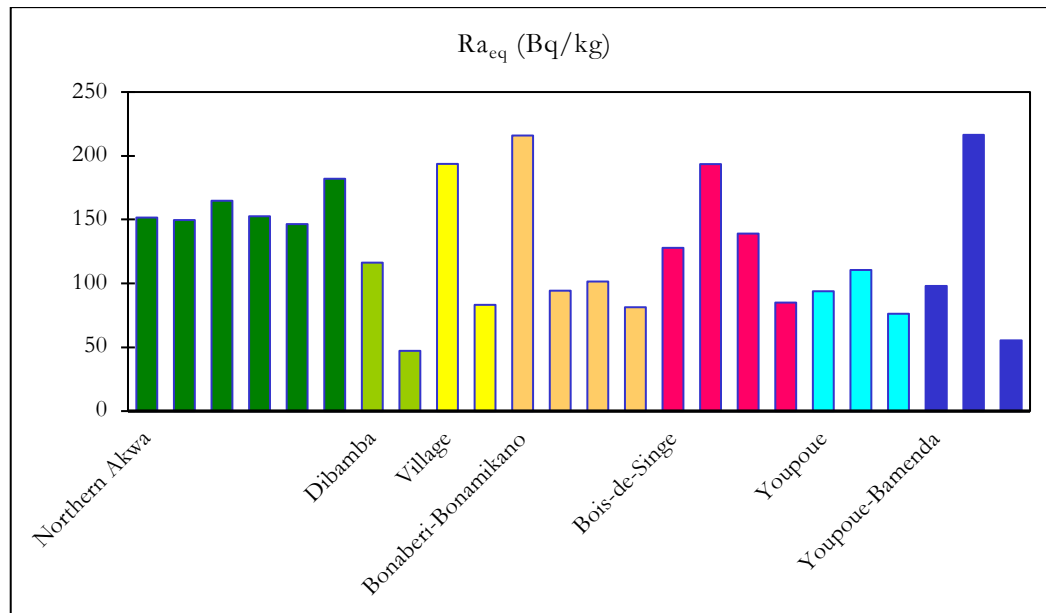


Figure 4-5: Calculated mean values of Radium equivalent activity (Ra_{eq}) of sand from Douala Littoral Region. The results are from the seven quarries investigated.

4.5. Radiological parameters and radiation hazard

4.5.1. Absorbed γ dose rate (D_{out}) and annual effective dose rate (AED).

In the third column of Table 4-7, the mean value of the γ dose rate in air for various samples of sand building material is provided. The maximum γ dose value from Table 4-7 was found to be $101.47 \text{ nGy h}^{-1}$ in *Youpoue-Bamenda* sand specimens (YB_2), whereas the minimum sand concentration value from *Dibamba River* (DI_2) was about 22.17 nGy h^{-1} . D_{out} 's estimated mean value based on equation shown in the previous chapter was 58.89 nGy h^{-1} in the studied samples, which is lower than the worldwide average value of 60 nGy h^{-1} reported by UNSCEAR and ICRP [1, 193, 194].

The mean value of the Annual Outdoor Effective Dose rate found in different sand samples is also given in fourth column of Table 4-7. These values ranged from 27.19 for DI_2 to 124.45 for YB_2 expressed in $\mu\text{Sv y}^{-1}$. As it is expressed in microSv per year, it is easy to draw the conclusion of non-high radioactive area. The estimated mean value of the annual effective dose rate of $72.22 \mu\text{Sv y}^{-1}$ is lower than the allowance limit of 1.00 mSv/year . The mean value of AED estimated for all sand samples are below the external worldwide mean annual effective dose of 1 mSv y^{-1} published by UNSCEAR, 2000 [98, 153]. This value cannot be discussed in a strict way, but the fact is that no alarm

can be reported as the average value is lower than the minimum reported value of concern and each sampling site's value is also as low as the average worldwide value. The deviation is not as expanded as in other studies.

Table 4-6: Inter-comparison of specific activities and Ra_{eq} from Douala Littoral Region sand samples with other areas of the world. The comparison is defined for primordial radionuclides activity concentration and the radium equivalent activity.

Country sample	Activity concentration (Bq/k g)			Ra_{eq} (Bq/kg)	References
	Ra-226	Th-232	K-40		
	Algeria	12	07		
Australia	3.7	40	44.4	64.32	[129]
China	39.4	47.2	573	151.017	[2, 182]
Cuba	17	16	208	55.90	[2]
Egypt	9.2	3.3	47.3	17.5611	[2, 183]
Greece	18	17	367	70.6	[156]
Hong Kong	24.3	27.1	841	128	[2]
India	40	55	590	164.1	[184]
India	43.7	64.4	455.8	170.8	[158]
India, Namakkal	2.27	21.72	352.8	59.68	[185]
Malaysia	60	13	750	136	[186]
Netherland	8.1	10.6	200	38.6	[2]
Pakistan	20	29	383	91	[187, 188]
Palestine	20.6	18.8	26.3	-	[189]
USA	37	33.3	18.5	86	[2]
Xianyang, China	25.8	26.8	553.6	106.7	[190]
Yemen	20.78	27.68	1118.36	164.5	[191, 192]
Douala-Cameroon	40.09	43.24	341.79	128.24	This work

Hazard indices

The Internal and External hazards indexes parameters were calculated to assess the level of risk to which residents may be exposed and are detailed in Table 4-7. The recorded values of external and internal indexes range from 0.13 to 0.59 with a mean value of 0.35 and from 0.18 to 0.98 with a mean value of 0.045, respectively. In both cases, there is not value higher than the unity in individual site sample value. The mean values of H_{ex} and H_{in} are both below the recommended level of 1[1]. As a result, the samples investigated in the present research project are not subject of specific radiological concern in view of radiation protection based on the assessed data. Therefore, materials considered in this study can be safely used in the construction of buildings. The radiological concern of residents of

the building should not be directly related to the sand from the quarries investigated, but as there are different building materials involved in the construction, the conclusions drawn from this study do not imply other material. Only sand has been subjected to investigation as the conclusions are drawn only on sand that contribute to 40 to 85 % volume concentration (71.3% on average) of the material involved in the construction [2].

α and γ index

The computed values of the α and γ indices (I_α and I_γ) are also given in Table 4-7. It can be observed in Table 4-5 and Table 4-7 that the activity concentration values of ^{226}Ra in all sand samples are less than the recommended exemption level of 100 Bq kg^{-1} and $I_\alpha < 1$. As the α and γ indexes are related to radon exposure (internal exposure), important conclusions must be drawn from their assessment. The recommendation that the value of α index should be less than unity is based on assumption related to the fraction of time spent indoor. This fraction varies from one country to another and from culture to culture, depending on the resident's habits. As some inhabitants are forced to stay indoor because of the winter climate, there are some other countries without such climate restriction. Therefore, radon gas inhalation from the sand samples under investigation is not so large as to restrict the use of these samples in construction activities [2]. Similar conclusions have been suggested by different authors about building material in other countries [7, 195–197].

γ index I_γ was estimated using *equation shown in previous chapter*. The I_γ in building materials varied between 0.17 and 0.76 with an average of 0.46. All the values of I_γ are lower than the unity. Therefore, radon inhalation under investigation is not so large as to restrict the use of these sand in construction. The annual effective dose delivered by the investigated samples is smaller than the annual effective dose constraint of 1 mSv y^{-1} . The highest values of I_α and I_γ are 0.76 and 0.73, respectively. The obtained mean values of I_γ and I_α in the present study are lower than the recommended values of 1 and 0.5, respectively (European Commission, 1999) excepted the mean value of I_α in sand sample from Youpoue-Bamenda (YB_2). Hence these building materials can be exempted from all the radiological restriction and no concern was reported for detailed investigation [2].

The plotted diagram of investigated radionuclide is given in **Erreur ! Source du renvoi introuvable.** and Figure 4-6. The scale on different axis shows the weighed importance of different radionuclides (0 to 25 for Th-232, 0 to 40 for Ra-226, and 0 to 250 for K-40). The statistical representation of activity concentrations and their frequency distributions are described in Figure 4-6, the radiation dose and effective annual dose rate show useful distribution for data analysis. Although all the obtained curves are non-totally symmetric, there are some Gaussian and Poisson corrected distribution. For example, the potassium data shows a flat well-formed distribution close to Poisson distribution than to the Gaussian distribution. As radionuclides are not uniformly distributed in the Earth crust, these results could be expected and show advanced understanding of the variability of radioisotope's distribution in soils and sand samples under investigation.

Table 4-7: Mean values of γ Dose rate, Annual Effective Dose rate, and Hazard indexes for sand samples. External and internal indices, and α and γ indexes calculated are reported in the last columns of the table. All the equations used for computation are presented in the previous chapter.

Quarry	Sample Id	D _{out} (nGy/h)	ADE (μSv/y)	H _{ex}	H _{in}	I _γ	I _α
Northern Akwa	AN_1	72.21	88.56	0.41	0.51	0.57	0.19
	AN_2	70.87	86.92	0.40	0.49	0.56	0.16
	AN_3	77.50	95.05	0.45	0.54	0.62	0.18
	AN_4	72.48	88.89	0.41	0.52	0.57	0.19
	AN_5	71.21	87.33	0.40	0.54	0.55	0.27
	AN_6	85.88	105.32	0.49	0.52	0.69	0.06
Dibamba	DI_1	51.86	63.60	0.31	0.39	0.41	0.14
	DI_2	22.17	27.19	0.13	0.18	0.17	0.10
Village	VI_1	84.69	103.86	0.52	0.61	0.68	0.17
	VI_2	37.21	45.63	0.22	0.31	0.29	0.15
Bonaberi-Bonamikano	BB_1	96.11	117.87	0.58	0.74	0.76	0.29
	BB_2	46.76	57.34	0.25	0.34	0.36	0.16
	BB_3	48.39	59.34	0.27	0.32	0.39	0.09
	BB_4	39.84	48.86	0.22	0.32	0.31	0.18
Bois-De-Singe	BS_1	56.63	69.46	0.35	0.47	0.44	0.24
	BS_2	85.57	104.94	0.52	0.74	0.67	0.40
	BS_3	61.54	75.48	0.38	0.50	0.49	0.24
	BS_4	37.92	46.51	0.23	0.31	0.30	0.14
Youpoue	YO_1	41.47	50.86	0.25	0.32	0.33	0.12
	YO_2	49.15	60.28	0.30	0.43	0.38	0.25
	YO_3	33.88	41.55	0.21	0.26	0.27	0.10
Youpoue-Bamenda	YB_1	43.61	53.48	0.27	0.36	0.34	0.18
	YB_2	101.47	124.45	0.59	0.98	0.76	0.73
	YB_3	24.98	30.64	0.15	0.20	0.20	0.10
Min		22.17	27.19	0.13	0.18	0.17	0.06
Max		101.47	124.45	0.59	0.98	0.76	0.73
Average		58.89	72.22	0.35	0.45	0.46	0.20
Worldwide	Range	18-93	-	-	-	-	-
[1, 153]	Average	60.00	1 mSv.y ⁻¹	<1.00	<1.00	<1.00	<0.50

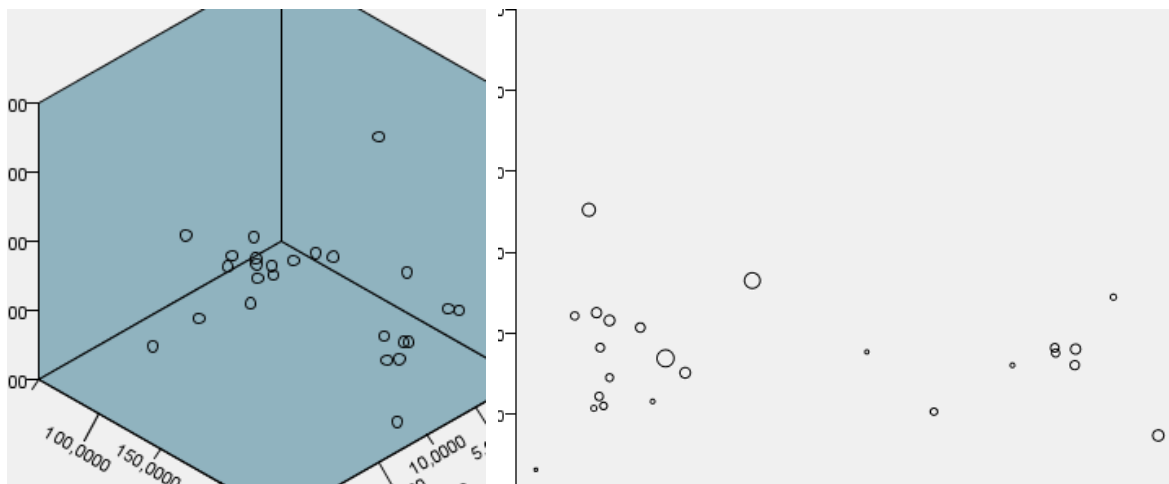


Figure 4-6. Triple representative diagrams of radionuclides investigated in the samples from Douala. The diagram correlates the activity concentrations of ^{226}Ra , ^{232}Th , and ^{40}K . The left diagram shows three axis representation while the right one is a 2D with point surface for Th-232 (presented as Ac-228 in the figure).

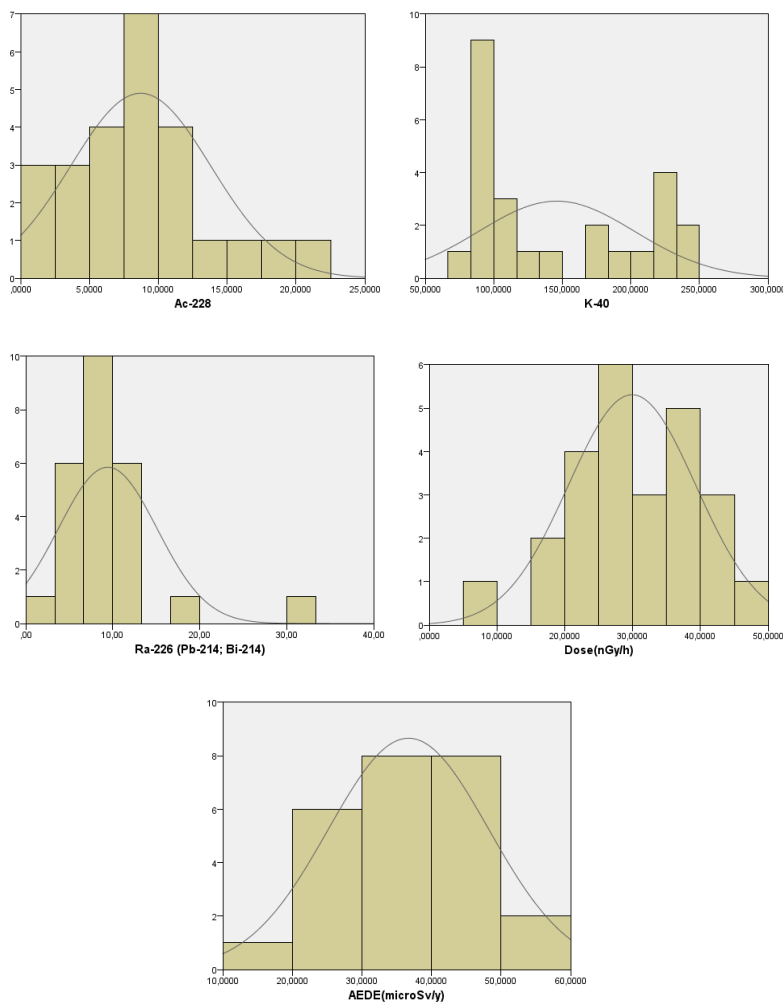


Figure 4-6: Activity concentrations of measured radionuclides and radiological parameters as presented in previous paragraphs. Statistical representation of obtained data after investigation, the x-axis is in %.

4.6. Conclusion

In this chapter, γ -ray spectrometry was used to evaluate ^{226}Ra , ^{232}Th , and ^{40}K levels of activity concentrations in soil samples from the University of Douala's two campuses and sand samples used as building materials in Cameroon's (Douala) Littoral Region. The investigated sand samples were originated from seven big sand quarries in the economic capital of Cameroon, Douala, and its surroundings. Radiological parameters and radiation hazards as radium equivalent activity, absorbed γ dose rate in indoor air, and corresponding annual effective dose, external and internal hazard indices were calculated to quantify the radiological hazard risk associated to the studied samples. It is important to highlight that the internal and external indices, as well as the α and γ indexes were evaluated for sand only. This is because the investigated sand is used as building material and the residents of the building constructed are likely to be exposed to radon and its daughter products by inhalation.

For samples from the University of Douala, the level of concentration activity was very low as well as that of the radium equivalent activity. In addition, this part of the study was completed by comparing results from two different detectors in view to point-out recommendations on the use of germanium detector for environmental monitoring. The broad energy germanium detector showed the best stability and accuracy for assessing samples in view of measuring low energy γ -rayray (^{226}Ra and ^{232}Th). The BEGe detector was found appropriate for low background activity measurement and for low energy γ emitters while the detector GC0818-7600SL show stability in measuring high γ -ray emitter as ^{40}K . Comparison with values measured in different countries for the same type of sample showed comparable results in the interval recommended by UNSCEAR [1, 13, 153].

In the present chapter, the measured activity concentrations of ^{226}Ra , ^{232}Th , and ^{40}K were smaller than the prevalent worldwide values associated with them, reported by international organization as UNSCEAR, or ICRP. It is therefore found that the acquired radiological parameters are normal and within the suggested boundaries. Consequently, in the construction of dwellings, the use of these sands as building material is believed to be acceptable for tenants, in view of natural radiation exposure. In addition, thousands of workers in various quarries of sand in the investigated area of Cameroon's Littoral are under global exposure limits. As they may spend their working time with the investigated sand and may dwell in buildings constructed using the same material. Even in that case, the exposure level was found to be acceptable, within the UNSCEAR limits. The values of terrestrial radionuclides assessed can be used as a helpful database to create a radiation map of the region under investigation and to monitor and quantify possible changes in ecological radioactivity owing to radiation, contemporary, and other human behavior. Results achieved indicate that the annual dose in Douala received by the residents is below the acceptable limit of 1.0 mSv year^{-1} . Therefore, as building material, most of the sand's types studied and integrated in buildings appear secure and safe for building construction or to be on the beaches for those who are likely to spent time on it. The results of this study will be helpful in assessing the radiation risks for human related to sand building material used and in initiating a sand database along with a radiological map of the concerned region. The result obtained did not show questionable sampling point that necessitates additional detailed investigations.

CHAPTER 5. X-RAY FLUORESCENCE ANALYSIS

This chapter presents X-ray fluorescence methodology and result of analysis of the samples from the campuses (campus 1 and 2) of the University of Douala as well as those from the extending area of study in this thesis (seven biggest sand quarries of the Douala city and its surroundings). The interest is shown on the presentation of the method based on both Energy and Wavelength Dispersive X-Ray Fluorescence methods (EDXRF and WDXRF). The sample preparation is described and finally, the obtained results and discussion follows. Samples used for X-ray characterization were the same as for γ -ray spectrometry.

5.1. Interest of XRF Analysis

X-Ray Fluorescence (XRF) Spectrometry, a technique used in several research areas (Physics, Chemistry, Geology, Archeometry, Astrophysics, ...) nowadays, is a broadly used method for the environmental monitoring of land (geological) material, especially the presence of heavy metal and the elemental characterization of samples [198–202]. It consisted of a differentiation of major elements (element with concentration expressed in percentage) from the minor elements (with concentration expressed in ppm) and to the trace elements (elements present in a sample in very small fraction compared to major and minor elements). The analysis can be very simple, but due to the complexity and large variety of minerals contained in a geological sample, different steps have to be handled delicately. Major elements for example in silicate rocks and sedimentary soils are usually determined by analysis on pellet and glass discs [199, 203].

Typical use of X-Ray Fluorescence spectrometry includes the analysis of petroleum oils and fuel, plastic, rubber and textiles, pharmaceutical products, foodstuffs, cosmetics and body care products, fertilizers, geological materials, mining feeds, slags and tails, cement, heat-resistant materials, glass, ceramics, catalysts, wafers; the determination of coatings on paper, film, polyester; metals and alloys, glass and plastic; forensics; multi-layer thin films on silicon wafers, photovoltaics and rotating storage media as well as pollution monitoring of solid waste, effluent, cleaning fluids, pools and filters. In addition, X-ray Transmission (XRT) gauges are employed to measure sulfur (S) in crude oil and marine bunker fuel. So, the fields of application of XRF analytical method are widely expended and all related nuclear physics applications can employ XRF technique. WDXRF and EDXRF [218, 220, 221] spectrometers are the elemental analysis tool of choice, for many applications, in that they are smaller, simple in design, and cost effective to operate than other technologies like induced coupled plasma optical emission spectroscopy (ICP-OES) and atomic absorption (AA) or atomic fluorescence (AF) spectroscopy. In addition, XRF method is not time consuming as γ -ray spectrometry [217, 222]. The method has been used for decades and was proven to be useful for related applications and those cited above.

Since the elemental composition and the natural radioisotope activity concentration in soil vary from place to place and sometime in the same geological formation with the geomorphological and the topographic components of the investigated site, sampling method for such analysis must be representative. The representativeness of a sampling method usually allows the well assessment of an area without necessary taking an infinite number of samples, difficult to assess, and without missing important information from the investigated zone [213, 214]. It is then important for different research brands to assess and create a radiological map as well as know the elemental composition of their environment in view of protection and prediction of the future. Specifically, sand stores are the afteref-

fect of disintegration and weathering processes that have been involved in Littoral and coastal areas for a while, of rocks from metamorphic and igneous type. The levels of natural radionuclides in an area could be a subject of concern of international community due to harmful effects of the radiations. The investigation of the radioactivity level in the area of investigation by analyzing sand samples allowed the assessment of the radiological risk parameters due to the natural external γ radiation exposure for the sandblaster, masons, and residents of building and individuals who spend their holidays on the beaches as well as workers of these quarries. In another hand, elemental characterization [215–219] of an area can allow decision making process depending on the level of heavy elements concentration found and would probably contribute to the understanding of the origin of geology and the impact of weathering phenomenon in that studied area.

The principle of X-Ray Fluorescence spectrometry is described in the following figure (Figure 5-1) The emission of characteristic "secondary" (or fluorescent) X-rays from a material that has been excited by being bombarded with high-energy X-rays is used to characterize the material under investigation. The interaction of the incident X-ray with the shell electron is the origin of the method as the excited atom will undergo fluorescence to be stabilized in the fundamental state. This emission is characteristic of the atoms present in the sample under investigation. From the energy spectra, it becomes easy to determine the elemental composition of the sample.

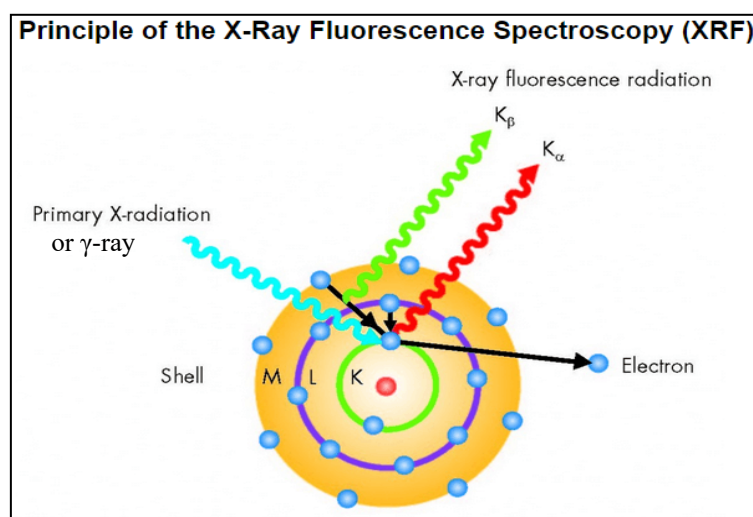


Figure 5-1: Descriptive principle of X-ray Fluorescence spectrometry. The incident photon is either γ - or X (in most cases)-ray in this case, even though it is not the only representative case found in Physics.

5.2. XRF Protocol and Experiment

In this regard, the calibration process is very important, but required and overview of a guessed of the content of a sample subjected to investigation. The preparation of these disks and pellets challenged the particle size, mineralogical effects as well as matrix correction due to inter-element absorption and enhancement. Trace elements for heavy metal with an atomic number $Z > 26$ are preferably analyzed on pressed pellets made from dry powder [204, 205]. As regard to the weakening of the sample in the glass, glass discs are less sensitive for trace elements analysis [206–209] and researchers usually preferred one method to another depending on the purpose of the assessment. The substantial number of reference tests now accessible [210–212] permits to investigate samples that are particularly well-suited and contain elements that are excited by X-ray and can emit lower energy radiation to recover their stability. Some of these elements are well-suited for assessments that involved

bulk chemical measurements of major elements and others for minor elements.

Major elemental characterization took place at the laboratory of Geology with WDXRF and minor elements at the laboratory of Physics (Nuclear Physics) and the method was based on EDXRF technic. The same sample used for γ spectrometry were used for X-Ray Fluorescence analysis base on the same sampling method. So the description of sampling method and sample preparation is restricted here to the differences between γ -and X-ray spectrometry. Only the sample preparation method differs from γ spectrometry to Energy Dispersive X-Ray Spectrometry (EDXRF) and Wavelength Dispersive X-Ray Spectrometry (WDXRF) [209, 218, 220].

5.2.1. Sample preparation

The analysis conditions were described in research done by Duchene and Bologne [209]. Overlap corrections were implemented to account for the overlap of TiK_{β} on VK_{α} , Vk_{β} on CrK_{α} , and SrK_{β} on ZrK_{α} , either by evaluating the contribution of the interfering component (Sr, Cr) or by selecting a suitable background (V), assuming the TiK_{β} symmetric profile curve. On glass disks and pellets, both Ti and Mn were evaluated to assess the calibration process. This allows, if needed, to operate the two techniques separately. The content of magnetite pellets was used to correct matrix effects on V and Cr without the need of measuring significant components on glass disks [223–225].

Major and minor analysis were performed on an ARL 9400XP equipped with an Rh anode, end window X-ray tube. The ARL PERFORM'X spectrometer used for these tests was a 4200 W system. This part of the project experiment was achieved using glass disc made in the laboratory of Geology. For traces elements, the experimental setup used to perform measurement was a MOXTEK source (MAGNOM model with Ag target, 50 kV and 5 W). The detector used was an AMPTEK SDD123 model. This part of study was performed directly on the surface of different pellets realized in our laboratory (the laboratory of Nuclear Physics).

i) Glass Discs' preparation

Different samples in powder form were melt at high temperature (1000°C) during two hours in a porcelain crucible (in a muffle furnace). The cooling down process in this step took place during about six hours, as the sample stayed in the muffle furnace for 12 hours. Different quantities as presented in the following description were mixed together, melt at 1000°C (15 minutes) again and cooled down quickly to make the melt sample a glass form [209, 226]. The main steps of the process are described in the following figure (Figure 5-2).

The following mixture was used as the preparation protocol: 0.2 g (powder sample) + 4 g flux (50% Lithium tetraborate & 50% Lithium metaborate) in Pt-5% Au alloy. Melting temperature (1000°C) during (15 minutes), put into Pt mould (28 mm diameter x 02 mm thickness). Then, the sample was labelled accordingly and stored properly, ready for acquisition during a several weeks only, because of the count rate changing for iron as indicative of segregation of the sample [203, 209]. Glass disc were made only for major concentration determination based on WDXRF. The sample preparation technics differ for major and trace element analysis. The preparation for major analysis took place at the laboratory of geology where the analysis was based on wavelength dispersive X-Rays (WDXRF). The software used for the data collection and analysis of major elements was the package OXSAS v2.3.1 with the ARL PERFORM'X spectrometer [209].

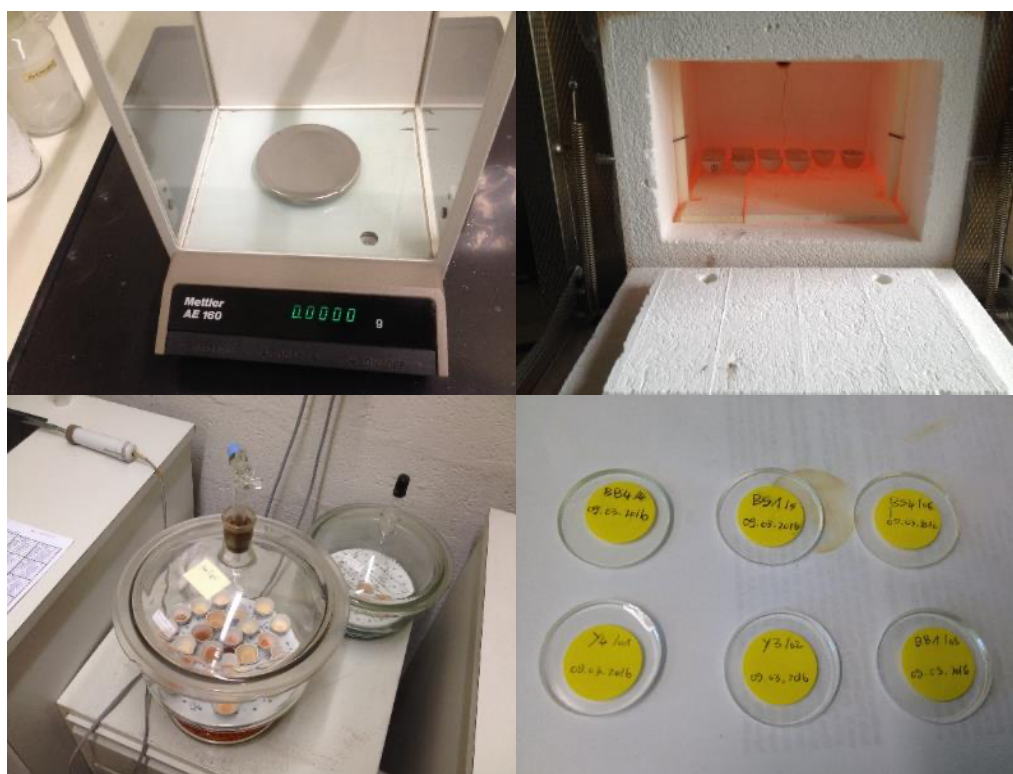


Figure 5-2: Glass disk preparation for major and minor elemental characterization of the investigated samples. On the top left, the sensitive balance is presented, as it is used for quantity (mass) measurement. It is followed by the porcelain crucible used to dry samples at melting temperature. Bottom left, is presented different samples in a desiccator, used to desiccating samples prior to the second melting process and quick cooling down for glass disk making. The last picture displays glass disks made in our laboratory for WDXRF analysis.

ii) Pressed pellets

For EDXRF measurements, which is a non-destructive method at all (as the sample are not melt down as for WDXRF), all the analysed samples and standards were pressed into pellets directly without mixing (as 100% or approximately pure sample) as 20 mm-diameter pellets under 4.0 t cm^{-2} during a period of five minutes. It is important before pressing the sample to form a pellet, to make sure that the particle grain size is at least five time smaller than the beam diameter. In this regard, the samples were gridded into mesh less than $2.5 \mu\text{m}$. This particle size was set very small enough as the beam line of the X-ray tube could overcome a size larger than it. Thin-walled aluminium cup was used for the stability, mobility, and to facilitate the handling of the sample during acquisition [209, 227]. The cleaning system during preparation of samples is a very important and delicate step for handling due to risk of contamination. During this step, different components were cleaned using 80% ethanol prior to the preparation of another sample. An example of prepared sample as pressed pellets is presented in the following figure where it can be seen the original sample for γ -ray spectrometry in a cylindrical container (polyester), the powder with a grain size smaller than the beam dimension and the pellets prepared for EDXRF measurement.



Figure 5-3: Pressed pellet preparation process for EDXRF measurement. All samples were labelled, and the labelling process took place at each step of the preparation as well. The measurement (irradiation) was performed on the sample side facing the ground without any labelling mark. Different colors of the pressed pellet represent the color of the sample (sand present in chapter 4).

iii) Reference samples

Since every scientific measurement or experiment is covered with uncertainties, the validation process is a reliable way to verify the accuracy of the measurement. It was then necessary to check the accuracy of the obtained results using reference materials, prepared in advance by certified material and with well-known concentration. These reference materials are a subject of a major concern in practical analyses of Fe-Ti oxide minerals as the number of elements covering the scope of explored substance for different elements present in samples is too large. In this sense, the number can be larger than the expectation of the experimenter and some elements present in the samples may not be covered by the reference material. In this regard, many reference materials are used to cover as much as possible a large number of important elements to be investigated in a sample. It is decisive to check the accuracy and efficiency of the system when performing such an analysis to avoid deviation and wrong data from wrong calibration. The list of the samples used for major determinations are presented by Duchene, and for detailed procedure, the original reference could be consulted [209].

For trace analyses, reference materials were provided by the National Institute of Standards and Technology (NIST). A total of seven reference materials well prepared by NIST was used, including DR-N, BE-N, MESS-3, SRM-610, PACS, UB-N, and MA-N [203, 228, 229]. These standard reference materials (SRMs) were produced and certified to facilitate the improvement of compound strategies for analyzing trace elements. They were prepared in rod form and have been sliced into wafers. These reference materials are conserve in powder form in the Laboratory of Nuclear Physics and are pressed into pellet for specific experiment at the convenient time.

In addition, a total number of four (04) reference samples were used for EDXRF calibration procedure as described in Table 5-1. These samples were certified reference material (CRM) and were made and provided by the National Institute of Standards and Technology (NIST) [150, 218, 228]. It included NIST - SRM-610, PACS -2, MESS-3, and BE-N. These standard reference materials (SRMs) have been manufactured and licensed to promote the enhancement of compound approaches in geological samples to analyze elemental composition. They were made in rod shape and in our laboratory, they were sliced into wafers. SRM-610 was used in a special way as it contains almost all the elements present in the samples. It is used to detect the presence of most of the existing elements in the sample before refining its concentration with the other reference samples. The spectra of the reference element used for system setup are presented in Figure 5-6.

Table 5-1: Certified reference materials used for the calibration of the instrumental setup (GeoReM material. Additional details can be found on the web site: http://georem.mpch-mainz.gwdg.de/sample_query.asp).

No	Code	Description
1	NIST-SRM 610	Trace element in glass disc samples: Used for instrument's calibration and for the evaluation of the analytical techniques. Main reference material for trace element characterization in inorganic matrices, its nominal glass composition (SRMs 610 – SRMs 617) is: 72% (SiO ₂), 12% (CaO), 14% (Na ₂ O), and 2% (Al ₂ O ₃). (www.ionflight.com)
2	PACS-2	Sediment, marine powder from the National Research Council of Canada (NRCC), M12, Montreal Road, Ottawa, Ontario, K1A 0R6, Canada "NRC-CNRC, Marine sediment reference materials for trace metals and other constituents analysis as HISS-1, MESS-3, PACS-2" http://inms-ienm.nrc-cnrc.gc.ca/en/calserv/crm_files_e/HISS-1_MESS-3_PACS_2_certificate.pdf [2004]; (http://new.aslo.org)
3	MESS-3	Sediment, marine powder used for similar matrix composition analysis: NRCC
4	BE-N	Basalt powder from "Centre de Recherches Pétrographiques et Géochimiques", CNRS, B.P. 20, Vandoeuvre-lès-Nancy Cedex 54501, France (for more details, the website can be followed http://georem.mpch-mainz.gwdg.de)

iv) Matrix Corrections

Some dilution of the sample with the flux (lithium borate) was produced to achieve a homogeneous and translucent glass disk for glass disk manufacturing prior to the major and minor elements measurement. Therefore, by implementing corrections, it is essential to consider the 1/20 percentage of the sample mixed with this Li-borate. This method likewise crosses mineralogical effects and thus allows the use of synthetic standard compounds such as Fe₂O₃ and TiO₂ to calibrate Fe and Ti. The impacts of mass absorption with Compton scattered tube were taken into consideration for Nb, Zr, Ni, and Zn analysis. The concentration of different components was evaluated using the OXSAS v2.3.1 software package, an accurate method for measuring 11 components using 15 certified materials to determine the alignment line [198, 218, 230]. This measurement was based on wavelength dispersive X-rays spectrometry (WDXRF). For the trace elements assessment, however, the software PyMCA

version 5.1 was used and the analysis were based on the energy dispersive X-rays spectrometry (EDXRF) technics [231]. Minor and trace elements, however, have been evaluated using the software PyMCA version 5.1 [218, 220, 232, 233].

v) Validation of XRF results

Some norms have been evaluated and the values acquired have been found in agreement with the reported values. As shown in Table 5-2, all standard deviation values between the reference and measured values were found within the limit described in the literature and are all below 6% in line with the valid measure. The concentration of SiO₂, Al₂O₃, K₂O, TiO₂, and Fe₂O₃ were measured with WDXRF equipment, while Na₂O, MgO, CaO, MnO, and P₂O₅ concentrations were determined with both WDXRF and EDXRF equipment, in view of validating also both of them [218, 220]. Comparative validation as in the case of γ -ray spectrometry is not presented in the present report but is seen as future prospect for detailed investigation about the XRF methodologies and detection systems.

Table 5-2: Confidence about the XRF reported values. Validation of the XRF measurements based on comparison between reported value by the standard sample's manufacturer and the data obtained in our laboratory

Reference material		Fe ₂ O ₃	TiO ₂	MgO	MnO	CaO	Al ₂ O ₃	SiO ₂
SARM-59 South African Bureau of Standards, Ilmenite (RBM)	Reported value	50.3	48.8	0.56	1.05	0.05	0.61	0.75
	This work value	49.8	49.1	0.54	0.87	0.05	0.59	0.73
ILM-6703: AG Der Dillinger Hüttenwerke, Ilmenite X6703181002-1	Reported value	58.51	28.74	2.47	0.2	0.99	3.4	5.67
	This work value	57.6	29.03	2.30	0.3	1.1	3.6	6.0
S-102: GBW 07221 Crude ore, Panzhihua Iron & Steel research Institute, China	Reported value	/	10.63	6.16	5.29	6.38	8,26	20.33
	This work value	0.02	11.0	5.99	5.72	5.99	8.8	21.0
BE-N	Reported value	12.70	2.61	13.06	0.20	13.99	9.98	38.22
	This work value	11.9	3.0	12.99	0.21	14.05	10.15	37.4
Average	Reported value	30.38	22.70	5.56	1.69	5.35	5.56	16.24
	This work value	29.83	23.03	5.46	1.78	5.30	5.79	16.28
Standard deviation (%)		1.80	1.49	1.93	5.34	1.03	4.00	0.25
		Al₂O₃	Fe₂O₃	K₂O	Na₂O	SiO₂	MgO	CaO
SRM-610	Reported value	5.68	0.50	2.97	10.14	58.04	0.33	2.18
	This work value	6.0	0.52	3.11	9.77	57.79	0.32	2.14
Standard deviation (%)		5,63	4,00	4,71	3,65	0,43	3,03	1,83

5.2.2. Equipment and principle

The EDXRF instrument used in this project is a strong tool that can be very efficient in validating both the absence and the presence of certain components in soil samples. This commercial spectrometer could be used to rapidly detect the existence in geological samples of elements such as Pb, Ni, As, Cr, Cd, Cu, Zn, and Hg [234]. The mobile XRF spectrometer used during acquisition consists of a Rh X-ray tube MOXTEK tool (Ag target, 50 kV, and 5 W). The resulting radiation (X-rays) is collimated by a collimator made of Ta ($Z = 73$) bringing a beam of 5 mm diameter to the surface of the sample. All the samples are placed at the same distance of 55 mm from the SSD detector outlet beam. The

SSD (Super Silicon Drift) detector used for experiments is a 25 mm² detection area with 500 μm thickness and with 12.5 μm ⁷Be window. More details are provided in the technical user manual. The energy resolution is about 2% of 140 eV at 5.9 keV. The angle between the incident and the emitted beam is 90 ° (with preferences of 45 ° optimization between the incident collimated X-rays and the ordinary surface of the sample) as shown in Figure 5-4. It demonstrates the arrangement of the actual system during the sample acquisition.

The geometry arrangement is optimized in a way that the background noise due to Compton scattering is reduced considerably. The sample position is selected to fall at the focal point of the two X-ray beams: this position allows efficient irradiation and detection compared to other dispositions of the geometry. Specification on the X-Ray generator indicates that it operated on 50 kV and 50 A with an acquisition time of 900-seconds (this acquisition time is conservative as the data obtained are statistically acceptable). In the laboratory, only experimental set-up arrangements and measurement conditions are set; the detector and software used were built by manufacturers and software builder [232, 235–237]. Measurements were taken under Air-Atmosphere as the sample-detector distance was set shorter enough and there was no need to use inert gas as Helium to lower down the interaction between air particles and proton. In the present case, interaction between air particles and X-ray photons was considered as negligible since the characteristic spectra of elements detected were corrected.

Measurements were performed at three different points of the sample surface and the considered result was the average of the three values from each measurement point in the case very low deviation was observed. When the measurement deviation for different points was high, additional irradiation was done on the concerned sample and the average value was taken over six different points (some points were removed). The experimental setup used to perform our experiment was proposed and well described by Wenbin et al. [235, 236, 238] and is represented in Figure 5-4 and Figure 5-5. Once acquired the XRF spectra, the PyMCA software package was used for data analysis and treatment. The output data choosing Excel format allows easy data interpretation and result display in tables.

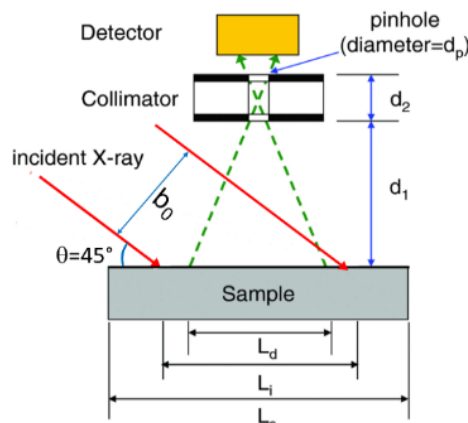


Figure 5-4: Detection system used for EDXRF measurement (x-ray incident beam and the geometry). The system is from the Silicon Drift Detector X-123SDD design: θ varies in different measurement but in our experiment, $\theta=45^\circ$ [238].

To analyze the findings acquired, PyMCA (Python Multichannel Analyzer) was used as software. It's an application that was built with C++ Qt programming toolkit, based on Python language. Here it should be pointed out that Qt is a C++ toolkit for cross-platform development [232, 239–244, 244–246]. Background measurement was subtracted from the experimental measurement of the sample

before the fluorescence peaks were fitted and interpreted in the least squares. PyMCA implements a fitting mode in which the continuum is represented by an analytical function before different concentrations are determined [246, 247]. The PyMCA tool advantage is related to its ability to display the result in either numbers (elemental concentration of samples under investigation) or displaying the color charts.

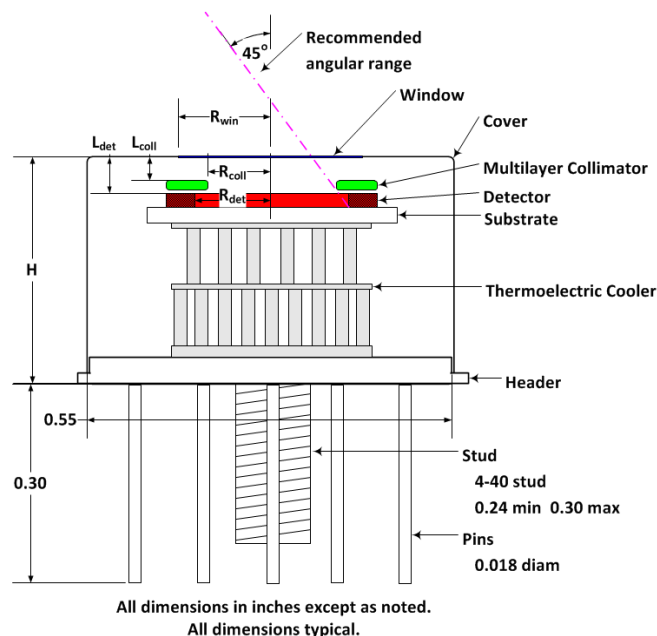


Figure 5-5: Schematic description of the complete X-Ray Spectrometer with Silicon Drift Detector X-123 SDD

5.3. XRF-Results and Discussion: Elemental composition

5.3.1. Soil samples from the two campuses

The first part of this section is dedicated to the description of the results obtained from the study of campuses 1 and 2 of the University of Douala – Cameroon. Major and trace compounds and elements investigated in the eighteen (18) soil samples are recorded in Table 5-3 and Table 5-4. The first table shows the major elements' concentrations measured in the investigated soil samples. The followings are some key points of the obtained results that are detailed in different tables (Table 5-3 and Table 5-4).

- In *Campus 1*, the most abundant compound found in all investigated soil samples was SiO_2 (with a mean value of 45.85 %), follows by the Fe_2O_3 (with a mean value of 17.79 %). The presence of TiO_2 , CaO , Al_2O_3 , K_2O , and MnO (with mean concentration values of 10.10, 10.79, 5.11, 3.87, and 3.87 in term of percentage, respectively) is also relevant. Due to the environment of the detection threshold during experiments, minor (trace) components such as Na_2O and P_2O_5 were not identified in the major and minor assessment. The elemental concentration of campus samples taken individually are displayed in Table 5-3 and Table 5-4 and they are summarized in Table 5-5, Table 5-6, and Table 5-7. But the combined results of both campuses are also presented as color graphs also (see Figure 5-8).
- From *campus 2*, SiO_2 was the most abundant elements found in all investigated samples with an average concentration value of 45.14 %, followed by Fe_2O_3 (with a mean value of 18.47

%). The highest concentration of Fe_2O_3 was 22.26 % found in sample UD9, in campus 2. It is appealing to discuss the high concentration of the iron oxide measured in the investigated sample. Concentrations of this range are rarely measured in soil samples, but this could be justified by the historical background of the campuses of the university of Douala. The presence of other compounds of interest as TiO_2 , CaO , Al_2O_3 , K_2O , and MnO (with mean concentration values of 11.68, 9.31, 5.71, 2.95, and 4.11%, respectively) was also relevant.

The high concentration of the Fe in the soil samples is something uncommon. The concentration found in the majority of the investigated soil samples put into evidence that the analyzed sample can be classified as Fe-soil or Fe-sand. This has been suggested after investigating the concentration of Fe in different soil samples. This is due to the high concentration levels of Fe. It is not very surprising that the concentration of Fe in samples is higher compared to what is found in the same analysis in other countries. This can be explained by the historical background of the campus, which was the valley of waste at the early foundation of the city of Douala. As industrial wastes contained metallic objects in the past before the recycling process was considered in waste management, the process has been likely the main contributor to the high Fe concentration in the studied site. As the area falls into the Douala Bassa area, generally known as the biggest industrial area in the country, human activity may be involved in this high concentration. Many iron factories are under operation in the City.

Table 5-4 displays the elemental concentrations of trace elements found in soil samples. Elements as S, Ca, Cr, Ni, Cu, Zn, Ga, As, Sr, Zr, Nb, and Ag were detected in the experiment performed in the lab with mean concentration values of 240.0, 30.8, 5.3, 75.4, 23.6, 31.1, 2.4, 11.8, 3.1, 32.6, 2.0, and 21.7 $\mu\text{g/g}$ for the samples from Campus 1 and 227.0, 26.6, 6.3, 76.0, 22.0, 26.2, 2.2, 11.6, 3.4, 29.9, 2.4, and 21.8 $\mu\text{g/g}$ for the samples from Campus 2, respectively. As trace element, the value presented in the Table 5-4 are in ppm unit. It is though the reason they are referred to as trace elements.

Table 5-3 and Table 5-4 outlined the similarities in the elemental content measured in the soil under investigation and this information can be included in the Cameroon baseline information as well as in the Central African sub-region database. The structure of the soil differs slightly from one sample point to another. These differences are observed in figures displaying the spectra of the investigated samples. For instance, in Figure 5-7-Figure 5-11 and in Table 5-3 and Table 5-4, the mean elemental content of all the elements obtained in eighteen analyzed samples is presented and additional display is given by color graph shown in Figure 5-8. Non-uniform distribution of soil characteristics and geological and geochemical properties of the earth is likely to be the origin of large and small concentration variation and content fluctuation. As already suggested in the previous chapter, the elemental distribution of chemical element and radionuclide in the soil is subject to many phenomena. Among those phenomena, the erosion and weathering processes are well known in the vicinity of the area under investigation (Douala basin). Results present in the literature display similarity with the obtained result for the majority of compounds or elements detected except the case of Fe, that the concentration values were quite higher than that measured in similar samples [219, 219, 239–241, 243, 245, 248, 249]. Standard reference material curves used for calibration are shown in Figure 5-6.

Figure 5-7 presents EDXRF spectra of soil samples from Campus 1, and similar spectra from Campus 2 were analyzed after acquisition simultaneously and presented in detail in the Figure 5-7, Figure 5-9, Figure 5-10, and Figure 5-11. Only one spectrum was pick-labelled as all other spectra have similar pick-annotation. The presented spectra were obtained with an equipment calibrated for acquisition of energy gap ranged from 0.12 to 30.5 keV covering important energy ranges (including α , β , and γ lines) [209, 250–252].

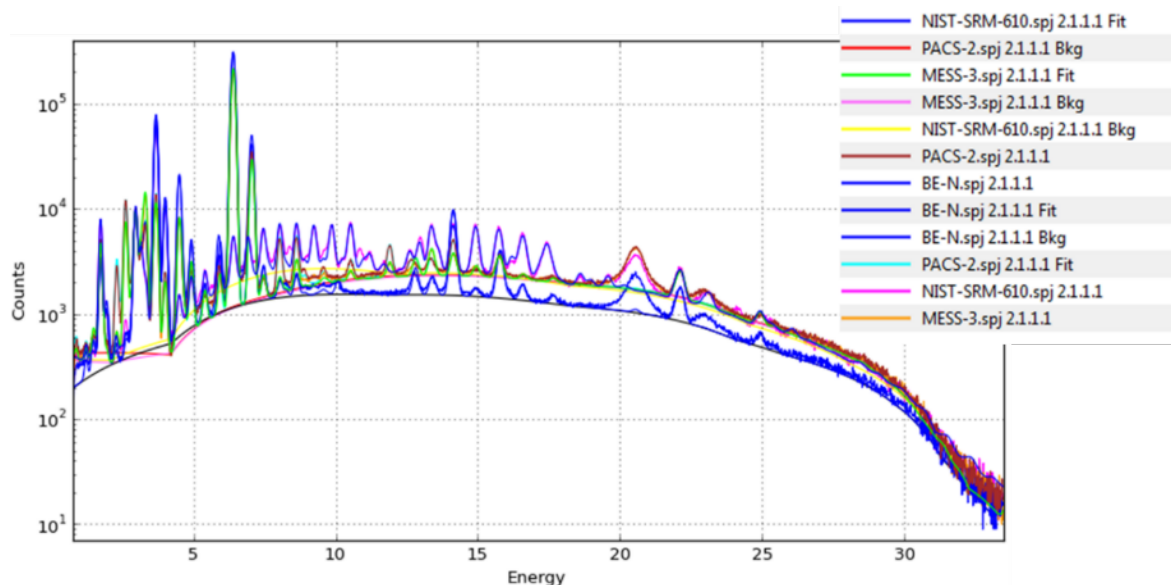


Figure 5-6. EDXRF Spectra of the reference material used for calibration and result validation. Four elements used in this process included NIST-SRM 610, PACS-2, MESS-3, and BE-N.

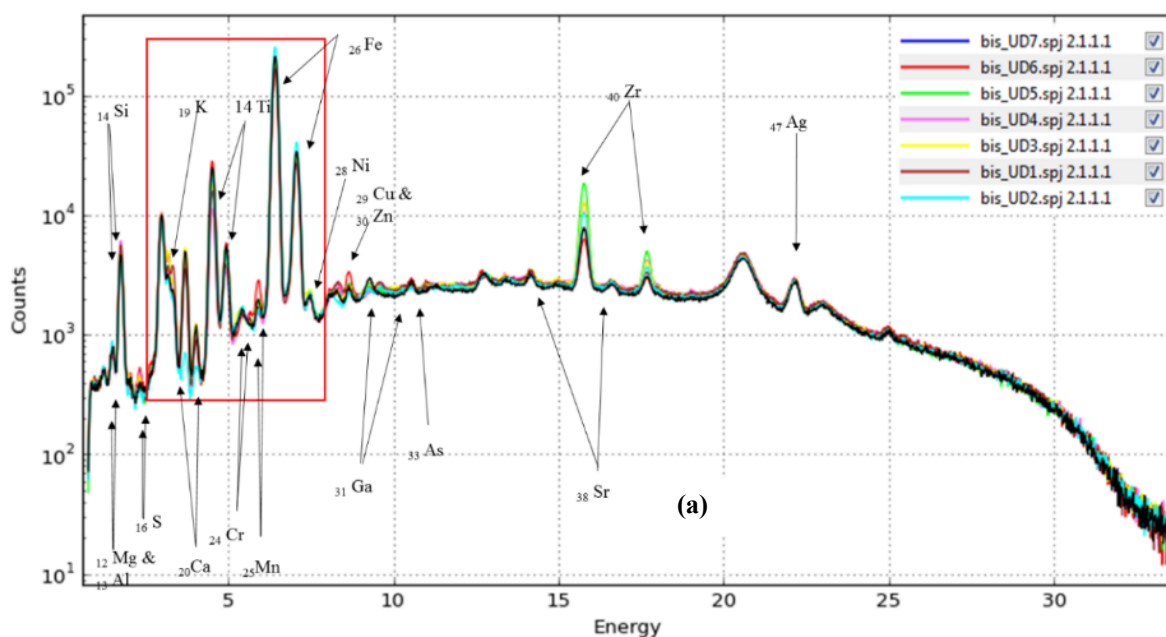


Figure 5-7. Spectra of different samples (UD1 to UD7) from Campus 1. Labelled spectra for campus 1 investigation. This labelling and annotation is valid for spectra from both campuses as the elements and compounds assessed are similar. Detailed views are presented in the following figures.

From the obtained result, it can also be observed that the calibration procedure was well performed because the peaks of all elements are fixed at the same energy range (no translation of peaks can be observed) but only a difference in the count rate, the pick surface, or in the concentration expressed here in term of counts integral. For instance, Fe concentrations were packed, for separate soil samples, in the interval of 14.78 - 22.26 %. A slight variation can be noted (owing to the background and difference discovered in various samples) and can be explained as earlier stated by the small statistical variation due to measuring time, equipment, and the historical background of the studied site. The observed variations are likely to suggest that various concentration levels found in soil samples

are related to their age (geological age of the formation), origin (geological components included in their formation), and various previous human operations. This historical background as waste disposal site also justified the higher level concentration of K_2O in the studied site compared to other sites around the world [219, 239–241, 241, 243, 243, 245, 248]. If the interest is about the peak determination and associated concentration values, it is essential to solve background changes or fluctuations.

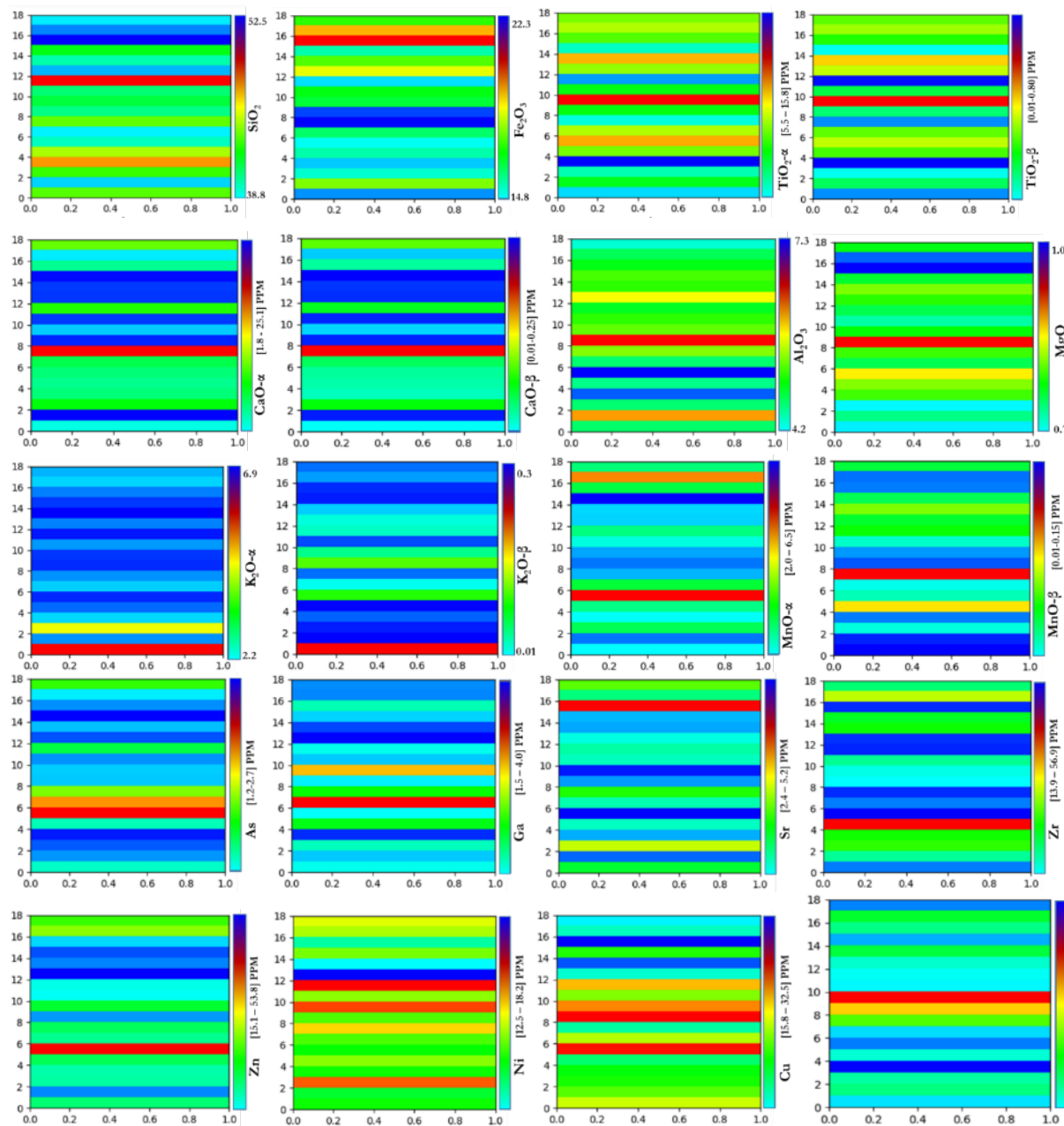


Figure 5-8: Color graphs of major compounds, minor and trace elements found in the investigated samples. The color graph displays the elemental concentration while the y-axis lists the sampling site of sample Id.

Table 5-3: Concentrations of major elements and their standard deviation (s) in terms of percentage (%) of all soil samples from the two campuses (07 samples from Campus 1 and 11 from Campus 2).

Sample Point	SiO ₂	s	Al ₂ O ₃	s	K ₂ O	s	Fe ₂ O ₃	s	TiO ₂	s	MgO	s	CaO	s	MnO	s
UD-1	48.55	0.24	5.21	0.09	6.99	0.12	17.04	0.02	7.84	0.03	0.80	0.03	9.64	0.11	2.17	0.44
UD-2	48.76	0.11	7.26	0.11	3.51	0.10	21.08	0.02	12.56	0.04	0.98	0.03	1.82	0.08	2.07	0.60
UD-3	44.53	0.09	4.83	0.08	4.99	0.11	15.87	0.01	8.35	0.03	0.74	0.02	14.98	0.12	3.87	0.43
UD-4	51.92	0.10	4.43	0.08	3.13	0.10	17.68	0.02	5.56	0.02	0.83	0.02	12.06	0.11	2.64	0.42
UD-5	45.66	0.09	4.68	0.08	2.52	0.09	17.00	0.02	10.84	0.03	0.79	0.02	11.03	0.10	5.61	0.41
UD-6	40.57	0.09	4.21	0.08	2.65	0.10	18.25	0.02	13.21	0.03	0.85	0.02	12.09	0.11	6.54	0.45
UD-7	40.93	0.09	5.14	0.09	3.28	0.11	17.64	0.02	12.34	0.03	0.82	0.03	13.94	0.12	4.20	0.47
Min	40.57	0.09	4.21	0.08	2.52	0.09	15.87	0.01	5.56	0.02	0.74	0.02	1.82	0.08	2.07	0.41
Max	51.92	0.24	7.26	0.11	6.99	0.12	21.08	0.02	13.21	0.04	0.98	0.03	14.98	0.12	6.54	0.60
Average	45.85	0.12	5.11	0.09	3.87	0.10	17.79	0.02	10.10	0.03	0.83	0.03	10.79	0.11	3.87	0.46
UD-8	39.11	0.08	4.53	0.07	2.41	0.10	14.78	0.02	6.78	0.02	0.69	0.02	25.16	0.13	5.09	0.34
UD-9	48.39	0.10	6.98	0.11	3.11	0.10	22.26	0.02	11.57	0.03	1.04	0.03	2.71	0.08	2.15	0.45
UD-10	45.38	0.09	5.56	0.09	2.75	0.09	18.07	0.02	15.81	0.04	0.84	0.03	7.41	0.10	2.45	0.47
UD-11	49.31	0.10	6.08	0.10	3.33	0.10	19.38	0.02	11.75	0.03	0.90	0.03	3.34	0.08	4.08	0.53
UD-12	49.88	0.09	4.66	0.08	2.27	0.09	15.56	0.01	6.23	0.02	0.73	0.02	14.86	0.11	4.37	0.38
UD-13	45.03	0.10	6.59	0.10	3.40	0.10	20.58	0.02	13.87	0.04	0.96	0.03	3.31	0.09	4.53	0.59
UD-14	45.87	0.10	5.81	0.09	2.60	0.09	19.78	0.02	14.86	0.04	0.92	0.03	3.25	0.08	5.08	0.52
UD-15	52.46	0.11	6.26	0.10	2.93	0.09	20.31	0.02	10.00	0.03	0.95	0.03	1.90	0.08	3.34	0.52
UD-16	40.30	0.09	5.94	0.10	3.19	0.11	17.76	0.01	12.81	0.04	0.83	0.03	13.36	0.13	3.91	0.63
UD-17	42.04	0.09	5.64	0.09	3.54	0.10	17.70	0.01	13.49	0.04	0.83	0.03	8.88	0.11	5.80	0.58
UD-18	38.82	0.08	4.71	0.08	2.95	0.10	17.03	0.01	11.28	0.03	0.79	0.02	18.18	0.13	4.45	0.47
Min	38.82	0.08	4.53	0.07	2.27	0.09	14.78	0.01	6.23	0.02	0.69	0.02	1.90	0.08	2.15	0.34
Max	52.46	0.11	6.98	0.11	3.54	0.11	22.26	0.02	15.81	0.04	1.04	0.03	25.16	0.13	5.80	0.63
Average	45.14	0.10	5.71	0.09	2.95	0.10	18.47	0.02	11.68	0.03	0.86	0.03	9.31	0.10	4.11	0.50

Table 5-4: Concentrations of minor and trace elements and their standard deviation (s) in term of ppm of all the investigated soil samples from the two campuses. The concentrations are presented following by the standard deviation of the measurement (denoted “s”).

Sample Point	S*	s	Ar	s	Ca	s	Cr	s	Ni	s	Cu	s	Zn	s	Ga	s	As	s	Sr	s	Zr	s	Nb	s	Ag	s
UD-1	34	3	0.1	0.0	27.5	0.3	4.6	0.2	15.1	0.2	25.0	0.4	30.3	0.5	2.2	0.0	1.7	0.1	3.5	0.1	21.1	0.1	2.0	0.1	21.0	0.7
UD-2	49	3	0.1	0.0	5.2	0.2	7.4	0.2	17.5	0.2	27.9	0.5	23.1	0.5	2.4	0.1	1.7	0.1	3.3	0.1	38.3	0.1	2.7	0.1	22.7	0.6
UD-3	36	3	0.1	0.0	42.8	0.3	4.8	0.2	16.8	0.2	20.7	0.4	26.3	0.4	2.1	0.0	1.2	0.0	3.7	0.1	38.1	0.1	2.0	0.1	24.7	0.6
UD-4	48	3	0.1	0.0	34.5	0.3	4.9	0.2	14.4	0.2	21.0	0.4	26.8	0.4	1.5	0.0	1.2	0.0	2.8	0.1	38.1	0.1	1.6	0.1	21.0	0.6
UD-5	30	2	0.0	0.0	31.5	0.3	5.0	0.2	14.5	0.2	18.5	0.4	28.7	0.4	2.5	0.0	1.5	0.0	2.9	0.1	56.9	0.1	1.9	0.1	17.4	0.6
UD-6	54	3	0.0	0.0	34.6	0.3	4.9	0.2	14.2	0.2	27.8	0.4	53.8	0.5	2.0	0.0	2.7	0.0	2.4	0.1	14.5	0.1	1.8	0.1	25.5	0.7
UD-7	30	3	0.1	0.0	39.8	0.3	5.3	0.2	15.4	0.2	24.4	0.4	28.8	0.5	4.0	0.1	2.6	0.1	3.2	0.1	20.9	0.1	2.0	0.1	20.0	0.7
Min	30	2	0.0	0.0	5.2	0.2	4.6	0.2	14.2	0.2	18.5	0.4	23.1	0.4	1.5	0.0	1.2	0.0	2.4	0.1	14.5	0.1	1.6	0.1	17.4	0.6
Max	54	3	0.1	0.0	42.8	0.3	7.4	0.2	17.5	0.2	27.9	0.5	53.8	0.5	4.0	0.1	2.7	0.1	3.7	0.1	56.9	0.1	2.7	0.1	25.5	0.7
Average	40	3	0.1	0.0	30.8	0.3	5.3	0.2	15.4	0.2	23.6	0.4	31.1	0.5	2.4	0.0	1.8	0.0	3.1	0.1	32.6	0.1	2.0	0.1	21.7	0.6
UD-8	12	2	0.0	0.0	71.9	0.4	3.3	0.1	13.8	0.1	15.8	0.3	25.1	0.4	2.2	0.0	1.8	0.0	2.9	0.1	13.9	0.1	2.0	0.1	16.9	0.6
UD-9	42	3	0.1	0.0	7.7	0.2	5.2	0.2	17.1	0.2	32.5	0.5	22.0	0.5	2.3	0.1	1.6	0.1	3.1	0.1	29.9	0.1	3.1	0.1	29.9	0.7
UD-10	13	3	0.1	0.0	21.2	0.3	7.5	0.2	18.2	0.2	27.5	0.4	33.0	0.5	3.6	0.1	1.5	0.0	2.6	0.1	28.2	0.1	3.0	0.1	21.0	0.6
UD-11	33	3	0.1	0.0	9.5	0.2	7.1	0.2	17.8	0.2	26.5	0.5	27.4	0.5	2.2	0.1	1.6	0.1	3.5	0.1	35.7	0.1	2.3	0.1	22.2	0.6
UD-12	22	2	0.1	0.0	42.4	0.3	4.0	0.2	16.4	0.2	23.4	0.4	22.0	0.4	1.9	0.0	1.6	0.0	2.8	0.1	14.8	0.1	1.8	0.1	20.2	0.6
UD-13	37	3	0.1	0.0	9.5	0.2	7.6	0.2	12.5	0.2	21.2	0.5	15.1	0.5	1.7	0.1	1.5	0.1	3.5	0.1	19.7	0.1	2.4	0.1	24.4	0.7
UD-14	34	3	0.1	0.0	9.3	0.2	6.1	0.2	13.9	0.2	16.6	0.4	20.2	0.5	1.8	0.0	1.6	0.1	3.0	0.1	41.8	0.1	2.4	0.1	21.4	0.6
UD-15	41	3	0.1	0.0	5.4	0.2	7.1	0.2	17.9	0.2	25.4	0.5	19.0	0.5	2.3	0.1	1.3	0.1	3.3	0.1	42.3	0.1	2.2	0.1	21.4	0.6
UD-16	16	3	0.1	0.0	38.2	0.4	8.4	0.2	15.3	0.2	16.0	0.4	25.2	0.5	2.6	0.1	1.6	0.1	5.2	0.1	19.1	0.1	2.5	0.1	21.7	0.7
UD-17	22	3	0.1	0.0	25.4	0.3	6.4	0.2	17.5	0.2	20.6	0.5	44.1	0.5	2.0	0.0	1.7	0.1	3.6	0.1	51.5	0.1	2.5	0.1	21.1	0.7
UD-18	26	3	0.1	0.0	51.9	0.4	6.1	0.2	15.7	0.2	17.0	0.4	35.3	0.5	1.7	0.0	2.0	0.0	3.6	0.1	31.7	0.1	1.8	0.1	19.4	0.6
Min	12	2	0.0	0.0	5.4	0.2	3.3	0.1	12.5	0.1	15.8	0.3	15.1	0.4	1.7	0.0	1.3	0.0	2.6	0.1	13.9	0.1	1.8	0.1	16.9	0.6
Max	42	3	0.1	0.0	71.9	0.4	8.4	0.2	18.2	0.2	32.5	0.5	44.1	0.5	3.6	0.1	2.0	0.1	5.2	0.1	51.5	0.1	3.1	0.1	29.9	0.7
Average	27	3	0.1	0.0	26.6	0.3	6.3	0.2	16.0	0.2	22.0	0.4	26.2	0.5	2.2	0.0	1.6	0.1	3.4	0.1	29.9	0.1	2.4	0.1	21.8	0.6

* S denotes sulfur in this case.

Table 5-5: Summary of the elemental concentrations of major elements and their standard deviation (s) in term of percentage (%): Range and averaged con-

centration of samples from the two campuses.

Sample Sites		SiO ₂	s	Al ₂ O ₃	s	K ₂ O	s	Fe ₂ O ₃	s	TiO ₂	s	MgO	s	CaO	s	MnO	s
Campus 1	Min	40.57	0.09	4.21	0.08	2.52	0.09	15.87	0.01	5.56	0.02	0.74	0.02	1.82	0.08	2.07	0.41
	Max	51.92	0.24	7.26	0.11	6.99	0.12	21.08	0.02	13.21	0.04	0.98	0.03	14.98	0.12	6.54	0.60
Average		45.85	0.12	5.11	0.09	3.87	0.10	17.79	0.02	10.10	0.03	0.83	0.03	10.79	0.11	3.87	0.46
Campus 2	Min	38.82	0.08	4.53	0.07	2.27	0.09	14.78	0.01	6.23	0.02	0.69	0.02	1.90	0.08	2.15	0.34
	Max	52.46	0.11	6.98	0.11	3.54	0.11	22.26	0.02	15.81	0.04	1.04	0.03	25.16	0.13	5.80	0.63
Average		45.14	0.10	5.71	0.09	2.95	0.10	18.47	0.02	11.68	0.03	0.86	0.03	9.31	0.10	4.11	0.50

Table 5-6: Concentrations of minor and trace elements and their standard deviation (s) expressed in ppm: range and averaged concentration of samples from the two campuses.

Site	S	s	Ar	s	Ca	s	Cr	s	Ni	s	Cu	s	Zn	s	Ga	s	As	s	Sr	s	Zr	s	Nb	s	Ag	s
Min1*	30	2	0.0	0.0	5.2	0.2	4.6	0.2	14.2	0.2	18.5	0.4	23.1	0.4	1.5	0.0	1.2	0.0	2.4	0.1	14.5	0.1	1.6	0.1	17.4	0.6
Max1	54	3	0.1	0.0	42.8	0.3	7.4	0.2	17.5	0.2	27.9	0.5	53.8	0.5	4.0	0.1	2.7	0.1	3.7	0.1	56.9	0.1	2.7	0.1	25.5	0.7
Average	40	3	0.1	0.0	30.8	0.3	5.3	0.2	15.4	0.2	23.6	0.4	31.1	0.5	2.4	0.0	1.8	0.0	3.1	0.1	32.6	0.1	2.0	0.1	21.7	0.6
Min2*	12	2	0.0	0.0	5.4	0.2	3.3	0.1	12.5	0.1	15.8	0.3	15.1	0.4	1.7	0.0	1.3	0.0	2.6	0.1	13.9	0.1	1.8	0.1	16.9	0.6
Max2	42	3	0.1	0.0	71.9	0.4	8.4	0.2	18.2	0.2	32.5	0.5	44.1	0.5	3.6	0.1	2.0	0.1	5.2	0.1	51.5	0.1	3.1	0.1	29.9	0.7
Average	27	3	0.1	0.0	26.6	0.3	6.3	0.2	16.0	0.2	22.0	0.4	26.2	0.5	2.2	0.0	1.6	0.1	3.4	0.1	29.9	0.1	2.4	0.1	21.8	0.6

* 1 and 2 referred to the campus 1 and campus 2, respectively.

Elemental concentration of major compounds, minor, and trace elements were displayed in color graphs to show clear evidence of the concentration from one sample to another or from point to point. Color graphs presented below include the cases of SiO₂, Fe₂O₃, TiO (both α and β K shells), CaO (both α and β K shells), Al₂O₃, MgO, K₂O (both α and β K shells), and MnO (both α and β K shells) as major or minor compound. In addition, As, Ga, Sr, Zr, Zn, Ni, Cu, and Nb elemental concentrations were plotted using color graphs. Color graph has the advantage to display the overall concentration per site and to clearly highlight the area of high concentration.

Soil's composition changes within the content of each element detected. These differences are evidenced in Figure 5-7 to Figure 5-11 where the mean elemental content of all the elements obtained in eighteen analyzed soil is presented. The values achieved are in line with the literature and have been achieved using the PyMCA software package v. 5.1.1 [232] where fundamental parameters are still used as a basis for quantitative analysis. Furthermore, it also requires to consider that norms and unknowns have a similar matrix structure (cellulose) and therefore, the absorption impacts in both sampling sites (samples from both sites) should be comparable.

Figure 5-7 to Figure 5-11 present EDXRF spectra of soil samples from campus 1 (Figure 5-7 and Figure 5-9), from campus 2 (Figure 5-10), and from both campuses (Figure 5-11). The presented spectra were measured in an energy range from about 0.12 to 30.5 keV fluorescence lines (all the energy lines are expressed in keV) [209]. Lead fluorescence lines are very well separated up to natural lead level in the soil material which is closed to the detection level of the EDXRF technique. Figure 5-11 (a, b, c, d) depicted the well-measurement process. Slightly variation can be observed to the background when zooming on the spectra and it could be explained by the low statistical and time measurement (05 to 15 minutes). It's not necessary to fix these background fluctuations in the case that the interest is about the pick determination and the related concentration values 95 to 100% related to the peak than the background count.

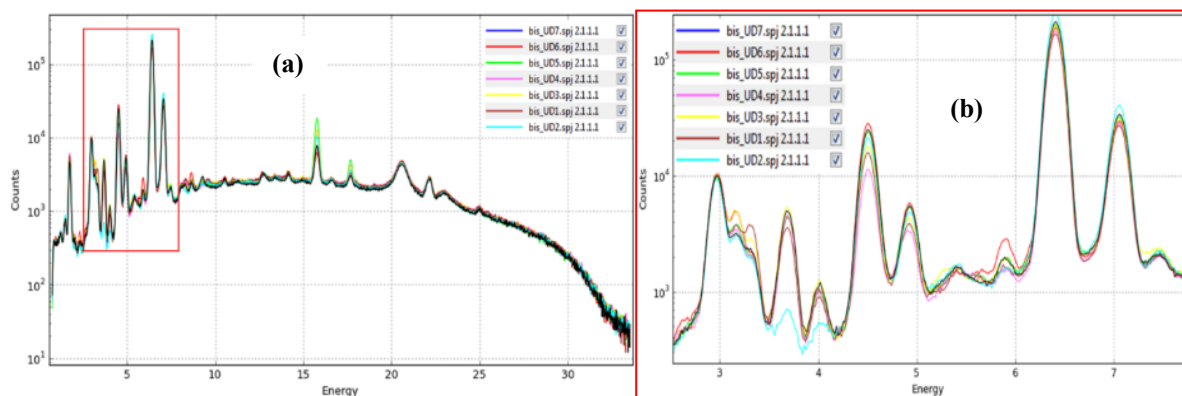


Figure 5-9: Spectra of different samples (UD-1 to UD-7) from campus 1. (a) All picks (related to major compounds and trace and minor elements concentration) are presented in the same graph. (b) Zoom of the Fe and another surrounding representative picks.

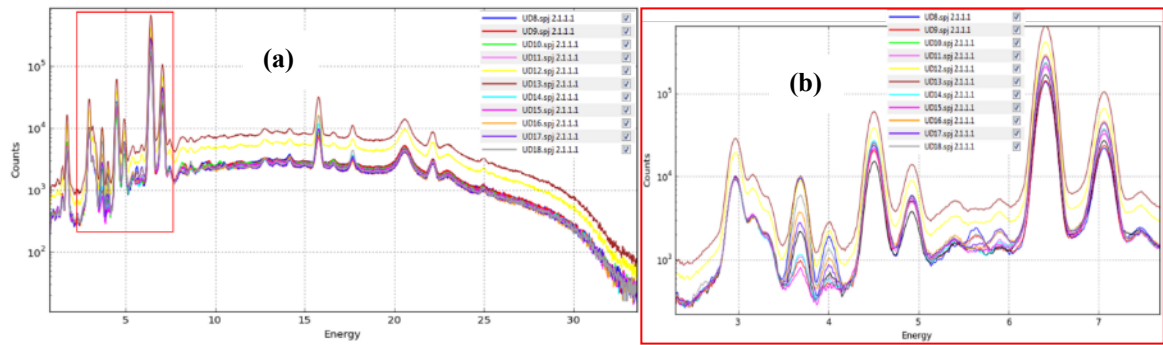


Figure 5-10: Spectra of different samples (UD-8 to UD-18) from campus 2. (a) All picks (related to major compounds and trace and minor elements concentration) are presented in the same graph. (b) Zoom of the Fe and another surrounding representative picks.

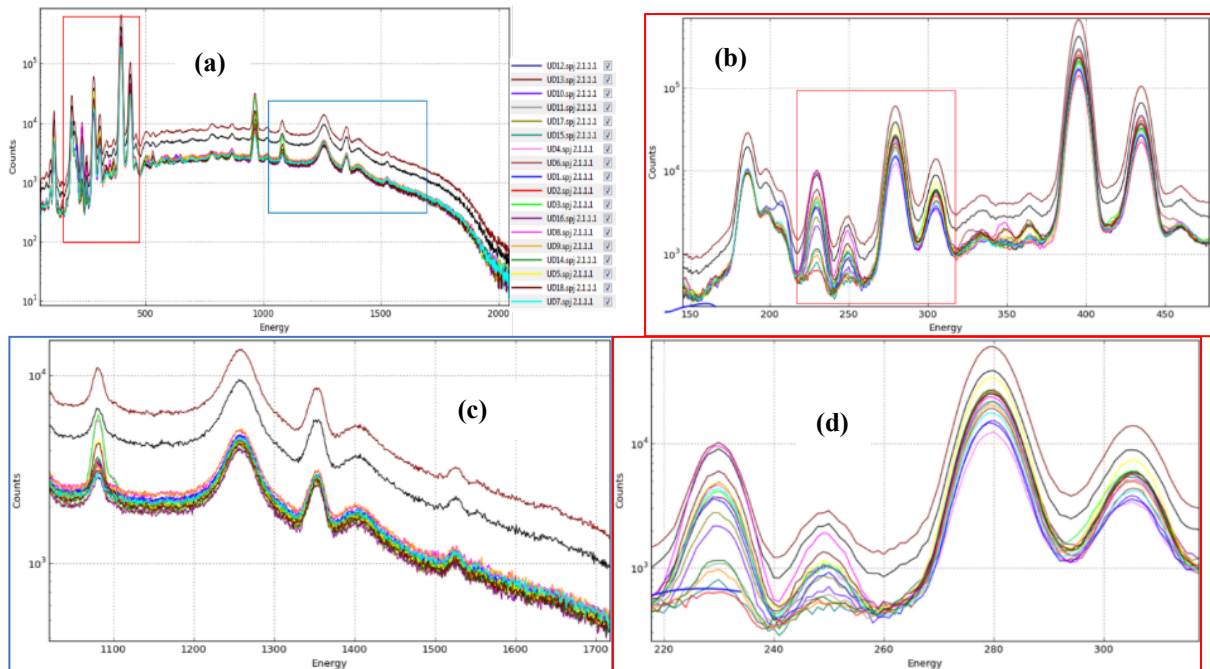


Figure 5-11: Spectra of all investigated samples (UD-1 to UD-18) from both campuses. Energy in deV (2000 deV = 20 keV): (a) All picks (related to major compounds and trace and minor elements concentration) are presented in the same graph. (b) Zoom on the Ar, Ni, Sr, and Ag and other closed representative picks (c) Zoom of the As, Zr, Sr, Kr, Rb, and other surrounding representative picks. (d) Zoom on the S, Ar, and Si k-lines.

5.3.2. Sand samples from Quarries

Table 5-7 reported the result of the X-ray Fluorescence analysis for both major and minor elements, measured from seven big quarries in the city of Doula and surroundings. SiO₂ was found to be the most abundant elements found in all the investigated samples (with a mean concentration value of 95.51 %) follows with Al₂O₃ (mean value of 2.68 %). The presence of K element with mean concentration value of 1.11 % for K₂O compound was also reported as well as the Fe₂O₃ that the mean concentrations follows the same trend as K₂O with a mean value of 0.75 %. The TiO₂ was also observed with an average concentration of 0.41%. With a mean value of 0.34, the average CaO concentration ranged from 0 to 0.80 %. Similarly, MgO and Na₂O concentration’s levels ranged from 0 to 0.07%

and 0 to 0.5%, respectively. In "Youpoue Bamenda 2" the largest levels of MgO was measured, while the largest levels of Na₂O was found in "Northern Akwa 3" and "Bonaberi Bonamikano 4." Another minor elements detected are MnO and P₂O₅ (with mean concentration value of 0.02 % for both).

In Table 5-7, the SiO₂, Al₂O₃, K₂O, TiO₂, and Fe₂O₃ concentrations were displayed. They were obtained using WDXRF analysis. This is due to the context that all the above elements are major and need glass disk preparation prior to the measurement and were assessed in the department of Geology. The last column of Table 5-7 shows the Loss-On-Ignition (LOI) during experimental measurement: it shows an inverse relationship with percentage dry weight values (because the sample used in WDXRF analysis were heated at 1000°C in a porcelain crucible). The LOI is a test used in inorganic analytical chemistry and soil science, particularly in the analysis of minerals and the chemical makeup of soil (sand). It refers to the mass loss of combustion residue whenever it is heated in an air or oxygen atmosphere at high temperature.

These results indicate that the elevated elemental concentration levels of Si and Al in the definition of subgroups can be extremely helpful and provide valuable insights into the crude products used in the process of glass manufacturing in Cameroon as several glass manufacturing firms in Cameroon (such as SOCAVER) use sand and rock with a very large Si composition (Figure 5-12). The advantage resides in the ability to make easy glass disk from material with large Si mineral composition.

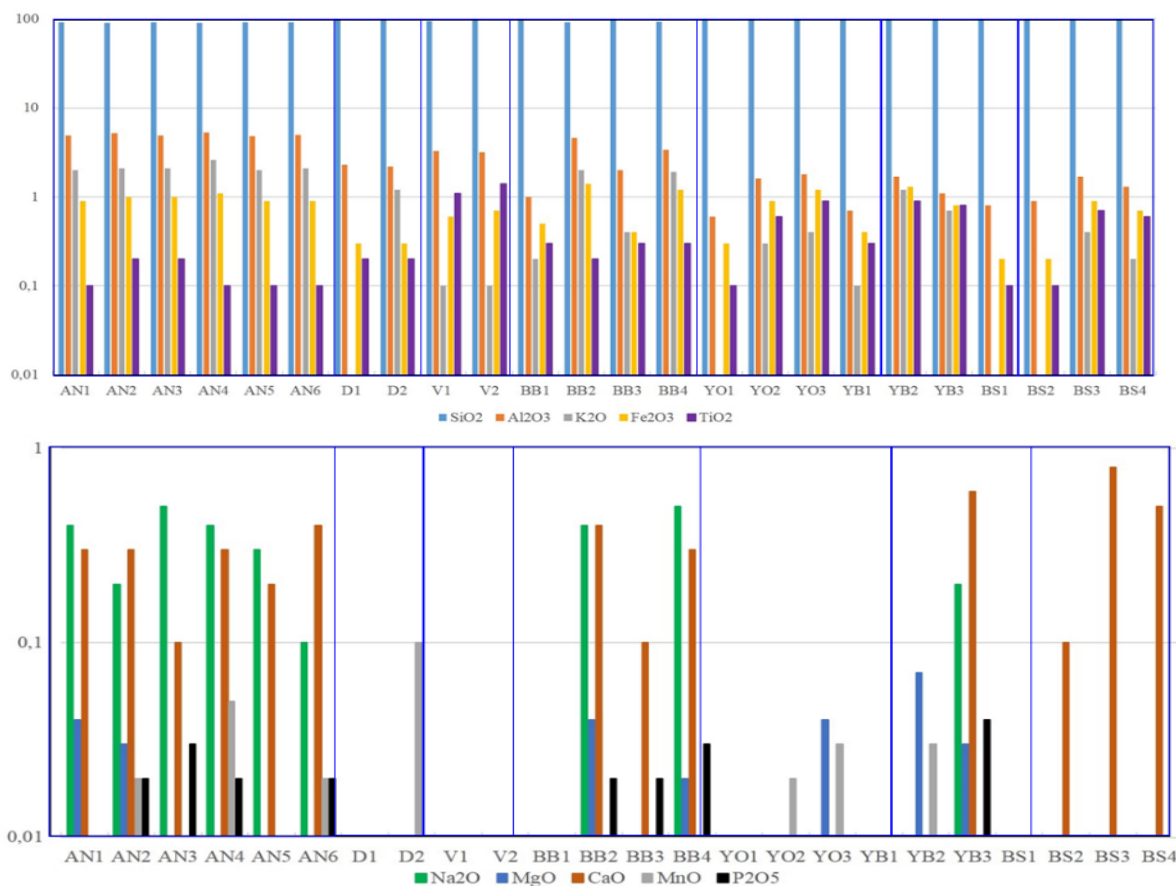


Figure 5-12: Elemental composition of major and minor compounds from XRF-measurement of all investigated sand samples: (a) Correspond to major compounds assessed measured (all compounds have their maximum detected concentration higher than the unity) and (b) Correspond to minor compound concentrations (all compounds have their maximum detected concentration less than the unity) [209, 232].

Table 5-7: Concentrations (in term of percentage %) of major and minor elements in sand samples from the seven investigated quarries. Result obtained using WDXRF

Sampling Quarry	Sample Id	SiO ₂	Al ₂ O ₃	K ₂ O	Fe ₂ O ₃	TiO ₂	Na ₂ O	MgO	CaO	MnO	P ₂ O ₅	LOI
Northern Akwa	AN-1	91.2±4.5	4.9±0.4	2.0±0.1	0.9±0.1	0.1±0	0.4±0	0.04±0	0.3±0	0.01±0	0.01±0	0.7
	AN-2	90.7±2.4	5.2±0.6	2.1±0.0	1.0±0.0	0.2±0	0.2±0	0.03±0	0.3±0	0.02±0	0.02±0	0.8
	AN-3	91.4±4.2	4.9±0.5	2.1±0.1	1.0±0.1	0.2±0	0.5±0	ND	0.1±0	0.01±0	0.03±0	0.6
	AN-4	90.0±2.15	5.3±0.7	2.6±0.1	1.1±0.1	0.1±0	0.4±0	ND	0.3±0	0.05±0	0.02±0	0.7
	AN-5	91.4±3.9	4.8±0.6	2.0±0.1	0.9±0.1	0.1±0	0.3±0	ND	0.2±0	0.01±0	ND	0.7
	AN-6	90.9±3.2	5.0±0.8	2.1±0.1	0.9±0.0	0.1±0	0.1±0	ND	0.4±0	0.02±0	0.02±0	0.9
Dibamba	D-1	97.65±2.2	2.3±0.9	ND	0.3±0	0.2±0.1	ND	ND	ND	ND	ND	0.59
	D-2	96.8±2.1	2.2±0.8	1.2±0.3	0.3±0.1	0.2±0	ND	ND	ND	0.1±0	ND	0.62
Village	V-1	94.6±3.2	3.3±0.7	0.1±0	0.6±0	1.1±0.1	ND	ND	ND	0.01±0	ND	0.90
	V-2	95.2±3.3	3.2±0.7	0.1±0	0.7±0.1	1.4±0.2	ND	ND	ND	0.01±0	ND	0.71
Bonaberi-Bonami kano	BB-1	98.7±2.1	1.0±0.1	0.2±0	0.5±0	0.3±0.0	ND	ND	ND	ND	ND	0.33
	BB-2	91.0±3.6	4.6±0.8	2.0±0.2	1.4±0.3	0.2±0.0	0.4±0.0	0.04±0.0	0.4±0.1	0.01±0.0	0.02±0.0	0.63
	BB-3	96.8±2.3	2.0±0.6	0.4±0	0.4±0	0.3±0.0	ND	ND	0.1±0.0	ND	0.02±0.0	0.73
	BB-4	93.3±3.4	3.4±0.9	1.9±0.1	1.2±0.2	0.3±0.0	0.5±0.0	0.02±0.0	0.3±0.0	ND	0.03±0.0	0.78
Youpoue	YO-1	99.9±4.2	0.6±0.1	ND	0.3±0.0	0.1±0.0	ND	ND	ND	ND	ND	0.89
	YO-2	98.1±4.2	1.6±0.3	0.3±0.0	0.9±0.1	0.6±0.0	ND	ND	ND	0.02±0.0	ND	0.70
	YO-3	98.5±4.0	1.8±0.3	0.4±0.0	1.2±0.1	0.9±0.1	ND	0.04±0.0	ND	0.03±0.0	ND	0.91
Youpoue Bamend	YB-1	98.3±2.6	0.7±0.1	0.1±0.0	0.4±0.0	0.3±0.0	ND	ND	ND	0.01±0.0	ND	0.6

X-RAY FLUORESCENCE ANALYSIS

XRF-Results and Discussion: Elemental composition

a	YB-2	96.5±2.2	1.7±0.1	1.2±0.2	1.3±0.3	0.9±0.1	ND	0.07±0.0	ND	0.03±0.0	ND	0.74
	YB-3	97.2±2.4	1.1±0.1	0.7±0.0	0.8±0.01	0.8±0.0	0.2±0.0	0.03±0.0	0.6±0.0	ND	0.04±0.0	0.81
Bois-de-Singe	BS-1	98.9±3.9	0.8±0.1	ND	0.2±0.0	0.1±0.0	ND	ND	ND	ND	ND	0.45
	BS-2	99.1±4.1	0.9±0.1	ND	0.2±0.0	0.1±0.0	ND	ND	0.1±0.0	ND	ND	0.64
	BS-3	97.8±3.1	1.7±0.2	0.4±0.03	0.9±0.1	0.7±0.0	ND	ND	0.8±0.1	ND	ND	0.83
	BS-4	98.3±4.5	1.3±0.1	0.2±0.0	0.7±0.0	0.6±0.0	ND	ND	0.5±0.0	ND	ND	0.102
Min		90.0±2.15	0.6±0.1	ND	0.2±0.0	0.1±0	ND	ND	ND	ND	ND	0.59
Max		99.9±4.2	5.3±0.7	2.6±0.1	1.4±0.3	1.4±0.2	0.5±0.0	0.07±0.0	0.8±0.1	0.1±0	0.04±0.0	0.91
Average		95.51	2.68	1.11	0.75	0.41	0.33	0.04	0.34	0.02	0.02	0.73

In this study, the XRF presets was done, and the observed results allowed the grouping of detected elements or compounds in the analyzed sand samples into major and minor categories. As the most abundant elements found in all investigated sands are SiO_2 (with the mean value of $\sim 96\%$) and Al_2O_3 (with an average value of 2.4%), it shows that the levels of Si and Al measured can be exceptionally useful in subgroup definition and give valuable insights to the crude materials used for glassmaking in Cameroon.

5.4. Sample Classification and geological provenance

5.4.1. Samples from Campuses of the University of Douala

A positive correlation of K_2O and Al_2O_3 (Figure 5-13) infers that the concentrations of the K-bearing minerals have a noteworthy impact on Al distribution and suggests that the relative abundance of these components is basically controlled by the substance of mud minerals. Considering these proportions, all analyzed soil samples can be classified chemically as Fe-soil. The discriminant functions of Roser and Korsch [253–256] uses Al_2O_3 , TiO_2 , Fe_2O_3 , MgO , CaO , Na_2O , and K_2O elements as variables, intended to discriminate between four sedimentary sources: Mafic-ocean island arc; Intermediate-mature island arc; Felsic-active continental margin; and Recycled-granite, gneissic, or sedimentary. Using that discriminant function, the comparison confirmed that all the analyzed soil samples are originated from Continental margin [256, 257].

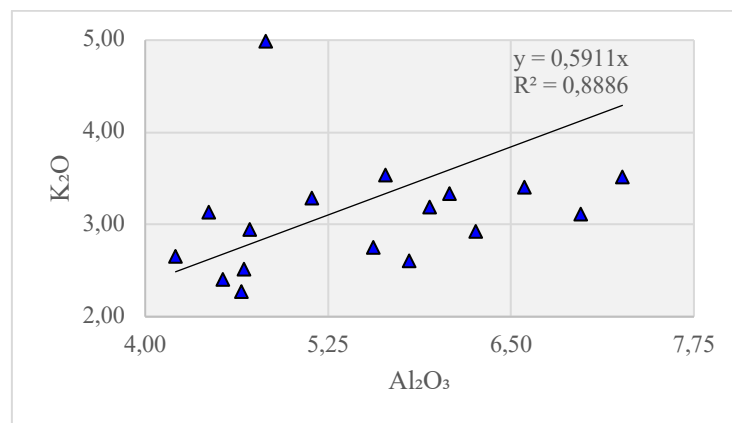


Figure 5-13: The positive correlation trend between K_2O and Al_2O_3 for the 18 investigated samples from the campuses of the University of Douala.

i) Soil Classification

As shown in Figure 5-13, the positive correlation between K_2O and Al_2O_3 concentrations indicates that the K-bearing minerals have a notable effect on the distributive presence of Al in the samples and highlights the relative abundance of these elements (compounds) in the fundamental control set by the mud mineral substance. Considering the concentration of Fe in soil samples, it is found that most of the samples analyzed can be chemically classified as Fe-soil [258–260]. The discriminant functions of Roser and Korsch is simply used to display the classification of different types of investigated soils [253]. The diagram used different variable oxide component concentrations as variables of the discriminant function: Al_2O_3 , TiO_2 , Fe_2O_3 , MgO , CaO , Na_2O , and K_2O [231, 261]. The purpose of using this feature was to show four distinct sediment provenances. The oceanic one so-called "Mafic-ocean island arc," the solid mainland one so-called "Felsic-active continental margin," the middle of the previous two highlighted called "Intermediate-mature island arc," and the last one, "Recycled-Granitic, Gneissic." The comparison performed confirms that all the analyzed soil samples are originated from Continental margin [231, 253]. These findings are further backed by low $\text{Al}_2\text{O}_3/\text{SiO}_2$ ratios

(as shown in Figure 5-14 and Figure 5-15) which permitted the classification of fewer samples as Litharenite (only two specimens) and Fe-sand or Fe-soil owing to the greater Fe_2O_3 concentrations found in the studied region (soil from other 16 sampling points) [254, 262, 263].

ii) Provenance

The previous discriminant function, the discriminant function of Roser and Korsch [253] use major compounds detected as variables. Provenance discrimination diagrams built using the major elements measured in the samples are not the most reliable because of the change, alteration, and high mobilization of the segment amid. Therefore, levels of trace components are very helpful and some suitable ones are used for sediment provenance and tectonic evaluation, compared to major compounds [258, 259, 261]. Their moderately low mobility in sedimentary procedures and their low residence time in seawater (elevated solubility and disintegration) are some factors that affect them. The element Ti is very helpful for evaluating this sort of component for determining the geological provenance of the samples studied.

Figure 5-15 reports the concentration ratio $\text{Al}_2\text{O}_3/\text{SiO}_2$ as a function of Fe_2O_3 and MgO (%) for the total eighteen analyzed samples from Douala and the so-called *diagram for the tectonic discrimination*, given in this section intends to discriminate the provenance of sediment where the investigated samples are originated from [260, 264, 265]. Description shown in Figure 5-15 indicates that the origin of the analyzed soil samples is likely to be the Passive Margin. Such results show that the alteration or erosion process was not heavily engaged in the studied region over the previous centuries, but in tectonic procedures and processes.

Different comparable studies conducted in other regions of the world have been examined in view to determine the provenance of the geological samples studied in the current study, and judge through comparison. It was noted from the outcomes that the Douala Basin samples were probably derived from the dismantling, weathering, and transport of raw materials present in the "Gulf of Guinea" [46, 266–268]. The erosion activities in the past could be counted as one of the effects of the geology observed today in the investigated region as well as in many of the world's coastal regions and large basins. On the remaining coastlines there are passive continental margins. Because there is no collision or subduction, tectonic activity is negligible, and the weathering and erosion processes of the earth are winning and are the effects that affect in a large extend the Douala Basin. Sand and rock from the Gulf of Guinea (known also as the Rio Del Ray Basin) are acid intrusive igneous (such as granites) and metamorphic rocks (such as gneiss, which contain about 20 percent of quartz). Therefore, the obtained results illustrated the existence of SiO_2 in analyzed soil samples at elevated levels, and justify the geological provenance deduced from the plotted diagrams [43, 268].

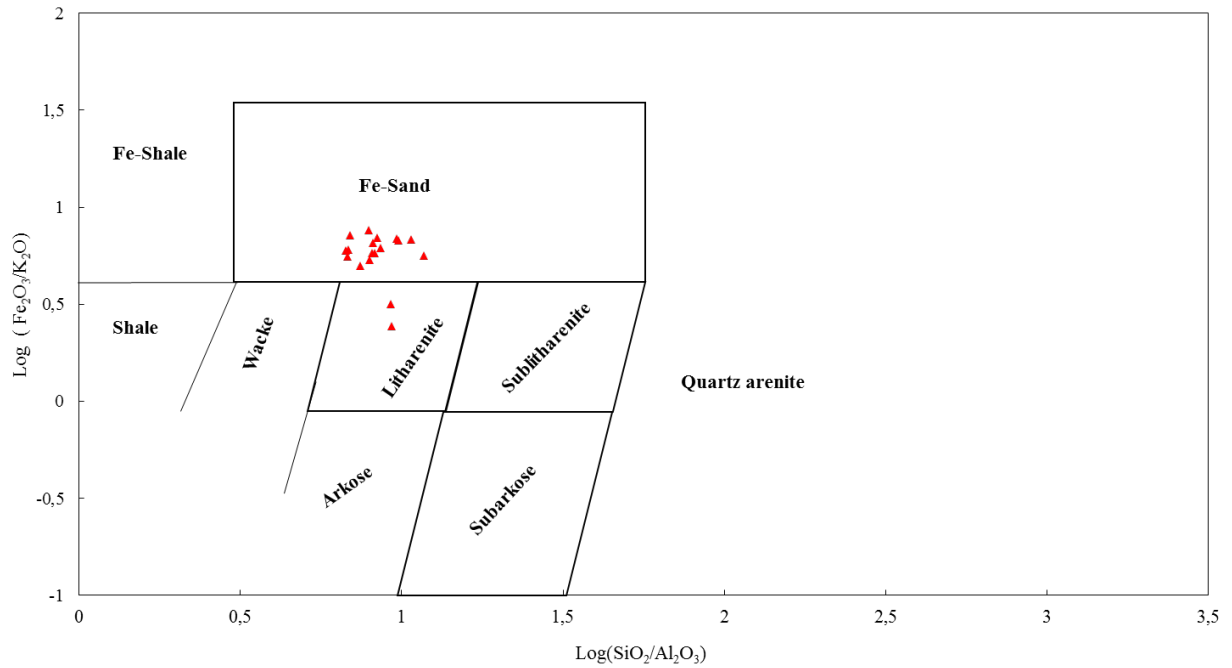


Figure 5-14. Diagram of chemical classification of the investigated samples from Douala – Bassa area based on binary diagrams; $\log (\text{SiO}_2/\text{Al}_2\text{O}_3)$ as a function of $\log (\text{Fe}_2\text{O}_3/\text{K}_2\text{O})$ diagram of Herron. Among the nine types displayed, the investigated samples are from two main types and the majority from Fe-sand type.

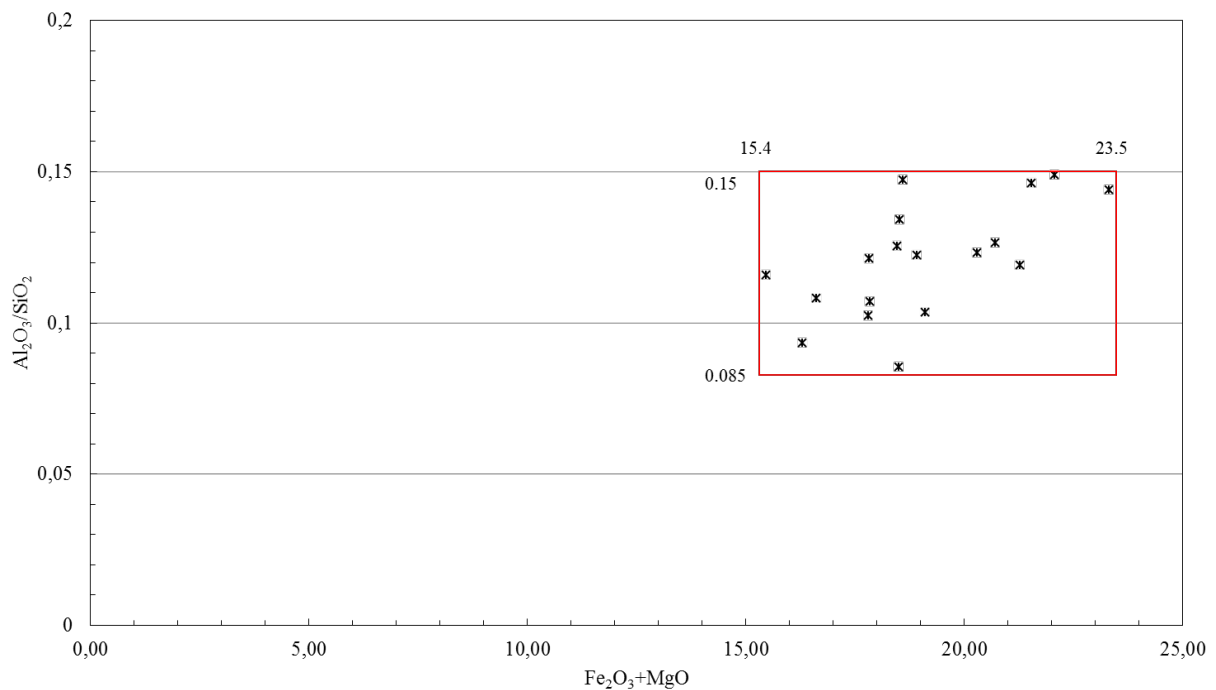


Figure 5-15. $\text{Al}_2\text{O}_3/\text{SiO}_2$ concentration ratio as a function of Fe_2O_3 and MgO concentration (%) for investigated samples from Douala – Bassa area (the so-called discrimination diagram of tectonic for the determination of sediment provenance).

5.4.2. Extending area of investigation (sand's quarries)

i) Sand Classification

K-feldspar and a few micas are attributed to the high ratio of K_2O / Na_2O to the generally regular proximity of K-bearing minerals [231, 257, 262, 269]. Figure 5-16 demonstrates a positive gradient in the correlation between K_2O and Al_2O_3 . This positive correlation between K_2O and Al_2O_3 as shown in Figure 5-16 suggests that the levels of K-bearing minerals have a notable effect on the distribution of Al in the samples from the investigated region and therefore, the relative influx of these elements (K_2O and Al_2O_3) is essentially regulated by the mud minerals substance [231]. Considering the Herron diagram as shown in Figure 5-17 and Figure 5-18, 37.5% of the studied samples were chemically categorized as subarkose type (samples from Northern Akwa site and from Youpoue Bamenda YB2 and YB4...), 12.5 % were categorized as Fe-sand (sand from Village site, and Bonaberi Bonamikano BB3) and 25 % were categorized as Subliarenite (sand from Bonaberi Bonamikano BB3). These findings are further supported by low Al_2O_3/SiO_2 ratios that made it easy to classify some other samples, the remaining 25 % as quartz arenites (sand from Dibamba D2, Youpoue Bamenda YB2 and YB3, and Bois de Singe BS3 and BS4...) [254, 262].

ii) Sand's Provenance

Due to weathering, alteration processes, and modification of the mobilization of the discriminant variables, the built provenance discrimination diagrams are not 100% reliable considering distinct variables as their mobilization. Major components are topics of real interest in this regard as some minor components in seawater have low mobility and low resistance and are then more reliable for provenance diagram than the major compounds. TiO_2 , Fe_2O_3 , MgO , and CaO are therefore the most suitable chemical components used to determine geological provenance and the required tectonic setting [258, 259, 261]. This argues and defends the weathering process ongoing in Douala and surrounding areas, which are located in the coast of the Gulf of Guinea. As a coastal area in a basin, the sedimentation process has been involved for years and the studied sand samples are products of this geological processes.

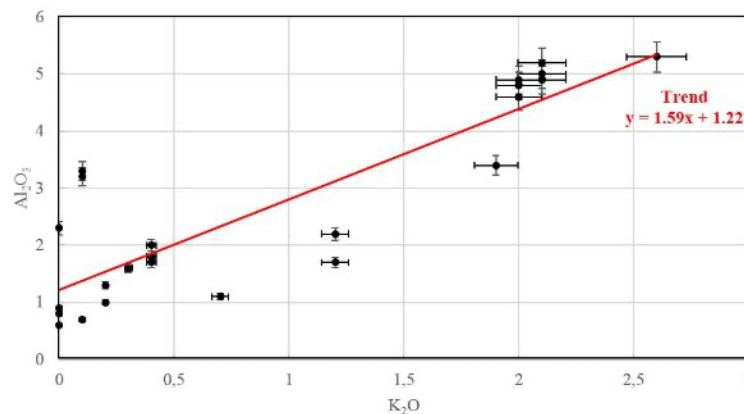


Figure 5-16: Positive correlation between K_2O and Al_2O_3 . The trend shows a regression line that implies relevant correlation between concentrations of both compounds.

Figure 5-19 reports the concentration of TiO_2 (%) as a function of $Fe_2O_3 + MgO$ concentrations (%). These values were compared with the well-known diagram for the tectonic discrimination of geological land or sediment provenance published by Bhatia [258, 260]. Comparison evidenced that all investigated samples are illustrative dragged from the Passive margin, as previously highlighted.

As shown on the figure, these data can be useful in developing models to understand the past weathering activities and try to develop simulation for the prediction of the future. It is also additional value for resource management as such data provides dedicated resource information. Figure 5-20 reports the concentration ratio $\text{Al}_2\text{O}_3/\text{SiO}_2$ (%) as a function of Fe_2O_3 and MgO concentration (%) and a diagram for the tectonic discrimination of sediment provenance which can be used to assess the origin of the geology in view to understand some processes undergoing in the research zone [260, 265]. This diagram demonstrates as a double-plot, that the investigated sands are residue from Passive margins. No doubt, results confirmed by both diagrams are subject of interest for geologists and for the government as useful data.

The examination of a set of bibliography was feasible in light to determine the provenience (geological) of the investigated area. Based on the obtained data, it can be observed that the investigated samples presumably emerge from the disassembly and movement of the material present in the “Gulf of Guinea” [46, 266–268, 270–272]. The remaining coastlines contain passive continental margins, as the investigated zone fall into the Wouri basin, which is part of the Rio Del Rey basin extended from the Cameroon coastline to the South America (Brazil) coastline. Since no collision or subduction occurs, tectonic activity is negligible, and the weathering and erosion processes of the earth have been increasing in the region under investigation. This results to a lot of low-relief (flat) soil developing both shoreline bearings, long river systems (Wouri, Dibamba, Mungo, Doctor Anse River and Atlantic Ocean), and the collection of thick piles of sedimentary trash on comparatively broad continental shelves [46]. The sand and rocks of the “Gulf of Guinea” are acid intrusive igneous as granite rock type and metamorphic as gneiss rock type that warrant elevated concentrations of SiO_2 and Al_2O_3 , while small concentrations of CaO , K_2O , Na_2O and MgO are noted because of their elevated solubility and low molecular strength in water as the annual precipitation level in the investigated region is really high [268, 270].

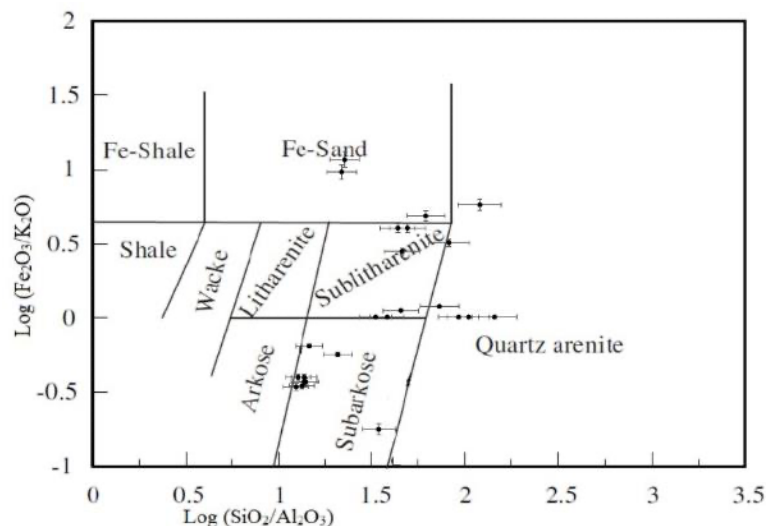


Figure 5-17: Chemical classification of analyzed geological samples from Douala and surrounding areas based on binary diagrams; discrimination plot of $\log (\text{SiO}_2/\text{Al}_2\text{O}_3)$ as a function of $\log (\text{Fe}_2\text{O}_3/\text{K}_2\text{O})$ diagram of Herron [271, 272]. Evidence of the 04 classifications of analyzed sand samples from a total of nine different types.

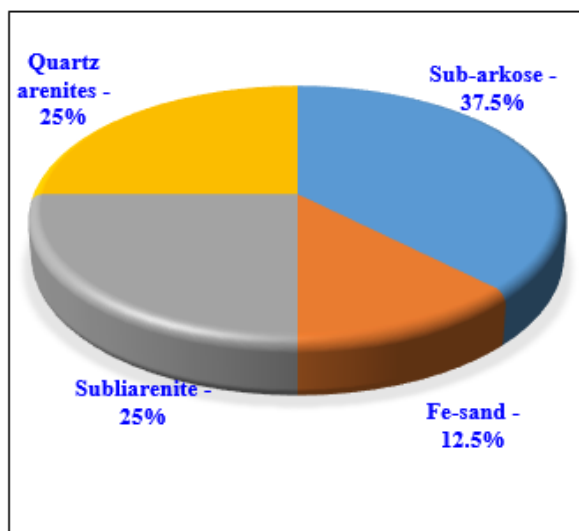


Figure 5-18: Diagram of Heron for the classification of different sample (in term of frequency), based on the only four types assessed in this project.

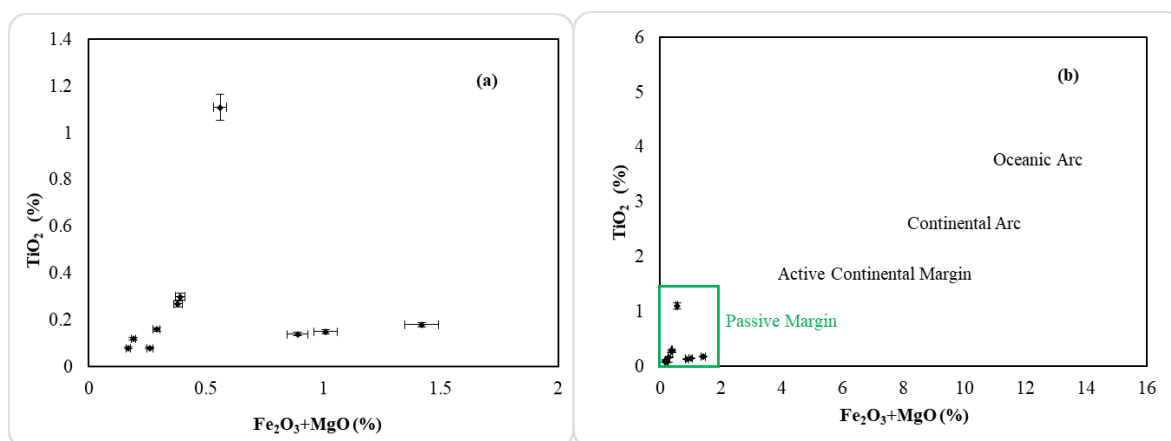


Figure 5-19: TiO_2 (%) as a function of Fe_2O_3 and MgO (%) for all investigated samples: (a) Normal scale for overall view; (b) high scale visualization with labelling display.

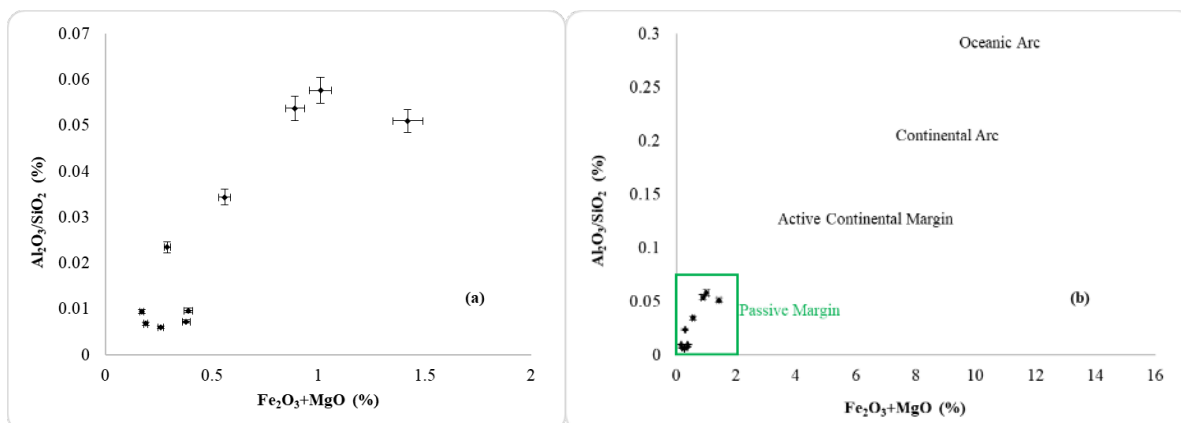


Figure 5-20: The diagram for the tectonic discrimination of sediment provenance based on Al_2O_3/SiO_2 concentration ratio as a function of Fe_2O_3 and MgO concentration (%) for all investigated samples points: (a) Normal scale for overall view; (b) high scale visualization for labelling display.

These results respond to our expectations as the Gulf of Guinea is part of the Atlantic Ocean's passive margin, closes the Central African Equator. The Gulf of Guinea is defined by the existence in Cameroon of a volcanic field forming the oceanic segment of the active Cameroon Volcanic Line (CVL), a line extending over 1500 km from the Atlantic Ocean to the continent of Africa with its oceanic segment highlighted by the following volcanic islands: Bioko, Principe, Sao Tome, Annobon. The CVL continental segment starts at Mt Cameroon (4100 m), which has been the primary active volcano along the CVL since the 19th century with at least 17 eruptions. The geology of the Gulf of Guinea is completed by sedimentary formations that are presently under exploitation (hydrocarbons and oil exploration) [270–273]. Thomas Schluter explains the previous outcomes as follow: the offshore basins of Douala and Rio-del-Rey are typical passive margin basins that started in the midst of the Atlantic Ocean, boarding Cameroon mainland. They created a continuous sedimentary basin stretching from cretaceous to Miocene times, expending from Nigeria to Southern Cameroon [273].

5.5. Conclusion

XRF analysis based on both WDXRF (Wavelength Dispersive X-Ray Fluorescence) and EDXRF (standing for Energy Dispersive X-Ray Fluorescence) spectrometry methods were performed to characterize different soil and sand samples from Douala-Bassa area covering the campuses of the University of Douala and quarries in the city and surroundings. The characterization consisted of elemental composition investigation of different samples using both an ARL PERFORM'X spectrometer for WDXRF measurements (that uses the package OXSAS v2.3.1 as analysis software) and an SDD spectrometry chain (Silicon Drift Detector, SDD123) for EDXRF assessment. The most important part of the elemental investigation was carried out using the PyMCA software package, for the case of EDXRF investigation. Both WDXRF and EDXRF elemental concentration of different elements and compounds obtained in this study are useful to characterize the soil samples from the Douala – Cameroon.

Spectra from the eighteen soil samples revealed that measurements were performed in an appropriate manner and the region of interest formed by picks in spectra facilitate the data assessment. The plot of correlation between K_2O and Al_2O_3 shows a positive gradient between the two compound's concentrations. The obtained positive slope suggested a relative abundance of these components that are basically adjusted by the substance of mud minerals. As the investigated area is part of the Douala-Bassa area, an area in the Douala Basin, these data could be justified by the presence of sedimentary basin. This fit the assumptions and expectation set three years ago when designing and adjusting the research project. It also proved that analyzed samples have the same origin and provenance (according to the obtained concentration values of Al_2O_3 , TiO_2 , Fe_2O_3 , MgO , CaO , Na_2O , and K_2O). The investigation intended to draw the discriminant functions of Roser and Korsch [253] allows the classification and the geological provenance of the analyzed soil samples and the following conclusion had been drawn. The investigated site geology can be classified chemically as Fe-soil. All analyzed soils are illustrative dregs from Continental margin as it was discussed previously.

In addition, the elemental characterization of samples from the extended study site (quarries in the economic capital city of Cameroon and its surroundings) was performed through both EDXRF and WDXRF. This was done in view to determine their elemental composition, and the concentration of major and minor compounds as well as trace elements found were presented in tables (the obtained results). Additional data were presented based on color graph plotting, which allow an easy visibility of the packed concentration site by site in the investigated area, displayed on spectra. From the obtained results (tables and different diagrams), it was observed that the investigated area's geology is formed by sediments from Passive margins and probably come from the degradation (or weathering) of materials of the "Gulf of Guinea", where the main characteristics of the rocks are acidic intrusive igneous and metamorphic. Important notice is that the Gulf of Guinea (where the study area fit within)

is defined by a diverse geological environment comprising volcanic islands presently under severe subterranean operations (hydrocarbons exploration and well-logging) with sedimentary formation. Even though these activities can affect the environment under investigation, it is important to relate human activity to the undergoing natural processes only if the background studies were performed prior human actions. In this regards the obtained data will likely be useful insights for future investigation, not as a pure background, but as control data.

Their characterization as sediments from passive margin confirms the fact that the plate of the Douala basin belongs to an active one because it was built by the sedimentation of an ancient rift determined by a transitional lithosphere. The basin is thus considered as a transition between oceanic and continental lithosphere. X-Rays Spectrometry results showed important value of different element and compounds, both major and minor. This chapter leads to important knowledge for the elemental characterization of samples. It also helps to clearly differentiate the application of X-ray, from atomic origin to that of γ -ray, from nuclear origin.

Future Investigation

As XRF was used for the characterization of the studied area, it is important to compare the method to other similar procedures. The combined and simultaneous use of PIXE (Particle Induced X-ray Emission) and PIGE (Particle Induced γ -ray Emission) techniques for the analysis samples will be implemented in the future. The primary goal will be the assessment whether both methods are time and cost effective efficient for geological sample assessment and environmental monitoring. The efficiency and accuracy of both methods will be compared to the XRF analytical procedure. Interest on these nuclear technics has been shown with experiments performed on the samples from Douala. The analysis and interpretation are one of the perspectives of this thesis.

CHAPTER 6. MONTE CARLO METHOD AND GEANT4 TOOLKIT

6.1. Introduction

The Monte Carlo methods are known as statistical random numbers-based calculation, in a simplest way. As numerical techniques, the Monte Carlo (MC) methods are statistical techniques of simulation where statistical simulation represents any technique that uses random number sequences to achieve the simulation [274–276]. The Monte Carlo simulation is now used in various fields of activity from the simulation of some complex physical events such as the transport of radiation in the earthly atmosphere and the sub-nuclear processes that happen at high energy to the simulation of a video game. The method is intended to solve problems that are deterministic in principle. They are the key to solve some problem that are not solvable by other ways for providing an analytical reliable solution. In addition, Monte Carlo methods are used in physics and mathematics to solve problems with a large degree of freedom, model phenomena with significant uncertainties in inputs variables or parameter, and to solve any problem that have probabilistic interpretation. This chapter will not discuss the Monte Carlo method in general, as the method is applicable in various field, but that relates to the context of this project, the transport of photon throughout a medium [22].

In the Monte Carlo calculation, quantities of interest for the application are computed through statistical sampling of interaction processes. A Monte Carlo algorithm implies that the physical system is described by the function so-called “probability density function” which allows the generation of random number for each step and multiple times, and the result is taken as an average of numbers which were observed (the final result is the median of different results obtained from repetition of the process). As some problem cannot be solved analytically, scientist in the previous century were interested in solution behavior instead of looking at the deterministic solution itself. For this reason, for example, radiation particles that are emitted spontaneously and follows the decay law cannot be counted or analytically estimated exactly for a given time. The statistical fluctuation needs real measurement instead of prediction based on a simple equation of exponential decay. The observation highlighted some issues that need to be approached, not analytically, but in a different way. It may be essential to move to a Monte Carlo method to offset these problems (as it was done in the previous century). To achieve numerical outcomes, computer algorithms based on this technique depend on repeated random sampling. It enables a smooth definition of physical parameters for more precision in the final result during particle transport. In addition, this technique is especially appropriate for multi-particle transport issues and complex geometries involving multi-materials and different densities. In the following paragraphs, the technique applied to particle transport in Monte-Carlo is detailed in terms of application in radiation protection codes and characteristics and dosimetric issues. Special details are given for γ spectrometry only (with γ particle interaction with matter). It has become crucial to use computer codes to predict the different radiometric and dosimetric amounts earlier identified and that are part of this project. This works with numerical calculation techniques with approximations that influence the true value of the required quantities under investigation.

A Monte Carlo computation therefore, involves running a large number of occasions of particles until some worthy statistical uncertainty of the desired calculated quantity has been reached. Γ -ray spectrometry is a non-destructive method used in nuclear physics to analyze γ -ray emitter radionuclide quantitatively and qualitatively and the MC methods in this chapter are combined with, to provide efficiency calibration method in the spectroscopic laboratory. This assessment is carried out by

calibrating the detector, counting, and evaluating the individual photo-peak emitted from the sample [2, 102]. Building a Monte Carlo application for radiation detection is not an easy task as there are dozens of data and code portions to be involved. For example, for a single photon transport in a room, there is a need to build the geometry both of the room and the γ path if it has to penetrate the room from somewhere else; describe the physical processes that depicts the behavior of the γ in the room; and the generation of the γ at least. The physics includes more than the equations described in chapter 2 and 3 of this report, not simply written but transformed in a code. As a result, it is important to use pre-built application to build our own Monte Carlo code for a particular simulation in radiation detection. GEANT4 toolkit-based simulation offers more data on the latest γ -ray spectrometry technique. As photons can interact with matter through the photoelectric effect, Compton scattering, pair production, or Rayleigh scattering, and the likelihood of each type of interaction depends on energy, many scientists set a path for the equations to be used: among them, there are Baro et al., Biggs and Lighthill, Born, Butcher and Messel, Ford and Nelson, Gavrila, Grichine et al., Heitler, Hubbell et al., Kenneth, Messel and Crawford, Rossi, and Berger [36, 38, 85, 88, 91, 277–281, 59, 60, 67, 68, 79–82].

The physical processes were directly simulated with one condition to define the system's behavior: the system must be defined by the probability density function, which is the key point for the simulation using MC methods. The description of the probability density function is the sensitive part as the result depends on. If the function is well-known, the Monte Carlo-based simulation can proceed to generate random number from the probability density function. Monte Carlo simulation is regarded as a new method for assessing environmental radioactivity in γ -ray spectrometry [2, 23, 281]. Furthermore, when coupled γ -ray spectrometry to the Monte Carlo simulation based on GEANT4 code, there are many advantages that advance the science. This technique reduces the high price and risk associated to the use of radioactive sources to calibrate the detectors and is nowadays a significant assignment that favors the creation of MC techniques. If successful, in the event of efficiency calibration of HPGe, the geometry built by MC simulation can be very helpful as it is likely to be shape-adjusted to fit the sample geometry for example. The validation of this technique has been proven by studies carried out globally and worldwide [27, 33, 42, 110, 142, 173, 282–284]. Therefore, many labs found out that the calculated values acquired with MC simulation differed considerably from the experimental values and even vary from one laboratory to another. This interest is due to the problems experienced during the detectors' experimental calibration, as well as the statistical nature of the study.

6.2. State of the art

Different scientists and researcher all over the world had been using different codes as MCNP and MCNPX to compute the detection efficiency of the γ detector (high purity germanium detector and scintillator, but the first one is the type used in the present project). The following description highlights some key progresses in the field, achieved by other studies.

- Akkurt study the sodium Iodine detector. He used MCNPX code in his simulation and the obtained results for NaI(Tl) detector system were compared to result from experimental study carried in parallel [23]. While comparing the simulation result of his work to experimental data, he found good agreement between MC calculation-based MCNPX code and experiment.
- Furthermore, detector performance as well as geometry based on GEANT4 code performed by some researchers discovered this technique to be a very helpful option, which also offers higher flexibility in detector response and measurement efficiency [26, 30, 42, 53, 110, 130, 141, 142, 173, 283, 285–297]. Valuable insights are in some case, the agreement between ex-

perience and simulation, in others the risk reduction and the time saved for routine process usually performed in the laboratory.

- Britton [286] developed from 2012 to 2015, during his PhD project, a full GEANT4 model for the simulation of a broad-energy germanium detector. The project covers other detector's type and not only the efficiency was regarded as subject of concern to be improve, but also Compton suppressed method. After performing Monte Carlo simulation for a particular detector, the obtained data were compared to the experimental ones. The results from the comparison highlighted 3 % accuracy within 95 % confidence level, for γ -ray lines, covering the energies between 30.00 and 3,000.00 keV.
- Gang Li conducted an efficiency correction survey to determine the ^{137}Cs concentration in environmental soil samples using the comparative measurement method and GEANT4 simulations [289]. The GEANT4-based simulation he carried out was found to be in agreement with experimental data and the GEANT4 code he built was validated.
- Hurtadoa used the GEANT4 toolkit to simulate Ge detectors response in low-level (low background or well-shield detectors) γ spectrometry. Also, the comparison of the computed values with the experimental data was done. It was discovered that both experimental data and result of simulation were in agreement with the confidence limit of 10 % [291].
- Chagren used the CERN GEANT4 code to calculate the peak efficiency of γ -ray spectrometry in High Pure Germanium [287]. As a result, his calculation is a reference data-based research for peak efficiency assessment in γ -ray spectrometry.
- Jelena Nikolic performed Monte Carlo simulation for calibration of three different HPGe detector types: The Closed coaxial - p type Canberra with Al entry window, the closed reversible coaxial - n type Canberra with Be entry window, and the Closed coaxial - p type Canberra with Be entry window. As previous cited authors, he used the GEANT4 toolkit as base for his application building while EFFTRAN software was used for efficiency transfer computation [293].
- Saed Dababneh used GEANT4 to carry out crucial adjustments in close geometry for self-absorption and real coincidence summing in environmental sample assessment based on γ -ray spectrometry measurement [141].
- To calibrate two HPGe detectors, Nikolic implemented GEANT4 simulation to evaluate liquid and soil-like samples in barrel shaped geometry [295].

These researchers have demonstrated the precision and accuracy of the GEANT4 toolkit in the calibration of γ -ray spectrometry detectors as the overall comparison between simulation and experiment was, for the most part, found to be less than 10% within 95 % confidence limit. The difference is due in part to distinct detector parameters that differ from date to date and can be more optimized from the simulation point of view than that of the experiment. Therefore, more attention needs to be paid to simulating different detector models to enhance scientific cooperation between different team's work, sharing methods and code developments and improvements, and finally promote the involvement of scientists from developing countries in conducting environmental radioactivity research without any expense of purchasing multi- γ radioactive calibration sources in developed countries. For examples, there are GEANT4 schools every year all over the world, but it has not been yet

organized in sub-Sahara region, even though there is a real need in Cameroon as well as in the sub-region (Central Africa). Interestingly, no or very little attention has been paid to simulating a wide energy germanium detector, particularly the model BE6530 used for low background measurement. Nevertheless, LabSOCS and ISOCS calibration software have been developed to facilitate calibration based on Monte Carlo algorithms in view to facilitate the efficiency calibration procedure for characterized detector. These MC calibration software have been using in the laboratory of spectrometry of the NRPA in Cameroon for detector efficiency calibration purposes [14, 149, 298].

The present chapter aims to present developed Monte Carlo methods and principle related to γ -ray metrology. The theory of the GEANT4 toolkit is associated to the description of the Monte Carlo algorithms used, but only the part related to γ metrology is the subject of interest in this chapter. The analytical development performed here are done with mindful intention to facilitate the efficiency calibration of the broad energy germanium detector type BEGe-6530 used in the laboratory were experiments were carried on. As the calibration of BEGe was intended for environmental samples assessment, the model was built for an axial detector. As the next chapter will present main result obtained based on the development of this chapter, a full GEANT4 model of the broad-energy BEGe detector will be presented with different views of the geometry construction and efficiency curves.

6.3. Monte Carlo Method

A Monte Carlo calculation comprises a run of an extensive number of particle occasions until some worthy statistical uncertainty of the coveted computed amount has been reached. It is though a demanding computational method as it requires large number of particles and complex probabilistic equations used to describe the particle “motion” in the geometry defined. These individual events sequentially computed on a single CPU framework or keep running in parallel on a CPU cluster are generally called particle histories. As a broad class of computational algorithms that rely on repeated random sampling to obtain numerical results, Monte Carlo methods for real problems usually relies on computers for calculation as it cannot be timely achieve by human hands.

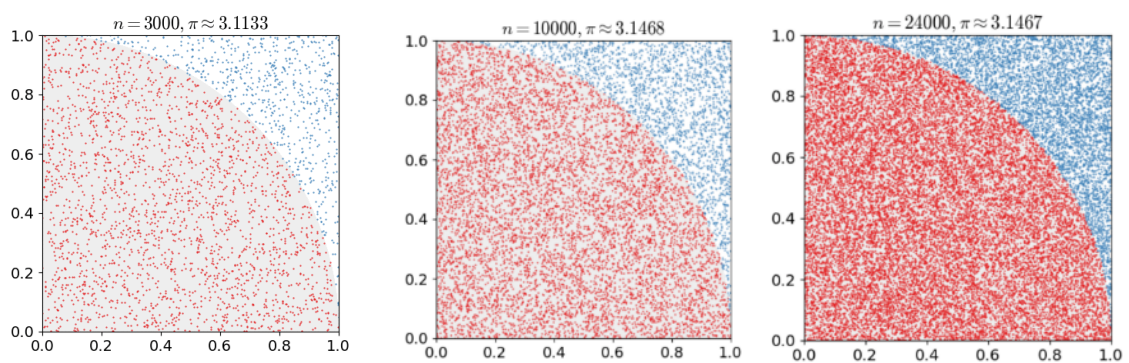


Figure 6-1: Monte Carlo method applied to approximating the value of π (real value is given by $\pi = 3.1415926535897932384626433832$ with 28 decimal characters). As a statistical method, the accuracy of the result obtained depends on the number of particles generated and tracked.

A simple example of Monte Carlo application is given in the Figure 6-1, where the value of π is computed using a quart of a circle. While throwing arrows on the square surrounding the $\frac{1}{4}$ circle, it is possible to estimate the value of π by counting the number falling on into the circular part of the geometry and the total falling into the overall geometry (here, the square). The physical processes are directly simulated with one condition to define the system's behavior: the system must be defined by the probability density function as mentioned previously. The Monte Carlo simulation can be pro-

ceeded, if this function is known, by generating random numbers from the probability density function. The outcome is an average of different figures observed as outputs of the simulation. It is a very important task to limit the high cost and risk associated to the use of radioactive sources while calibrating detectors [276, 281, 299]. Many studies performed nowadays as those described in the section entitled "State of the art", were done to facilitate radiation detection measurement. Prior to the governing equations description, it is crucial to describe the concept of MC applied to radiation transport.

6.3.1. Principle Monte Carlo Methods Applied to the Radiation Transport

Figure 6-2 presents the flow chart of the calculation process of the Monte Carlo method used for the transport of particles (as electrons, proton, neutron, heavy charged particles in some cases, and photon, the case adapted to this project). The general concept is explained as a large number of particles are produced by a random source and their trajectory and "history" will be probabilistically determined. There are different steps involved, but the description will be given on those contributing mainly to γ interaction processes with the detector material.

- First, a random selection routine code assigns a set of initial parameters to each particle derived from the source (spatial coordinates x, y, z ; release direction u, v, w ; energy E ; time t if the calculation includes time dependence or the four temporal-space coordinates described by Einstein in the relativity concept $[x, y, z, ct]$ where c is the light speed in the vacuum). These parameters' values are "selected" from the spatial probability distributions, direction, energy, time, and momentum.
- The source is therefore defined by a sampling of computer-generated random number distributions [276, 278, 282, 295, 300]. Such a random selection method to characterize the physical intrinsic parameters in the particle transport is indeed the foundation of the Monte Carlo method.
- The next stage consists of selecting the particle transport length to be achieved before the particle interaction with the medium. This length is described as the "mean free path" and is expressed in distance units. It varies from one particle type to another and is energy-dependent parameter.

An input file (or so-called built code) defines the source geometry, materialized areas, detectors, and system boundaries. All these variables are defined to reflect the real geometry in the laboratory where experiments are carried on. For various nuclear materials and interactions that can be found in the scene, cross-sections and physical models are introduced and are essential part of the simulation as each transported particle has its own probabilistic behavior throughout the medium. A path calculation algorithm uses the mean free path of the particle acquired from interaction cross-sections in the medium to determine the spatial coordinates of the collision point. For example, when a photon of a particular energy interacts with a medium, the interaction probability of a particular process is energy dependent: A single photon born from the decay of U-238 (with average energy ~ 186 keV) will never achieve pair-production process. When the interface between two media is crossed, at the crossing stage, the coordinates are calculated to follow the particle's path. If the system's outer boundary exists, the particle disappears and that's the end of its history: in the GEANT4 or MC language, it is usually said "one stops tracking the particle". Then a new source of particles is attracted and monitored again until his death. The process is repeated many times (millions of times, billions of times or more for accurate result with less uncertainties). The calculation ends when the tracking of all the particles produced from sources and secondary particles is achieved [53, 104, 301].

The particle may be engaged in one or more collisions during transportation, as it is usually the

case for photon transport in all medium except for the ideal vacuum. An algorithm for collision chooses whether the particle is scattered or absorbed. This selection process is one of the most important steps in the metrology of γ -ray interaction, for the full absorption of the photon will contribute to the characteristic spectra of a radionuclide. The scattering nucleus and reaction type (elastic or inelastic response) are sampled in turn, following the previous step. If the distribution is selected, the scattering angle is selected by a collision routine using a random number to calculate the scattered energy and the direction of the fixed laboratory coordinate system is transformed. The code returns to the calculation algorithm at the path length step. And the particle's history continues throughout the system till the particle is killed or escapes the system. Quantities of interest are calculated then based on the outcome of the simulation: it could be the number of particles that undergo a specific type of interaction, the energy, or a correlation between both. The outcome is achieved by averaging the scoring on all the source-drawn particles generated in the system. The result cannot be 100 % accurate and must be accompanied by statistical uncertainty as it is in the experimental measurements due to several parameters [53, 76].

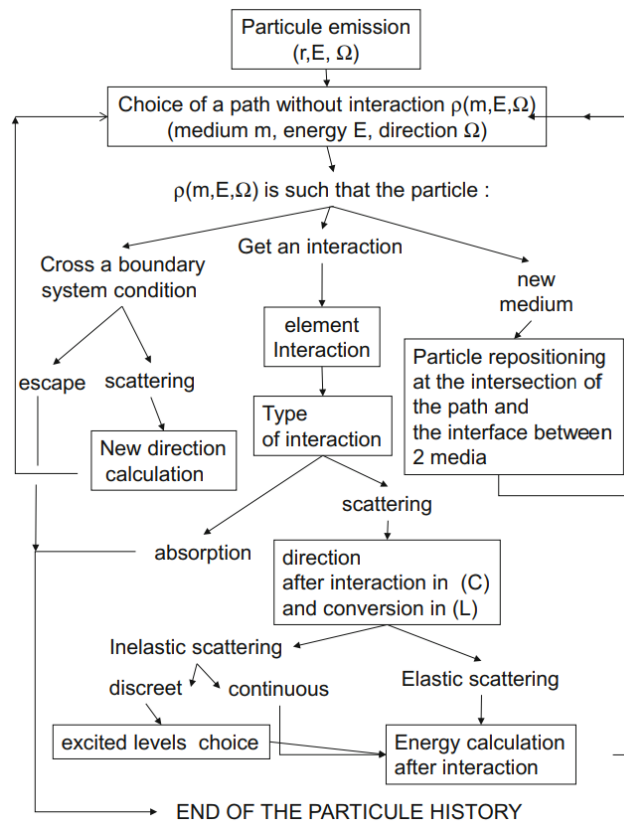


Figure 6-2: Monte Carlo based algorithm for particle tracking in a system to be assessed. The particle track starts at particle generation or emission to its death (total absorption) or escape from the system [103, 302–304]

6.3.2. Random Number Generator

The cornerstone of the Monte Carlo method is the random number selection principle. To perform the sampling on the different probability densities of the different physical parameters of the transport characteristics of a particle in the material, it is necessary to generate sequences of random numbers. A random number generator function was defined for this purpose in the previous century [305]. A well-known and worldwide-used technique is based on the linear congruence approach [95, 103, 274, 302–305] is generally used to generate these random numbers. Many other methods are available, but

the concept is not deviating that much. In the strategy referred to previously, the concept is to produce a series of random X_n integer so that the following inequality can be observed and always be verified:

$$0 \leq X_n \leq m \quad \text{with } m \in \mathbb{N} \tag{6-1}$$

Random numbers with values range from 0 to 1, are then defined by the following equation and inequality (6.2):

$$\xi_n = \frac{X_n}{m} \quad 0 \leq \xi_n \leq 1 \tag{6-2}$$

The random sequence of integers is obtained through the recurrence relation (6.3). It is also known as the congruence modulo relation, as defined in arithmetical mathematical relations.

$$X_n = (aX_{n-1} + b) \pmod{m} \quad n \geq 0 \tag{6-3}$$

This relation can be rewritten as the following equation:

$$X_n = aX_{n-1} + b - mk_n \tag{6-4}$$

where k_n is the largest positive integer $\left\lfloor \frac{aX_{n-1} + b}{m} \right\rfloor$;

m is the upper module 0;

a , the multiplier is a number defined between 0 and m ; and

b the increment, also defined between 0 and m . The first value of the sequence X_0 called “random seed” is set as an integer value between 0 and m and is regularly used in MC method. The relations described in this section are known as the basis of the Monte Carlo methods principle or random number generator, the number that defines the method being used.

The previous equations could be easily understood by an explicit demonstration. For example, let us characterize the module 5 sequence with multiplier, increment and seed set at 3 and the random numbers associated [95, 305]. The following relations then describe all the meaning and associated comprehension behind the congruence modulo relation or the random number generator. These relations are summarized and the full description can be found in the literature [82, 86, 103, 305].

$$\left\{ \begin{array}{l} X_0 = 3 \\ X_1 = (3 \times 3) + 3 - 5 \left\lfloor \frac{(3 \times 3) + 3}{5} \right\rfloor = 2 \\ X_2 = (3 \times 2) + 3 - 5 \left\lfloor \frac{(3 \times 2) + 3}{5} \right\rfloor = 4 \\ X_3 = (3 \times 4) + 3 - 5 \left\lfloor \frac{(3 \times 4) + 3}{5} \right\rfloor = 0 \\ X_4 = (3 \times 0) + 3 - 5 \left\lfloor \frac{(3 \times 0) + 3}{5} \right\rfloor = 3 \end{array} \right. \Rightarrow \left\{ \begin{array}{l} \xi_0 = \frac{3}{5} = 0.6 \\ \xi_1 = \frac{2}{5} = 0.4 \\ \xi_2 = \frac{4}{5} = 0.8 \\ \xi_3 = \frac{0}{5} = 0.0 \\ \xi_4 = \frac{3}{5} = 0.6 \end{array} \right. \tag{6-5}$$

A sequence in MC methods usually includes $m-1$ random numbers; it requires the biggest module to get the greatest possible frequency. Typically, the maximum size of a "word" can be reached in a computer numerical sense, as the computer uses bites for information processing: for a 32-bit machine,

the module would be $m = 2^{32}$ or a sequence of $2^{32}-1 = 4.3 \times 10^9$ random numbers. It relates more specifically to pseudo-random numbers as they are produced by recurring analytical expression. But as new advanced computer systems are developed, this number became insignificant. Clusters are usually appropriate for intense Monte Carlo calculation, for the generation of billions particles that can be tracked for a month depending on cut-off set [95, 305].

6.3.3. Monte Carlo Methods context

Monte Carlo techniques are computational calculations in view of random sampling to get reasonable statistical results that are closest to the real solution. The method was initially developed and presented for Nuclear Weapons program known as the Manhattan project, in 1940s. Nowadays, Monte Carlo algorithms are broadly utilized as a part of tools appropriate in many fields, for example chemistry, atomic, material and nuclear science, dosimetry, economics, telecommunications, and PC games... etc. With the creation of computer methods, Monte Carlo (MC) techniques have been increasingly used in many fields to identify or solve problems that cannot be really understood with classical analytical techniques or that analytical resolutions are beyond man hand used. It is important to consult the publications of Butcher and Messel, Messel and Crawford, or Ford and Nelson for a full record of the MC methods [36, 38, 61, 87]. In the case that we wish to sample x in the interval $[x_1, x_2]$ from the appropriation $f(x)$, the normalized probability density function can be expressed as:

$$f(x) = \sum_{i=1}^n N_i f_i(x) g_i(x) \tag{6-6}$$

where $N_i > 0$;

$f_i(x)$ are normalized density functions with the variable x defined in the interval $[x_1, x_2]$; and

$0 \leq g_i(x) \leq 1$.

Most numerical sets with the ability to include the generation of random numbers can also produce random numbers with other distributions of probability such as Poisson or Gaussian distributions. The advantage of such distributions is that the coveted probability distribution conveyance is given by the bundle, that execution should be utilized, in light of the fact that it is probably going to be much more productive than a self-coded calculation [35]. Also, the use of predefined, tested, and validated probability density functions allows the achievement of a short-term project (05 years for example). As indicated by this strategy, x can be tested using MC method based on the following algorithm (for example, if we want to evaluate the value of π):

- i. Select an arbitrary number x_i in the interval 0 and 1 . This random number denote a point on the x pivot.
- ii. Evaluate the related y coordinate y_i , which lies on a hover with x_i as the x coordinate

$$y_i = \sqrt{1 - x_i^2} \tag{6-7}$$

Pick a random number, r_i , in the interval $[0, 1]$. Check whether this number is less than or equal to y_i . On the off chance that $r_i \leq y_i$ then the point (x_i, r_i) exists within the circle: this event is known as a hit. Otherwise, it is considered as fail event [95, 305–307].

- iii. The repetition of this sequence many times unmistakably ‘paints’ or ‘tests’ the area with random points, and clearly for a large number of events the quotient of the region under the cir-

cle and the aggregate range measures up to the quantity of hits partitioned by the aggregate number of events.

$$\frac{A_{Circle}}{A_{Total}} = \frac{N_{Hits}}{N_{Events}} \tag{6-8}$$

Since the area of the quarter circle is $\pi/4$ and the total is 1 in this case, it can be estimated that the number π is

$$\pi = 4 \frac{N_{Hits}}{N_{Events}} \tag{6-9}$$

The evaluation of the value of π can be explain in the following table (Table 6-1) [22].

Table 6-1: Evaluation of the value of π and the precision and accuracy of MC methods used for its evaluation

N	π
10	3.20
100	3.08
1,000	3.2040
10,000	3.1356
100,000	3.1406
1,000,000	3.141221
1,000,000,000	3.14159218
π	3.14159265359

Inversion Monte Carlo method

In this situation, the probability distribution function $p(x)$ is considered, with the aim of producing random numbers after this distribution function. The function is the monitor or the law that the method is built on. This is the MC technique used for simulating the passage of particles through matter in nuclear physics. As a functional case, estimation of the connection purpose of a photon along a path will now be considered. The probability that a photon is not interacting is [95, 305]:

$$p(x) = \mu \cdot e^{-\mu x} \tag{6-10}$$

x = coordinate along the path;

μ = interaction coefficient.

The total distribution function has been figured utilizing the reversal MC method [35], and the outcome is the integral of $p(x)$ as described in the following equation.

$$P(x) = \int_0^x p(x') dx' = 1 - e^{-\mu x} \tag{6-11}$$

$$r = P(x) = 1 - e^{-\mu x} \tag{6-12}$$

This condition can be rearranged logically as follow:

$$\begin{cases} e^{-\mu x} = 1 - r \\ -\mu x = \ln(1 - r) \\ x = -\frac{1}{\mu} \ln(1 - r) \end{cases} \quad 6-13$$

If r is a random number in the interval $[0, 1]$ then $1 - r$ is likewise a random number in the same interval. Thus, we can rewrite x as:

$$x = -\frac{1}{\mu} \ln(r) \quad 6-14$$

The Monte Carlo method used the mathematical development of cross-section when related to the radiation interaction with matter. This is in accordance with different sampling functions used in simulation [22, 35, 89, 305]. The main descriptive equations are those presented in the section “T-ray interaction with matter”, in the Chapter 2.

6.3.4. Sampling a Discrete Distribution, Application to Choose the Type of Collision

How the random number between 0 and 1 is used to select one of the discrete events of the distribution of probability is explained in the following description: the case of a photon that can interact with matter through photoelectric effect, Compton scattering, or pair production is regarded as an instance and is the whole appealing interest. The probability that a specific mode will interact is defined in the following equations [95, 305]:

$$\begin{cases} p_1 = \frac{\sigma_{pe}}{\sigma_t}; \\ p_2 = \frac{\sigma_c}{\sigma_t}; \\ p_3 = \frac{\sigma_{pp}}{\sigma_t}; \\ \sigma_t = \sigma_{pe} + \sigma_c + \sigma_{pp} \end{cases} \quad 6-15$$

$$\sum_{i=1}^n p_i = 1 \quad 6-16$$

In this case, $n = 3$ as referred to the three-interaction process described for γ photon.

Let us consider arbitrarily a case where $p_1 = 0.2$, $p_2 = 0.5$, $p_3 = 0.3$. The discrete probability distribution of a particular effect can be represented as shown in Figure 6-3. This representation reflected the previous equation as the γ -ray interaction is described in term of probability. It will also define the cumulative probability as (6.5), which could be translated as the probability of getting a value $i < j$. The equation is simply written as following:

$$P(i < j) = \sum_{i=1}^j p_i \quad 6-17$$

According to the photon interaction type, Figure 6-3b provides a schematic representation of the cumulative probability distribution [95, 305]. Both figures (a) and (b) are for the same purpose and

describe the same content in different manners. Now, if a random number ζ is generated such as $0 < \zeta < 1$ and is assigned to the result of the cumulative probability distribution, the following relation is verified if the k^{th} interaction is selected:

$$P(k-1) < \zeta < P(k) \tag{6-18}$$

For example, for the problem we highlighted in the previous paragraph, if the random number sampled leads to $\zeta = 0.35$, the corresponding interaction is the Compton effect, as shown in Figure 6-3b. And if the random number sampled is $\zeta = 0.1$, the corresponding interaction is photoelectric effect. It is then reasonable to generalize the system selection filter by the following three simple relations.

- $0 < \zeta < 0.2 \rightarrow$ Photoelectric interaction;
- $0.2 < \zeta < 0.7 \rightarrow$ Compton scattering process is involved;
- $0.7 < \zeta < 1 \rightarrow$ Pair production is the process.

In fact, as ζ is uniformly distributed on the unit interval, each type of interaction is sampled with probabilities $p_1 = 0.2$, $p_2 = 0.5$ and $p_3 = 0.3$. [95, 305]. The process is represented in the following figure (Figure 6-3).

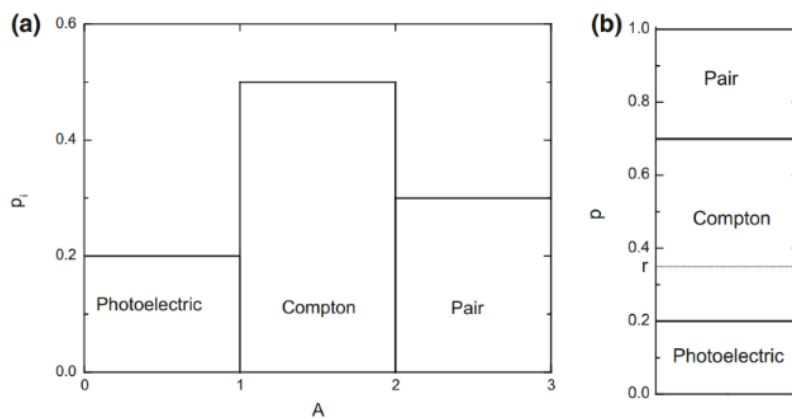


Figure 6-3: (a) Representation of probability of interaction for the photoelectric effect, Compton scattering, and pair production described previously (b) Representation of the cumulative probability distribution for the same case as in (a) [95, 305].

When assessing samples using the previous probability density function, the following interaction occurrences should be observed: 50% Compton scattering, 20% photoelectric effect, and 30% pair creation. Statistical fluctuations can be important for a small number of samples and Compton scattering can be chosen above or below 50%. Statistical sampling therefore needs a large number of particles to be sampled in order to correctly estimate the value or obtain results with low and acceptable standard deviations. For radionuclide sampling, a line spectrum with N energy rays $E_{\gamma,n}$ is emitted with Γ_n percentages [95, 305].

The essential components of the Monte Carlo algorithm are the following:

- the probability density function;
- the generator of aleatory numbers;
- the sampling rules;
- the recording of results into a table;
- the errors estimation;

- the reduction methods of the variable parameters;
- the parallel or vectorial calculations.

6.3.5. Concept of Statistical Weight, Analog and Implicit Tracking

Monte Carlo calculation's stochastic nature includes the following specificity: each particle is correlated with a W (weight) statistical weight. A default weight of 1 or unity (the maximum value that the weight can have) is allocated to each particle emitted by the source. The particle can be tracked by two approaches, that are considered as either analog or implicit methods. A direct simulation is performed in the analog approach, in which the "real" physics is used for particle monitoring. This monitoring mode does not result in modifications in the particle's statistical weight. In addition, with this strategy, each particle produced in a collision interaction is monitored with the same weight as the particle that gave birth to it, the primary particle. For illustration, let consider a flux of neutrons interacting with a hydrogen target. Based on the incident neutron inputs (energy, angle...) and conservation laws (time, mass...), energy and angle of the recoil proton and scattered neutron are sampled in the analog strategy. Thus, by following this example, during an elastic scattering, if the incident neutron has an original energy of 5 MeV and the scattered neutron carries 4 MeV, the recoil proton produced will necessarily have an energy significantly equivalent to 1 MeV through the conservation of kinetic energy, according to the classical mechanic or classical physics. The weight of the recoiling nucleus and the dispersed neutron is the same as the original neutron as the sum of four and one is equivalent to five, the initial neutron's energy [35, 95, 305].

Both energy and angular deflection of the neutron and the recoil nucleus are determined randomly in the implicit approach but based on the input information of the incident neutron (if talking about the previous example in the implicit approach): for instance, the interacting 5 MeV neutron can give birth to both 3 MeV proton and 4 MeV scattered neutron, which is not compatible with energy conservation (classical view). The statistical weight of secondary released particles is fixed and adjusted to overcome the faults of the conservation laws [35, 95, 305]. This concept requires relativity of quantum mechanics approach as well as more computational resource compared to the analog approach described previously. As the result accuracy differ slowly, both methods can be used in MC simulation.

6.3.6. Application of Monte Carlo Codes for Semi-Conductor Detectors

As previously demonstrated, Monte Carlo codes enable the modeling of various HPGe detectors. Efficiency simulation and optimization of different detector parameters have been carried out by Monte Carlo related codes. By means of pulse-dose estimator, the pulses scored in the sensitive detector volume can be evaluated. For instance, this characteristic is compatible with a popular radiation measurement implementation that consists of determining a transfer function and quantities such as counts per second, considered in radioactive decay as Becquerel of source or contaminant, for a particular geometry and given radionuclides. The detector's self-noise and the transfer function determines the minimum detectable activity (MDA) [53, 104] [35, 95, 305]. The method is applied to computed γ photon behavior when it enters a medium. The energy distribution of the pulses scored in the cell modeling of the sensitive volume of the detector can also be determined. The detector's response or simulation output is typically comparable to the spectrometer operating mode result. A Gaussian expansion of the absorption peaks can be obtained in order to take into consideration the energy resolution depending on the physico-chemical structure of the scintillator. Conventionally, by the $FWHM = 2.35 \sigma$ relationship, the enlargement parameter σ determines the full width at half maximum peak (FWHM).

6.4. Geant4 Toolkit overview

Geant4 [32, 33, 306, 308] is a publicly available Monte-Carlo toolkit developed at CERN, which enables the user to create accurate simulations of particle propagation through and interaction with matter. Originally it was used to model particle and nuclear physics experiments, however Geant4 is now used in a wide range of fields including nuclear medicine and radiation protection. As the cost of computing facilities decreases (the main limitation for computer-based modelling), Monte Carlo simulations have become essential when developing new equipment, providing substantial cost savings on prototyping and design work. Such simulations also provide a method to improve understanding of existing processes, and critical discussion points on an experimental setup. Alternatives to GEANT4 were considered, including MCNP6 [282] and FLUKA [290], however none of these code is as versatile setup as GEANT4. This is due to the unique ability to modify both the code base of the GEANT4 toolkit and of the simulations themselves, something that is not possible with the other two Monte Carlo packages. GEANT4's flexibility, large user-base, and comprehensive physics models ultimately make it ideal for the analysis of existing systems, and the development of a new, Compton Suppressed Low Energy γ spectrometer [22].

Unlike the other Monte Carlo codes as EGS, MCNP, MCNPX, FLUKA, GATE, PENELOPE, SRIM ...etc, Geant4 is not an executable program but rather a set of C++ class libraries which contains predefined C++ classes. For this reason, the researcher should build his own code or application from the beginning or modify appropriate built code. The first option is the best while the scientist is a good C++ informatician programmer. In GEANT4 simulation, there are many quantities of interest, that should be assessed. Information about each particle can be obtained at both the pre-step and post-step points, including the energy deposited per step or the energy the particle still has at any point, the type of particle, the number of secondary particles as well, their position and trajectory etc. By combining the information across all different steps, information for each event can be obtained, and therefore used to create useful outputs, such as energy spectra [34, 290]. An event is one of the important data outputs as one uses GEANT4 toolkit for metrology of radiation.

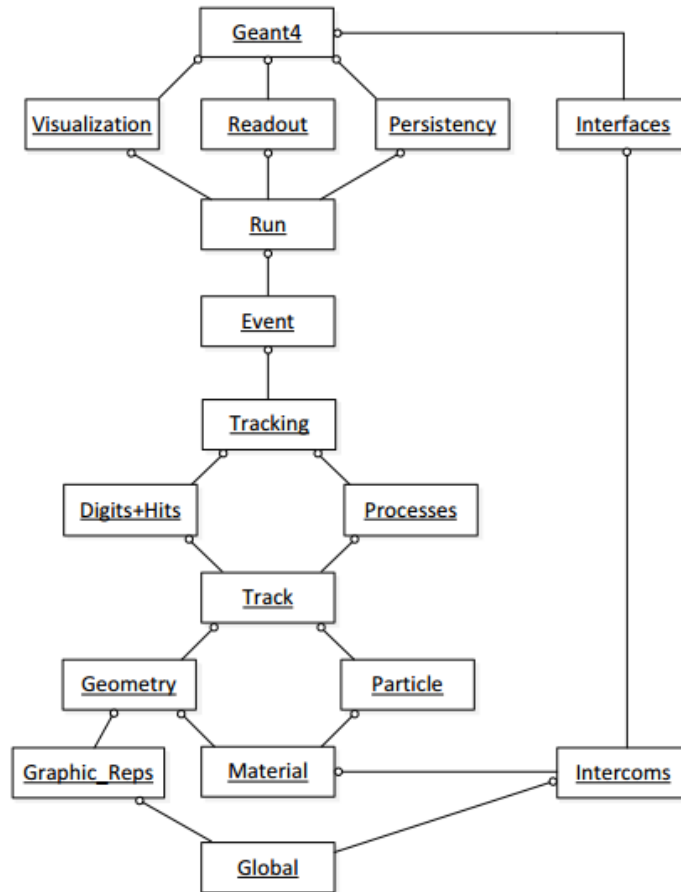


Figure 6-4: Geant4 class categories (Geant4 Collaboration 2017). GEANT4 classes overall functioning diagram for radiation simulation.

To create a simulation, the user must define a world, and populate this with materials and geometries. The material filling the geometry is the real material in the physical laboratory geometry. For example, the ambient air in the laboratory room should be set according to the room temperature and the air density can easily be adjusted. As the ideal vacuum does not exist, the vacuum can be defined in a simulation, but it is important to consider it as air at appropriate atom density ($<10^{-6}$ time the ambient air). Primary particles (e.g., γ -rays from a radioactive source, proton beam, electron beam, etc.) must then be defined, and the physics processes required for the simulation added. Geant4 will then simulate the passage of the primary particles through the world, transporting each particle via a series of steps. For each step through the simulated geometry, GEANT4 calculates the mean free paths for any competing physics processes, and ‘chooses’ a process based upon the relative strengths of each interaction channel and a random number generator. This determines the step length and the physics process to be simulated. Step lengths can also be defined by the user and will be limited if the step encounters a physical boundary. Each primary particle is known as an event, and Geant4 stops tracking it when the particles kinetic energy reaches a cut-off threshold, or it exits the world volume. A user-defined number of events are run, creating the Monte Carlo simulation, and generating data to explore [22]. Usually, the world volume is defined larger if one wants to track the photon for long distance, but it is always simulation type-dependent. The world volume dimension for cosmic ray simulation is far larger than that of the HPGe for γ spectrometry assessment.

Information on each particle can be acquired at both pre- and post-step levels, including deposited energy per step of the simulation, particle type, number of secondary particles as previously men-

tioned, but each step's information should be collected individually and summed-up to form the event information. As different other Monte Carlo codes (Particle and Heavy Ion Transport code System - PHITS), GEANT4 recent versions provide an operator interface. The Geant4 visualization system, which is based on graphics libraries, such as OpenGL and Qt is one of the improvements that allows the end users to check their simulation and to see the beauty of the physics, especially that of the interaction of radiation with matter. The system can help the users to visualize geometries, particles trajectories, and volume overlapping errors in 2D or 3D views. The transformation used for geometry rotation is additional parameter that the user can use to check the complex geometry as that of a γ -ray spectrometer. Derived classes can be implemented in the main function to make the visualization using OpenGL or Qt as well as additional plotting applications available, such as HepRApp or DAWN [27, 33, 279]. The user could decide to install a complete GEANT4 on a virtual machine, that includes all basic packages for a complete simulation. It is also possible to install GEANT4 as personal application by deciding which component to add to our system when we want to use them. The first way is less complex and reduce errors for new users but requires additional disk space on the hard drive compared to the second option.

For appropriate simulation with Geant4, a user needs in addition to background knowledge in physics, but also basic knowledge of C++ programming and especially in oriented object. Physics processes should be added manually though Geant4 based on C++ programming for advanced users, but the beginners could possibly use an existing library or combination of libraries for their own simulation. Therefore, the user should be fully aware of which processes should be included for a selected interaction process (corresponding processes for γ photon from decay origin, for electron, for proton, ...). A Geant4 application, which is implemented with mandatory classes, does not give standard information produced in a simulation as other codes. For example, in PHITS code, the user can choose to have only one input file and could also decide the format of the output file that contains the information needed at the end of the simulation. In GEANT4, all information of interest should be extracted manually, or a fraction of code should be dedicated for such purpose. Fortunately, volumes can be set sensitive if the detector class is assigned in Geant4 and this easier the crucial information extraction. User defined detector or built-in detector can be applied. If a user defined detector is used, the information or simulation result needs to be extracted manually [309].

In GEANT4 toolkit machine, predefined detector classes can be used to provide or assess standard information. There are hundreds of predefined classes in GEANT4 toolkit and still, a large number is under construction by the CERN collaboration as well as research institutes or independent researchers all over the world. To get more information or retrieve data in different ways, following classes and functions can be employed:

```
G4UserRunAction;  
G4UserEventAction;  
G4UserStackingAction;  
G4UserTrackingAction;  
G4UserSteppingAction.
```

The following is a brief summary of the role of each class category in Geant4 [81, 88, 283]. For detailed description of the classes used in GEANT4 simulation, the user manual should be consulted [33]. The following classes are those used in our simulation and implemented mainly.

- **The Global** category covers the system of units, constants, and numeric and random number handling. It is important for normalizing quantities during a simulation using Monte Carlo methods based on GEANT4.
- **The two categories' materials and particles** are mainly used to describe the physical properties of particles and materials for the simulation of particle-matter interactions.
- **Run and Event** are categories related to the generation of events, interfaces to event generators, and any secondary particles produced. Their roles are principally to provide particles to be tracked to the Tracking Management. As particles move before they are tracked, a Run usually defines the dynamic or movement of the particle prior the interaction. The event is the assessment of the particle from its generation to its death (killed or escalation from the geometry)
- **Tracking and Track:** The important aspect of the model is that a simplified method of GEANT4 physical processes (or interaction) can execute actions, whether placed in space or in time, and in combination of both space and time (and all possible combinations that could be built from these cases). These are classes relevant to the particle propagation by evaluating the variables that restrict the step (in a particle life or existence in the system) and implementing the relevant physics.
- **Processes:** Track class includes courses for tracks and steps, used by the **processes** category, which includes applications of physical interaction designs: lepton electromagnetic interaction, photons, hadrons and ions, and hadronic interactions. Processes are subject of importance as each physical process in the computation uses it.
- **Geometry and Magnetic Field:** These categories manage the geometrical definition of a detector (solid modeling) and the computation of distances to solids (also in a magnetic field). The geometry is an important part of the system definition as it usually varies from one simulation to another. Even though the same equipment is used for the same experiment in different laboratories with different arrangement, it is important to adjust the geometry. For this reason, each simulation is in time and space unique. A key feature of the GEANT4 geometry is that the volume definitions could be independent of the solid representation. The treatment of the propagation in the presence of fields has been provided within specified accuracy and one can only call models that have been developed and validated for the same purpose.
- **Particle Definition and Matter:** As the radiation with matter interaction is a probabilistic phenomenon depending on the particle type, the particle of interest should be defined for a particular simulation and the geometry composition should be set. These two categories manage the definition of materials and particles.
- **Physics:** This class handles all physical processes involved in particle interactions in the system. Models can be chosen based on the energy range, particle type, material defining the medium, etc. Data encapsulation and polymorphism enable transparent access to cross-sections (regardless if one chooses to read from an ascii type file, interpolate from a tabulated array, or analytically compute from an equation). In such a model, electromagnetic and hadronic mechanics have been treated uniformly, closing up the physics to the users.
- **Hits and Digitization:** These two categories manage the creation of hits and their use for the digitization phase. The basic design and implementation of the Hits and Digit had been realized, and also several prototypes, test cases and scenarios had been developed and are ready

to use. A user could decide to adjust these classes or to use the default one already built in GEANT4 toolkit.

- **Visualization:** This category manages the visualization of solid geometry, trajectories, and hits. It allows interaction with underlying graphical libraries (the Visualization class category) to provide beautiful 2D or 3D graphs. The OO design of the visualization component allowed Geant4 community to develop several drivers independently, such as for OpenGL, Qt and OpenInventor (for X11 and Windows), DAWN, Postscript (via DAWN) and VRML. One can choose the most appropriate visualization component for his application depending on the computer system and available computer resources.
- **Interfaces:** This category handles the production of the graphical user interface (GUI) and the interactions with external software (OODBMS, reconstruction etc). It is possible to adjust the displayed interface by adding or removing some shortcut in the menu bar or clipboard.
- **Readout:** Even though this class category is not commonly used, it allows the handling of pile-up during a simulation project [34].

6.5. GEANT4 for γ -ray spectrometry

6.5.1. Physics Lists

Low energy electromagnetic physics models (physics models dealing with energy range valid from 250 eV - 100 GeV) are used to model photon interactions with materials throughout all the simulations. This is implemented via a modular physics list, which uses the built-in GEANT4 particle definitions. This includes common bosons, leptons, mesons, baryons, and an ion constructor. Modular physics lists are useful because they allow the user to turn on / off certain processes, and even select different sub-lists to be included (such as Livermore, EGS model, or Penelope based lists, which may use different models for photoelectric absorption, Compton scattering, etc.) [34]. The option to turn on / off a physics process in a model is a practical suggestion from the developers, as we don't need to track a particle type in all existing process that it may undergo (including those with branching ratio lower than one thousandth, or one millionth, or one billionth...). Within the physics list, all available electromagnetic processes are defined, as well as transportation through the geometry, radioactive decay, and an explicit stepping process. Fluorescence photons, Auger emission, and Photon Induced X-ray Emission (PIXE) are all enabled by default, while the minimum energy for the electromagnetic physics tables is reduced to 10 eV (from 100 eV in the case of γ radiation from nuclear origin). But X-ray model are projected for future investigations as only γ -ray detection was modeled in the present study. The stepping process allows the user to modify the length of the step for each particle type (which can result an increasing / decreasing of the 'resolution' of the simulation). The cuts used (which defines the cut-off threshold for each process), are also defined here by the user for particular simulation by using the default set by developers [34, 68, 83, 310].

6.5.2. Particle Generation

Primary particles are those that are defined within the primary generator and are then propagated throughout simulated geometry. To define a particle, the type is specified (γ , neutron, etc.), and given a position and initial momentum/ direction. To generate radioactive decays, ions are created using Z, A, and excitation values, and placed with no initial momentum. These are then disintegrated using two methods. The first uses the radioactive decay module built into GEANT4, which (if the optional radioactive decay library is installed) disintegrates each primary event probabilistically to reproduce the

decay behavior happening in the physical laboratory [34]. Although this method is the default one set, if well selected and implemented, the simulation result should be accurate at an acceptable extend.

The second method uses a framework developed for the input of decay particles. In this mode, the user can specify his own set of decay libraries, which reside in the same folder as that project. Multiple nuclides can be specified in a macro file (with the appropriate weightings) and the particle generator will search the user defined library for each isotope. If no corresponding library file is found, the simulation will use the GEANT4 decay libraries as default setting (allows to reduce bugs in the code development), however if it is available then the particle generator will generate the specified particles individually by firing them isotopically. This second method is appropriate for those with advance knowledge in GEANT4 and C++ programming, but for the beginners, the first method is easier to implement event though there might be some discrepancies that need to be adjusted.

6.5.3. Source Reproduction

The source matrix is reproduced by defining the source size, position, and material (or mixture of materials), and then creating the object within the simulated geometry. The geometry information for the source is currently supplied by an external library file, which allows access to this information for particle generation. A decay can therefore be generated at a random coordinate within the source geometry, which can also be supported by casings / source holders as necessary. The source geometry is one of the most important parameters to be considered while defining the source. The effect of a 1 Ci point source is completely different from that of 1 Ci disk source (that is distributed in a disk form and the effect of the geometry source as self-attenuation is non-negligible), and that of a spherical or cylindrical source. In addition, the encapsulated source versus an open-source accountancy should be considered as the source enclosure play an attenuation effect if the source activity is not measure at the surface of the enclosure. Summing effects due to the source activity are simulated by calculating the probability of a detector seeing from 1-20 events within the detectors characteristic decay time, and using this probability to generate extra decays in a corresponding number of events [34, 280, 305]. The characteristic decay time in this part is one of the important parameters as it defines the accuracy and the capacity of the detector to count a certain number of particles in a time interval. For example, if the decay time is 10^{-9} second, and the decay source emits 10^{10} particles per second in the direction of the detector, all cannot be detected: only a maximum of 10^9 could be which is less than one tenth of the real situation.

6.5.4. Experimental Geometry

The geometry of the simulation is recreated as fully and accurately as possible by the user (or his team), as he only knows the real experimental condition to be reproduced in the simulation. Complex shapes are created using boolean combinations, and all major collections of components are implemented as assembly volumes. This allows the user to create all the individual parts of a detector, assemble them in their correct positions, and then position the entire assembly as one object. The benefits of this are two-fold, firstly the source code is much easier to manage, and secondly, the user can place as many copies of the detector in the simulation as needed (especially useful when modelling large arrays, for example) [34, 280, 305]. Recent developments in GEANT4 code have extended the number of simple Boolean operation combination for simple geometry creation as can be seen in Figure 6-5 [33, 311]. As results, some complex geometries built using GEANT4 will be presented in the next chapter as for the detector (BEGe 6530 model) simulation [22].

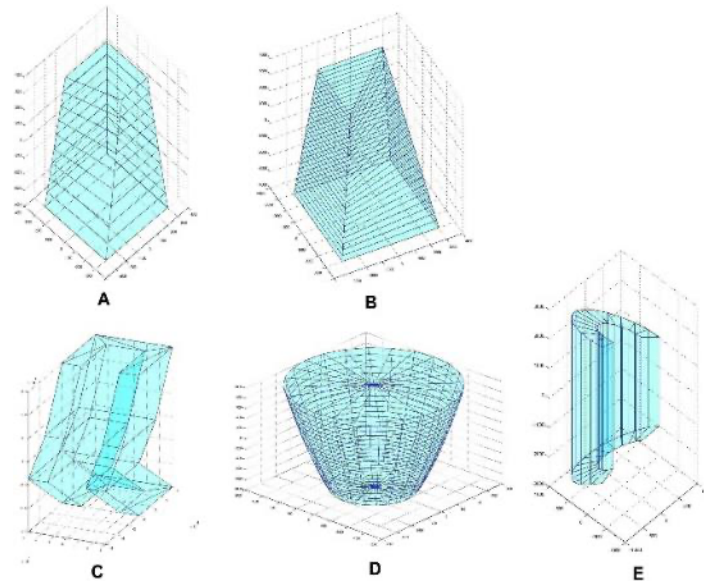


Figure 6-5: Recent geometrical primitives added in Geant4 by Alison et al. [33, 311]: generic trapezoid (A,B), extruded solid (C), parabolic solid (D), and cut tube (E), for the end-users simulation purposes.

6.5.5. Simulation

The GEANT4 simulation starts with a loop starting with the production of a γ -beam photon from the origin (the source can be the standard source given by IAEA or generated from our laboratory work) and then monitoring photons in various geometry areas. A single photon's monitoring is ceased when it reaches the outer volumes, escapes from the controlled volume or the active volume, has less energy than the cuts set (or when the photon's energy moves toward becoming lower than the specified maximum esteem cut-off energy). This method, also known as sampling, is repeated as many times as possible, taking into account the end goal of reducing the measurable fluctuation of different parameters of interest below the prescribed limits [22]. For good statistical analyses, running on more than 10^9 photons was performed for each information point in our simulation. Source biasing technique was used to increase the efficiency reproduction. Template geometry was designed taking into account the Canberra's actual parameters in the Broad Energy Germanium (BEGe 6530 model) detector's technical manual.

As there is a new version every year, or at least an updated version, the version 10.2 of the GEANT4 (Geometry and Tracking fourth generation) Monte Carlo code, released in December 2015 was used for the simulations built in this work [32, 306]. Even though the version used has been updated, the result presented in this project are data obtained by the version 10.2 of GEANT4. All types of relevant interactions of photons and electrons/positrons with matter were considered during the simulation, using low-energy data packages available in GEANT4 database as G4EMLOW6 model, model G4EmLivermorePhysics model. The G4EmLivermorePhysics model includes two optional physics sub-packages, the “Livermore” model and the “Penelope” model. The Penelope model was not developed by GEANT4 collaboration directly, but for the Penelope code and could be imported into GEANT4 or other MC calculation code. The goal was to adapt the code to our laboratory's environment and to benefit from network research that is already achieved. By specifying a 1D histogram for the deposited energy per event for the sensitive detector response, G4AnalysisManager was used to build and fill histogram (the related spectrum). The histogram plotting was activated using UI commands available in GEANT4 guide and the obtained result could be discussed and compared to

other research works or experimental data [309]. Configuration with the Root browser (or Root as additional package) was used to generate spectra plots and root files. The spectra collected were then compared with the experimental one to evaluate how the code could be improved.

The energy deposition in the detector's sensitive volume was histogrammed and extended to copy the behavior of the signal processing electronics with an energy-dependent peak form feature. The spectrum was eventually stored in a file that was previously defined as an ASCII file type. In all simulations, a 64-bit Linux (Scientific Linux) computer was used, 10^9 initial photons were generated in 4 cases that currently took around 2-6 hours on an Intel i5 personal computer. With clusters, this calculation time could be reduced by a factor of 10 or 100, or even more. As the previous number of particles is generated, it produces around 5000 to 40000 particles tracked in the sense of counts. With this number of particles, the statistical precisions are generally similar to the experimental one and data comparison could be meaningful. The background of each single primary particle during the simulation involves its emission by the source, its move into the system and interaction with the detector sensitive volume or surrounding materials, the creation and propagation of secondary particles, their monitoring until the photon escapes and undergoes a photoelectric reaction in the crystal, depositing all its energy. The cut-off energy of the simulation was set below 0.5 keV [301]. Each particle with energy below 0.5 keV was no longer tracked in the geometry and was killed.

As the detector under investigation in the present project is the BEGe, the broad energy germanium detector's active volume size and the dead layer thickness are key parameters for obtaining accurate simulation results. Therefore, it is important to take this parameter into account when planning and designing detection systems for γ spectrometry assessment based on semiconductor technology. A point-like source of ^{241}Am was used to evaluate the thicknesses of the front and side dead layers, but the simulation was conducted periodically and each time the thickness value of the corresponding dead layer in the detector system was modified and the dependence of the detection efficiency on the thickness of the dead layer was interpolated along with the correlation found. As the descriptive function of the process is found at the latest stage of this measurement, the dead layer thickness of the detector is considered as a defined parameter [282]. The detector's effective volume was checked with a collimated point-like ^{133}Ba source. The detector's dimensions were the basic factors that contributed to the simulation as a larger detector has a large sensitive volume, if well designed: the diameter and length of the crystal, the width and length of the crystal cavity, the top and side dead layer dimensions, the size of the shield, the end cap dimension, the window thickness, and the window to crystal distance. In the experiment, bulletization, dead layer, and window to crystal distance are used as variables to minimize the difference and fluctuation between simulated and experimental data [22].

In spite of directional bias, the implementation of a basic variance reduction system boosts simulation. The purpose of this method is to measure only primary photons released from a sample in the direction of the detector (the sensitive volume of the detector). Implementing an algorithm described in detail by Hurtado et al. using GEANT4 code simplified the simulation [282]. Sample measurements were also carefully measured, and sample volumes were built appropriately in the simulation code as the geometry built by the code and the real one should have similarity in an acceptable rate (volume calculation with less than 1 % standard deviation). Primary photons were created in the sample volumes with uniformly random positions and momentum directions in full space (4π) as described in GEANT4 user's manual [301]. But since the detector's solid angle for the detection purpose is a small fraction of 4π , the use of transforms in the simulation could be difficult tasks. For this reason, only a few numbers of generated particles from the source reached the detector sensitive volume and are counted statistically. The calculation time is then extended in the case we want to improve the simulation statistic, but it could be improved by using parallel computation. The parallel computing

mode in GEANT4 is known as multithreaded GEANT [33].

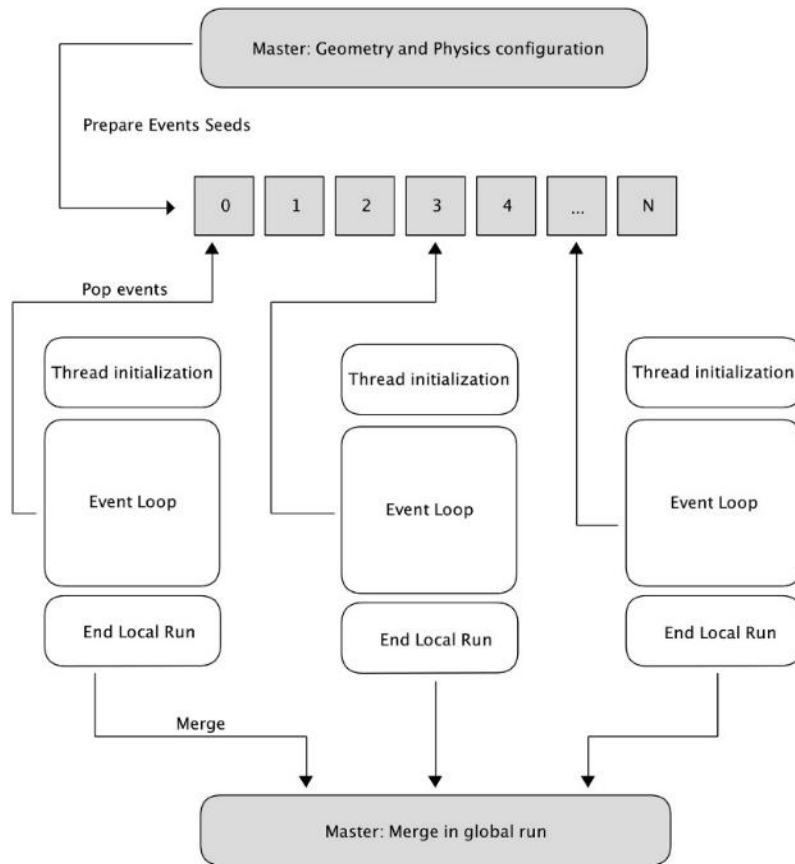


Figure 6-6: Simplified diagram representing the multithreaded Geant4 application: the *master* thread plans simulation setups for geometry and physics, and the *worker* threads complete events to be simulated; otherwise they are separate [33].

The development’s aim of multithreaded Geant4, when a system with n cores is used, is to substitute n separated instances of a Geant4 loop with a single, identical process utilizing multi-core machine threads in a memory-efficient, scalable manner. For example, when a 7-core computer is being used in parallel computer mode, a maximum of 7 processes could be run simultaneously and the result are combined at the end of the simulation. The simulation ran seven times maximum faster than the case without multithreaded GEANT4 computation. A simplify version of the diagram used for multi-threading, described by Alison et al. is shown in Figure 6-6 [33, 311].

By defining main interfaces of certain groups, user-defined code can be implemented and applied for specific applications. The threading model is specifically defined by the G4UserWorkerInitialization class, which defines threads’ configuration in term of descriptive procedures. The key classes of Geant4 applicable to a multithreaded application are shown in Figure 6-7. Both interfaces are also usable in sequential mode so that the user code can be executed in multi-threaded or sequential Geant4 mode with minimal changes for a simulated code [33, 311].

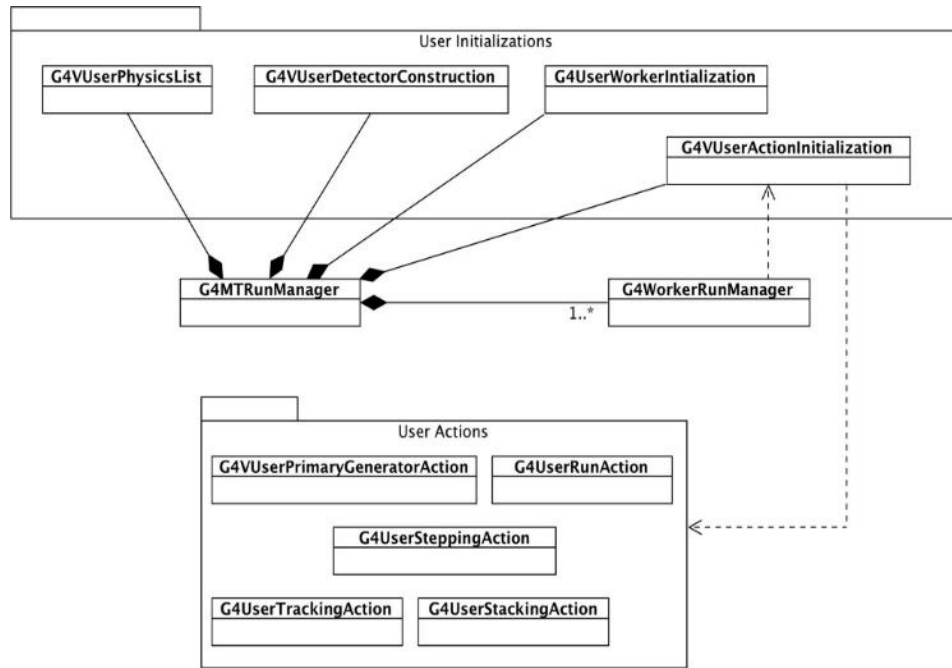


Figure 6-7: Main user interfaces' class diagram used in GEANT4 computer code. User initializations, including geometry and physics list, are distributed between threads and allocated to G4MTRunManager's single instance, while user actions are generated for each thread through G4VUserActionInitialization class, and assigned to G4WorkerRunManager's private thread [33].

6.5.6. Extracting Information

There are two main methods for extracting information from a simulation. The first can be controlled via a macro file and allows the user to create a scoring mesh. This places a grid of a defined size, position, and resolution over the geometry, and accumulates the required quantities over the simulation (such as energy deposited, the dose deposited, the number of steps recorded, surface flux, etc.). These values can then be written into a file for later processing (usually txt, ASCII, or Excel files are easy to store, access, and process). The second method involves setting sensitive regions in the geometry and implementing code to read out the energy deposited within these sensitive regions every step / event as required. For most of the simulations in this thesis, the second method was used, with the detector crystals set as sensitive volumes. The energy deposited at each step by an impinging particle is recorded, and these steps are then summed up to calculate the total energy deposited per event (which is equivalent to the energy deposited in a detector within the laboratory). GEANT4 simulations, however, record the energy exactly, giving the simulated detector a perfect resolution, which slightly differ from the reality [301].

6.5.7. Simulating Coincidence Systems

In the laboratory, coincidence detectors (γ - γ systems, Compton suppression systems, etc.) are controlled using complex electronics with highly accurate timing systems. These systems synchronize the two processes, allowing a gate to be set (in either hardware or software) that records coincident events (depending on the system). The timing of this gate is dependent on the electronics of each system, and the charge-collection time of the detector, but in each case the charge collection time should be small enough to overcome the signal stagnant problem. Scintillation detectors are generally much faster than semi-conductor based systems, however charge-collection in either type of crystal is far slower (typically by up to 10^3 times) than radiation transport within the system. Monte Carlo models can therefore replicate coincidences by recording when energy is deposited in multiple detectors with-

in the same event, as the meshing of the detector in small detector volume is easily simulated. This would be equivalent to a perfect system, as there will be no losses due to electronics that would be seen in the laboratory. For a well set up system, however, these losses are minimal [95, 301, 305].

6.6. Experimental Setup for GEANT4

The detector under investigation is a commercial p-type BEGe detector (BE6530 Model), a product manufactured by Canberra. Major descriptions and specifications of the detector used for Monte Carlo simulation and include in the GEANT4 code are presented in Table 6-2. As the code required additional information that are not provided in the user manual of the detector, important collaboration and communication were needed between researchers and the Canberra manufacturer firm. Figure 6-8 shows a schematic design view of the detector configuration used in the present project. The data acquisition systems in this work involve a charge-sensitive pre-amplifier, an integrated digital signal analyzer and detailed part presented in the chapter 3 and the Genie-2000 software versus 3.2. coupled to LaBSOCS mathematical calibration software.

Table 6-2: Specifications of the BEGe detector used in the laboratory for experimental study (BE6530) and used for MC based GEANT4 toolkit simulation. Some parameters as voltage related ones are for experimental understanding.

Descriptions	Detector
Detector type (Canberra)	BE6530
Detector geometry	Plan
Detector active area-facing window (mm ²)	6500
Active diameter (mm)	91.5
Thickness (mm)	31.5
Distance from window (outside) (mm)	5.0
Window thickness (mm)	0.6
Aluminum endcap distance from window (mm)	8.0
Window material	Carbon epoxy
Relative efficiency at 1332.5 of ⁶⁰ Co (%)	60
Full Width Half Maximum (FWHM) Resolution (keV) at 5.9KeV	0.478
Full Width Half Maximum (FWHM) Resolution (keV) at 122KeV	0.695
Full Width Half Maximum (FWHM) Resolution (keV) at 1332.5KeV	1.785
Depletion voltage	(+)4000
Recommended bias voltage Vdc	(+)4500
Time constant (μs)	4
Cryostat description	Vertical dipstick
Peak shape (FWTM/FWHM) for ⁶⁰ Co	1.88
Cooling system	Electric

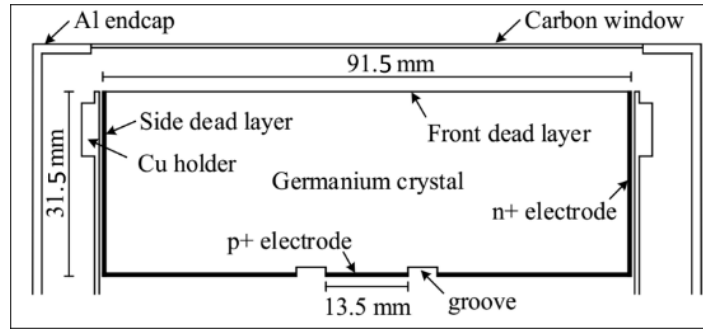


Figure 6-8: Schematic view of the BEGe detector (BE6530) with real dimension needed for GEANT4 simulations. Precise dimensions and geometry shapes are needed for accurate simulation and meaningful comparison of computer data with experimental ones.

The detector uses a carbon epoxy window to shield the detector's crystal and reduce low-energy photon attenuation and background radiation from the laboratory environment and from the earth and cosmos (cosmic radiation). It reduces photon response below 10 keV as compared with an Aluminum window (which reduces photon response up to below 30 keV) or a Beryllium window (which can allow energy photons under 2 keV only), which is substantially more stable. Certain detector safety composers include aluminum endcap, lithium dead layer, lead shielding, boron sheet, and copper used in this case to minimize the impact of X-rays produced by the lead shielding device as explained in chapter 2 and 3. The interaction of γ -ray with the lead (from shielding material) produce secondary generated particles and X-ray are produced in a large number. For this reason, copper is used to cover the lead shield interior as different other low background material. These components are taking into account in the simulation and a slightly difference could be observed from the obtained result.

In subsequent calculations, the knowledge of detection geometry is important [274, 279]. Therefore, any data was only accessible to the Canberra on a special request if it affects the outcome of the simulation. For example, the actual dimension and structure of the germanium crystal can be obtained by cooperation with Canberra, which gives more specific details, or through a scanner's picture of the detector. Experimentally, the efficiency ϵ for a given photon energy is assessed throughout the following formula:

$$\epsilon = \frac{N_c}{A t P_\gamma} \prod_{i=1}^n C_i \tag{6-19}$$

where N_c is the total number of counts in the peak,

t is the detection time,

A is the nuclide activity, and

P_γ is the photon emission.

C_i contains correction factors due to dead-time, radionuclide decay, self-absorption, and coincidence summing corrections.

As the calibration of the equipment was done for both energy and efficiency, it is important to highlight that energy calibration is a basic simple task that is easily achieved. But the efficiency calibration is the most difficult exercise and only efficiency simulation is considered and discussed in the following chapter of this project. The uncertainty on the efficiency calculation ($\Delta\epsilon$) was calculated using the following equation:

$$\frac{\Delta\varepsilon}{\varepsilon} = \sqrt{\left(\frac{\Delta N}{N}\right)^2 + \left(\frac{\Delta P_\gamma}{P_\gamma}\right)^2 + \left(\frac{\Delta A}{A}\right)^2 + \left(\frac{\Delta M}{M}\right)^2} \quad 6-20$$

Where ΔN is the count rate uncertainty,

ΔP_γ is the emission probability uncertainty found in the nuclear data tables as provided by different national laboratories,

ΔA the relative uncertainty of the activity concentration of the radioactive source provided by the manufacturer and ΔM , the mass uncertainty.

Point sources of ^{241}Am , ^{152}Eu (for energy calibration), ^{137}Cs , ^{109}Cd , ^{88}Y , ^{65}Zn , ^{60}Co , ^{57}Co , and ^{54}Mn were used for the GEANT4 simulation process. To record at least the highest counts for each full-energy peak and minimize the statistical counting error, the counting time of γ point sources was adjusted accordingly [22, 128]. Data from each sample or radionuclide investigated are presented in the following chapter.

6.7. Conclusions

Monte Carlo methods applied to the radiation detection technology have been discussed in this chapter. From the physical point of view, Monte Carlo simulation provides valuable insights to solve problems that are almost impossible to be solved analytically. As different MC codes have been developed all over the world in different application fields, there are many applied in Nuclear physics as well. But the GEANT4 toolkit was used in the present study as it is an open source and free library application for tracking the interaction of particles through matter. The description of GEANT4 was presented and important relations applicable to γ spectrometry measurements. Different MC equations used for the simulation and important classes for GEANT4 application development were described. As MC methods are based on random numbers, a random number generator function used by physicists and in the Nuclear field was presented.

The validation process of the experimental efficiency calibration was done accordingly based on the techniques presented in this chapter. The valuable results obtained from this validation process are presented and discussed in the following chapter. The influence of the decay scheme of nuclides, the sample geometry and composition, the detector features on the activity concentration of radionuclides in the sample, and the cascade summing effect were automatically corrected using the peak to total (P/T) curve as usually done for real experiment [140]. The code developed during this project is an outstanding achievement as the results presented in the following chapter will demonstrate. For this achievement, it is important for future investigation to compare the result obtained using different nuclear libraries and to develop a similar GEANT4 code for X-ray interaction in the case of XRF detection system. Improvement could also be implemented in view to share achievements and to test the code in real measurement situation in the laboratory.

The present chapter detailed the MC methods and the GEANT4 toolkit used for the validation of efficiency calibration of γ spectrometer. The description of the following steps was covered in the chapter:

- The MC algorithms, its principles and applications to the radiation transport and interaction;
- Random number generation in MC calculations, the context and use of inversion Monte Carlo methods;
- The sampling of a discrete distribution and application to select the collision type;

- The concept of statistical weight and analogue (implicit tracking used in GEANT4);
- The GEANT4 overview and related MC equations, including important classes; and
- The GEANT4 implementation for γ -ray spectrometry.

The following chapter will discuss the obtained results and the validation of the simulation model built in this thesis.

CHAPTER 7. GEANT4 VALIDATION STUDIES

The present chapter is devoted to the simulation of a broad energy germanium detector and its response. As described in the previous chapter, the Monte Carlo methods implemented in GEANT4 code are used to reproduce the detector efficiency. The GEANT4 toolkit had been used to give attention to the geometry and the BE6530's efficiency response reproduction. To maximize efficiency, this sort of detector has a short or thin and planar shape that reduce the recombination effect inside the sensitive volume prior to the electron acceleration. The sample's geometry, shape, and matrix were similar at this stage, so as the measurement throughout the sample and the reference sample determine the effectiveness of the system: the only difference is directly related to the efficiency calibration. In γ -ray spectrometry, this is a requirement for environmental assessment where no information from the sample activity could be guessed before the performance of the measurement: the calibration source and the sample space occupation must be of the same structure and similar matrix (regarding the type, composition, and density). Regarding the problem of coincidence summing, no corrections are needed if a natural sample is measured in a similar configuration with respect to a norm of the same radionuclide. While the same geometry, same sample matrix, and same radionuclides in both reference material and sample to be assessed is assumed, the efficiency is already corrected for such issue (coincidence summing). For this reason, the geometry design has been subjected to study in this research using GEANT4. In the present work, the configuration of the BEGe detector (model BE6530) was designed firstly and then, utilizing various radionuclides at different energy rates to simulate their efficiency response.

The efficiency obtained with GEANT4 was compared to experimental results. Comparison between experimental and simulated values demonstrated good agreement and proved the code to be well built. The objective was to see whether the results obtained in the present study falls in agreement with our expectation, this comparison will be presented in detailed. The demonstration of the capability and robustness of a GEANT4 model on predicting detection efficiencies for the broad-energy germanium spectrometer (BEGe 6530) used in our laboratory was completely performed, even though some improvements are still under investigation [22].

7.1. Geometry and material definitions

A detector geometry in GEANT4 is made of several different volumes. These volumes are considered sensitive as the particle can be tracked in. The largest volume is known as the World volume and it must include all other volumes in the structure of the detector, with some margin. Usually, particles outside the World volume are no longer considered in the geometry and are consequently forgiven. Other quantities, including in the different smaller volumes, were produced, and included within the previous volume. A box is the easiest (and most effective) way to represent the World volume ("universe"). Each volume is created by describing its form and dimension, its physical characteristics, and then placing it inside a container, known as mother and usually referred to as physical volume [34]. The previous volumes are known as daughter volumes when they are put within another volume and the latter volume is referred to as the mother volume. The reference coordinate used to determine where the daughter volume is located, is the mother volume coordinate system. The solid definition is usually used to explain the shape and form of an object or a volume in GEANT4. A solid is a mathematical description of a shape or a surface / volume that has a structure and unique values occupying the space. Examples of solids are a 10 cm radius sphere or a circle with 30 cm diameter or a 10 cm

side cube [34, 309]. Volumes are usually simple to define, but attention should be paid to avoid their overlapping and geometry errors.

We use logical volume to describe the volume's complete properties and characteristics. This requires the solid's descriptive features, including physical properties: the density material; whether it has any sensitive detector elements; the magnetic field; etc. We still must explain how the volume should be placed, how the particles are moving inside volumes, the crossing surfaces as particles are likely to travel regardless a specific volume. They could propagate through different volumes. To achieve this task, we create a physical volume, which places a copy of the logical volume inside a larger volume. The placement of the physical volume in the geometry is correlated to that of the world volume and logical volume. These three volumes are essential to build a GEANT4 application for the simulation of γ -ray interaction with matter. In general, material in the code is defined as Chemical compounds, Mixtures, or elements (including isotopes). These three descriptions are the base of material definition in GEANT4. In addition, GEANT4 provides an updated table of major elements that can be used and allows the developers to create their own material with the desired characteristics (density, chemical composition, energy, dynamics,...) [22, 309]. Our application used the combination of *G4Element* and *G4Material* to describe material composition in the geometry class and its implementation.

The *G4Element* class describes the properties of the atoms and provides the following information for the user application:

- Atomic number (Z),
- Number of nucleons (A),
- Atomic mass,
- Shell energy,
- As well as quantities such as cross sections per atom, etc.

The *G4Material* class describes the macroscopic properties of matter and provides the following information for the user application:

- Density,
- State,
- Temperature,
- Pressure,
- As well as macroscopic quantities like radiation length, mean free path, dE/dx , etc.

The *G4Material* class is visible to other part of the code and information related to this class is always accessed by the code while computing other quantities of interest as the radiation dose, the dose rate, or the effective dose, the γ flux, and the kerma. It is used by the tracking, the geometry, and the physics and defined by the use in the case, and if not, there are always default value set by the GEANT4 developers (in the case the user is modifying a precompiled application in GEANT4 machine) [309].

i. Particle Definition

G4VUserPhysicsList is one of the mandatory user base classes described and used in GEANT4 simulation. Within this class all particles and physics processes to be used in our simulation were defined. To access the detailed information used in our simulation, the class *G4VUserPhysicsList* should be consulted as additional file to the present report. The code could be shared on reliable demand for

beginners or advance user of GEANT4 as well as by the developers. The range cut-off parameter should also be defined in this class [309]. GEANT4 provides various types of particles for different use in simulations and the following were defined by default in our simulation:

- Ordinary particles, such as electrons, protons, γ -rays, X-rays, Geantino (particle defined only in GEANT4 simulation for only propagation without interaction), positron, and neutron (important notice is that γ - and X-rays are all considered as photons);
- Resonant particles with very short lifetimes, such as vector mesons and delta baryons (these particles are highly explored in the field of high energy physics);
- Nuclei, such as deuteron, α , and heavy ions or heavy charged particles (including hyper-nuclei, carbon ion, lithium ion, ...);
- Quarks, di-quarks, and gluons (explored in particle Physics as well as for the standard model explanation – quantum electrodynamic)

Each particle is represented by its own class, which is derived from *G4ParticleDefinition*. This class describes only characteristics of single elementary particles known up to date. Exception is for the heavy nuclei and heavy charged particles that are defined using *G4Ions* class. Particles are organized into six major categories that are listed below (they are classes of particles as defined in high energy physics or particle physics) [306, 309]:

- Lepton,
- Meson,
- Baryon,
- Boson,
- Short-lived and
- Ion,

Each of these classes of particle is defined in a corresponding sub-directory under *geant4/source/particles* and can be accessed for detailed information or understanding of the code. There is also a corresponding additional library for each particle category as each particles category includes different type of particles with their own physical processes of interaction. For example, among the fermions, there are electrons (e ; ν_e), muons (μ ; ν_μ), and tau (τ ; ν_τ) with different masses, and other characteristics.

ii. Physics Processes

Physics processes are used in GEANT4 to describe how particles interact with different materials. GEANT4 provides seven major categories of processes as listed below [309]:

- Electromagnetic (as the measured class for the γ -ray interaction processes as well as ion, particles, and nuclei interactions),
- Hadronic (related to hadron interaction as used in high energy physics),
- Transportation (Geantino particle is usually the best example to be propagated through this process and particle in an ideal vacuum),
- Decay (very important for radioactive decay used in this project and for radiation detection and measurement based on γ -ray spectrometry technique),
- Optical (important for example for the transport of optical photon),

- Photo-lepton-hadron, and
- Parameterization.

All physics processes are derived from the *G4VProcess* base class. Different classes of importance in this case are presented in the following table (Table 7-1) along with their corresponding method implemented in GEANT4 simulation. These classes describe the behavior of a physics process when they are implemented in a derived class. The details of these methods are described in Physics Processes [309]. For extended detail about the Physics Processes class, the GEANT4 user manual should be consulted as well [31, 34].

Table 7-1: G4VProcess classes and methods implemented and used in the GEANT4 simulation

Class name	Implemented method name
<i>AtRestDoIt</i>	<i>AtRestGetPhysicalInteractionLength</i>
<i>AlongStepDoIt</i>	<i>AlongStepGetPhysicalInteractionLength</i>
<i>PostStepDoIt</i>	<i>PostStepGetPhysicalInteractionLength</i>

iii. Generating Primary Events

One of the mandatory classes available to generate our own concrete class in the GEANT4 environment is *G4VuserPrimaryGeneratorAction*. It is important to specify how primary events or primary particles are generated throughout the system. Concrete classes of *G4VPrimaryGenerator* should be defined for specific generation of primary particles, as discussed in the following steps. The user should configure the specific category of the *G4VuserPrimaryGeneratorAction* without confusion. GEANT4 provides three *G4VPrimaryGenerator* essential classes for primary particle generation or production. These three classes are *G4ParticleGun*, *G4GeneralParticleSource* and *G4HEPEvtInterface*. Only the *G4GeneralParticleSource* (GPS) will be discussed here, in the following paragraph. *G4HEPEvtInterface* class is not discussed here as it is a sub class of the Event Generator Interface as well and is not a measured class for the detector efficiency simulation [309].

iv. GEANT4 General Particle Source

The *G4GeneralParticleSource* (GPS) is part of the high-energy Monte Carlo particle transport used in GEANT4 computation. In general, this class is purposed to make measurements of the primary source particles ' source, using spatial and angular distribution. Here is a description of the GPS class used in our simulation. The configuration's system covers the GPS application for a user application, and Macro Commands describes the macro command interface. Macro command for interface display allows particle visualization to check whether the source definition and particle from the source are well done. *G4GeneralParticleSource* is used the same way as *G4ParticleGun* in a GEANT4 application. In existing applications one can simply change your *PrimaryGeneratorAction* by globally replacing *G4ParticleGun* with *G4GeneralParticleSource*. In addition, the GEANT4 user interface allows the compilation of the code by adjusting some classes directly in the terminal instead of generating a separated class. GPS may be configured via command line or macro based input, in this regard and many non-programmer users may feel comfortable and save time for coding [309].

7.2. Geometry built in this thesis

Preliminary simulation started with the geometry construction of the detector to be simulated. As

the detector type is Germanium semiconductor based detector (BEGe), the geometry took into account the detector crystal and the lead shielding cask with other components. The lead shielding was primarily defined as World volume and other part of the detector were built successively one after another to reflect the real geometry displayed in the laboratory. The physical volume, the mother volume, and sensitive volume were implemented in the world volume accordingly using GEANT4 routines as describe in GEANT4 user manual [309]. After several code compilations with the world volume as the entire room where the spectrometer is located, as the lead shielding system, and as the box in which the detector is located, the choice has been made on lead shielding system only. This part is that to be presented in this section. The sample was easily simulated as a real sample with point like source and approximately 120 cm^3 cylindrical volume sample (5 cm diameter and 7.6 cm height). These dimensions were measured on a real cylindrical container used for experimental measurement using the same detector.

As presented in Figure 7-1, Figure 7-2, and Figure 7-3, the geometry construction code was developed and the output result for geometry drawn are presented. Real dimension of the geometry usually necessitates more resource for first-time construction and compilation. It is worthy as all other code execution sequences will access the built geometry briefly while running. And the geometry plot is not required at each execution as it is computer resource demanding. Instead, after the validation of the geometry, the large number of particles could be run in an input file without visualization, for the visualization process allows time consumption [2, 22, 101, 102, 309].

It was illustrated in three dimensions with ground coloration to improve representation while considering the sample to be simulated in the geometry. When drawing the different part of the detector geometries, the Qt and Open OGL visualizations were used. These additional packages have just the role of making difference in the geometry and check whether it was correctly defined. And for the purpose of presentation, the geometry drawn allows well description and understanding of the simulated components of the geometry. In this way, the geometry presented in the following paragraphs and figures was set with the following rules: The Germanium detector crystal is shown in the purple color. The sample cylinder is displayed with green color. This makes geometry drawing easier and easier to change and adjust. It also reduces the risk of confusion in the geometry's partition and overlapping [22, 33, 306]. The detector is defined in the center of the geometry. The surrounding lead shield and liners are also simulated, with yellow and white corresponding to lead and copper surrounding the internal surface of the lead shielding system. As the X-rays photon contribution from the lead should be reduce as much as possible, the lead shield internal enclosure surfaces are covered by copper.

Some details are missing and are not visible, from the electrodes and other background protection in this representation. As aluminum protection, or carbon steel used for enclosure as well as the thin paint used on the outer surface of the detector. Different parts of the simulated equipment and sample were presented in Table 7-2. Data presented in this table are major parts that have to be defined for our simulation. All these materials were used in our application and the result presented later in this chapter are influenced by such givens.

Table 7-2: Simulated elements (material that the geometry was built with) in the geometry of the detection system. Mat. Name stands for material name; NComp for number of chemical components in the defined material. Some are predefined in the GEANT4 data base while other (the sample simulated) were created in this project and include in our GEANT4 application.

Simple material (Elements that are generally found in GEANT4 data base)									
Mat. Name	Element	NComp	Density (g.cm ⁻³)	I(eV)	Geant4 command name				
Beryllium	Be (Z=4)	1	1.848	63.7	G4_Be (Input window materials)				
Support	Al (Z=13)	1	2.699	166	G4_Al (Aluminum used for the detector protection)				
Germanium crystal (>99.9%)	Ge (Z=32)	1	5.323	350	G4_Ge (sensitive volume of the detector)				
Copper (Shielding material)	Cu (Z=29)	1	8.960	322	G4_Cu (copper shield material)				
Tin	Sn (Z=50)	1	7.31	488	G4_Sn (tin shield material)				
Tungsten	W (Z=74)	1	19.3	727	G4_W (tungsten shield)				
Lead (Shield material)	Pb (Z=82)	1	11.35	823	G4_Pb (lead shield: the primary material for shielding)				
Compounds (Predefined in GEANT4 data base or could be easily defined from other data base as NIST)									
Carbon Epoxy	H (1), C (6), O (8), Cl (17)	4	1.6	/	New G4Material (Molecule definition: C ₂₁ H ₂₅ ClO ₅) Base Mat: G4_AIR				
Word Volume (default)	Air	4	0.00120479	85.7	Mass fraction: C (0.000124), N (0.755268), O (0.231781), Ar (0.012827)				
Cooling way	stainless steel + LN ₂		7.85	/	Mass fraction (%) : C(0.08), Mn(2.0), P(0.45), S(0.3), Si(0.75), Cr(18), Ni(8), N(10), Fe(71) + Liquid Nitrogen				
Polyethylene terephthalate (PET)	Sample container	3	1.38	/	New G4Material [Molecule definition: (C ₁₀ H ₈ O ₄) ₅]				
Sample SS1 elemental composition in % (New G4Material: Compound). The elemental composition of a sample could necessitate the use of X-ray fluorescence spectroscopy described in chapter 5 of this project.									
SiO ₂	Al ₂ O ₃	K ₂ O	Fe ₂ O ₃	Na ₂ O	TiO ₂	CaO	MgO	MnO	P ₂ O ₅
91.0	4.9	2.0	0.9	0.4	0.2	0.3	0.01	0.01	0.01

As shown in Figure 7-2, the preliminary simulation of the detector geometry consists of only the Germanium detector crystal and the lead shielding instruments. Different colors are used according to background color, to differentiate parts of the system for easy correction in case of geometry errors, or information / signal treatment in it. The first graph in Figure 7-1, with black background, presents the

simple geometry as follow: the lead shielding is set using yellow color and the detector (germanium crystal of the spectrometer) using white color. On the second graph in the same figure, the yellow component from the first graph changes to blue component and white to green with white background. A transformation (double rotation in xy plan and xz plan) was applied to allow three dimensions' view in the third case, the third graph. All these Figure 7-2 (a - c) are just for preliminary visualization. For important geometry construction are to be presented later in this section. The following figure is then considered as a simple representation and starting point for the geometry construction

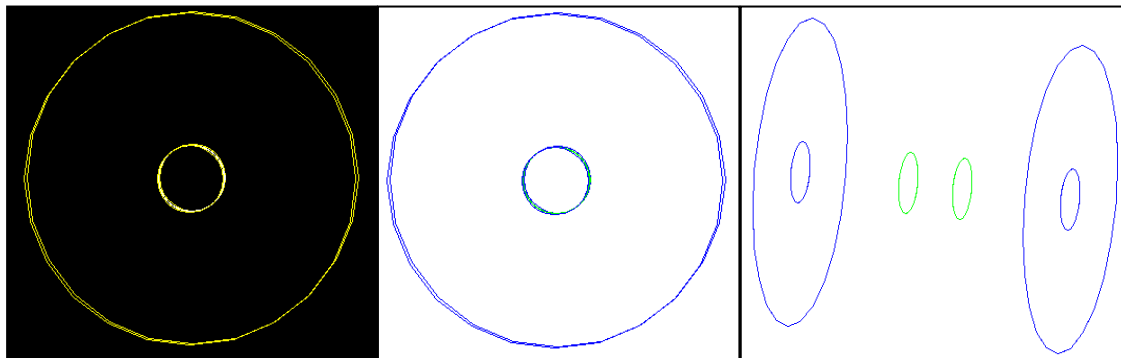


Figure 7-1: A simulated cross-section of the experimental setup used in real experiment (cross-section of germanium crystal and lead shield compartment). The detector is defined in the center (green color on the last graph). The surrounding lead shield contours are described with yellow (in the left graph) and blue (in the two others). Some details are missing from the electrodes and other background protection in this representation, and the dead layers in the Germanium crystal detector are not shown.

When considering the sample in the geometry, it was plotted in three dimension and surface coloration to optimize visualization. The Qt and Open OGL visualizations are used when drawing different parts of the detector geometry. The crystal of Germanium detector is not visible in the first capture, Figure 7-2 (a), but is shown in the center with purple color, in Figure 7-2 (b - f). In this representation, additional part of the geometry is provided by adding the sample shape, which is a cylinder shown with white color. Figure 7-2 (a to f) are the same representation when applying transformation and having the half view of the system. The view section could be misleading if it is not well selected and if there are overlapping sections in the geometry. Drawing geometry in this way is more comfortable and beautiful, as the user have the possibility to verify what has been built.

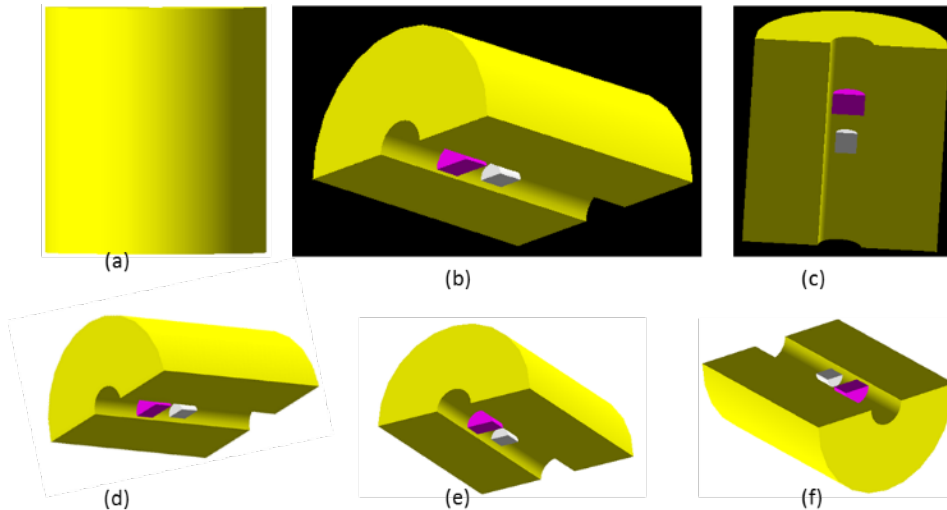


Figure 7-2: A 3D view of the simulated geometry cross-section of the experimental setup. The crystal of Germanium detector is not visible in the first picture (a) but is shown in the center (purple color on the (b to f) graphs). The surrounding lead shield and liners are also simulated in this case and shown in yellow color corresponding to lead. Some details are missing from the electrodes and other background protection in this representation, and the dead layers in the Germanium crystal detector are not shown. An example of source or sample to be assessed is presented on the top of the detector (the white cylinder). The distance between detector and sample varies depending on experimenter and experimental design.

In the following design, which is almost the complete geometry of our detection system, there is no visible lead with or without a closed door. The internal dimensions are roughly 28 cm in diameter and 41 cm wide, filled with the air in the condition present in the physical laboratory. The end-cap carbon epoxy has been used and is shown by blue color in the geometry. It is only possible to use carbon epoxy and beryllium, not both materials as the window entrance of the detector should be an easy passage for incident particle. The sample is the green component and the germanium detector's crystal is the purple part of the geometry built and presented in the following figure (Figure 7-3). Geometry provided by Canberra at left (data from detector user manual [108]) and simulated in the present work at the right.

The geometry developed in this section for the simulation purposes and shown in the following figure includes the following components:

- The lead shielding enclosure;
- The copper for lead enclosure protection (X-ray emission from the lead);
- The sample to be assessed for validation purpose;
- The germanium crystal of the detection system (including all major components related, vacuum, collection system);
- The carbon epoxy (or beryllium when the carbon epoxy is not used);
- The support (made of aluminum or other usable material that has less influence on γ radiation measurements);
- The cooling system.

The complete geometry is presented in Figure 7-4 using different transformations as well, for appropriate view. Similar complex geometries were developed by Britton in his thesis and published in different international journals [27, 42, 313, 53, 110, 142, 173, 173, 283, 286, 312]. Complex geometries and simulation are perspectives under construction and will be continuously built for the science better life. The top views and side views presented in Figure 7-4 allows different visualization angles and better understanding of the geometry of our system. As γ spectrometry is not as complex as a nuclear reactor, the detailed code built in this project for simulation can be requested by collaborators for comparative studies. As the complete code including different classes implemented and developed in this research are thousands of lines of C++ code, it is not recommendable to annex it to the present document.

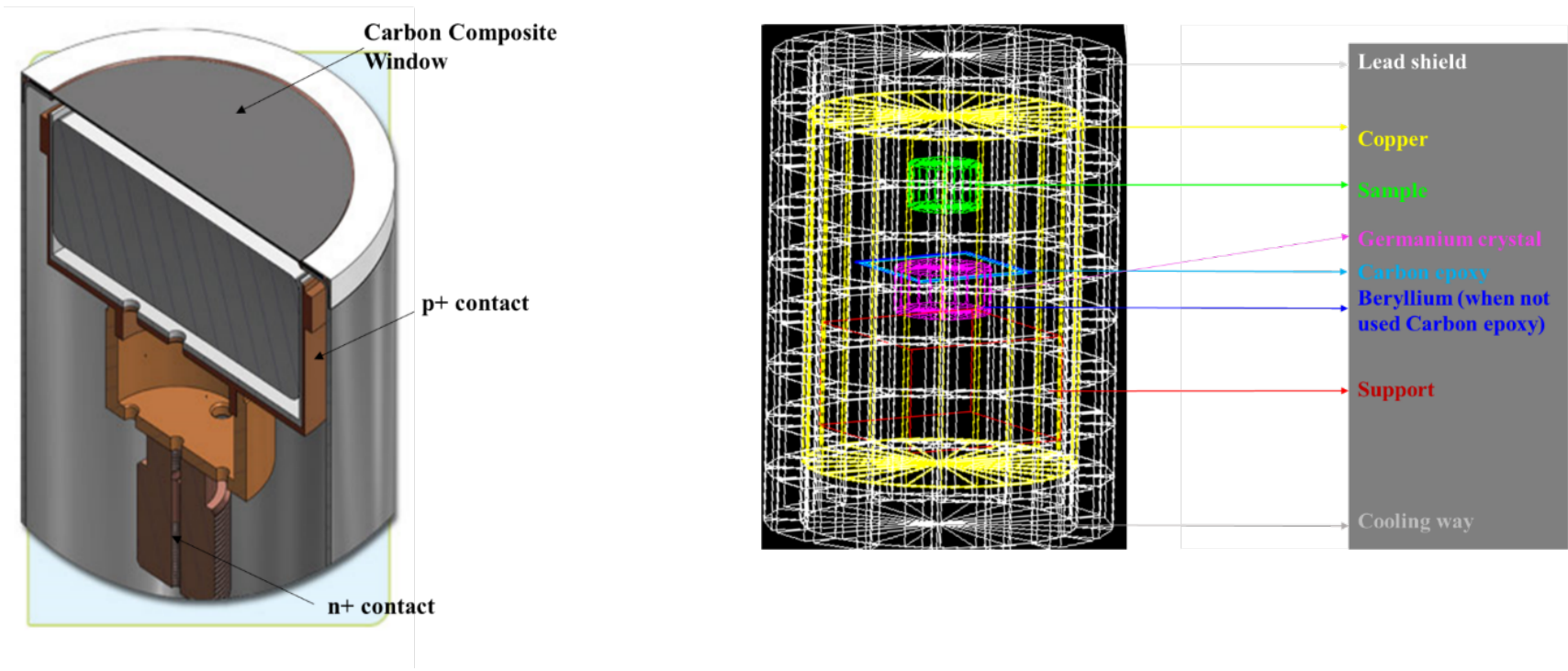


Figure 7-3: Geometry design of the detector for BEGe detector (model BE6530). The system's design has a lead shielding enclosure with 10 cm thickness (presented here in white color) and is jacketed by an external metal cask of 9.5 mm thickness. The graded lining is made up of a Tin (Sn) 1 mm thick surface and a 1.5 mm thick copper sheet (the part represented in yellow color).

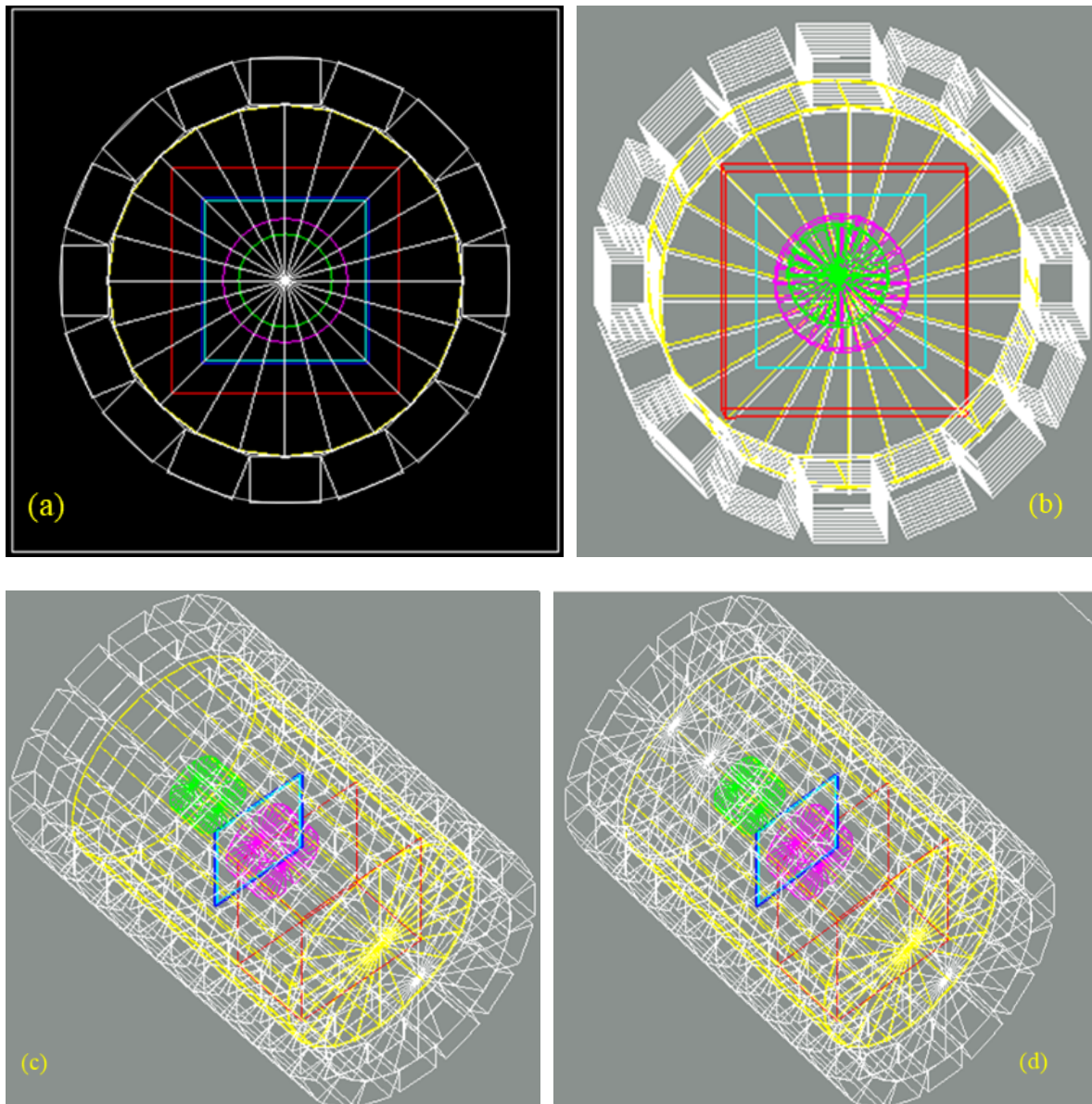


Figure 7-4: Specific geometric layout of the simulated system in 2D and 3D views: (a) two-dimensional top view of the planar representation. (b) Bottom view-three-dimensional representation resulting from (a) with small angle transformation. (c) 3D 45 ° inclined perspective geometry view using rotational transformation. The bulk of the lead shielding cask is open. (d) The lead cask cover is on the top of the detector in position ready for an acquisition. (c and d) 3D views without and with the cover on the top of the detector (lead shield capsule), respectively.

As shown in the above figures, simulating the geometry with rings for the best view of various components is more accurate and details transparent view for internal components without necessary perform a cut set or cross-sectional view. A commonly neglected important part in the high purity germanium detector's simulation is the structure of the sample in the detection system. For a given sample dimension, the sample should be properly disposed in the system to limit the sample sensitive detector volume distance. When this process is well set in practice contaminations are avoided in the laboratory environment, especially for the detector itself. For high sensitivity and large collection of photons from the decay process undergoing in the sample, the sample size should be as large as possible. But attention should be paid on the correction factors as self-attenuation, detection angle (which

defined the relative and geometrical efficiency of the detector). A perspective to consider for further understanding is the absorption of γ -rays within the sample under investigation itself which can be achieved by measurement and rarely by GEANT4 simulation (but parallel codes and software have been developed for this purpose) [22]. GEANT4 enables the creation of complex geometry.

Broad Energy Germanium detector has a low-form cylindrical shape that is of large detection area, entrance window being made of composite carbon epoxy. This design is an advantage for the system as the geometry allow one of the highest detection efficiencies among the semiconductor detector. Geometry and efficiency calibrations are expensive in term of time, technology, and cost. Therefore, it is possible to use Monte Carlo Simulation based on Geant4 toolkit to optimize the work consisting of using different source for efficiency calibration in the laboratory. The simulation of different sample's geometries and importation of the simulated calibration files in Gamma vision or Genie 2000 will probably reduce difficulties encountered during calibration process [2, 149]. In addition, it is possible to construct the real dimension of our sample geometry if known and built a personal MCA application for GEANT4 implementation with the physical system (as long-term perspectives).

Detectors might be obviously characterized by restrictive programming or language influence in various circumstances, be that as it may, Monte-Carlo simulation is a useful, valuable, inexpensive or cheap option that additionally provides more noteworthy adaptability, greater flexibility and gained time while determining the detector response and efficiency during an environmental measurement [2, 14, 101, 102]. But as many researchers in applied nuclear physics do not have computer programming advance knowledge, collaboration between different scientists and laboratory is a useful tool for the rapid progress of developed methods. As the detection geometry is completed, the efficiency simulation can be implemented.

7.3. Efficiency Simulation

Well-known activity sources have been used as unidentified samples to determine which method produces better or acceptable results. This comparative study was based on examination of acquired spectra and the measurement of radionuclide's concentrations. The estimate was based on two steps: first step consists of quantifying operation (activity calculation) using the experimental efficiency curve by applying self-absorption and true coincidence summing correction using Genie 2000 cascade summing correction [21, 22, 175, 314]. The second step consists of activity computation using the simulated efficiency's values from GEANT4 Monte Carlo code. Simulated values of the efficiency obtained from GEANT4 were compared to experimental value prior to their substitution if activity calculation procedures. The efficiency simulation required the optimization of the GEANT4 code used as the simulated BEGe detector covers a large range of energy from 3 keV to 3 MeV (including low range energy). As the efficiency is the most important parameter for quantitative measurement as the energy calibration is for qualitative characterization, agreement between simulated and experimental data should be proved less than 10 % at least at 95 % confidence level. If the uncertainties are less than 5 %, the obtained results can be confidently used for activity calculation. At this step, it is important to remember different parameters that account for the efficiency calculated in this project.

The geometrical efficiency expresses the ratio of the number of photons emitted towards the detector by the number of photons emitted by the source. This equation shows the only source-detector geometry of the geometrical efficiency. The geometrical efficiency of the detector is defined as follow, where Ω = solid angle between source and detector for a point source.

7.3.1. Full-Energy Peak Efficiency (FEPE): $\varepsilon_p(E)$

$\varepsilon_p(E)$ depends on the geometrical conditions and on the energy by the following equation:

$$\varepsilon_p(E) = \varepsilon_G \cdot \varepsilon_I(E) \quad 7-1$$

where ε_G is the Geometrical efficiency determined by the measurement conditions while $\varepsilon_I(E)$ is the intrinsic efficiency of the detector.

- Geometrical efficiency

Ω = solid angle between source and detector (sr) for a point source

For a point source:

$$\Omega = 2\pi \left(1 - \frac{d}{\sqrt{d^2 + r^2}} \right) \quad 7-2$$

and the Geometrical efficiency expresses the ratio of the number of photons emitted towards the detector by the number of photons emitted by the source.

$$\varepsilon_G = \frac{\Omega}{4\pi} \quad 7-3$$

This equation shows the only source-detector geometry of the geometrical efficiency.

- Optimization of the geometrical efficiency

For a point source:

$$\Omega_1 = 2\pi \left(1 - \frac{d}{\sqrt{d^2 + r^2}} \right) \quad \text{and} \quad \Omega_2 = 2\pi \left(1 - \frac{(d+e)}{\sqrt{(d+e)^2 + r^2}} \right) \quad 7-4$$

For very thin layer detector, $e \ll d \rightarrow$ the ratio $\frac{\Omega_1}{\Omega_2} \approx 1$ and for very thick detector, the ratio is

less than the unity.

- Intrinsic efficiency

$\varepsilon_I(E)$ describes the ratio of the number of counts in full-energy peak by the number of impinging photons. It depends on the incident photon energy (transmission [material composition, detector geometry arrangement], absorption [the medium where the photon travel before it is detected], and full-energy deposition). It is quite difficult to evaluate the exact value of intrinsic efficiency which change with time because of the complexity of exact material composition.

7.3.2. Calculation of the detector FEP efficiency

Transmission probability through material I with thickness x_i follows the Beer-Lambert law:

$$P_T(E, x_i) = e^{-\mu_i(E) \cdot x_i} \quad 7-5$$

Thus, the interaction probability in the same material is:

$$P_I(E, x_i) = 1 - P_T(E, x_i) \quad 7-6$$

To be count into the interaction spectrum, we assumed that the photon must be emitted in the Ω solid angle, cross the screens (air, window, dead layer, ...) without being absorbed, and be totally absorbed in the detector active volume (not passing through). In that case, the calculation of the detector efficiency is given by the following formula, including transmission term through screens, interaction in the detector volume term, and the probability of total absorption in the detector.

$$R^P(E) = \int_{\Omega} \prod_i \left(e^{-\mu_i(E) \cdot x_i} \right) \left(1 - e^{-\mu_d(E) \cdot x_d} \right) P_p(E) d\Omega \quad 7-7$$

$$P_p(E) = \frac{\tau_d(E)}{\mu_d(E)} \quad 7-8$$

where $P_p(E)$ is for low energy. It is a very complex multiple scattering dependent for high energies.

These equations describe the method used to assess the efficiency, the absolute efficiency of the detector, the geometrical efficiency, and the relative one. As the simulated source is isotropic one, the geometrical efficiency was taken into account in the simulation. According to the detector geometry and dimensions, the source-detector distance, and the source geometry and dimensions, the geometrical efficiency is variable. High geometrical efficiency allows high total efficiency and high-count rate, and consequently, the acquisition time for experimental spectra or the simulation time could be reduced considerably.

Approximately 7200 to 21600 second's data were obtained, and multi-source experiments were conducted to verify the model. Throughout the simulation process, the distance between the carbon epoxy window and the crystal was adjusted down to 4.7 mm, and the dead layers remained unchanged from the requirements of the detector supplier (the Canberra firm). As dead layer assessment is important for the detector lifetime and measurements' correction, it is necessary to use its actual value in the computation. The optimized parameters of the physical detector were important inputs for parallel simulation of the detector, especially the detector's response. As shown in Figure 7-5, correlations of the obtained spectrum with Genie 2000 and simulated data using GEANT4 code were made. As the measurement of an unknown sample is possible experimentally, it is not "possible" from the GEANT4 point of view as the decay data Library used for a sample should be known first. The easier simulation case is for single radionuclides in a point source, and especially in a cylindrical source bearing the sample geometry. After that, the simulated sample can include multi- γ source as contain and finally, a well-known source of calibration can be used. The spectra from ^{137}Cs , ^{152}Eu , and ^{57}Co point sources placed in the reference geometry are presented in the following figures. The agreement of the spectral shapes was astounding for the whole energy range and insignificant changes could be observed in the after-major peak area. This accounts for the data library used as well as the uncertainties of the simulation: the difficulty to reproduce a perfect geometry of both source and detector that reflects the physical actual system in the laboratory. In addition, the simulated sample used for experiment is not as pure as the simulated one, as it is under its environmental influence or degradation. The obtained results profiles demonstrates the GEANT4 capacities for reproducing γ -ray spectrometers through MC simulation [22].

Figure 7-5 displays Broad Energy Germanium spectra modeled using the GEANT4 Monte Carlo toolkit for single and complex sources, with improved geometry parameters. Both experimental and simulated data are presented on a graph for comparison and GEANT4 code validation. There are not significant differences between the modeled and the experimental spectra as can be seen in the figures (related to the four samples simulated). A sand NORM sample named SS1 was also assessed using GEANT4 code and its displayed spectra with the experimental one show agreements for both spectra (overlapping for the corresponding energy range). This results enables wealth tests for a variety of radionuclides found in the analyzed sample to be calculated and proves the GEANT4 code built to be effective in reproducing the experimental protocol from computer machine-base [22].

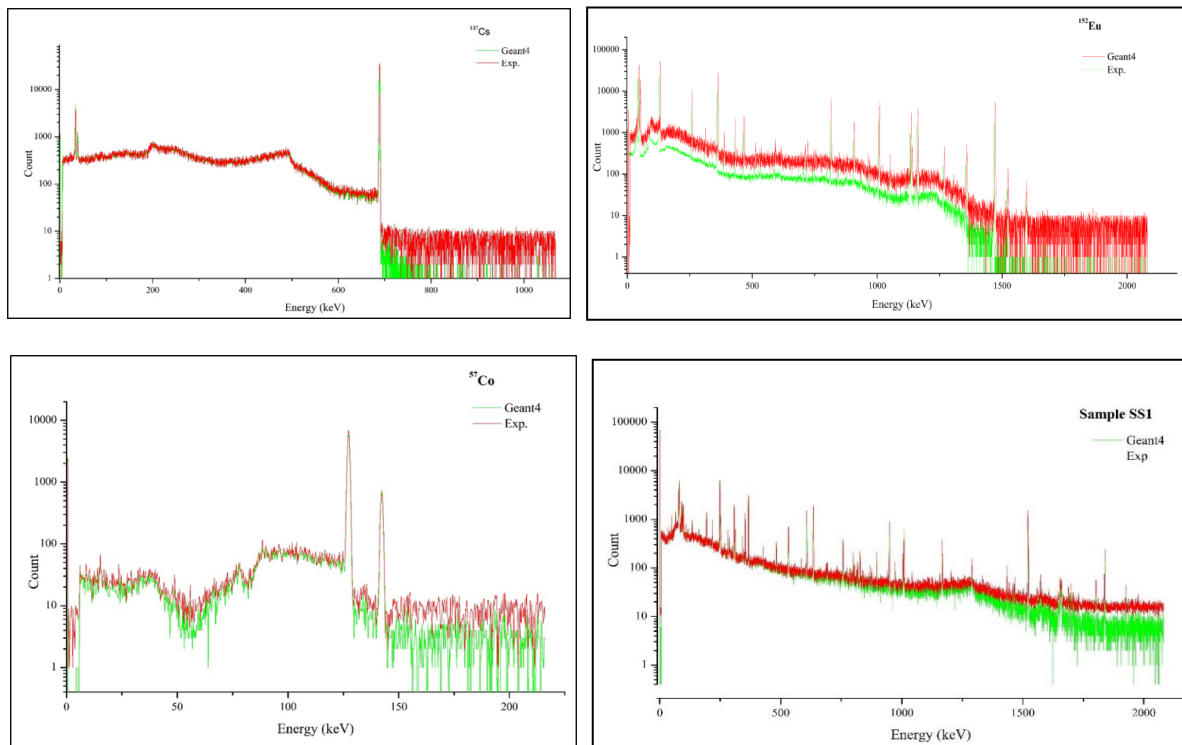


Figure 7-5: Energy spectra from experimental measurements and from the simulation using the full GEANT4 decay library. Both spectra of the following radionuclides are displayed: ¹³⁷Cs, ¹⁵²Eu and ⁵⁷Co source in both the convenient real and simulated geometry. The events were generated at a randomized coordinate within the source geometry, uniformly throughout the total source geometry, and sum peaks where photons (γ) were recorded could be clearly seen on the plotted spectra. Accordance is observed in the peak areas compared to the background area where the GEANT4 background is lower than experimental data. The last graph is for a reference sample named SS1.

The simulated performance dependent on GEANT4 toolkit using MC approach has been given and is in good agreement with our expectations. As shown in Figure 7-6, there is concordance at low energies and minor differences at high energies in the correlation between simulated and experimental efficiency as demonstrated by different curves. Using the following fitting function, simulated and experimental values were fitted [22, 315]:

$$\ln \varepsilon = \sum_{i=1}^n a_i \cdot (\ln E_\gamma)^i \tag{7-9}$$

where ϵ is efficiency to be evaluated, E_γ is energy given in keV, and a_i are fitting coefficients.

It was found that the best calibration measurement bend is obtained by using $i = 6$ for the detector used. The fitting approximated relation is used as part of any practical calculation to produce a reference curve that would be used. Figure 7-6 demonstrates modification bends for both experimental and modeled (simulated) geometry efficiency included in this chapter. The findings, simulated efficiency curves, can be interpreted as been in relatively good agreement with experimental values obtained directly from the experimental measurement. The improvements can be rendered taking into account the detector structure and the samples' chemical composition, density, and weight. These parameters are important in γ -ray spectrometry assessment as their change alter the result of a measurement. Recreated outcomes must reach legitimate confidence by fluctuating the above parameters [22].

This result shows the capabilities of the GEANT4 code built to simulate the response of γ -ray spectrometer. Comparison between the experimental and simulated calibration curves shows evidence and significance of the MC approach in applied nuclear physics, particularly in γ -ray spectrometry (this could be extended to other applications with the relation of random number or probabilistic character). The comparison shows good agreement between experimental and simulated results except for the multi- γ source with a high energy spectrum (at high energy range). Nonetheless, it was found that the reported discrepancies were likely due to ^{60}Co and ^{88}Y true coincidence summing. Such anomaly was likely due to the actual summing of uncertainty induced by the sample emission of ^{60}Co and ^{88}Y energy lines or γ -rays with energy close to that of the reference ray-lines (^{137}Cs , ^{152}Eu , ^{57}Co , ^{60}Co , and ^{88}Y). With respect to the estimation of environmental radioactivity, high energy spectrum value is limited: the primordial radionuclides released low γ -rays' energy and the ^{40}K is known to be the one with high γ energy emission at around 1460 keV. For this reason, the agreement between experimental and simulated data was found to be a good outcome for Broad Energy Germanium detectors (especially BEGe6530) made for environmental purposes. The data presented in this section of the project could be improved as the code is ameliorated. Results obtained using the GEANT4 toolkit were helpful and allowed us to calibrate the BEGe detector with considerable reduction of the radioactive source number [22].

The highest performance was shown by the modeling setup using 120 ml sample in cylindrical geometry, as shown in Figure 7-6 d and Figure 7-6 e. It is important to note that the 120 ml cylindrical geometry is set in our laboratory as a simple and prescribed geometry for more than 90 % environmental γ spectrometry monitoring. The parameter of the solid angle may help as its value is high, and the geometrical efficiency presented few paragraphs, before depends on its value. But at low energy rate, a small split between experimental and simulated graphs is observed in Figure 7-6 (d and e). Since the detector configuration designed with GEANT4 was not as full as the experimental detector, observed differences can be presumed to be predicted as stated by Park et al.: the secondary photon emitted after first interaction in the detection system [32, 33, 316]. Furthermore, the sample's self-absorption determines the result at low energy, and the self-attenuation should be taken into account by applying appropriate corrections. Since the dead layer thickness exceptionally influences the tests outcomes and may change significantly from its value defined by the manufacturer, it was important to re-evaluate its value in the case of the detector studied in the present research. Best results have to be obtained after the corrected value of the dead layer is applied. The application of the real value, different from the manufacturer's value, lead to the optimized efficiency result, but still some correction should be made to improve the obtained data (including geometry construction) [141, 295, 296].

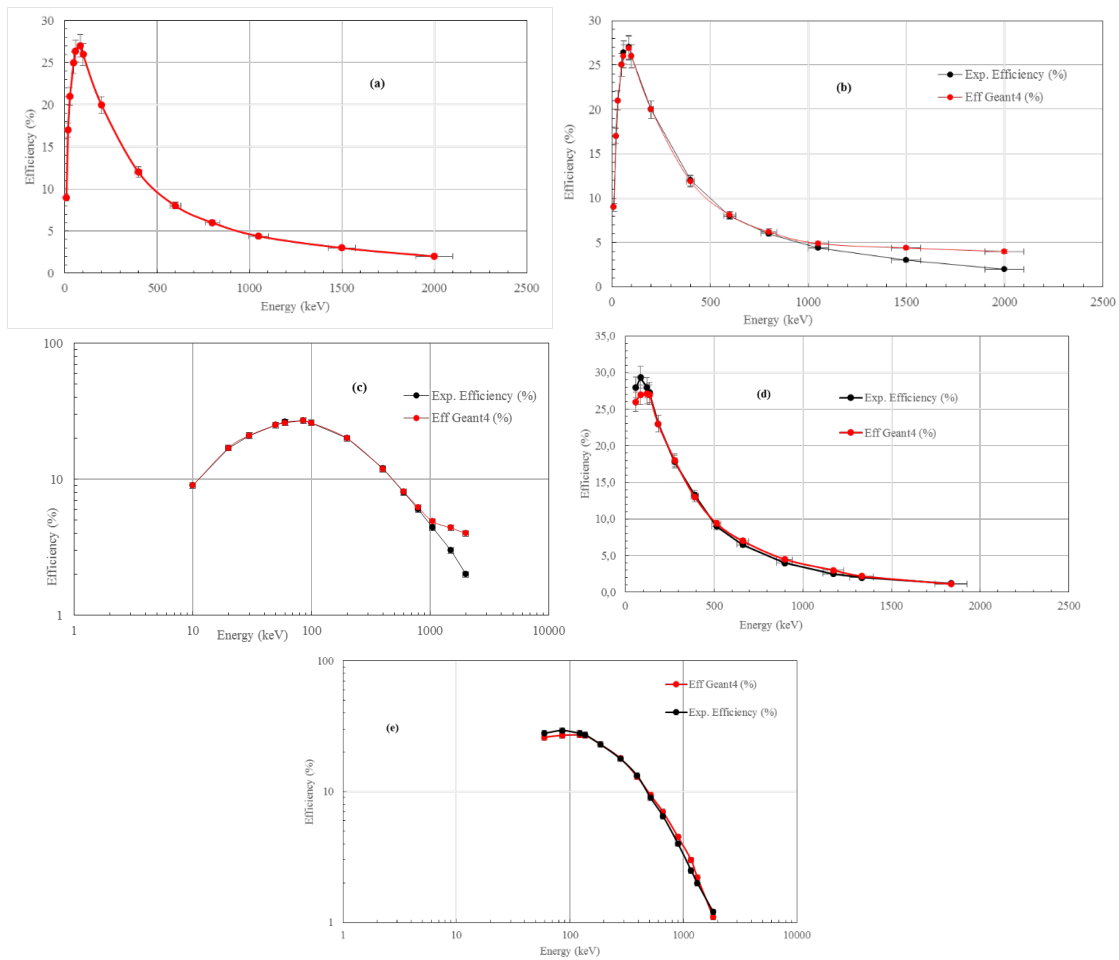


Figure 7-6: Simulated and experimental efficiency calibration curves for BEGe detector (BE6530 model). Red curve represents results obtained by GEANT4 and black represent experimental results in all presented graphs. (a) ^{152}Eu as single source. No comparison for single source for the efficiency purposes; (b and c) are results from 2nd sample of multi- γ source containing the following radionuclides: ^{241}Am , ^{152}Eu , ^{137}Cs , ^{109}Cd , and $^{60,57}\text{Co}$; (d and e) data from 120 ml cylindrical container of PET containing 320 Bq of soil sample (with the following chemical composition of material in percentage: $\text{SiO}_2=91\pm5$; $\text{Al}_2\text{O}_3=4.9\pm0.4$; $\text{K}_2\text{O}=2.0\pm0.1$; $\text{Fe}_2\text{O}_3=0.9\pm0.1$; $\text{TiO}_2=0.2\pm0$; $\text{Na}_2\text{O}=0.4\pm0$; $\text{MgO}=0.01\pm0$; $\text{CaO}=0.3\pm0$; $\text{MnO}=0.01\pm0$; $\text{P}_2\text{O}_5=0.01\pm0$). $(\text{C}_{10}\text{H}_8\text{O}_4)_n$ is the chemical formula of PET used with $n = 5$ in GEANT4 code. This sample code was described in Table 7-2

As previously mentioned, the estimated efficiency relied on the geometry and dimensions of the sample, density, and the distance from the detector. Efficiency changes completely as a result of these parameters for the detectors used as part of the γ spectrometry study. In this case, each counting geometry needs an efficiency match, using in the same geometry, a well-known standard source that includes multiple γ -ray energies: the ^{152}Eu reference can only be used for energy calibration. The calculation of the counting efficiency was guided by factors such as:

- The attenuation of photons within the sensor due to absorption in the sample content;
- The attenuation of photons in the canning material above the detector's entrance face;

- The fraction of photons emitted by the source that reaches the detector's sensitive volume; and
- The fraction of the photons hitting the detector that adds their contribution to the full-energy peak [32, 296, 317]. Because not all the photon that reach the detector and have an interaction could be count in the peak contribution. There is a recombination process and some scatterings that do not count for full peak absorption...

For all the mathematical plans that were used as part of the laboratory work, it is not experimentally straightforward to determine the efficiency esteems at different energy values. It is standard practice along these lines to get prepared calibration samples for analysis and to empirically access the detector's efficiency. Similarity must be preserved in all aspects between the reference samples and the field samples reserved for measurement. This contains the following characteristics: matrix composition, physical form, and dimensions. The arrangement of field sample in the same position with respect to the detector used for the efficiency assessment must be conceivable in the process. Calibration samples subjected to investigation should also contain different nuclides to protect the energy range of interest in the study. Therefore, operations of their measurement must be correctly understood and traceable. They must be mechanically solid (to avoid detector contamination) and chemically safe (to insure that the active elements are isolated from the matrix) [22].

As highlighted in the previous paragraph, it is really challenging to manufacture calibration source for efficiency purposes, considering all different geometries that could be used for a measurement in the laboratory. Also, buying calibration standard sources that satisfy each of these requirements is generally impracticable, and the researcher is constrained to set this up in the laboratory environment. It requires a lot of improvement, in terms of fair concerns, and the laboratory inspector (for quality control and quality assurance purposes) should periodically discuss the matter. The problem can be simplified to some degree if a fixed number of geometric configurations for sample preparation is defined with the goal of decreasing the number of efficiency calibration samples. The previous plan should be applied to improve the detector geometry's significance and to perform another practical calculation using more appropriate reference materials and associated geometries [294, 296, 318, 319]. Improvements can be rendered considering the detector structure and the sample's chemical composition and thickness. Through the modification of these parameters in the program or algorithm used in the GEANT4 code, simulated results obtained must approximate the real value with sophisticated sample geometry and specific detector dimensions and shape.

7.3.3. Result validation

The observed mean discrepancy was found to be less than $\pm 2\%$ between the simulated and experimental efficiency as can be seen in Figure 7-7. The discrepancies could likely be the effect of the inadequate knowledge of the real detector shape and dimension, and incomplete detector crystal charge-collection of the signal selection used in our simulation. Figure 7-6 shows that both experimental and simulate output values are too closed and that the simulation findings can be used properly for our detector calibration. It is usually too difficult to obtain less than 2 % confidence in both experimental and simulated results. As 2 % is smaller than 5 % acceptable value, the result obtain in the present thesis is an outstanding achievement. In the case of environmental radioactivity monitoring, the Monte Carlo simulation functionality based on the Geant4 toolkit would be more suitable as demonstrated from the previous result. In particular, the simulations will help to determine the Broad Energy Germanium detector's optimal operating mode for a specific energy range [22].

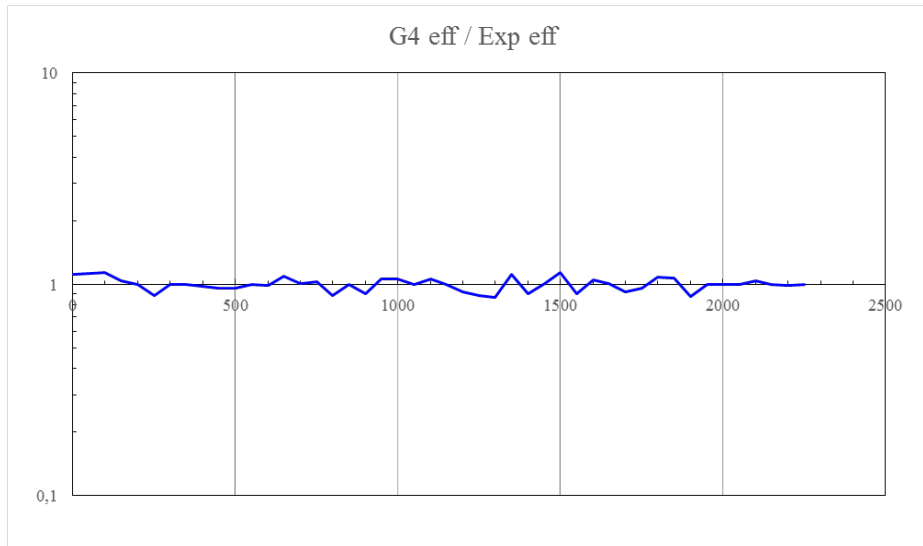


Figure 7-7: Ratio of the simulated and experimental efficiencies depending on γ energy. The average fluctuation ration between both experimental and simulated values is less than 2 %.

Table 7-3 includes the correlation of simulated and experimental values obtained in this analysis. By comparing experimental or simulated values with reference values, all investigated radionuclides showed good agreement. Therefore, it can be concluded that the GEANT4 model developed in this thesis can be used for the detector efficiency simulation (the code will be adapted for γ spectrometry measurements). In terms of variance reduction between experiment and computation, the ^{152}Eu displays the largest value, but the proportion of standard deviation at 95 % confidence level highlighted a strong agreement.

Table 7-3: Simulated and experimental values of the activity concentration obtained with the mix γ standard source SS1. Simulated activity concentration values are obtained with efficiency curve from GEANT4 simulation presented in Figure 7-6.

Nuclide	Energy (keV)	Emission probability	Activity concentration (Bq/kg)					Sim/Exp ratio
			Experimental	%Unc	Simulated	%Unc	Target values	
Am-241	59.54	0.36	418.20	2.60	398.00	2.23	420	0.95
Cd-109	88.03	0.04	1510.80	6.20	1495.68	6.21	1550	0.99
Co-57	122.06	0.86	43.30	1.50	44.78	1.53	45	1.03
Cs-137	661.66	0.85	370.10	1.90	367.37	1.62	380	0.99
Mn-54	834.84	1.00	190.30	1.40	193.28	1.29	200	1.02
Y-88	898.04	0.94	139.80	1.90	143.83	1.58	140	1.01
	1836.20	0.99	139.80	1.90	143.83	1.58	150	1.01
Zn-65	1115.55	0.51	329.90	1.90	329.06	1.80	335	1.00
Co-60	1173.24	1.00	398.20	1.50	410.32	1.77	400	1.03
	1332.50	1.00	398.20	1.50	410.32	1.77	420	1.03

7.4. Conclusions

The present study used GEANT4 based MC simulation to model the HPGe detector (BE6530 model) geometry and efficiency response. The addition of a simple variance reduction scheme to represent only the primary photon, released in the direction to the effective area of the detector, simplified the analysis and enabled the time consumption reduction for calibration procedures. Simulation and importation of different sample geometries from the GEANT4 to the Genie 2000 software used for γ spectrometry assessment is then the closure task for this achievement. It reduces the difficulties encountered during efficiency calibration of the detector in the laboratory. Therefore, when established, the actual dimension and shape of our sample geometry can be created from GEANT4 code and the simulated result used for activity calculation. BE6530 detector's actual geometry was designed, and its efficiency response was performed. Using Qt and OGL visualizations, 2D and 3D geometries were created for geometry views and display. Because of the best views it offers, rings have been used for geometry design in the displayed geometry results.

For experimental measurements, the multi- γ reference samples used in our laboratory were used. Comparison of experimental and simulated calibration curves shows good match for low γ energies and a slight difference for large γ range energies. Discrepancies are likely due to a real ^{60}Co coincidence summing effect as it emits two different γ -ray lines. It was found that the γ spectrometry approach can be used with MC methods based on GEANT4 developments. The obtained results were found to be more accurate and precise compared to experimental values. Consequently, this approach was found to be a reliable, affordable, reliable, and time-gaining alternative which additionally offers more prominent adaptability when deciding the response and efficiency of the detector during an environmental monitoring assessment.

As new capabilities are being established to tackle the high-energy research concerns, particularly nuclear physics and γ -ray spectroscopy, the increasing use of GEANT4 in other fields will also lead to new developments in the toolkit. It is expected to model and provide more accurate geometry response to γ spectrometry studies in the near future, with all components varying from protection (shielding enclosure) to electronics and their contribution to the low background γ -ray measurements. Monte Carlo methods in light with random sampling are widely used as a part of various fields for the ability of tracking issues with an expensive number of coupled degrees of freedom. Simulating the geometries of different samples and then, exporting computed measurement files in Gamma vision software or in Genie 2000 can lower and reduce the difficulties encountered during the process of efficiency calibration.

CHAPTER 8. CONCLUSIONS AND OUTLOOK

8.1. General conclusions

The detection of γ photons is a technique in progressive development and with an increasing range of applications, including the environmental radioactivity assessment. In this thesis we used γ spectrometry technique to assess radioactivity level in samples from both campuses (campus 1 and 2) of the University of Douala and the seven biggest sand quarries in Douala city and surroundings. In parallel, X-ray fluorescence (XRF) spectrometry using Energy Dispersive XRF (EDXRF) and Wavelength Dispersive XRF (WDXRF) were used for elemental characterization of the same samples. To improve the efficiency of the germanium detector used as well as calibration methods, Monte Carlo simulations based on GEANT4 Toolkit were introduced with the objective of the validation of the study and the improvement of scientific used of simulation for efficiency calibration of germanium semiconductor based detectors.

The study used the combination between γ spectrometry-ray, development of related Monte Carlo (stochastic simulation that represents any method which utilizes the sequences of random numbers to realize the simulation) method, and the GEANT4 toolkit for γ -ray spectrometry simulation (simulation of the interaction of photon through matter) validation. The simulation was focused on Broad Energy Germanium detector used in our laboratory (the model BEGe 6530). The chapter 2 of this thesis reported detailed information about the γ -ray interaction with matter. The photon (γ) interaction processes were discussed with their interaction cross-section. As the γ -ray interaction is defined in term of probabilistic events, reference data were provided for clarification. It was very important to illustrate such interaction of radiation with matter before introducing the experimental method used during this thesis: the γ spectrometry method. Chapter 03 presented the methodology of γ -ray spectrometry and metrology of γ -ray. The description of the sampling method, sample preparation, and the selected sites for sampling was done and presented accordingly. The detection system details were described with different major parts of the BEGe necessary to understand the detection procedure. This part described formula used to assess activity concentration as well as radiation hazards and radiological parameters as radium equivalent activity in geological samples, Outdoor absorbed γ dose rate, Outdoor Annual effective dose (AED), External and internal Hazards indexes, and α and γ indexes (I_α, I_γ).

Chapter 4 discussed the γ -ray spectrometry results obtained for both studied sites (two campuses and extending area of research). The parameters presented in the above paragraphs were assessed. The chapter presented the activity concentrations of ^{226}Ra , ^{232}Th , and ^{40}K found in samples from the two campuses of the university of Douala and sand samples used as building materials from the Douala Littoral Region of Cameroon (from the seven investigated quarries). Radiological parameters and radiation hazards as radium equivalent activity, absorbed γ dose rate in indoor air and corresponding annual effective dose, external and internal hazard indices were calculated to qualify and quantify the radiological hazard associated to the studied zones. Chapter 5 presented X-ray fluorescence methodology and result of analysis of the samples from the campuses of the University of Douala as well as those from the extending area of study in this thesis. All details from experimental protocol to the obtained results were presented in this part. Elemental characterization of samples was performed through XRF analyses (based on both EDXRF and WDXRF) in view to determine their elemental composition. The obtained data were used for the assessment of geological provenience and origin of the study area.

Chapter 06 and chapter 07 presented the Monte Carlo methods and GEANT4 toolkit used for simulation as well as the result of validation. The description of the principle of the method was detailed in the first chapter. The content of Chapter 6 also included the detailed description of the use of random number in MC simulation. Principal classes used in GEANT4 for an appropriate simulation of the detector efficiency were described. The second part focused on the obtained results in terms of Geometry of the detection, Efficiency calibration of the Broad Energy Germanium detector based on GEANT4, and the validation of the code built in this thesis. The attention had been given on the reproduction of the geometry by the GEANT4 code and the simulation of the efficiency response of the BE6530. Sophisticated geometries built were presented in graphs obtained with 3D and 2D visualizations. Efficiency curves were plotted and compared with the experimental values. Good agreements between experimental and simulated efficiency were highlighted by the correlation between both values. The methods used in this thesis were found to be very prominent and we can deduce the specific conclusions from the obtained results presented here.

8.2. Specific Conclusions

8.2.1. γ Spectrometry measurements and results.

i) Methodology

The measurement of radioactive material or the determination of exposure due to natural radionuclide in environmental samples is a process that aims to reliably and efficiently identify any isotopes present within the source matrix, and accurately quantify these to allow interpretation of a variety of factors. These factors may include safety concerns, doses that exposure may incur, and the origin of the isotopes that are present. For non-destructive testing, γ -ray spectroscopy provides the most effective measurement technique, as γ -ray emissions may be the only detectable radioactivity to escape the source matrix (as γ range is high compared to that of α or β particles). Typically, larger and more efficient detectors are employed to collect more radiation, and therefore enhance sensitivity of the system. The most used in the recent decades are semi-conductor detectors since the semi-conductor technology has been developed and improved worldwide (from cellphone, computer, and TV to spaceship object).

Two HPGe detectors were used in this research, one in Cameroon: a Broad Energy Germanium detector (BEGE-6530 model) and a second one at the Laboratory of Nuclear Physics of the University of Liege in Belgium: a HPGe (GC0818-7600SL model) [2, 101]. It is important to highlight that there were many HPGe detectors in Nuclear Physics lab in Belgium, but only one was used for our environmental assessment-based γ -ray spectrometry. The fields of the experiment were well-known regions that covered the two campuses of the University of Douala – Cameroon, a site located within the basin of Douala, named “Douala – Bassa” zone ($04^{\circ} 03'14.8'' - 04^{\circ} 03'29.7''$ N and $09^{\circ} 44'00.1'' - 09^{\circ} 44'45.2''$ W). For the second part of the experimentation, the fields of experiment were carried out in seven quarries in the vicinity of Douala and its surroundings, namely “*Bonaberi Bonamikano, Northern Akwa, Bois-de-Singe, Youpoue, Youpoue-Bamenda, Dibamba, and Village*”. The experimental process performed in view to obtain valuable result at the end follows the following steps:

Step 1: Sampling and sample preparation

During sampling processes, details about site location, sample point number, geographical coordinates, and sample type were recorded. Samples were packed-in and properly sealed into polyester bags in order to avoid cross-contamination during shipment and transportation with other samples. Each bag or container was correctly set. Throughout sampling process, drying, and grinding, all the

required precautions were taken in the use of equipment to prevent cross contamination of samples. Cleaning system for both in-situ sampling and in-lab preparation was a major component of the procedure. To reach Secular Equilibrium, samples were sealed and stored for at least one-month prior the sample acquisition and analysis. Samples were weighted and the data recorded for Genie 2000 input during the activity concentration calculation step.

Step 2: Detector calibration procedure: energy and efficiency calibration

Both energy and efficiency calibrations are required for qualitative and quantitative assessment of environmental samples, respectively. During determination of intensity of the natural radionuclides a careful selection of region of interest (ROI) on the spectrum and with consistent window for all samples was ensured. The standard reference materials provided by IAEA used for calibration (usually the energy calibration step) of the γ -ray detector and calculation of activity of the samples provided a standard procedure for the analytical technique of measurements. For efficiency calibration, Monte Carlo methods base on GEANT4, LaBSOCS, or other software are developed. In our laboratory, LabSOCS was provided by Canberra and this project developed a GEANT4 setup for detector calibration.

Step 3: Measurements of the activity concentration

This part took into account the background and subtracted it from the spectra to be analyzed before any calculation. Some quantities as mass of the sample and date of the acquisition are necessary as inputs as the decay scheme of the series could be involved. The computed process is based on the equations presented in the Chapter 3 and the results are displayed with uncertainties in the unit of Bq / kg.

Step 4: Assessment of radiation hazard and radiological parameters

This step is based on the evaluation and interpretation of different quantities as Radiation hazard, Outdoor absorbed γ dose rate, Outdoor Annual effective dose (AED), External and internal Hazards indexes in the investigated soil and sand samples. These parameters were evaluated using equations described in Chapter 3.

ii) Results

Concerning soil samples from the University of Douala, the level of activity concentration was very low as well as that of the radium equivalent activity. In addition, this part of study was completed by comparing results from two different detectors in view of pointing-out recommendations on the use of germanium detector for environmental monitoring. The broad energy germanium detector showed the best stability for assessing samples in view of measuring low energy γ -ray (^{226}Ra and ^{232}Th) emitters, while the GC0818-7600SL-model detector showed stability in measuring high γ -ray emitter (^{40}K). Comparison with values measured in different countries for the same type of sample showed comparable results in the interval recommended by UNSCEAR [1, 2, 49, 101]. From the safety point, the investigated area was not found to be a high background radiation area, and there is not evident risk related to radiation exposure to be highlighted here.

For sand samples from the quarries in Douala and surroundings, the measured specific activities of ^{226}Ra , ^{232}Th , and ^{40}K in this thesis were lower than the related common worldwide values except that of the Thorium. The average investigated value of Radium equivalent activity (Ra_{eq}) in the studied samples range from 47 to 216 Bq kg^{-1} , which are underneath the worldwide value of 370 Bq kg^{-1} recorded by UNSCEAR. The α and γ index values were found to be smaller than both the internationally accepted 0.5 and 1 values, respectively. The values of the internal and external risk indexes (H_{in}

and H_{ex}) correlated with the use of the analyzed samples were found under the reference value of unity. The absorbed dose rate level varied from 22.17 to 101.47 $nGy.h^{-1}$ with a mean value of 58.9, similar to the recommended worldwide value of 60 $nGy.h^{-1}$. The outdoor annual effective dose rate in air ranged from 27.19 to 124.45 $\mu Sv.y^{-1}$, was recorded below the 1 $mSv.y^{-1}$ internationally accepted value. It is therefore assumed that the radiological parameters collected in the present study are ordinary and within the prescribed limits. Consequently, in the design of buildings, the use of the investigated sands as building material is considered to be radiologically safe for occupants, based on the assessed parameter. In addition, thousands of workers in various sand quarries in the Littoral region of Cameroon are below international exposure limits for the public [2, 101].

The values of terrestrial radionuclides detected can be used as a valuable inventory from a practical viewpoint to produce a radiation map of the area at stake and to track and measure possible changes to environmental radioactivity due to natural radioactivity and human actions. The obtained results indicated that the average dose rate received by the residents is less than 1.0 $mSv year^{-1}$, attributable to sand building use in Douala [1, 2, 98, 101]. The outputs from this research will be useful to assess the radiation hazards of sand building material in humans and to initiate a sand database together with a radiological map of the area at stake.

8.2.2. X-Ray Fluorescence Analysis

For X-Ray Spectrometry analysis, sampling process was the same as in γ -ray spectrometry (same samples analyzed), and sample preparation was based on the following steps:

- Grinding and Sievert sample to a grain size lower than 100 μm ;
- Glass Discs' preparation and Pressed pellets;
- Utilization of reference samples for the equipment setting;
- Matrix Corrections; and
- Validation of XRF results

Equipment description was detailed to understand the experimental protocol and the used of reference materials and PyMCA software for data analysis.

XRF-based EDXRF processing was conducted to chemically classify numerous soil samples from the Douala-Bassa region covering the University of Douala campuses (I and II) and sand samples from seven large quarries in and around Douala. The same sample used for γ spectrometry were used for X-Ray Fluorescence analysis base on the same sampling method. Only the sample preparation method differs from γ -ray spectrometry to Energy Dispersive X-Ray Spectrometry (EDXRF) and Wavelength Dispersive X-Ray Spectrometry (WDXRF) [218, 220].

For samples from the two campuses of the university of Douala, the characterization consisted of elemental composition investigation of different samples using an SDD spectrometry chain (Silicon Drift Detector). The most important part of the elemental analysis after spectra acquisition was carried out using the PyMCA software package. EDXRF values obtained in this study are useful to characterize the soil samples from the Douala region of Cameroon as Fe-soil. All spectra from the eighteen soil samples revealed that measurements were well performed. Correlation graphs were plotted in view to determined geological characterization of the investigated area. Correlation Graphs showed a positive gradient between the variation of K_2O and Al_2O_3 . The positive slope suggested a relative abundance of these components that are basically adjusted by the substance of mud minerals. This fit our findings and proved that analyzed samples in this study have the same origin and provenience (according to

the obtained concentration values of Al_2O_3 , TiO_2 , Fe_2O_3 , MgO , CaO , Na_2O , and K_2O). The investigation about discriminant functions of Roser and Korsch [253, 258–260] allows us to classify the geological provenience of analyzed soil samples. It can be observed that soil samples can be classified chemically as Fe-soil. All analyzed soils were found to be illustrative dregs from Continental margin.

For the analyzed sand samples, Elemental characterization was performed through both EDXRF and WDXRF analyses in view to determine their elemental composition. The after-analysis data were used for the assessment of geological provenience and origin of the study area. From the obtained results (tables and different diagrams), it was observed that the investigated area's geology is formed by sediments from Passive margins and probably come from the degradation (or weathering as the effect of this process in the region is noticeable) of materials of the "Gulf of Guinea", where the main characteristics of the rocks are acidic intrusive igneous and metamorphic [320]. The Gulf of Guinea is characterized with a diversified geological environment, comprising volcanic islands with a sedimentary formation currently under intense underground activities (hydrocarbons development).

The seven sampling sites were dispatched around the Atlantic Ocean in the coastal region of Littoral - Cameroon. Their classification as passive margin sediments confirm the fact that the Douala basin tectonic plate belongs to an active plate because it was formed by a transient lithosphere-determined by sedimentation process of an ancient rift. The Douala basin is therefore a transition between the oceanic and continental lithosphere. The result from X-Rays Spectrometry measurements showed significant importance for various elements, both major and minor. It suggested the relevant Si and Al amount that could be very useful for the raw material used in glassmaking manufacturing process in Cameroon (and the sub-region) as well as the scientific involvement in the subgroup description. It also contributes to significant appreciation for the continent's characterization.

8.2.3. Monte Carlo simulation and GEANT4 Validation

As new capabilities are being established to tackle the high-energy research concerns, particularly nuclear physics and γ -ray spectroscopy, the increasing use of GEANT4 in other fields will also lead to new developments in the toolkit. It is expected to model and provide more accurate geometry response to γ -ray spectrometry studies in the near future, with all components varying from protection (shielding enclosure) to electronics and their contribution to the low background γ measurements. Monte Carlo methods in light of random sampling are widely used as a part of various fields for the ability of tracking issues with a large number of coupled degrees of freedom. Simulating the geometries of different samples and then, exporting computed measurement files in Gamma vision software or in Genie 2000 can lower and reduce the difficulties faced during the process of efficiency calibration.

Monte Carlo methods in light of random sampling are widely used as a part of various fields for the ability of tracking issues with a large number of coupled degrees of freedom. In this work, the overview of Monte Carlo methods was effectively discussed for simulations in γ -ray spectrometry field. Details were presented in three parts: The Monte Carlo methods, a mathematical formulation, and the Geant4 toolkit [42, 53, 306]. An overview of Monte-Carlo simulations methods has been presented here for the application of γ -ray spectrometry. It reduces the difficulties encountered during efficiency calibration of the detector in the laboratory. Therefore, when established, the actual dimension and shape of our sample geometry can be created from GEANT4 code and the simulated result used for activity calculation. BE6530 detector's actual geometry was designed, and its efficiency response was performed through MC simulation based GEANT4. Using Qt and OGL visualizations, 2D and 3D geometries were created for geometry views and display. Because of the best views it offers, rings have been used for geometry design in the displayed geometry results.

For γ -ray spectrometry simulation, the combination of γ -ray spectrometry, the design of the related Monte Carlo system, and the GEANT4 (GEometry ANd Tracking) toolkit has been established for better feature. The main objective was to validate in our laboratory, the simulated models of broad energy germanium (BEGe BE6530 model) detector geometry. This third part of the research was devoted to simulating the HPGe detector (BE6530 model) geometry and efficiency response. The Monte Carlo methods have been used successfully in this section to model the HPGe detector. For experimental measurements, the multi- γ reference samples used in our laboratory were used. Comparison of experimental and simulated efficiency calibration curves shows good matches for low γ energies and a slight difference for large γ energy range. Discrepancies are likely due to a real ^{60}Co coincidence summing effect as it emits two different γ -ray lines. It was found that the γ spectrometry approach can be used with MC methods based on GEANT4 developments. The obtained results were found to be more accurate and precise compared to experimental values. Consequently, this approach was found to be a reliable, affordable, accurate, and time-gaining alternative which additionally offers more prominent adaptability when deciding the efficiency response of the detector during an environmental monitoring [34].

For the detector systems themselves, a combination of experimental work and Monte Carlo simulation has been used to develop and validate computer models of the laboratory systems, which have then been utilized to improve the performance of all system components. Monte Carlo models (using the GEANT4 toolkit) were initially used to reproduce the detector response of a BEGe detector system, with the geometry parameters tuned to reproduce the peak efficiencies for a range of photon energies. Simulations of the detector shielding materials revealed that the majority of 'background' events originated from source photons that scatter out of the shielding, and into the primary crystal. This can be reduced by increasing the interior radius of the cave and minimizing the amount of low Z material in the immediate vicinity of the detector. Experimental results were contrasted with the model performance curves using MC methods based GEANT4. Calculation errors for simulation as well as experimental efficiency curves were assessed to see if the results of the practical calculation came below sufficient cut-off points [22]. Validated, the models developed were used for routine detector characterizations, and proved to be useful for the efficiency calibration of sources that were supplied in non - standard configurations.

8.3. Future Work

Building upon the tools and designs developed as a result of this project, several opportunities have been identified that may improve the detection limits further for high sensitivity of the γ -spectroscopy systems and related techniques as XRF, PIXE, and PIGE. Also, the γ -ray spectrometry system based on Germanium detector is not perfect in term of efficiency calibration. Improvements and optimization are still required and different ways of determining the efficiency curves. As the outcome of the present thesis highlighted, the GEANT4 code built is still under optimization process taking into account the real geometry and shapes or the detector sensitive volume, the sample, and the measurement environment. There are many tasks to be pursued as life goal or to be shared by other researchers in the field with strong interest.

Firstly, the combined and simultaneous use of PIXE (Particle Induced X-ray Emission) and PIGE (Proton Induced γ -ray Emission) techniques for the analysis samples will be implemented in the future. Interest on these nuclear technics has been shown with experiments performed on the samples from Douala. The analysis and interpretation are one of the perspectives of this thesis. Using PIXE and PIGE for geological sample characterization can be time gaining and very useful for transition to the new technology and simulation capability of the accelerator systems using Monte Carlo Method

based GEANT4 toolkit. This extension would be in term of experimental work in the laboratory, as irradiation was performed on some samples from Douala.

Secondly, the use of Monte Carlo method based on GEANT4 toolkit to simulate the XRF (EDXRF and WDXRF) would be planned soon. This will be with the objective to check whether or not the calibration procedure using reference samples from institute of standards can be improved, and how to improve it if so. This project would be held in parallel with the PIXE and PIGE Monte Carlo validation by GEANT4. Since laboratory experiment or measurement is, as any simulation and physical measurements, affected by errors, the objective would be the reduction of uncertainties and the optimization to fit the exact values. Considering the energies of emitted photons by the atomic de-excitation package, the error values will be compared with NIST database (with the objective of setting it down to less than 2.5 %), and well below for most of the transitions. Regarding K-Shell and L-shell transitions, the relative error shows a clear dependency on atomic number; Iron falls within the elements showing themselves to have a higher emission energy than Geant4's simulated one. Attention would be paid on K-Shell deviance in comparison to NIST database. For this purpose, we have to implement a Geant4 code that simulates an energy dispersive X-ray fluorescence spectrometer as well as wavelength dispersive X-ray fluorescence spectrometer [306, 321].

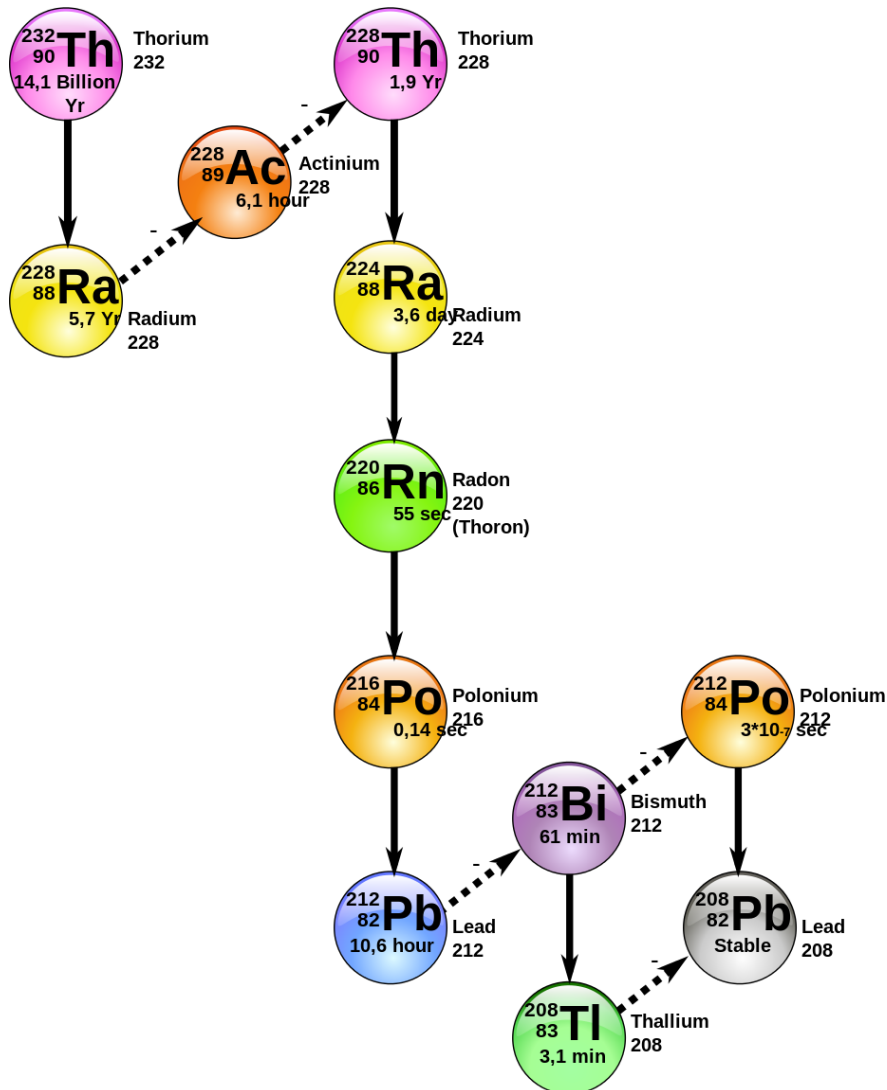
Finally, an elemental composition of samples from Cameroon will be largely developed and the determination of the relation between radiation exposure/ attenuation that they may lead to the inhabitants or public in their daily life will be the main task. Additionally, it will be established the link between the elemental composition of these studied areas, the radioactivity they produce, and the relative dating of the sediment. Projection of Monte Carlo method will allow the characterization of samples from any other place in Cameroon as in the world. As other developed Monte Carlo Codes can be used for detector simulation, comparison between different codes will be performed in view to use the most appropriate setup for physical characterization in the laboratory. The Particle and Heavy Ion Transport code System (PHITS) will be the next code for detector simulation in this regard.

Appendix A: Decay Chains

There are four major naturally occurring decay chains, and each is known by the most stable isotope within it. Three of these (^{232}Th , ^{235}U , and ^{238}U) are long lived that they are still present within the earth in significant quantities, allowing us to measure them today. Small amounts of the fourth series (^{237}Np) may also be present in the environment due to the artificial production of ^{241}Pu (the head of the ^{237}Np decay chain) since the 1940's. Naturally occurring ores of these materials are generally assumed to be in secular equilibrium, however geological activity or isotope extraction/ore processing can significantly alter their concentration and equilibrium. Each decay chain is detailed below (note that where additional decay branches are identified in the captions, these are restricted to branches that decay via α and β modes) with illustrations [53].

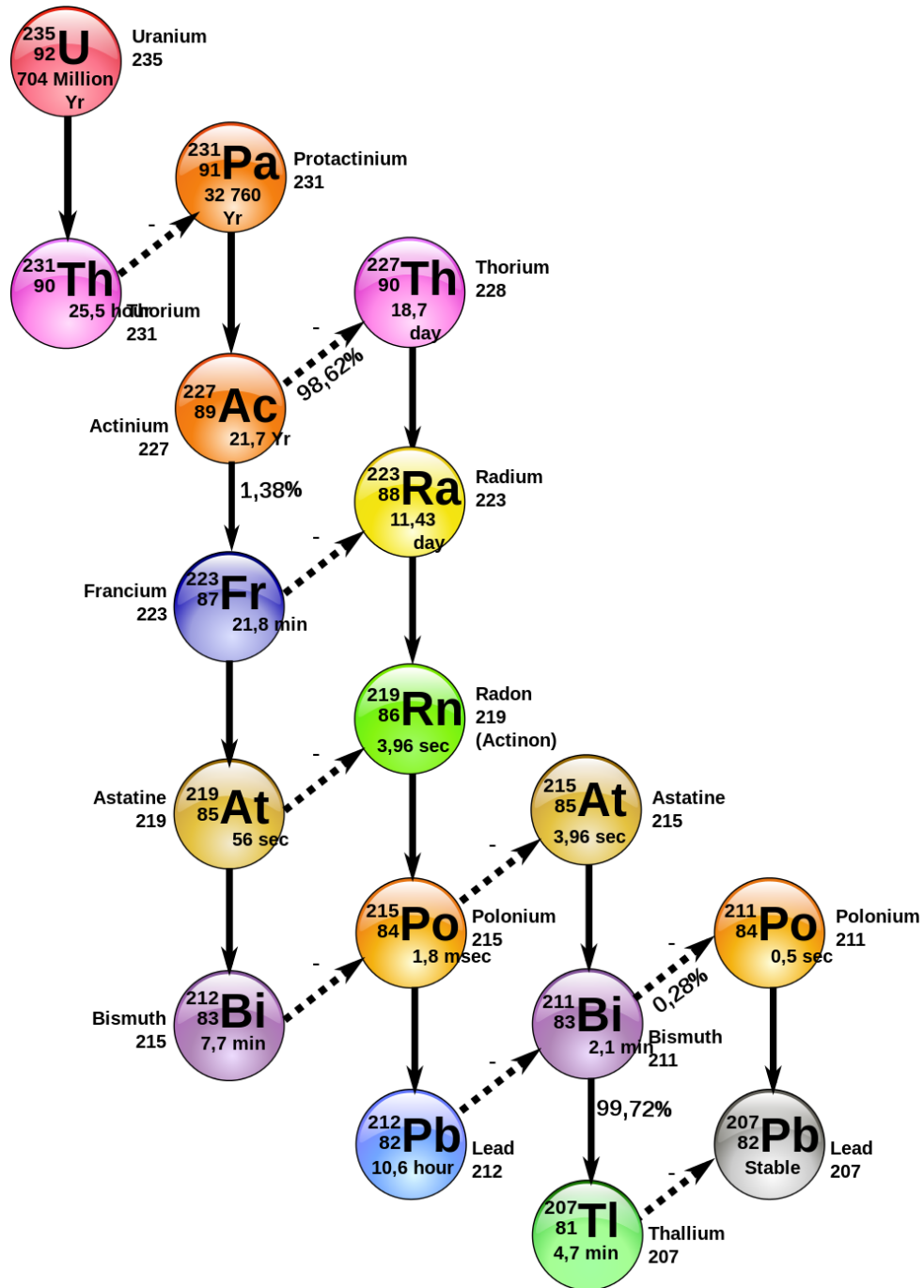
A.1. The ^{232}Th decay chain.

All nuclides in the decay chain will be present in samples that contain thorium, and if left undisturbed for a sufficiently long time, be in equilibrium with ^{232}Th (with the possible exception of ^{220}Rn , which may escape the sample as it is a noble gas). ^{232}Th makes up almost all of the natural thorium found in the earth.



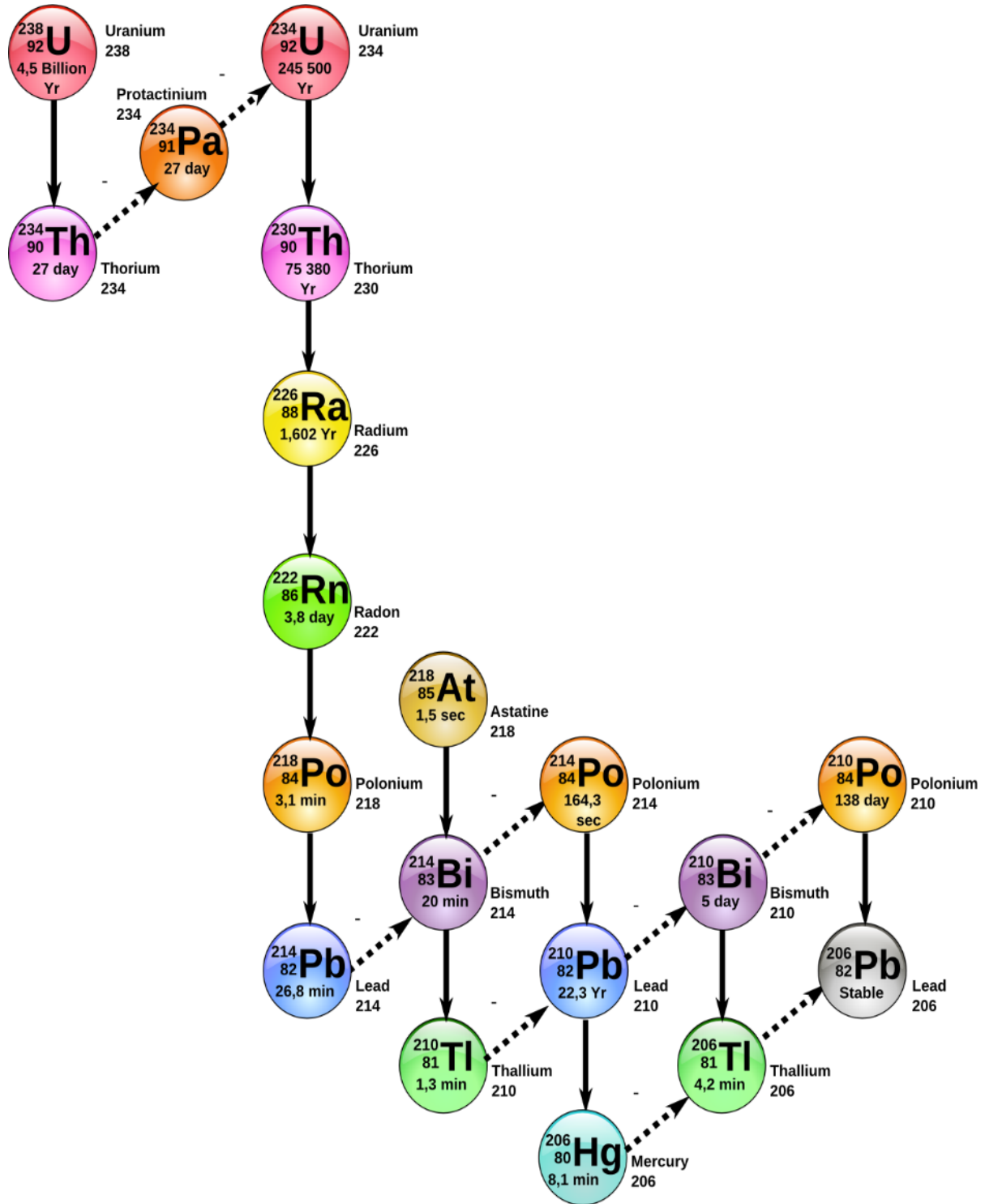
A.2. The ^{235}U decay chain

In addition to the nuclides seen, there is a weak decay branch from ^{231}Th , which may decay through the α decay process into ^{227}Ra before decaying back into the main branch. This decay chain actually starts at ^{239}Pu , however as ^{235}U has a much longer half-life only this is found in (natural) terrestrial sources.



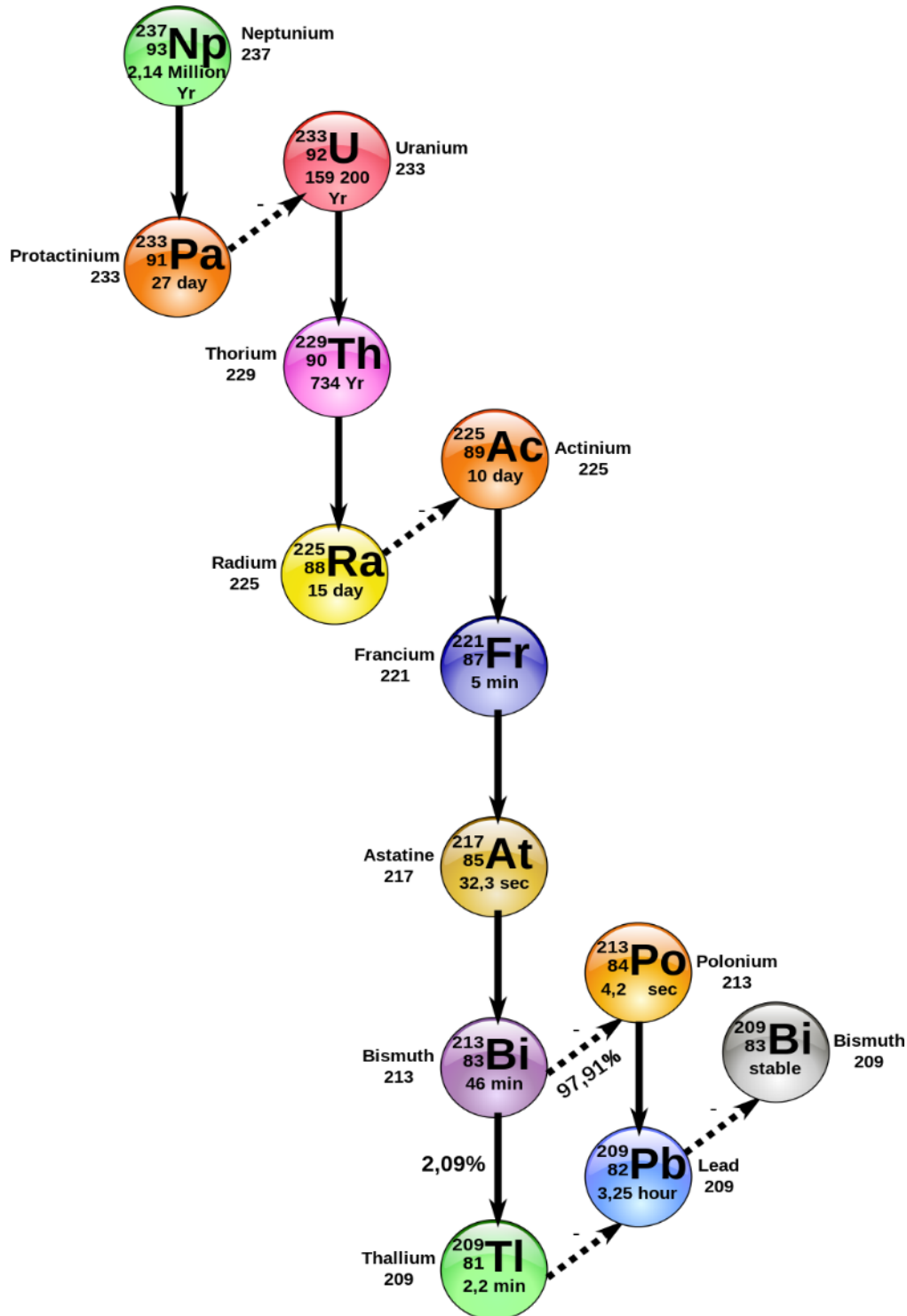
A.3. The ^{238}U decay chain.

Weak decay branches include ^{218}Po β decaying through ^{218}At to ^{218}Rn (with both daughter nuclides also α decaying back into the main chain).



A.4. The ^{237}Np decay chain.

The head of this chain is ^{241}Pu , which β decays into ^{241}Am . This subsequently α decays into ^{237}Np , which is the longest lived nuclide in the chain. This decay chain has gained importance since the production of Plutonium for early nuclear weapons.



Appendix B: HPGe and EDXRF methodology

The present section summarizes the sample preparation method for both γ -ray spectrometry and Energy Dispersive X-ray spectrometry.

I. γ - & X-ray spectrometry

1. Sampling method

- The sampling method was a combination of simple random sampling and stratified sampling. Sampling point geographic coordinates were taken with a Global Positioning System (GPS);
- 2 kg of soil was taken at 5-25 cm depth to avoid contamination with new raw material and human activity;
- Collection of 5 sub-samples at each sampling point (04 at the corners of a 2.5 x 2.5 m² surface squares and 01 at the center). The 5 sub-samples form one sample for each sampling location;
- Packing samples in polyester bags to avoid contamination. Cleaning of the sampling tools;
- Labeling of samples and transfer to the laboratory for preparation;

2. Γ -ray spectrometry preparation

- In the laboratory, samples were dried in two steps: 1st step consists of drying at ambient temperature for several days, up to one week. The 2nd step consists of drying at 105°C for 24 hours in an oven dedicated for γ spectrometry sample preparation;
- Samples were grounded and sieved to achieve a particle size of 250 μm maximum. This is done for homogeneity of the sample so that the density could be considered as uniform when correcting the self-absorption effect of the sample. The process is described in the figure below;
- Samples were weighed and transferred into a 120 ml cylindrical polyester backer and sealed. The cylindrical container was labelled accordingly;
- Sealed samples were stored for secular equilibrium. The storage time was set as 30 days before the acquisition. Checking the availability of the High Purity Germanium (HPGe) detector for measurements (cooling down the detector);
- After radioactive equilibrium between Ra-226 and its daughter isotopes, the samples were ready for acquisition. Both energy (using europium multi- γ source) and efficiency (using LabSOCS Monte Carlo code) were done before the acquisition of the sample spectra;
- Background measurement for 48 hours was followed by sample acquisition of spectra using Genie 2000 [21] software;
- Spectra analysis and activity calculation based on the following equation described in chapter 3. The activity calculation process included several steps as the nuclide library search, the energy calibration, the efficiency calibration, the background subtraction, the ROI location, the surface integration, and the activity calculation;

- Radium equivalent activity calculation based on the values of activity concentration of ^{226}Ra , ^{232}Th , and ^{40}K and frequency distribution of different radionuclides evaluated based on the range of their radioactivity in the investigated soil samples.

3. Energy Dispersive X-Rays fluorescence

- Using the same samples as used in γ spectrometry
- In the laboratory, samples were drying in two steps as for γ spectrometry for the 1st step of drying at ambient temperature for several days, up to one week. But the 2nd step consists of drying at 60°C for 48 hours in an oven since pellet will be made instead of glass discs (used for WDXRF analysis only);
- Samples were grounded and sieved to achieve a particle size of 100 μm maximum. This is done as the X-ray beam diameter should cover several particles in the sample, and for homogeneity of the sample so that the density could be considered as uniform on the surface of the sample under investigation;
- No additional flux or component was added to the sample as in WDXRF measurement where borate fluxes are used. 100% pure samples were prepared;
- Sample weighted and density measurement. A similar density of different sample led to the use of the same pressure for pellet making;
- Both powder sample and standard reference material for calibration were pressed directly into 20 mm-diameter pellets under 4.0 tons.cm⁻² for five minutes;
- Effective cleaning system after each prepared sample to avoid contamination of the next sample to be prepared;
- Five minutes' acquisition for each point on a sample and three measurement points per sample for statistical achievement. A total of 15 minutes were needed for acquisition per sample. The concentration per sample is the average of the three measurement points;
- DR-N, BE-N, MESS-3, SRM-610, PACS, UB-N, and MA-N standard reference materials (SRMs) from National Institute of Standards and Technology (NIST) were used as reference material to validate the obtained results;
- Result validation by analyzing some reference material and compared the result to the certified value referred by the manufacturer. If the values of the standard deviation are all lower than 5%, the measurement method is acceptable and achievable. All the obtained values in this research were lower than 6%, which is scientifically sounded;
- Using PyMCA for elemental concentration assessment and output data as color graphs based on the concentration ratio using temperature color bar chart;
- Excel sheet for compound concentrations determination. Correction of Ag, W, and other elements present in the background measurement as in the detector system or the collimator. Report of the result for the next step;

4. Sand classification and Provenance

- Using major and minor element concentrations to draw the sedimentary classification diagrams (ratio of $\text{K}_2\text{O}/\text{Na}_2\text{O}$; $\log(\text{SiO}_2/\text{Al}_2\text{O}_3)$ and $\log(\text{Fe}_2\text{O}_3/\text{K}_2\text{O})$);

- Using diagram for the tectonic discrimination of sediment provenance: TiO_2 (%) as a function of the Fe_2O_3 and MgO (%) diagram; Al_2O_3/SiO_2 (%) as a function of Fe_2O_3 and MgO (%) to draw the origin formation of the samples;
- Deduction from the previous diagrams and Heron diagram, the investigated area class and the origin of the geological formation.

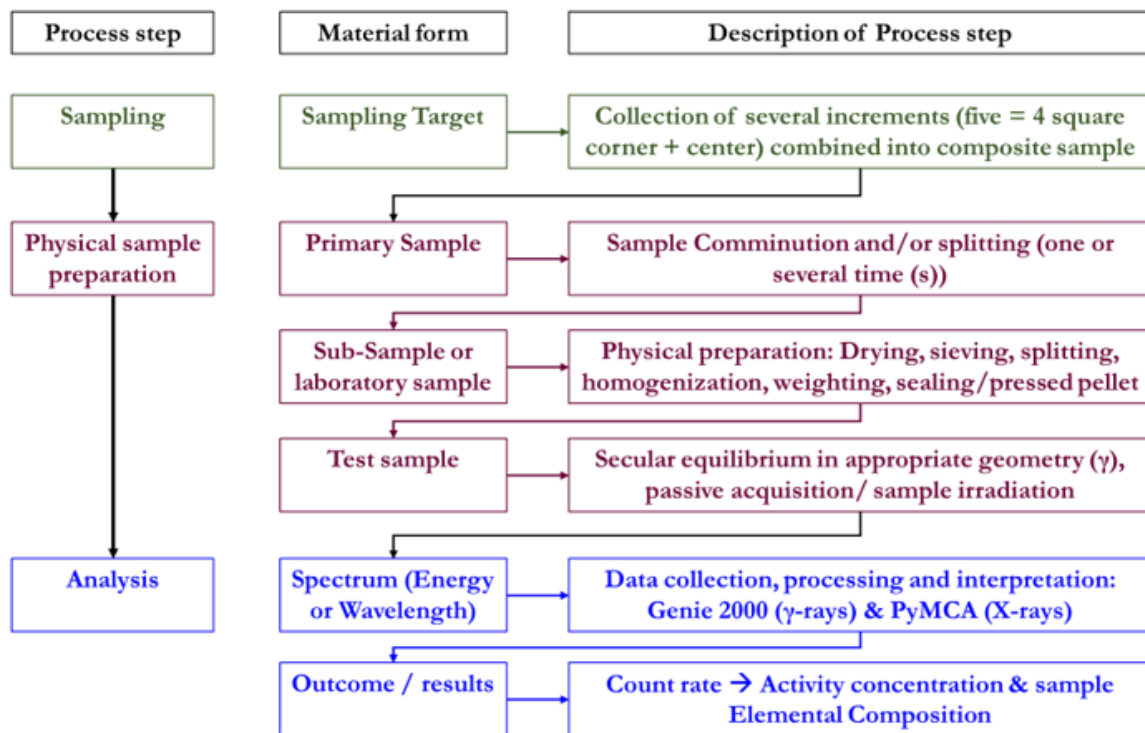


Figure B1. Sampling process, Sample preparation steps, and analysis description of the methodology used

Appendix C: List of Scientific Contribution

Scientific Publications as first or corresponding author

1. **Guembou Shouop C.J.**, Ndontchueng Moyo M., Nguelem Mekongtso E.J., Et al. (2021) ²⁴¹AM/BE SOURCE OPTIMUM GEOMETRY FOR DSRSS MANAGEMENT-BASED MONTE CARLO SIMULATIONS. AIP Advances 11, 000000 (2021) <https://doi.org/10.1063/5.0063005>
2. **Guembou Shouop C.J.**, Tayou Kamkumo C., Nguelem Mekongtso E.J., Beyala Ateba J.F., Ndontchueng Moyo M., Simo A., Strivay D. (2021) Recovering and restitution of unknown, unidentified, and unlabeled samples in laboratories using EDXRF analysis, MethodsX: 8, <https://doi.org/10.1016/j.mex.2021.101435>
3. **Guembou Shouop C.J.**; Ndontchueng Moyo M.; Nguelem Mekongtso E.J.; Motapon O.; Strivay D. (2021) Application of Energy Dispersive X-ray Fluorescence, γ -ray Spectrometry and Multivariate Statistical Approach for the Soil Classification of Samples from Douala – Cameroon; Radiation Physics and Chemistry 109589 <https://doi.org/10.1016/j.radphyschem.2021.109589>
4. **Guembou Shouop C.J.**, Ndontchueng Moyo M., Nguelem Mekongtso E.J. et al. (2021) Erratum to Radiological protection requirements with regard to cosmic ray exposure during air travel. Eur. Phys. J. Plus 135, 438. <https://doi.org/10.1140/epjp/s13360-021-01401-3>
5. **Guembou Shouop C.J.** and Sang-In Bak (2020) Shielding design for high-intensity Co-60 and Ir-192 γ sources used in industrial radiography based on PHITS Monte Carlo simulations. The European Physical Journal Plus 135: 784 <https://doi.org/10.1140/epjp/s13360-020-00797-8>
6. **Guembou Shouop C.J.**, Sang-In Bak, Ndontchueng Moyo M., Nguelem Mekongtso E.J., and David Strivay (2020) New Cf-252 neutron source shielding design based Monte Carlo simulation using material combination. AIP Advances 10, 075203 (2020); <https://doi.org/10.1063/1.5144923>
7. **Guembou Shouop C.J.**, Ndontchueng Moyo M., Nguelem Mekongtso E.J. et al. (2020) Radiological protection requirements with regard to cosmic ray exposure during air travel. Eur. Phys. J. Plus 135, 438. <https://doi.org/10.1140/epjp/s13360-020-00468-8>
8. **Guembou Shouop C.J.**, Ndontchueng Moyo M., Mekongtso Nguelem E.J., et al (2019) Determination of the natural radioactivity, elemental composition and geological provenance of sands from Douala in the littoral region of Cameroon using X-ray and γ -ray spectrometry. Appl Earth Sci 1–14. <https://doi.org/10.1080/25726838.2019.1637656>
9. **Guembou Shouop C.J.**, Moyo Ndontchueng M., Mekongtso Nguelem E.J., et al (2019) Elemental quantification and radioactive characterization of soil from Douala Bassa area: littoral region of Cameroon using X- and γ -rays spectrometry. Environ Res Commun 1:065001. <https://doi.org/10.1088/2515-7620/ab1d72>
10. Hazou E., **Guembou Shouop C.J.**, Nguelem Mekongtso E.J., et al (2019) Preliminary assessment of natural radioactivity and associated radiation hazards in a phosphate mining site in southern area of Togo. Radiat Detect Technol Methods. <https://doi.org/10.1007/s41605-018-0091-x>
11. **Guembou Shouop C.J.**, Moyo Ndontchueng M., Chene G., et al (2019) Simultaneously γ

- spectrometry & energy dispersive X-ray fluorescence-based color differentiation analysis of Douala-Bassa area's soil. Environ Technol Innov 100486. <https://doi.org/10.1016/j.eti.2019.100486>
12. **Guembou Shouop C.J.**, Ndontchueng Maurice M., Nguelem E., et al. (2018) Monte Carlo method for γ spectrometry based on GEANT4 toolkit: Efficiency calibration of BE6530 detector. <https://doi.org/10.1016/j.jenvrad.2018.03.015>
 13. **Guembou Shouop C.J.**, Ndontchueng Moyo M., Chene G., Nguelem E.J., Strivay D. (2017), Assessment of Natural radioactivity and associated radiation hazards in sand building material used in Douala Littoral-Region of Cameroon, using γ spectrometry. Environmental Earth Science 76:164 <http://dx.doi.org/10.1007/s12665-017-6474-3>
 14. **Guembou Shouop C.J.**, Samafou P., Ndontchueng Moyo M., Chene G., Nguelem E.J., Ngwa Ebongue A, Motapon O., Strivay D. (2017) Precision measurement of radioactivity in γ -rays spectrometry using two HPGe detectors (BEGe-6530 and GC0818-7600SL models) comparison techniques: Application to the soil measurement Elsevier MethodsX 4:42–54 <http://dx.doi.org/10.1016/j.mex.2016.12.003>
 15. **Guembou Shouop C.J.**, Samafou P., Ndontchueng Moyo M., Chene G., Nguelem Mekongtso E.J., Takoukam S.D., And Strivay D. (2017) Optimal measurement counting time and statistics in γ spectrometry analysis: The time balance. American Institute of Physics 1792 (100001): 1-6 <http://dx.doi.org/10.1063/1.4969040>

Additional Publications

16. Hazou E., Zorko B., Nečemer M., Essolakina, Haliba M., **Guembou Shouop C.J.**, Komi S., Tchakpele P. (2021) Heavy Metal Pollution Assessment Using Energy-Dispersive X-ray Fluorescence and Multivariate Statistical Approach of Soil from Phosphate Ore Sites, Southern Region of Togo. Water, Air, Soil Pollut. 2021 23212 232, 1–17. <https://doi.org/10.1007/S11270-021-05439-Y>
17. Kayo S.A., Moyo M.N., **Guembou Shouop C.J.**, Nguelem Mekontso E.J., Motapon, O. (2021) Multivariate statistical assessment of natural radioactivity and radiological hazards data of cement building materials mainly used in Cameroon. Arab. J. Geosci. 2021 1423 14, 1–12. <https://doi.org/10.1007/S12517-021-08717-5>
18. Penabei S., Bongue D., Maleka P., Dlamini T., Saïdou, **Guembou Shouop C.J.**, Halawlaw Y.I., Ngwa Ebongue A., Kwato Njock M.G. (2018) Assessment of natural radioactivity levels and the associated radiological hazards in some building materials from Mayo-Kebbi region, Chad. Radioprotection: 53(4), 265278
19. Nguelem E. J., Ndontchueng Moyo M., Motapon O., **Guembou Shouop C.J.**, E. O. Darko (2017) Radiological monitoring and statistical approach of primordial and anthropogenic radionuclides in surface soil of Mani-water site in the Western of Cameroon. Environ Earth Sci 76: 612. <https://doi.org/10.1007/s12665-017-6951-8>
20. Ndontchueng Moyo M. ; Nguelem E.J., Njinga R. L.; Simo A., **Guembou Shouop J.C.** (2014), Γ Emitting Radionuclides in Soils from Selected Areas in Douala-Bassa Zone, Littoral Region of Cameroon ISRN Spectroscopy Vol. 2014- 245125, <http://hdl.handle.net/2268/198175>
21. Ndontchueng Moyo M., Nguelem Mekongtso E.J., Motapom O., Simo A., **C.J. Guembou Shouop**, YEMELE B.C. (2015), Radiological Hazards from Bauxite Deposit Sites in Dschang

Settlement of Cameroon, <http://hdl.handle.net/2268/198174>

Scientific congresses, seminars and symposia

1. **Guembou Shouop CJ** et al. (2021, November) Monte Carlo forecast for DSRS management optimization, International Conference on Radioactive Waste Management: Solutions for a Sustainable Future (CN-294). <https://conferences.iaea.org/event/219/papers/19540/>
2. **Guembou Shouop CJ** (2020) Fukushima accident impact 13,000 km away and a lesson for developing countries. ICRP International Conference on Recovery After Nuclear Accidents Radiological Protection Lessons from Fukushima and Beyond
3. **Guembou Shouop CJ** et al. (2020) Radiation protection optimization in fixed industrial radiography based PHITS Monte Carlo code simulation. IAEA International Conference on Radiation Safety: Improving Radiation Protection in Practice, Vienna – Austria, Poster
4. **Guembou Shouop CJ** (2020) Radioactive Waste Management option for Cameroon: Current Practices towards an optimized management strategy in the future. Joint ICTP-IAEA International School on Radioactive Waste Cementation | (SMR 3484) – Poster
5. **Guembou Shouop CJ** et al. (2020) Barite concrete for Cf-252 spontaneous neutron shielding based on Monte Carlo computation. The Nuclear Materials Conference – NUMAT 2020 Elsevier. Ghent, Belgium
6. **Guembou Shouop CJ**, Bak S (2019) Maze influence to radiological protection around industrial radiographic sources (Co-60) under 100 Ci. In: Transactions of the Korean Nuclear Society Autumn Meeting Goyang, Korea, October 24-25, 2019. pp 3–6
7. **Guembou Shouop, C. J.**, Ndontchueng Moyo, M., Chene, G., & Strivay, D. (2016, June 21). Natural radioactivity and elemental composition of sands in the Douala region, Littoral of Cameroon Using Portable XRF and HPGe detector. Poster session presented at EXRS2016 European Conference on X-Ray Spectrometry, Gotheborg, Sweden. <http://hdl.handle.net/2268/199073>
8. **Guembou Shouop, C. J.**, Ndontchueng Moyo, M., Chene, G., & Strivay, D. (2016, July 11). Counting time measurement and statistics in γ spectrometry: the balance. Poster session presented at Γ 2016: 6th International Symposium on High-Energy Γ -Ray Astronomy, Heidelberg, Germany. <http://hdl.handle.net/2268/200754>
9. **Guembou Shouop, C. J.**, Ndontchueng Moyo, M., Chene, G., & Strivay, D. (2016, July 13). Γ -Ray Spectrometry: Experimental Measurement and Monte Carlo Simulation using GEANT4 toolkit. Poster session presented at 9th International Balkan School of Nuclear Physics 2016, Constanta, Roumania. <http://hdl.handle.net/2268/200622>
10. **NDONTCHUENG MOYO, M.**, **Guembou Shouop, C. J.**, & **NGUELEM MEKONTSO, E. J.** (2014, July 07). Origins of ^{137}Cs and ^{133}Xe in Soils from two Campuses in University of Douala-Cameroon. Poster session presented at International Conference on Advances in Nuclear Forensics - IAEA CN-218, Vienne, Austria. <http://hdl.handle.net/2268/197723>
11. **Ndontchueng Moyo M.**, **Guembou Shouop CJ.**, **Ngelem Mekontso EJ.**, & **Motapon O.** (2016, August 04). Investigation of ^{238}U , ^{235}U , ^{137}CS and ^{133}XE in Soils from the University of Douala-Cameroon. Paper presented at Deuxieme conference scientifique internationale de la diaspora, Douala, Cameroun, <http://hdl.handle.net/2268/200830>

12. Moyo NM., Kayo S., Ngelem E. J., Nana R., Motapon O., & **Guembou Shouop CJ.** (2016, August 04). Techniques et Méthodes nucléaires : Application de la Spectrométrie Γ au Cameroun. Poster session presented at Conference scientifique internationale de la Diaspora, Douala, Cameroun. <http://hdl.handle.net/2268/200721>

REFERENCES

1. UNSCEAR (2008) Sources and Effects of Ionizing Radiation. Report of the United Nations Scientific Committee on the Effects of Atomic Radiation to the General Assembly
2. Guembou Shouop CJ, Ndontchueng Moyo M, Chene G, et al (2017) Assessment of natural radioactivity and associated radiation hazards in sand building material used in Douala Littoral Region of Cameroon, using γ spectrometry. *Environ Earth Sci*. <https://doi.org/10.1007/s12665-017-6474-3>
3. (2006) Etude et validation d'un spectromètre γ pour la mesure de la composition chimique des surfaces planétaires Application à une mission vers Mercure
4. Nguelem EJM, Ndontchueng MM, Motapon O, et al (2016) Determination of ^{226}Ra , ^{232}Th , ^{40}K and ^{235}U in soil samples from bauxite core deposits in western Cameroon. *Radioprotection* 51:199–205. <https://doi.org/10.1051/radiopro/2016029>
5. Saïdou (2008) “Mesure de la radioactivite naturelle environnementale par spectrometries γ et β et calcul de la dose au public : application a la region uranifere de poli.” University of Douala
6. Ababneh AM, Masa'deh MS, Ababneh ZQ, et al (2009) Radioactivity concentrations in soil and vegetables from the northern Jordan Rift Valley and the corresponding dose estimates. *Radiat Prot Dosimetry*. <https://doi.org/10.1093/rpd/ncp064>
7. Ahmeti A, Xhixha G, Bezzon G, et al (2013) NATURAL RADIOACTIVITY IN CLAY BRICKS AND CEMENTS USED IN ALBANIA
8. El-Taher A (2012) Assessment of natural radioactivity levels and radiation hazards for building materials used in Qassim area, Saudi Arabia. *Rom Reports Phys*. <https://doi.org/10.1109/TLA.2016.7785939>
9. Akkurt I, Mavi B, Akyıldırım H, Günoglu K (2009) Natural radioactivity of coals and its risk assessment
10. Amekudzie A, Emi-Reynolds G, Faanu A, et al (2011) Natural Radioactivity Concentrations and Dose Assessment in Shore Sediments along the Coast of Greater Accra, Ghana. *World Appl Sci J* 13:2338–2343
11. Al-Jundi J, Ulanovsky A, Pröhl G (2009) Doses of external exposure in Jordan house due to γ -emitting natural radionuclides in building materials. *J Environ Radioact*. <https://doi.org/10.1016/j.jenvrad.2009.06.010>
12. Dietze G, Bartlett DT, Cool DA, et al (2013) ICRP: ICRP Publication 123. *Ann ICRP*. <https://doi.org/10.1016/j.icrp.2013.05.004>
13. Ndontchueng MM, M Nguelem EJ, Motapon O, et al (2015) Radiological Hazards in Soil from the Bauxite Deposits Sites in Dschang Region of Cameroon. *Br J Appl Sci Technol* 5:342–352. <https://doi.org/10.9734/BJAST/2015/13352>
14. Nguelem EJM, Ndontchueng MM, Motapon O, et al (2017) Radiological monitoring and statistical approach of primordial and anthropogenic radionuclides in surface soil of Mami-water site in the Western Cameroon. *Environ Earth Sci*. <https://doi.org/10.1007/s12665-017-6951-8>
15. López-García I, Viñas P, Romero-Romero R, Hernández-Córdoba M (2007) Fast determination of phosphorus in honey, milk and infant formulas by electrothermal atomic absorption spectrometry using a slurry sampling procedure. *Spectrochim Acta - Part B At Spectrosc*. <https://doi.org/10.1016/j.sab.2006.11.008>
16. Ateba JFB, Ateba PO, Ben-Bolie GH, et al (2010) Natural background dose measurements in South Cameroon. *Radiat Prot Dosimetry*. <https://doi.org/10.1093/rpd/ncq035>
17. Nguelem EJM, Ndontchueng MM, Motapon O, et al (2016) Determination of ^{226}Ra , ^{232}Th , ^{40}K and ^{235}U in soil samples from bauxite core deposits in western Cameroon. *Radioprotection* 51:199–205. <https://doi.org/10.1051/radiopro/2016029>
18. Nguelem EJ, Ndontchueng M, Akiti T, et al (2013) The Natural Radioactivity in groundwater from selected areas in Greater Accra region of Ghana by gross α and gross β measurements. *Radiat Prot*

REFERENCES

- Environ. <https://doi.org/10.4103/0972-0464.121814>
19. Mohanty AK, Sengupta D, Das SK, et al (2004) Natural radioactivity and radiation exposure in the high background area at Chhatrapur beach placer deposit of Orissa, India. *J Environ Radioact.* <https://doi.org/10.1016/j.jenvrad.2003.09.004>
 20. Wauters F, Kraev I, Zákoucký D, et al (2009) A GEANT4 Monte-Carlo simulation code for precision β spectroscopy. *Nucl Instruments Methods Phys Res Sect A Accel Spectrometers, Detect Assoc Equip.* <https://doi.org/10.1016/j.nima.2009.08.026>
 21. Laili Z, Yasir MS, Omar M, et al (2016) Genie™ 2000 Spectroscopy Software Operations. Canberra
 22. Guembou Shouop CJ, Ndontchueng MM, et al (2018) Monte Carlo method for γ spectrometry based on GEANT4 toolkit: Efficiency calibration of BE6530 detector. *J Environ Radioact* 189:109–119. <https://doi.org/10.1016/j.jenvrad.2018.03.015>
 23. Akkurt I, Tekin HO, Mesbahi A (2015) Calculation of Detection Efficiency for the Γ Detector using MCNPX. In: *Acta Physica Polonica A*
 24. Mowlavi AA, De Denaro M, Fornasier MR 7 Monte Carlo Simulation of Pile-up Effect in Γ Spectroscopy
 25. Russ W, Venkataraman R, Bronson F (2005) Validation testing of the genie 2000 Cascade Summing Correction. *J Radioanal Nucl Chem.* <https://doi.org/10.1007/s10967-005-0693-x>
 26. Baró J, Roteta M, Fernández-Varea JM, Salvat F (1994) Analytical cross sections for Monte Carlo simulation of photon transport. *Radiat Phys Chem* 44:531–552. [https://doi.org/10.1016/0969-806X\(94\)90053-1](https://doi.org/10.1016/0969-806X(94)90053-1)
 27. Britton R (2012) Compton suppression systems for environmental radiological analysis. *J Radioanal Nucl Chem.* <https://doi.org/10.1007/s10967-011-1362-x>
 28. Cantaragiu AM, Gheorghies C, Borcia C STUDY OF Γ SPECTRA BY MONTE CARLO SIMULATION
 29. Costache C, Sima O (2015) MONTE CARLO SIMULATION OF THE IBA END-STATION'S Γ SPECTROMETRY SYSTEM OF THE 3 MV TANDETRON ACCELERATOR AT IFIN-HH
 30. Gillam JE, Rafecas M (2016) Monte-Carlo simulations and image reconstruction for novel imaging scenarios in emission tomography. *Nucl Instruments Methods Phys Res Sect A Accel Spectrometers, Detect Assoc Equip.* <https://doi.org/10.1016/j.nima.2015.09.084>
 31. Agostinelli S, Allison J, Amako K, et al (2003) Geant4—a simulation toolkit. *Nucl Instruments Methods Phys Res Sect A Accel Spectrometers, Detect Assoc Equip* 506:250–303. [https://doi.org/10.1016/S0168-9002\(03\)01368-8](https://doi.org/10.1016/S0168-9002(03)01368-8)
 32. Allison J, Amako K, Apostolakis J, et al (2006) Geant4 developments and applications. *IEEE Trans Nucl Sci.* <https://doi.org/10.1109/TNS.2006.869826>
 33. Allison J, Amako K, Apostolakis J, et al (2016) Recent developments in GEANT4. *Nucl Instruments Methods Phys Res Sect A Accel Spectrometers, Detect Assoc Equip.* <https://doi.org/10.1016/j.nima.2016.06.125>
 34. Geant4 User's Guide for Application Developers. 391
 35. Berger MJ (1963) Monte Carlo calculation of the penetration and diffusion of fast charged particles. In: *Methods in computational physics 1*
 36. Butcher JC, Messel H (1960) Electron number distribution in electron-photon showers in air and aluminium absorbers. *Nucl Phys.* [https://doi.org/10.1016/0029-5582\(60\)90162-0](https://doi.org/10.1016/0029-5582(60)90162-0)
 37. Butcher JC, Messel H (1958) Electron number distribution in electron-photon showers. *Phys Rev.* <https://doi.org/10.1103/PhysRev.112.2096>
 38. Ford R. and Nelson W. (1985) SLAC-265, UC-32

REFERENCES

39. Desmaris G (2015) Cosmic radiation in aviation: radiological protection of Air France aircraft crew. Ann ICRP. <https://doi.org/10.1177/0146645316636009>
40. International Commission on Radiological Protection. (2007) The 2007 Recommendations of the International Commission on Radiological Protection. ICRP Publication 103. Ann ICRP. <https://doi.org/10.1016/j.icrp.2004.12.002>
41. Amako K, Guatelli S, Ivanchenko V, et al (2006) GEANT4 and its validation. Nucl Phys B - Proc Suppl. <https://doi.org/10.1016/j.nuclphysbps.2004.10.083>
42. Britton R, Burnett JL, Davies A V., Regan PH (2014) Monte-Carlo optimisation of a Compton suppression system for use with a broad-energy HPGe detector. Nucl Instruments Methods Phys Res Sect A Accel Spectrometers, Detect Assoc Equip. <https://doi.org/10.1016/j.nima.2014.05.113>
43. Ngon F NG, J NM, Tang NS, Yongue-fouateu R (2012) Trace elements geochemistry of clay deposits of Missole II from the Douala sub-basin in Cameroon (Central Africa) : a provenance study
44. Victor Asaah A, Festus Abimbola A, Emmanuel Suh C (2006) Strategic partnerships in higher education delivery and quality assurance View project
45. Olivry C.J. (1986). Fleuves et rivières du Cameroun. Collection Monographies Hydrologiques, ORSTOM No. 9, Paris, 733 p.
46. Marzoli A, Piccirillo EM, Renne PR, et al (2000) The cameroon volcanic line revisited: Petrogenesis of continental basaltic magmas from lithospheric and asthenospheric mantle sources. J Petrol. <https://doi.org/10.1093/petrology/41.1.87>
47. Ndontchueng MM, Jilbert E, Nguelem M, et al (2014) Γ Emitting Radionuclides in Soils from Selected Areas in Douala-Bassa Zone, Littoral Region of Cameroon. ISRN Spectrosc 8:. <https://doi.org/10.1155/2014/245125>
48. International Atomic Energy Agency (2014) Radiation Protection and Safety of Radiation Sources: International Basic Safety Standards (GSR Part 3). Int At Energy Agency Vienna 3:471. <https://doi.org/STI/PUB/1578>
49. UNSCEAR (2000) Sources and effects of ionizing radiation: United Nations Scientific Committee on the Effects of Atomic Radiation. UNSCEAR 2000 Rep to Gen Assem
50. Metropolis N (1987) The beginning of the Monte Carlo method. Los Alamos Sci Spec Issue
51. Metropolis N, Ulam S (1949) The Monte Carlo Method.pdf. J Am Stat Assoc. <https://doi.org/10.1080/01621459.1949.10483310>
52. Hartwig ZS, Gumplinger P (2014) Simulating response functions and pulse shape discrimination for organic scintillation detectors with Geant4. Nucl Instruments Methods Phys Res Sect A Accel Spectrometers, Detect Assoc Equip. <https://doi.org/10.1016/j.nima.2013.11.027>
53. Britton R (2014) Development of a Compton Suppressed Γ Spectrometer using Monte Carlo Techniques
54. Huber G, Thomson J, Trautmann N ACRONYMS, ABBREVIATIONS AND SYMBOLS. 1282
55. Arndt M, Nairz O, Vos-Andreae J, et al (1999) Wave-particle duality of C60 molecules. Nature. <https://doi.org/10.1038/44348>
56. Temple G, Dirac PAM (1935) The Principles of Quantum Mechanics. Math Gaz. <https://doi.org/10.2307/3606137>
57. Schmidt HT, Fischer D, Berenyi Z, et al (2008) Evidence of wave-particle duality for single fast hydrogen atoms. Phys Rev Lett. <https://doi.org/10.1103/PhysRevLett.101.083201>
58. Bianchini L UNITEXT for Physics Selected Exercises in Particle and Nuclear Physics
59. Biggs F. and Lighthill R. (1990) Preprint Sandia Laboratory, SAND 87-0070
60. Messel H., Crawford D. (1970) Electron-Photon shower distribution, Pergamon Press
61. Crawford DF, Messel H (1962) Energy distribution in low-energy electron-photon showers in lead

REFERENCES

- absorbers. *Phys Rev.* <https://doi.org/10.1103/PhysRev.128.2352>
62. Hamaguchi H, Iwata K (2016) Time-Resolved Raman Spectroscopy. In: *Encyclopedia of Spectroscopy and Spectrometry*
 63. Fromm M, Boulanouar O (2016) Low energy electrons and ultra-soft X-rays irradiation of plasmid DNA. *Technical innovations. Radiat Phys Chem.* <https://doi.org/10.1016/j.radphyschem.2016.05.025>
 64. Kajimoto T, Endo S, Tat Thanh N, Shizuma K (2015) Calculation of coincidence summing in γ -ray spectrometry with the EGS5 code. *Appl Radiat Isot.* <https://doi.org/10.1016/j.apradiso.2014.09.018>
 65. Climent-Font A, Demortier G, Palacio C, et al (1998) Characterisation of archaeological bronzes using PIXE, PIGE, RBS and AES spectrometries. *Nucl Instruments Methods Phys Res Sect B Beam Interact with Mater Atoms.* [https://doi.org/10.1016/S0168-583X\(98\)00553-9](https://doi.org/10.1016/S0168-583X(98)00553-9)
 66. Klanner R, Knoll GF, Siegbahn K NUCLEAR INSTRUMENTS AND METHODS IN PHYSICS RESEARCH Section A-Accelerators, Spectrometers, Detectors and Associated Equipment
 67. Krane KS, Halliday D (1987) *Introductory Nuclear Physics.* *Am J Phys.* <https://doi.org/10.1119/1.1934189>
 68. Born M. (1969) *Atomic physics*, Ed. Blackie and Sons
 69. L'Annunziata MF (2003) *Handbook of Radioactivity Analysis*
 70. L'Annunziata MF (2016) *Radioactivity and Our Well-Being.* In: *Radioactivity*
 71. Asner DM, Burns K, Campbell LW, et al (2015) Method of fission product β spectra measurements for predicting reactor anti-neutrino emission. *Nucl Instruments Methods Phys Res Sect A Accel Spectrometers, Detect Assoc Equip.* <https://doi.org/10.1016/j.nima.2014.09.076>
 72. Akkoyun S, Yildiz N (2012) Consistent empirical physical formula construction for recoil energy distribution in HPGe detectors by using artificial neural networks. *Radiat Meas.* <https://doi.org/10.1016/j.radmeas.2012.06.018>
 73. Holm SL, Lefmann K, Henry PF, et al (2016) HEIMDAL: A thermal neutron powder diffractometer with high and flexible resolution combined with SANS and neutron imaging - Designed for materials science studies at the European Spallation Source. *Nucl Instruments Methods Phys Res Sect A Accel Spectrometers, Detect Assoc Equip.* <https://doi.org/10.1016/j.nima.2016.05.046>
 74. Pham TQ, Incerti S, Perrot Y, et al Validation des modèles physiques et radiochimiques intervenant dans l'irradiation de molécules d'ADN en utilisant le logiciel GEANT4-DNA dans un environnement de grille
 75. PHYSICS USING IN SITU NEUTRON AND Γ -RAY SPECTROSCOPY
 76. Vesterlund A THESIS FOR THE DEGREE OF LICENTATE OF ENGINEERING Γ SPECTROMETRIC MEASUREMENTS OF NUCLEAR MATERIAL FOR NUCLEAR FORENSIC PURPOSES Study of signatures in ^{241}Am sources and evaluation of uranium categorization with low-resolution instruments
 77. Hubbel JH. et al. (1975) Atomic form factors, incoherent scattering functions and photon scattering cross sections, *J. Phys. Chem. Ref. Data* 4: 471 Erratum: *ibid.* 6:615 (1977)
 78. Gavrilă M, McEnnan J (1977) Radiative corrections to photoeffect and the high-frequency end of the Bremsstrahlung spectrum. *Phys Lett A.* [https://doi.org/10.1016/0375-9601\(77\)90650-8](https://doi.org/10.1016/0375-9601(77)90650-8)
 79. Gavrilă M (1960) On the relativistic K-shell photoeffect. *Nuovo Cim. Ser. 10*
 80. Heitler W. (1957) *The Quantum Theory of Radiation*, Oxford University Press
 81. Hubbell JH, Gimm HA, O'Verbo/ I (1980) Pair, Triplet, and Total Atomic Cross Sections (and Mass Attenuation Coefficients) for 1 MeV to 100 GeV Photons in Elements Z=1 to 100. *J Phys Chem Ref Data.* <https://doi.org/10.1063/1.555629>
 82. Salvat F, Fernández-Varea J, Sempau J (2011) PENELOPE, A code system for Monte Carlo simulation

REFERENCES

- of electron and photon transport. *Work. Proc.*
83. J.E. Turner (1995) *Atoms, Radiation, and Radiation Protection*, Wiley, New York, 1995, Chapter 5 “Interaction of heavy charged particles with matter”.
 84. Jenkins TM, Nelson WR, Rindi A (1988) *Monte Carlo Transport of Electrons and Photons*. Springer US, Boston
 85. Rossi B, Fretter WB (2005) High-Energy Particles. *Am J Phys*. <https://doi.org/10.1119/1.1933408>
 86. Nelson WR, Hirayama H, Rogers D (1985) *The EGS4 Code System*. Rep SLAC-265, Stanford Linear Accel Centre, Stanford, Calif
 87. MESSEL H, CRAWFORD DF (2013) THE PHYSICAL PROCESSES. In: *Electron–Photon Shower Distribution Function*
 88. Hubbell JH, Veigele WJ, Briggs EA, et al (1975) Atomic form factors, incoherent scattering functions, and photon scattering cross sections. *J Phys Chem Ref Data*. <https://doi.org/10.1063/1.555523>
 89. Williams MMR (2003) Introduction to health physics (2nd edn). *Ann Nucl Energy* 16:259. [https://doi.org/10.1016/0306-4549\(89\)90096-0](https://doi.org/10.1016/0306-4549(89)90096-0)
 90. Introduction A, Ea HP Protection and Dosimetry
 91. Berger MJ, Hubbell JH, Seltzer SM, et al (2010) XCOM: Photon Cross Section Database (version 1.5). *Natl. Inst. Stand. Technol.* Gaithersburg, MD
 92. Cole P (2013) Radioactivity and radiation
 93. Ripani M (2018) Energy from nuclear fission
 94. Ilboudo SDO, Sombi?? I, Soubeiga AK, Dr??bel T (2016) Handbook of nuclear. *Sante Publique (Paris)* 28:391–397. <https://doi.org/10.1017/CBO9781107415324.004>
 95. Antoni R, Bourgois L (2017) *Applied Physics of External Radiation Exposure: Dosimetry and Radiation Protection*
 96. (2011) *Progress in Medical Radiation Physics*
 97. K. Eckerman, J. Harrison, H-G. Menzel CHC (2007) *Annals of the ICRP* Annals of the ICRP. *Ann ICRP* 1–99. <https://doi.org/10.1016/j.icrp.2006.06.001>
 98. United Nations (2010) Sources and effects of ionizing radiation: United Nations Scientific Committee on the Effects of Atomic Radiation: UNSCEAR 2008 report to the General Assembly, with scientific annexes. United Nations, New York
 99. Amekudzie A, Emi-Reynolds G, Faanu A, et al (2011) Natural Radioactivity Concentrations and Dose Assessment in Shore Sediments along the Coast of Greater Accra, Ghana. 6
 100. Knoll. Glenn F. (1989) *Radiation Detection and Measurement*. New York: John Wiley & Sons. Inc. Second Edition
 101. Joel GSC, Penabei S, Ndontchueng MM, et al (2017) Precision measurement of radioactivity in γ -rays spectrometry using two HPGe detectors (BEGe-6530 and GC0818-7600SL models) comparison techniques: Application to the soil measurement. *MethodsX*. <https://doi.org/10.1016/j.mex.2016.12.003>
 102. Guembou Shouop CJ, Penabei S, Maurice NM, et al (2017) Optimal measurement counting time and statistics in γ spectrometry analysis: The time balance. *AIP Conference Proceedings*, p 100001
 103. Hernández F Dissertation for the Degree of Doctor of Philosophy in Physics presented at Uppsala University 2002 ABSTRACT Hernández, F. 2002. Optimisation of environmental γ spectrometry using Monte Carlo methods. *Acta Universitatis Upsaliensis*. Comprehensive Summaries of Uppsala Dissertations from the Faculty of Science and Technology 751
 104. De F, Físicas C, Picado E, et al (2013) UNIVERSIDAD COMPLUTENSE DE MADRID TESIS DOCTORAL Mejoras en la detección de rayos γ con cristales centelladores de última generación y aplicaciones Advances in Γ -Ray detection with modern scintillators and applications MEMORIA PARA

REFERENCES

- OPTAR AL GRADO DE DOCTOR PRESENTADA POR
105. Patrie PT (2013) ENVIRONNEMENTAUX PAR SPECTROMÉTRIE Γ : CAS DES SOLS DES CAMPUS I ET II DE L ' UNIVERSITE DE DOUALA Etude des échantillons environnementaux par Spectrométrie γ : cas des sols des campus I et II de l ' Université de Douala
 106. Cooper, P.N: Introduction to Nuclear Radiation Detectors. Cambridge: Cambridge University Press, 2011
 107. (1994) ENVIRONMENTAL INFLUENCES ON Γ RAY SPECTROMETRY by
 108. CANBERRA Manual (2013) “Nuclear Measurement Solutions for Safety, Security and the Environment”, Broad Energy Germanium Detectors (BEGe) C40426 – 11/13 <http://www.canberra.com/products/detectors/pdf/BEGe-SS-C40426.pdf>
 109. Chham E, García FP, El Bardouni T, et al (2015) Monte Carlo analysis of the influence of germanium dead layer thickness on the HPGe γ detector experimental efficiency measured by use of extended sources. *Appl Radiat Isot.* <https://doi.org/10.1016/j.apradiso.2014.09.007>
 110. Britton R, Burnett JL, Davies A V., Regan PH (2014) Monte-Carlo optimisation of a Compton suppression system for use with a broad-energy HPGe detector. *Nucl Instruments Methods Phys Res Sect A Accel Spectrometers, Detect Assoc Equip.* <https://doi.org/10.1016/j.nima.2014.05.113>
 111. Rizwan U (2015) Development of Γ -Ray Spectroscopy Techniques for Fundamental and Applied Research
 112. Sze, S.M. Semiconductor devices. Physics and technology, John Wiley & Sons, 1985
 113. Ljungvall, J. Characterisation of the Neutron Wall and of Neutron Interactions in Germanium-Detector System. *Acta Universitatis Upsaliensis. Digital Comprehensive Summaries of Uppsala Dissertations from the Faculty of Science and Technology* 66. viii+65pp.
 114. Mitchell LJ, Philips BF, Wulf EA, et al (2015) Γ -ray and neutron background comparison of US metropolitan areas. *Nucl Instruments Methods Phys Res Sect A Accel Spectrometers, Detect Assoc Equip.* <https://doi.org/10.1016/j.nima.2015.01.020>
 115. Halonen K 2 Master Thesis: Γ Spectrometry Analysis-Severe Accident Research
 116. Keyser, R.M. and Twomey, T.R. Efficiency for Close Geometries and Extended Sources of a P-type Germanium Detector with Low-energy Sensitivity. *Modern Trends in Activation Analysis - 11*, June 2004, Guildford, England.
 117. Folden III CM (2017) BASELINE MEASUREMENTS OF NATURAL RADIOACTIVITY AT THE TEXAS A&M ENGINEERING EXTENSION SERVICE-DISASTER CITY
 118. Leo, W.R. Techniques for Nuclear and Particles Physics Experiments. A How-to Approach. Second Revised Edition. Berlin: Springer-Verlag, 1994.
 119. Pittauerová D (2013) Γ spectrometry for chronology of recent sediments
 120. Taccetti, F. et al. Temperature and vacuum measurements on the commercial assembly of a largevolume Ge detector. *Nuclear Instruments and Methods in Physics Research A* 398 (1997) 238- 248.
 121. Bai J, Wang H, Ou J, et al (2016) Rapid “one-pot” preparation of polymeric monolith via photo-initiated thiol-acrylate polymerization for capillary liquid chromatography. *Anal Chim Acta.* <https://doi.org/10.1016/j.aca.2016.04.012>
 122. Koleška M, Viererbl L, Marek M, et al (2016) Determination of IRT-2M fuel burnup by γ spectrometry. *Appl Radiat Isot.* <https://doi.org/10.1016/j.apradiso.2015.10.001>
 123. Hugues Paradis PM, Elias Khan M, José Busto M, et al THESE DE DOCTORAT ECOLE DOCTORALE N° 576 PHENIICS : Particules hadrons énergie et noyau : instrumentation, image, cosmos et simulation Spécialité de doctorat : Imagerie médicale et radioactivité Composition du Jury
 124. Naem, S. Physics and Engineering of Radiation Detection. First Edition. USA: Academic Press Inc. Published by Elsevier, 2007

REFERENCES

125. Tsoufanidis, N. Measurement and Detection of Radiation. Second Edition. USA: Taylor & Francis, 1995.
126. Barichello G, Cervera-Villanueva A, Daniels DC, et al (2003) Performance of the NOMAD-STAR detector. Nucl Instruments Methods Phys Res Sect A Accel Spectrometers, Detect Assoc Equip. [https://doi.org/10.1016/S0168-9002\(03\)01379-2](https://doi.org/10.1016/S0168-9002(03)01379-2)
127. Fleuves et Rivières du Cameroun
128. Slaninka A, Slávik O, Nečas V (2010) Uncertainty analysis of in-situ γ spectrometry measurements of air cleaning filter cartridges and 200L drums by a HPGe detector. Appl Radiat Isot. <https://doi.org/10.1016/j.apradiso.2009.11.012>
129. Beretka J, Mathew PJ (1985) Natural radioactivity of australian building materials, industrial wastes and by-products. Health Phys. <https://doi.org/10.1097/00004032-198501000-00007>
130. Saraiva A, Oliveira C, Reis M, et al (2016) Study of the response of an ORTEC GMX45 HPGe detector with a multi-radionuclide volume source using Monte Carlo simulations. Appl Radiat Isot. <https://doi.org/10.1016/j.apradiso.2016.04.016>
131. ORTEC (2001) Modular Pulse Processing Electronics Catalog, Oak Ridge, USA, 83 – 84 www.ortec-online.com
132. ORTEC The Best Choice of High Purity Germanium (HPGe) Detector available from www.ortec-online.com
133. Keyser R., Twomey T., and Wagner S. (1990) “Benefits of using Super-Large Germanium Γ -Ray Detectors for the Quantitative Determination of Environmental Radionuclides,” Radioactivity and Radiochemistry, 1 (2): 46-56
134. Bajoga AD, Alazemi N, Regan PH, Bradley DA (2015) Radioactive investigation of NORM samples from Southern Kuwait soil using high-resolution γ -ray spectroscopy. Radiat Phys Chem. <https://doi.org/10.1016/j.radphyschem.2015.01.041>
135. Khandaker MU, Wahib NB, Amin YM, Bradley DA (2013) Committed effective dose from naturally occurring radionuclides in shellfish. Radiat Phys Chem. <https://doi.org/10.1016/j.radphyschem.2013.02.034>
136. Markovic N (2019) General rights Coincidence methods in γ -ray spectrometry for radioecological applications
137. Dowdall M, Bondar Y, Fristrup P, et al (2015) NKS-352, Advanced In-situ Γ Spectrometry Field Activity – Chernobyl (GAMFAC)
138. Shevelev AE, Khilkevitch EM, Lashkul SI, et al (2016) High performance γ -ray spectrometer for runaway electron studies on the FT-2 tokamak. Nucl Instruments Methods Phys Res Sect A Accel Spectrometers, Detect Assoc Equip. <https://doi.org/10.1016/j.nima.2016.05.075>
139. Dehimi FZ, Seghour A (2015) Neutron energy spectrum in a reactor exit channel with a single surface barrier sensor using GEANT4. Ann Nucl Energy. <https://doi.org/10.1016/j.anucene.2014.11.035>
140. Ababneh AM, Eyadeh MM (2015) Coincidence summing corrections in HPGe γ -ray spectrometry for Marinelli-beakers geometry using peak to total (P/T) calibration. J Radiat Res Appl Sci 8:323–327. <https://doi.org/10.1016/j.jrras.2015.05.003>
141. Dababneh S, Al-Nemri E, Sharaf J (2014) Application of Geant4 in routine close geometry γ spectroscopy for environmental samples. J Environ Radioact. <https://doi.org/10.1016/j.jenvrad.2014.02.019>
142. Britton R, Davies A V., Burnett JL, Jackson MJ (2015) A high-efficiency HPGe coincidence system for environmental analysis. J Environ Radioact. <https://doi.org/10.1016/j.jenvrad.2015.03.033>
143. Gharbi F, Oueslati M, Abdelli W, et al (2012) Exposure to radiation from the natural radioactivity in Tunisian building materials. Radiat Prot Dosimetry. <https://doi.org/10.1093/rpd/ncs045>
144. Amrani D, Tahtat M (2001) Natural radioactivity in Algerian building materials. Appl Radiat Isot.

REFERENCES

- [https://doi.org/10.1016/S0969-8043\(00\)00304-3](https://doi.org/10.1016/S0969-8043(00)00304-3)
145. Osae, E. et al. An empirical expression for the full energy peak efficiency of an N-type high purity germanium detector. *Journal of Radioanalytical and Nuclear Chemistry*, Vol. 242, Number 3 (1999) 617-622.
 146. C. S (1976) Comparison of Ge(Li) Well and N-Type Coaxial Detectors for Low-Energy γ Ray Analysis of Environmental Samples, *Radioelement Analysis: Progress and Problems*. In: Proc. of the 23er Conf. on Analytical Chemistry in Energy and Technology, Gatlingburg, Tennessee
 147. Xie F, Jiang W, Bai T, et al (2014) A study on activity determination of volume sources using point-like standard sources and Monte Carlo simulations. *Radiat Phys Chem*. <https://doi.org/10.1016/j.radphyschem.2014.05.042>
 148. Abbas MI, Badawi MS, Ruskov IN, et al (2015) Calibration of a single hexagonal NaI(Tl) detector using a new numerical method based on the efficiency transfer method. *Nucl Instruments Methods Phys Res Sect A Accel Spectrometers, Detect Assoc Equip*. <https://doi.org/10.1016/j.nima.2014.10.056>
 149. Hurtado S, Villa M (2010) An intercomparison of Monte Carlo codes used for in-situ γ -ray spectrometry. *Radiat Meas*. <https://doi.org/10.1016/j.radmeas.2010.06.001>
 150. XCOM Photon Cross Sections Database”, M.J. Berger et al, NIST, <http://www.nist.gov/pml/data/xcom/index.cfm>.
 151. Tari M, Moussavi Zarandi SA, Mohammadi K, Zare MR (2013) The measurement of γ -emitting radionuclides in beach sand cores of coastal regions of Ramsar, Iran using HPGe detectors. *Mar Pollut Bull*. <https://doi.org/10.1016/j.marpolbul.2013.06.030>
 152. Guembou Shouop JC, Moyo Ndontchueng M, Mekongtso Nguem JE, et al (2019) Determination of the natural radioactivity, elemental composition and geological provenance of sands from Douala in the littoral region of Cameroon using X-ray and γ -ray spectrometry. *Appl Earth Sci*. <https://doi.org/10.1080/25726838.2019.1637656>
 153. UNSCEAR (2000) Sources and Effects of Ionizing Radiation, United Nations Scientific Committee on the Effects of Atomic Radiation UNSCEAR 2000 Report to the General Assembly, with Scientific Annexes
 154. EC (1999) Radiological protection principles concerning the natural radioactivity of building materials - Radiation Protection 112
 155. Ravisankar R, Raghu Y, Harikrishnan N, Chandrasekaran A (2015) Assessment of Natural Radioactivity and Associated Radiation Hazards in Some Building Materials Used in Kilpenathur, Tiruvannamalai Dist, Tamilnadu, India. *African J Basic Appl Sci* 7:16–25. <https://doi.org/10.5829/idosi.ajbas.2015.7.1.1140>
 156. Stoulos S, Manolopoulou M, Papastefanou C (2003) Assessment of natural radiation exposure and radon exhalation from building materials in Greece. *J Environ Radioact*. [https://doi.org/10.1016/S0265-931X\(03\)00081-X](https://doi.org/10.1016/S0265-931X(03)00081-X)
 157. V.R. Krieger, Radioactivity of construction materials, *Betonwerk Fertigteil Technol*. 47 (1981) 468–473.
 158. Raghu Y, Harikrishnan N, Chandrasekaran A, Ravisankar R (2015) Assessment of natural radioactivity and associated radiation hazards in some building materials used in Kilpenathur, Tiruvannamalai dist, Tamilnadu, India. Longowal, India, p 020047
 159. Yang YX, Wu XM, Jiang ZY, et al (2005) Radioactivity concentrations in soils of the Xiazhuang granite area, China. *Appl Radiat Isot*. <https://doi.org/10.1016/j.apradiso.2005.02.011>
 160. Murty VRK, Karunakara N (2008) Natural radioactivity in the soil samples of Botswana. *Radiat Meas*. <https://doi.org/10.1016/j.radmeas.2008.10.004>
 161. Darko EO (2001) Natural radioactivity in soils and rocks within the Greater Accra Region of Ghana. *J Radioanal Nucl Chem*. <https://doi.org/10.1023/A:1013262702436>
 162. Yildiz N, Oto B, Turhan S, et al (2014) Radionuclide determination and radioactivity evaluation of

REFERENCES

- surface soil samples collected along the Erçek Lake basin in eastern Anatolia, Turkey. *J Geochemical Explor.* <https://doi.org/10.1016/j.gexplo.2014.07.013>
163. Rani A, Singh S (2005) Natural radioactivity levels in soil samples from some areas of Himachal Pradesh, India using γ -ray spectrometry. *Atmos Environ.* <https://doi.org/10.1016/j.atmosenv.2005.07.050>
 164. Samad O El, Alayan R, Baydoun R, Zaidan W (2012) RADIATION BASELINE LEVELS IN LEBANON: ENVIRONMENTAL SURVEY AND PUBLIC DOSE ASSESSMENT
 165. Al-Masri MS, Doubal AW (2013) Validation of in situ and laboratory γ spectrometry measurements for determination of ^{226}Ra , ^{40}K and ^{137}Cs in soil. *Appl Radiat Isot.* <https://doi.org/10.1016/j.apradiso.2013.01.009>
 166. Bellia S, Brai M, Hauser S, et al (1997) Natural radioactivity in a Volcanic Island: Ustica, Southern Italy. *Appl Radiat Isot.* [https://doi.org/10.1016/S0969-8043\(96\)00150-9](https://doi.org/10.1016/S0969-8043(96)00150-9)
 167. Steinhäusler F, Lettner H (2017) Radiometric Survey in Namibia. *Radiat Prot Dosimetry.* <https://doi.org/10.1093/oxfordjournals.rpd.a081602>
 168. Agbalagba EO, Onoja RA (2011) Evaluation of natural radioactivity in soil, sediment and water samples of Niger Delta (Biseni) flood plain lakes, Nigeria. *J Environ Radioact.* <https://doi.org/10.1016/j.jenvrad.2011.03.002>
 169. Agbalagba EO, Avwiri GO, Chad-Umoreh YE (2012) γ -Spectroscopy measurement of natural radioactivity and assessment of radiation hazard indices in soil samples from oil fields environment of Delta State, Nigeria. *J Environ Radioact.* <https://doi.org/10.1016/j.jenvrad.2011.10.012>
 170. Patiris DL, Tsabaris C, Anagnostou CL, et al (2016) Activity concentration and spatial distribution of radionuclides in marine sediments close to the estuary of Shatt al-Arab/Arvand Rud River, the Gulf. *J Environ Radioact.* <https://doi.org/10.1016/j.jenvrad.2016.02.025>
 171. Singh S, Rani A, Mahajan RK (2005) ^{226}Ra , ^{232}Th and ^{40}K analysis in soil samples from some areas of Punjab and Himachal Pradesh, India using γ ray spectrometry. *Radiat Meas.* <https://doi.org/10.1016/j.radmeas.2004.09.003>
 172. Senthilkumar B, Dhavamani V, Ramkumar S, Philominathan P (2010) Measurement of γ radiation levels in soil samples from Thanjavur using g-ray spectrometry and estimation of population exposure. *J Med Phys.* <https://doi.org/10.4103/0971-6203.55966>
 173. Britton R, Davies A V. (2015) Characterisation of a SAGE well detector using GEANT4 and LabSOCS. *Nucl Instruments Methods Phys Res Sect A Accel Spectrometers, Detect Assoc Equip.* <https://doi.org/10.1016/j.nima.2015.03.036>
 174. Fernandes JS, Appoloni CR, Andrello AC (2010) Applicability of an X-ray and γ -ray portable spectrometer for activity measurement of environmental soil samples. *Radiat Meas.* <https://doi.org/10.1016/j.radmeas.2010.03.007>
 175. Bronson FL (2003) Validation of the accuracy of the LabSOCS software for mathematical efficiency calibration of Ge detectors for typical laboratory samples. In: *Journal of Radioanalytical and Nuclear Chemistry*
 176. Tang X Bin, Meng J, Wang P, et al (2016) Simulated minimum detectable activity concentration (MDAC) for a real-time UAV airborne radioactivity monitoring system with HPGe and LaBr₃ detectors. *Radiat Meas.* <https://doi.org/10.1016/j.radmeas.2015.12.031>
 177. Azli T, Chaoui ZEA (2015) Performance revaluation of a N-type coaxial HPGe detector with front edges crystal using MCNPX. *Appl Radiat Isot.* <https://doi.org/10.1016/j.apradiso.2014.12.027>
 178. Hurtado S, Villa M, Manjón G, García-Tenorio R (2007) A self-sufficient and general method for self-absorption correction in γ -ray spectrometry using GEANT4. *Nucl Instruments Methods Phys Res Sect A Accel Spectrometers, Detect Assoc Equip.* <https://doi.org/10.1016/j.nima.2007.05.090>
 179. Asgharizadeh F, Abbasi A, Hochaghani O, Gooya ES (2012) Natural radioactivity in granite stones used as building materials in Iran. *Radiat Prot Dosimetry.* <https://doi.org/10.1093/rpd/ncr233>

REFERENCES

180. Kadum A, Bensaoula AH, Dahmani B (2013) Natural Radioactivity in Red Clay Brick Manufactured in Tlemcen-Algeria, Using Well-Shape NaI(Tl) Detector. Online
181. Exposure of radioactivity from building materials.pdf[1] “Exposure of radioactivity from building materials.pdf.” .
182. Zhang Y, Long Y, An J, et al (2014) Spatial patterns of ¹³⁷Cs inventories and soil erosion from earth-banked terraces in the Yimeng Mountains, China. *J Environ Radioact.* <https://doi.org/10.1016/j.jenvrad.2014.04.017>
183. Sharaf M, Mansy M, Sayed AEL, Abbas E (1999) Natural radioactivity and radon exhalation rates in building materials used in Egypt. *Radiat Meas.* [https://doi.org/10.1016/S1350-4487\(99\)00206-1](https://doi.org/10.1016/S1350-4487(99)00206-1)
184. Singh J, Singh H, Singh S, et al (2009) Comparative study of natural radioactivity levels in soil samples from the Upper Siwaliks and Punjab, India using γ -ray spectrometry. *J Environ Radioact.* <https://doi.org/10.1016/j.jenvrad.2008.09.011>
185. Ravisankar R, Vanasundari K, Chandrasekaran A, et al (2012) Measurement of natural radioactivity in building materials of Namakkal, Tamil Nadu, India using γ -ray spectrometry. *Appl Radiat Isot.* <https://doi.org/10.1016/j.apradiso.2011.12.001>
186. Ahmad N, Jaafar MS, Bakhsh M, Rahim M (2014) An overview on measurements of natural radioactivity in Malaysia. *J Radiat Res Appl Sci.* <https://doi.org/10.1016/j.jrras.2014.12.008>
187. Rafique M, Rehman H, Matiullah M, et al (2011) Assessment of radiological hazards due to soil and building materials used in Mirpur Azad Kashmir; Pakistan. *Iran J Radiat Res*
188. Khan K, Aslam M, Orfi SD, Khan HM (2002) Norm and associated radiation hazards in bricks fabricated in various localities of the North-West Frontier Province (Pakistan). *J Environ Radioact.* [https://doi.org/10.1016/S0265-931X\(01\)00030-3](https://doi.org/10.1016/S0265-931X(01)00030-3)
189. Thabayneh KM, Jazzar MM (2012) Natural Radioactivity Levels and Estimation of Radiation Exposure in Environmental Soil Samples from Tulkarem Province-Palestine. *Open J Soil Sci.* <https://doi.org/10.4236/ojss.2012.21002>
190. Huang Y, Lu X, Ding X, Feng T (2015) Natural radioactivity level in beach sand along the coast of Xiamen Island, China. *Mar Pollut Bull.* <https://doi.org/10.1016/j.marpolbul.2014.11.046>
191. El-Mageed AIA, Farid MEA, Saleh EE, et al (2014) Natural radioactivity and radiological hazards of some building materials of Aden, Yemen. *J Geochemical Explor.* <https://doi.org/10.1016/j.gexplo.2014.01.015>
192. Abd El-mageed AI, El-Kamel AH, Abbady A, et al (2011) Assessment of natural and anthropogenic radioactivity levels in rocks and soils in the environments of Juban town in Yemen. *Radiat Phys Chem.* <https://doi.org/10.1016/j.radphyschem.2011.02.025>
193. Petoussi-Hens N, Bolch WE, Eckerman KF, et al (2010) Conversion Coefficients for Radiological Protection Quantities for External Radiation Exposures. *Ann ICRP* 40:1–257. <https://doi.org/10.1016/j.icrp.2011.10.001>
194. ICRP (2007) ICRP Publication 103. *Ann ICRP.* <https://doi.org/10.1007/s13398-014-0173-7.2>
195. Alaamer AS (2012) Measurement of Natural Radioactivity in Sand Samples Collected from Ad-Dahna Desert in Saudi Arabia. *World J Nucl Sci Technol* 2:187–191. <https://doi.org/10.4236/wjnst.2012.24029>
196. Amiri J, Shirmardi SP, Eslamian JP (2014) Measuring natural radioactivity of bricks used in the constructions of Tehran
197. Gbenu ST, Oladejo OF, Olukotun SF, et al (2016) Assessment of radioactivity and radiological hazards in commercial ceramic tiles used in Ife-Central, local government area of Osun State, Nigeria. *Egypt J Basic Appl Sci.* <https://doi.org/10.1016/j.ejbas.2016.08.002>
198. Potts PJ (2013) X-ray fluorescence analysis: principles and practice of wavelength dispersive spectrometry. In: *A Handbook of Silicate Rock Analysis*
199. Potts PJ (2013) Energy dispersive x-ray spectrometry. In: *A Handbook of Silicate Rock Analysis*

REFERENCES

200. Potts PJ, Webb PC (1992) X-ray fluorescence spectrometry. *J Geochemical Explor.* [https://doi.org/10.1016/0375-6742\(92\)90052-A](https://doi.org/10.1016/0375-6742(92)90052-A)
201. Potts PJ (2013) Classical and rapid methods of analysis. In: *A Handbook of Silicate Rock Analysis*
202. Potts PJ (2013) Concepts in analytical chemistry. In: *A Handbook of Silicate Rock Analysis*
203. Norrish K, Hutton JT (1969) An accurate X-ray spectrographic method for the analysis of a wide range of geological samples. *Geochim Cosmochim Acta.* [https://doi.org/10.1016/0016-7037\(69\)90126-4](https://doi.org/10.1016/0016-7037(69)90126-4)
204. Reynolds R. C. J (1963) Matrix Corrections In Trace Element Analysis By X-Ray Fluorescence: Estimation Of The Mass Absorption Coefficient By Compton Scattering. *Am Mineral*
205. Reynolds R. C. J (1967) Estimation of mass absorption coefficients by Compton scattering: improvement and extensions of the method. *Amer Miner* 52:1493–1502
206. Enzweiler J, Webb PC (1996) Determination of trace elements in silicate rocks by X-ray fluorescence spectrometry on 1:5 glass discs: Comparison of accuracy and precision with pressed powder pellet analysis. *Chem Geol.* [https://doi.org/10.1016/0009-2541\(96\)00022-8](https://doi.org/10.1016/0009-2541(96)00022-8)
207. Vendemiatio MA, Enzweiler J (2007) Routine Control of Accuracy in Silicate Rock Analysis by X-Ray Fluorescence Spectrometry. *Geostand Geoanalytical Res.* <https://doi.org/10.1111/j.1751-908x.2001.tb00604.x>
208. Rousseau RM (2006) Corrections for matrix effects in X-ray fluorescence analysis-A tutorial. *Spectrochim. Acta - Part B At. Spectrosc.*
209. Duchesne JC, Bologne G (2009) XRF major and trace element determination in Fe-Ti oxide minerals. *Geol Belgica*
210. GOVINDARAJU K (1994) 1994 COMPILATION OF WORKING VALUES AND SAMPLE DESCRIPTION FOR 383 GEOSTANDARDS. *Geostand Newsl.* <https://doi.org/10.1046/j.1365-2494.1998.53202081.x-i1>
211. GOVINDARAJU K (1989) 1989 COMPILATION OF WORKING VALUES AND SAMPLE DESCRIPTION FOR 272 GEOSTANDARDS. *Geostand Newsl.* <https://doi.org/10.1111/j.1751-908X.1989.tb00476.x>
212. Govindaraju K (1994) Compilation of working values and descriptions for 383 geostandards. *Geostand Newsl.* <https://doi.org/10.1046/j.1365-2494.1998.53202081.x-i1>
213. Rangaswamy DR, Srilatha MC, Ningappa C, et al (2016) Measurement of natural radioactivity and radiation hazards assessment in rock samples of Ramanagara and Tumkur districts, Karnataka, India. *Environ Earth Sci.* <https://doi.org/10.1007/s12665-015-5195-8>
214. Carley, J., Pasternack, G., Wyrick, J., & Barker, J. (2012). Significant decadal channel change 58–67years post-dam accounting for uncertainty in topographic change detection between contour maps and point cloud models. *Environ Res Eng.* <https://doi.org/http://dx.doi.org/10.1016/j.nedt.2015.04.006>
215. Iyaka YA, Kakulu SE (2012) Heavy Metal Concentrations in Top Agricultural Soils around Ceramic and Pharmaceutical Industrial Sites in Niger State, Nigeria. *Res J Environ Earth Sci* 4:171–176
216. de Castilhos NDB, Melquiades FL, Thomaz EL, Bastos RO (2015) X-ray fluorescence and γ -ray spectrometry combined with multivariate analysis for topographic studies in agricultural soil. *Appl Radiat Isot.* <https://doi.org/10.1016/j.apradiso.2014.09.013>
217. Jozanikohan G, Sahabi F, Norouzi GH, et al (2016) Quantitative analysis of the clay minerals in the Shurijeh Reservoir Formation using combined X-ray analytical techniques. <https://doi.org/10.1016/j.rgg.201>
218. Hondrogiannis E, Peterson K, Zapf CM, et al (2012) The use of wavelength dispersive X-ray fluorescence and discriminant analysis in the identification of the elemental composition of cumin samples and the determination of the country of origin. *Food Chem.* <https://doi.org/10.1016/j.foodchem.2012.07.003>
219. Kubala-Kukuś A, Banaś D, Braziewicz J, et al (2014) X-ray spectrometry and X-ray microtomography

REFERENCES

- techniques for soil and geological samples analysis. *Nucl Instruments Methods Phys Res Sect B Beam Interact with Mater Atoms.* <https://doi.org/10.1016/j.nimb.2015.07.136>
220. Mintmier MA, Mills PR, Lundblad SP (2012) Energy-Dispersive X-Ray Fluorescence analysis of Haleakala basalt adze quarry materials, Maui, Hawai'i. *J Archaeol Sci.* <https://doi.org/10.1016/j.jas.2011.10.019>
221. Pessanha S, Gac A Le, Madeira TI, et al (2013) Elemental analysis by portable Ag and Rh X-ray sources of a Namban type folding screen. *Nucl Instruments Methods Phys Res Sect B Beam Interact with Mater Atoms.* <https://doi.org/10.1016/j.nimb.2013.01.078>
222. Forkapic S, Vasin J, Bikit I, et al (2017) Correlations between soil characteristics and radioactivity content of Vojvodina soil. *J Environ Radioact.* <https://doi.org/10.1016/j.jenvrad.2016.04.003>
223. Ramasamy V, Paramasivam K, Suresh G, Jose MT (2014) Role of sediment characteristics on natural radiation level of the Vaigai river sediment, Tamilnadu, India. *J Environ Radioact.* <https://doi.org/10.1016/j.jenvrad.2013.09.010>
224. Ramasamy V, Suresh G, Meenakshisundaram V, Ponnusamy V (2011) Horizontal and vertical characterization of radionuclides and minerals in river sediments. *Appl Radiat Isot.* <https://doi.org/10.1016/j.apradiso.2010.07.020>
225. Ramasamy V, Suresh G, Meenakshisundaram V, Gajendran V (2009) Characterization of minerals and naturally occurring radionuclides in river sediments. *Res J Appl Sci Eng Technol*
226. Tanaka R, Orihashi Y (1997) XRF analysis of major and trace elements for silicate rocks using low dilution ratio fused glass
227. Carmona N, Ortega-Feliu I, Gómez-Tubío B, Villegas MA (2010) Advantages and disadvantages of PIXE/PIGE, XRF and EDX spectrometries applied to archaeometric characterisation of glasses. *Mater Charact.* <https://doi.org/10.1016/j.matchar.2009.12.006>
228. Yatkin S, Belis CA, Gerboles M, et al (2016) An interlaboratory comparison study on the measurement of elements in PM10. *Atmos Environ.* <https://doi.org/10.1016/j.atmosenv.2015.10.084>
229. Ceccarelli L, Rossetti I, Primavesi L, Stoddart S (2016) Non-destructive method for the identification of ceramic production by portable X-rays Fluorescence (pXRF). A case study of amphorae manufacture in central Italy. *J Archaeol Sci Reports.* <https://doi.org/10.1016/j.jasrep.2016.10.002>
230. (2007) *Handbook of Practical X-Ray Fluorescence Analysis*
231. McLennan SM, Taylor SR, Eriksson KA (1983) Geochemistry of Archean shales from the Pilbara Supergroup, Western Australia. *Geochim Cosmochim Acta.* [https://doi.org/10.1016/0016-7037\(83\)90063-7](https://doi.org/10.1016/0016-7037(83)90063-7)
232. Solé VA, Papillon E, Cotte M, et al (2007) A multiplatform code for the analysis of energy-dispersive X-ray fluorescence spectra. *Spectrochim Acta - Part B At Spectrosc.* <https://doi.org/10.1016/j.sab.2006.12.002>
233. Stockmann U, Cattle SR, Minasny B, McBratney AB (2016) Utilizing portable X-ray fluorescence spectrometry for in-field investigation of pedogenesis. *Catena.* <https://doi.org/10.1016/j.catena.2016.01.007>
234. Radu T, Diamond D (2009) Comparison of soil pollution concentrations determined using AAS and portable XRF techniques. *J Hazard Mater.* <https://doi.org/10.1016/j.jhazmat.2009.06.062>
235. Blagoev K, Grozeva M, Malcheva G, Neykova S (2013) Investigation by laser induced breakdown spectroscopy, X-ray fluorescence and X-ray powder diffraction of the chemical composition of white clay ceramic tiles from Veliki Preslav. *Spectrochim Acta - Part B At Spectrosc.* <https://doi.org/10.1016/j.sab.2012.11.003>
236. Smith AL, Colle JY, Raison PE, et al (2015) Thermodynamic investigation of Na-U-O using Knudsen effusion mass spectrometry and high temperature X-ray diffraction. *J Chem Thermodyn.* <https://doi.org/10.1016/j.jct.2015.06.026>

REFERENCES

237. Franzen HF, Gilles PW (1965) High-temperature vaporization and thermodynamic properties of titanium monosulfide. *J Chem Phys.* <https://doi.org/10.1063/1.1696039>
238. Li W, Zhu J, Ma X, et al (2012) Geometrical factor correction in grazing incident x-ray fluorescence experiment. *Rev. Sci. Instrum.*
239. Baba Y, Shimoyama I, Hirao N (2016) Chemical state analysis of trace-level alkali metals sorbed in micaceous oxide by total reflection X-ray photoelectron spectroscopy. *Appl Surf Sci.* <https://doi.org/10.1016/j.apsusc.2016.05.067>
240. Baba Y, Shimoyama I, Hirao N (2016) Chemical state analysis of trace-level alkali metals sorbed in micaceous oxide by total reflection X-ray photoelectron spectroscopy. *Appl Surf Sci.* <https://doi.org/10.1016/j.apsusc.2016.05.067>
241. Towett EK, Shepherd KD, Cadisch G (2013) Quantification of total element concentrations in soils using total X-ray fluorescence spectroscopy (TXRF). *Sci Total Environ.* <https://doi.org/10.1016/j.scitotenv.2013.05.068>
242. Towett EK, Shepherd KD, Tondoh JE, et al (2015) Total elemental composition of soils in Sub-Saharan Africa and relationship with soil forming factors. *Geoderma Reg.* <https://doi.org/10.1016/j.geodrs.2015.06.002>
243. Kaniu MI, Angeyo KH, Mwala AK, Mangala MJ (2012) Direct rapid analysis of trace bioavailable soil macronutrients by chemometrics-assisted energy dispersive X-ray fluorescence and scattering spectrometry. *Anal Chim Acta.* <https://doi.org/10.1016/j.aca.2012.04.007>
244. Kaniu MI, Angeyo KH (2015) Challenges in rapid soil quality assessment and opportunities presented by multivariate chemometric energy dispersive X-ray fluorescence and scattering spectroscopy. *Geoderma.* <https://doi.org/10.1016/j.geoderma.2014.10.014>
245. Kaniu MI, Angeyo KH, Mwala AK, Mwangi FK (2012) Energy dispersive X-ray fluorescence and scattering assessment of soil quality via partial least squares and artificial neural networks analytical modeling approaches. *Talanta.* <https://doi.org/10.1016/j.talanta.2012.06.081>
246. van Espen P, Nullens H, Adams F (1977) A computer analysis of X-ray fluorescence spectra. *Nucl Instruments Methods* 142:243–250. [https://doi.org/10.1016/0029-554X\(77\)90834-5](https://doi.org/10.1016/0029-554X(77)90834-5)
247. Vekemans B, Janssens K, Vincze L, et al (1995) Comparison of several background compensation methods useful for evaluation of energy-dispersive X-ray fluorescence spectra. *Spectrochim Acta Part B At Spectrosc.* [https://doi.org/10.1016/0584-8547\(94\)00118-F](https://doi.org/10.1016/0584-8547(94)00118-F)
248. Kubala-Kukuś A, Ludwikowska-Kędzia M, Banaś D, et al (2013) Application of the X-ray fluorescence analysis and X-ray diffraction in geochemical studies of the Pleistocene tills from Holy Cross Mountains. *Radiat Phys Chem.* <https://doi.org/10.1016/j.radphyschem.2013.03.049>
249. Banaś D, Kubala-Kukuś A, Braziewicz J, et al (2013) Study of properties of chemically modified samples of halloysite mineral with X-ray fluorescence and X-ray powder diffraction methods. *Radiat Phys Chem.* <https://doi.org/10.1016/j.radphyschem.2013.05.028>
250. Hinrichs R, Bertol APL, Vasconcellos MAZ (2015) Analysis of trace elements in opal using PIXE. In: *Nuclear Instruments and Methods in Physics Research, Section B: Beam Interactions with Materials and Atoms*
251. Kotov YD, Yurov VN, Glyanenko AS, et al (2016) Solar X-ray polarimetry and spectrometry instrument PING-M for the Interhelioprobe mission. *Adv Sp Res.* <https://doi.org/10.1016/j.asr.2016.05.024>
252. Dao TH, Miao YX, Zhang FS (2011) X-ray fluorescence spectrometry-based approach to precision management of bioavailable phosphorus in soil environments. *J Soils Sediments.* <https://doi.org/10.1007/s11368-011-0347-2>
253. Roser BP, Korsch RJ (1988) Provenance signatures of sandstone-mudstone suites determined using discriminant function analysis of major-element data. *Chem Geol.* [https://doi.org/10.1016/0009-2541\(88\)90010-1](https://doi.org/10.1016/0009-2541(88)90010-1)
254. Pettijohn FJ, Potter PE, Siever R (2006) *Sand and Sandstone.* *Soil Sci.*

REFERENCES

- <https://doi.org/10.1097/00010694-197402000-00013>
255. WHETTEN JT (2016) PETTIJOHN, F. J., P. E. POTTER, AND R. SIEVER. 1972. Sand and sandstone. Springer-Verlag, New York. xvi + 618 p. \$31.10. . *Limnol Oceanogr.* <https://doi.org/10.4319/lo.1973.18.1.0182>
256. Grunert S (2007) F. J. Pettijohn, P. E. Potter, R. Siever. Sand and sandstones, Springer-Verlag; New York, Berlin, Heidelberg, London, Paris, Tokyo, 1987, 2nd ed., XVIII + 553 S., 355 Abb., 58 Tab., DM 118, —, ISBN 3-540-96350-2. *Cryst Res Technol.* <https://doi.org/10.1002/crat.2170230713>
257. Osaе S, Asiedu DK, Banoeng-Yakubo B, et al (2006) Provenance and tectonic setting of Late Proterozoic Buem sandstones of southeastern Ghana: Evidence from geochemistry and detrital modes. *J African Earth Sci.* <https://doi.org/10.1016/j.jafrearsci.2005.11.009>
258. Bhatia MR (2009) Plate Tectonics and Geochemical Composition of Sandstones: A Reply. *J Geol.* <https://doi.org/10.1086/628922>
259. Bhatia MR, Crook KAW (1986) Trace element characteristics of graywackes and tectonic setting discrimination of sedimentary basins. *Contrib to Mineral Petrol.* <https://doi.org/10.1007/BF00375292>
260. Bhatia MR (1985) Rare earth element geochemistry of Australian Paleozoic graywackes and mudrocks: Provenance and tectonic control. *Sediment Geol.* [https://doi.org/10.1016/0037-0738\(85\)90025-9](https://doi.org/10.1016/0037-0738(85)90025-9)
261. Taylor SR, McLennan S (1985) Continental crust: its composition and evolution. An examination of the geochemical record preserved in sedimentary rocks. Oxford, Blackwell Sci. <https://doi.org/10.1017/S0016756800032167>
262. Anani C, Moradeyo M, Atta-Peters D, et al (2013) Geochemistry and provenance of sandstones from Anyaboni and surrounding areas in the voltaian basin, Ghana 1*. *Int Res J Geol Min*
263. Anani C (1999) Sandstone petrology and provenance of the Neoproterozoic Voltaian group in the southeastern Voltaian Basin, Ghana. *Sediment Geol.* [https://doi.org/10.1016/S0037-0738\(99\)00063-9](https://doi.org/10.1016/S0037-0738(99)00063-9)
264. Fitton JG, Dunlop HM (1985) The Cameroon line, West Africa, and its bearing on the origin of oceanic and continental alkali basalt. *Earth Planet Sci Lett.* [https://doi.org/10.1016/0012-821X\(85\)90114-1](https://doi.org/10.1016/0012-821X(85)90114-1)
265. Fitton JG (2008) The Cameroon line, West Africa: a comparison between oceanic and continental alkaline volcanism. *Geol Soc London, Spec Publ.* <https://doi.org/10.1144/gsl.sp.1987.030.01.13>
266. Caldeira R, Munhá JM (2002) Petrology of ultramafic nodules from São Tomé Island, Cameroon Volcanic Line (oceanic sector). *J African Earth Sci.* [https://doi.org/10.1016/S0899-5362\(02\)00022-2](https://doi.org/10.1016/S0899-5362(02)00022-2)
267. Déruelle B, Ngounouno I, Demaiffé D (2007) The “Cameroon Hot Line” (CHL): A unique example of active alkaline intraplate structure in both oceanic and continental lithospheres. *Comptes Rendus - Geosci.*
268. Halliday AN, Davidson JP, Holden P, et al (1990) Trace-element fractionation in plumes and the origin of HIMU mantle beneath the Cameroon line. *Nature.* <https://doi.org/10.1038/347523a0>
269. Zhang HH, Yang CL, Wu ZF, et al (2008) Spatial Distributions and Potential Risk Analysis of Total Soil Selenium in Guangdong Province, China. *J Environ Qual.* <https://doi.org/10.2134/jeq2007.0154>
270. Pierre Tchouankoue J (2012) Petrology, Geochemistry, and Geodynamic Implications of Basaltic Dyke Swarms from the Southern Continental Part of the Cameroon Volcanic Line, Central Africa. *Open Geol J.* <https://doi.org/10.2174/1874262901206010072>
271. Herron M (1988) Geochemical classification of terrigenous sands and shales from core or log data. *J Sediment Petrol*
272. Michael M. Herron (2003) Geochemical Classification of Terrigenous Sands and Shales from Core or Log Data. *SEPM J Sediment Res.* <https://doi.org/10.1306/212f8e77-2b24-11d7-8648000102c1865d>
273. Schlüter T (2006) Geological Atlas of Africa: with notes on stratigraphy, tectonics, Economic Geology, Geohazard and Geosites of Each Country
274. Hranitzky C, Stadtmann H (2007) Monte Carlo study of a ⁶⁰Co calibration field of the Dosimetry

REFERENCES

- Laboratory Seibersdorf. In: Radiation Protection Dosimetry
275. Mora GM, Maio A, Rogers DWO (1999) Monte Carlo simulation of a typical ^{60}Co therapy source. *Med Phys.* <https://doi.org/10.1118/1.598770>
 276. Mainegra-Hing E, Kawrakow I, Rogers DWO (2003) Calculations for plane-parallel ion chambers in ^{60}Co beams using the EGSnrc Monte Carlo code. *Med Phys.* <https://doi.org/10.1118/1.1536291>
 277. Baró J, Sempau J, Fernández-Varea JM, Salvat F (1994) Simplified Monte Carlo simulation of elastic electron scattering in limited media. *Nucl Inst Methods Phys Res B.* [https://doi.org/10.1016/0168-583X\(94\)95341-4](https://doi.org/10.1016/0168-583X(94)95341-4)
 278. Kawrakow I, I. Kawrakow, Kawrakow I, I. Kawrakow (2013) The EGSnrc Code System : Monte Carlo Simulation of Electron and Photon Transport. *Med Phys*
 279. Grichine VM., Kostin AP., Kotelnikov SK. et al. (1994). *Bulletin of the Lebedev Institute no. 2 (3): 34*
 280. Fermi E (1932) Quantum theory of radiation. *Rev Mod Phys.* <https://doi.org/10.1103/RevModPhys.4.87>
 281. B hm J, Alberts WG, Swinth KL, et al (1999) ISO Recommended Reference Radiations for the Calibration and Proficiency Testing of Dosimeters and Dose Rate Meters used in Radiation Protection. *Radiat Prot Dosimetry.* <https://doi.org/10.1093/oxfordjournals.rpd.a032936>
 282. Budjáš D, Heisel M, Maneschg W, Simgen H (2009) Optimisation of the MC-model of a p-type Ge-spectrometer for the purpose of efficiency determination. *Appl Radiat Isot.* <https://doi.org/10.1016/j.apradiso.2009.01.015>
 283. Britton R, Burnett J, Davies A, Regan PH (2013) Determining the efficiency of a broad-energy HPGe detector using Monte Carlo simulations. *J Radioanal Nucl Chem.* <https://doi.org/10.1007/s10967-012-2203-2>
 284. Androulakaki EG, Kokkoris M, Tsabaris C, et al (2016) In situ γ -ray spectrometry in the marine environment using full spectrum analysis for natural radionuclides. *Appl Radiat Isot.* <https://doi.org/10.1016/j.apradiso.2016.05.008>
 285. Breier R, Laubenstein M, Povinec PP (2017) Monte Carlo simulation of background characteristics of a HPGe detector operating underground in the Gran Sasso National Laboratory. *Appl Radiat Isot.* <https://doi.org/10.1016/j.apradiso.2016.12.039>
 286. Britton R, Burnett JL, Davies A V., Regan PH (2013) Improving the effectiveness of a low-energy Compton suppression system. *Nucl Instruments Methods Phys Res Sect A Accel Spectrometers, Detect Assoc Equip.* <https://doi.org/10.1016/j.nima.2013.06.111>
 287. Chagren S, Tekaya M Ben, Reguigui N, Gharbi F (2016) Efficiency transfer using the GEANT4 code of CERN for HPGe γ spectrometry. *Appl Radiat Isot.* <https://doi.org/10.1016/j.apradiso.2015.11.026>
 288. Crespi FCL, Camera F, Million B, et al (2008) A novel technique for the characterization of a HPGe detector response based on pulse shape comparison. In: *IEEE Nuclear Science Symposium Conference Record*
 289. Li G, Liang Y, Xu J, Bai L (2015) Efficiency corrections in determining the ^{137}Cs inventory of environmental soil samples by using relative measurement method and GEANT4 simulations. *J Environ Radioact.* <https://doi.org/10.1016/j.jenvrad.2015.04.012>
 290. Hurtado S, García-León M, García-Tenorio R (2004) GEANT4 code for simulation of a germanium γ -ray detector and its application to efficiency calibration. *Nucl Instruments Methods Phys Res Sect A Accel Spectrometers, Detect Assoc Equip.* <https://doi.org/10.1016/j.nima.2003.09.057>
 291. Hurtado S, García-León M, García-Tenorio R (2004) Monte Carlo simulation of the response of a germanium detector for low-level spectrometry measurements using GEANT4. In: *Applied Radiation and Isotopes*
 292. Hansman J, Mrdja D, Slivka J, et al (2015) Efficiency study of a big volume well type NaI(Tl) detector by point and voluminous sources and Monte-Carlo simulation. *Appl Radiat Isot.* <https://doi.org/10.1016/j.apradiso.2015.03.003>

REFERENCES

293. Nikolic J, Vidmar T, Jokovic D, et al (2014) Calculation of HPGe efficiency for environmental samples: Comparison of EFFTRAN and GEANT4. Nucl Instruments Methods Phys Res Sect A Accel Spectrometers, Detect Assoc Equip. <https://doi.org/10.1016/j.nima.2014.06.044>
294. McNamara AL, Heijnis H, Fierro D, Reinhard MI (2012) The determination of the efficiency of a Compton suppressed HPGe detector using Monte Carlo simulations. J Environ Radioact.
295. Nikolic J, Puzovic J, Todorovic D, Rajacic M (2015) Application of PHOTON simulation software on calibration of HPGe detectors. Nucl Instruments Methods Phys Res Sect A Accel Spectrometers, Detect Assoc Equip. <https://doi.org/10.1016/j.nima.2015.08.002>
296. Nikolic JD, Jokovic D, Todorovic D, Rajacic M (2014) Application of GEANT4 simulation on calibration of HPGe detectors for cylindrical environmental samples. J Radiol Prot. <https://doi.org/10.1088/0952-4746/34/2/N47>
297. Sivers M V., Hofmann M, Mannel T, et al (2014) Low-level γ -ray spectrometry at the underground laboratory Garching. Appl Radiat Isot. <https://doi.org/10.1016/j.apradiso.2014.05.010>
298. Stanić G, Nikolov J, Tucaković I, et al (2019) Angle vs. LabSOCS for HPGe efficiency calibration. Nucl Instruments Methods Phys Res Sect A Accel Spectrometers, Detect Assoc Equip. <https://doi.org/10.1016/j.nima.2018.12.059>
299. Carley, J., Pasternack, G., Wyrick, J., & Barker, J. (2012). Significant decadal channel change 58–67years post-dam accounting for uncertainty in topographic change detection between contour maps and point cloud models. *Geomorphology* (173) 45 <http://ascelibrary.org/doi/abs/10.1061/40792>.
300. Lin YC, Huang T Te, Liu YH, et al (2015) Monte Carlo simulations and benchmark measurements on the response of TE(TE) and Mg(Ar) ionization chambers in photon, electron and neutron beams. Nucl Instruments Methods Phys Res Sect A Accel Spectrometers, Detect Assoc Equip. <https://doi.org/10.1016/j.nima.2015.01.061>
301. Geant4 User's Guide for Application Developers Geant4 Collaboration Geant4 User's Guide for Application Developers by Geant4 Collaboration
302. Scot V, Fernandez JE (2015) The Monte Carlo code MCSHAPE: Main features and recent developments. Spectrochim Acta - Part B At Spectrosc. <https://doi.org/10.1016/j.sab.2015.02.005>
303. Östlund K, Samuelsson C, Rääf CL (2015) Experimentally determined vs: Monte Carlo simulated peak-to-valley ratios for a well-characterised n-type HPGe detector. Appl Radiat Isot. <https://doi.org/10.1016/j.apradiso.2014.09.022>
304. Salvat F (2001) P ENVELOPE – A Code System for Monte Carlo Simulation of Electron and Photon Transport A Code System for Monte Carlo. In: Workshop Proceedings
305. Lehmer DH (1951) Mathematical Methods in Large-scale Computing Units. Ann Comput Lab Harvard Univ
306. Agostinelli S, Allison J, Amako K, et al (2003) GEANT4 - A simulation toolkit. Nucl Instruments Methods Phys Res Sect A Accel Spectrometers, Detect Assoc Equip. [https://doi.org/10.1016/S0168-9002\(03\)01368-8](https://doi.org/10.1016/S0168-9002(03)01368-8)
307. SHOUOP Cebastien Joel G, MOYO Maurice N, Ousmanou M, et al Questioning Paper Title: The interest of Muon-Antimuon ($\mu^- - \mu^+$) pair production: $\mu^- \mu^+ \rightarrow \mu^- \mu^+$
308. Tanaka S, Kelner S, Pfeiffer A, et al (2003) Geant4—a simulation toolkit. Nucl Instruments Methods Phys Res Sect A Accel Spectrometers, Detect Assoc Equip. [https://doi.org/10.1016/s0168-9002\(03\)01368-8](https://doi.org/10.1016/s0168-9002(03)01368-8)
309. Geant4 User's Guide for Toolkit Developers
310. Penelope (2001) - A Code System for Monte Carlo Simulation of Electron and Photon Transport, Workshop Proceedings Issy-les-Moulineaux, France, 5–7 November 2001, AEN-NEA
311. Allison J and others (2006) Geant4. Nucl Sci IEEE Trans (Volume53 , Issue 1). <https://doi.org/10.1109/TNS.2006.869826>

REFERENCES

312. Britton R, Burnett J, Davies A, Regan PH (2013) Preliminary simulations of NaI(Tl) detectors, and coincidence analysis using event stamping. *J Radioanal Nucl Chem.* <https://doi.org/10.1007/s10967-012-1811-1>
313. Szentmiklósi L, Belgya T, Maróti B, Kis Z CHARACTERIZATION OF HPGE Γ SPECTROMETERS BY GEANT4 MONTE CARLO SIMULATIONS
314. Canberra Industries (2013) Genie™ 2000 Customization Tools Manual v3.4
315. Osa E, Nyarko BJB, Serfor-Armah Y, Darko EO (1999) An empirical expression for the full energy peak efficiency of an N-type high purity germanium detector. *J Radioanal Nucl Chem.* <https://doi.org/10.1007/BF02347370>
316. Allison J (2007) Geant4 – A Simulation Toolkit. *Nucl Phys News* 17:20–24. <https://doi.org/10.1080/10506890701404297>
317. Joković DR, Dragić A, Udovičić V, et al (2009) Monte Carlo simulations of the response of a plastic scintillator and an HPGe spectrometer in coincidence. *Appl Radiat Isot.* <https://doi.org/10.1016/j.apradiso.2009.01.024>
318. Krmar M, Hansman J, Jovančević N, et al (2013) A method to estimate a contribution of Ge(n,n') reaction to the low-energy part of γ spectra of HPGe detectors. *Nucl Instruments Methods Phys Res Sect A Accel Spectrometers, Detect Assoc Equip.* <https://doi.org/10.1016/j.nima.2012.12.122>
319. Akkurt I, Gunoglu K, Arda SS (2014) Detection Efficiency of NaI(Tl) Detector in 511–1332 keV Energy Range. *Sci Technol Nucl Install.* <https://doi.org/10.1155/2014/186798>
320. Ngeve MN, Leermakers M, Elskens M, Kochzius M (2015) Assessment of trace metal pollution in sediments and intertidal fauna at the coast of Cameroon. *Environ Monit Assess.*
321. Berger M, Hubbell J, Seltzer S, et al (1998) XCOM: Photon cross sections database. NIST Stand Ref database